DOE/NV/10282--1013
Conf-830528--6

GUY SHERMAN, JR. TRAFFIC OFFICER
EG&G, INC. ENERGY MEASUREMENTS GROUP
AUTHOR

DOE/NV/10282--1013

DE83 011261

CHERYL A. LOPEZ, CHIEF TRAFFIC AGENT
REYNOLDS ELECTRICAL & ENGINEERING CO., INC.

ALFRED T. NEUMANN, TRAFFIC MANAGER
U.S. DEPARTMENT OF ENERGY, NEVADA OPERATIONS OFFICE
Co-Authors

DISCLAIMER

U.S. DEPARTMENT OF ENERGY/NEVADA OPERATIONS EXPERIENCE IN THE TRANSPORT OF SPENT NUCLEAR REACTOR FUEL ASSEMBLIES

This work was performed under the auspices of the U.S. Department of Energy under Contract No. DE-AC08-83NV10282.

THIS PRESENTATION WILL INVOLVE A DESCRIPTION OF OUR EXPERIENCES WITH THE TRANSPORT AND STORAGE OF SPENT NUCLEAR REACTOR FUEL ASSEMBLIES USING THE "DRY METHOD." THE ASSEMBLIES INVOLVED IN OUR DISCUSSION CAME FROM PRESSURIZED WATER REACTORS (PWR).

ON-SITE STORAGE POOLS AT NUCLEAR GENERATING PLANTS ARE RAPIDLY BECOMING CONGESTED; THEREFORE, IT WAS INEVITABLE THAT CONSIDERATION BE GIVEN TO NEW METHODS OF STORING LARGE QUANTITIES OF THESE HIGHLY RADIOACTIVE WASTE MATERIALS. THERE ARE A NUMBER OF PILOT PROJECTS BEING CONDUCTED THROUGHOUT THE UNITED STATES TO DETERMINE THE MOST ADVANTAGEOUS METHOD OF STORING THE MATERIALS FOR LONG PERIODS OF TIME. OUR PRESENTATION WILL COVER ONLY THE TRANSPORTATION OF THE SPENT FUEL ASSEMBLIES AND PORTIONS OF THE ONGOING PROGRAMS THAT ARE BEING EVALUATED AT THE NEVADA TEST SITE (NTS).

THE ESTABLISHED OBJECTIVE DURING THE STORAGE OF THE PWR SPENT FUEL ASSEMBLIES IS TO COLLECT DATA FROM SEVERAL DIFFERENT STORAGE CONFIGURATIONS UNDER VARIOUS AMBIENT CONDITIONS. DURING ALL REMOTELY HANDLED LOADING AND UNLOADING OPERATIONS AT THE NTS IN SHIELDED CONFIGURATION, PERSONNEL EXPOSURE WAS LESS THAN PRESCRIBED STANDARDS ALLOWED.

IN JULY 1979 AFTER DISCUSSIONS BETWEEN DOE, NRC, FLORIDA POWER AND LIGHT, AND WESTINGHOUSE, A DECISION WAS MADE TO SHIP THIRTEEN (13) SPENT FUEL ASSEMBLIES. THE SHIPMENTS ORIGINATED AT THE FLORIDA POWER AND LIGHT GENERATING FACILITY AT TURKEY POINT, FLORIDA, AND WERE TRANSPORTED TO THE BATTELLE MEMORIAL LABORATORY IN WEST JEFFERSON, MADISON COUNTY, OHIO, AND TO THE NEVADA TEST SITE, NORTHWEST

OF LAS VEGAS, NEVADA. ARRANGEMENTS WERE MADE TO SECURE THE SERVICES OF A CARRIER ABLE TO PROVIDE DRIVERS HOLDING A DOE SECURITY CLEARANCE. TWO TRAILERS AND CASKS WERE LEASED AS MATED UNITS AND USED IN TRANSPORTING THE SPENT FUEL ASSEMBLIES. BECAUSE OF THE WEIGHT RESTRICTIONS THROUGH CERTAIN STATES, IT WAS MANDATORY THAT THE TRANSPORT UNIT'S GROSS WEIGHT NOT EXCEED THE LEGAL LIMIT.

ADDITIONALLY, THE CARRIER WAS INSTRUCTED TO ASSIGN TWO DRIVERS TO EACH SHIPMENT. THE U.S. DEPARTMENT OF ENERGY REQUIRED THAT THE DRIVERS ASSIGNED TO THE OPERATIONS BE PROVIDED WITH BASIC TRAINING IN THE FOLLOWING AREAS:

1. SECURITY PROCEDURES WHILE ENROUTE.

2. COORDINATION WITH LAW ENFORCEMENT AGENCIES WHEN NECESSARY.

3. COMMUNICATION PROCEDURES WHILE ENROUTE.

4. FAMILIARIZATION WITH THE POTENTIAL RADIOLOGICAL HAZARDS INVOLVED IN SPENT FUEL ASSEMBLIES SHIPMENTS.

5. RADIOLOGICAL SAFETY PROCEDURES TO BE IMPLEMENTED AS REQUIRED IN THE EVENT OF AN INCIDENT OR ACCIDENT.

FOLLOWING THE TRAINING, EACH DRIVER WAS GIVEN A WRITTEN EXAMINATION OR AN APPROPRIATE APPRAISAL TO VERIFY READINESS IN CARRYING OUT ASSIGNED DUTIES AND RESPONSIBILITIES.

OTHER EMERGENCY PROCEDURES REQUIRED IN THE EVENT OF AN ATTEMPTED THEFT, HI-JACKING OR CIVIL DISORDER WERE AS FOLLOWS:

1. THE CAPABILITY OF ONE PERSON INSIDE THE CAB OF THE TRACTOR TO IMMOBILIZE THE TRANSPORT EQUIPMENT WITHOUT POSING A SAFETY HAZARD. AFTER IMMOBILIZATION, AT LEAST A 1/2 HOUR INTERVAL WOULD BE REQUIRED TO RETURN THE TRANSPORT VEHICLE TO OPERATION USING ONLY TOOLS AND MATERIALS FOUND ON THE VEHICLE.

2. SAFE HAVENS WERE ESTABLISHED ALONG THE ROUTE AT DISTANCES NOT EXCEEDING 400 MILES BETWEEN LOCATIONS.

AFTER THE PRECEDING ARRANGEMENTS WERE MADE AND REQUIREMENTS MET, EG&G, INC., WAS SELECTED TO BE THE SHIPPER OF RECORD FOR THE DEPARTMENT OF ENERGY AND ACCOMPLISH THE SHIPMENTS OF THE SPENT FUEL ASSEMBLIES. THREE (3) EG&G EMPLOYEES ATTENDED THE PRELIMINARY MEETING IN MIAMI TO DISCUSS THE COORDINATION NEEDED TO EFFECT THE SHIPMENTS, AND AFTER RECEIVING TRAINING AND INDOCTRINATION IN PLANT PROCEDURES AT TURKEY POINT, THE LOADING OF THE SPENT FUEL ASSEMBLIES BEGAN ON SEPTEMBER 6, 1979. THE FIRST TWO (2) SHIPMENTS WERE DISPATCHED TO BATTELLE ON SEPTEMBER 7, 1979, WITH SUBSEQUENT SHIPMENT TO BOTH BATTELLE AND THE NEVADA TEST SITE CONTINUING THROUGH NOVEMBER 8, 1979. ULTIMATELY, ALL ASSEMBLIES WERE TRANSPORTED TO THE NEVADA TEST SITE.

THE SHIPPING PROCESS BEGAN WITH:

1. IDENTIFICATION OF THE SPENT FUEL ASSEMBLIES TO BE SHIPPED.

2. THE PLACEMENT OF THE SPENT FUEL IN THE CASK (ALL OF THIS DONE UNDER WATER IN THE SPENT FUEL STORAGE POOL).

3. PLACEMENT OF THE INNER HEAD OF THE CASK.

4. REMOVAL OF THE CASK FROM THE STORAGE POOL AND PLACING THE CASK IN THE WASH DOWN WORK AREA FOR DECONTAMINATION.

5. MONITORING THE REMAINING CONTAMINATION OF THE CASKS BY HEALTH PHYSICS PERSONNEL USING RADIATION MEASURING INSTRUMENTS AND SMEARS.

6. LOADING AND SECURING THE CASK ON THE TRAILER.

7. FINAL MONITORING OF THE CASK BY HEALTH PHYSICS PERSONNEL PRIOR TO RELEASE FOR TRANSPORTATION.

UPON DEPARTING THE PLANT, THE DRIVERS WERE REQUIRED TO FOLLOW A PREPLANNED ROUTE TO THE DESTINATIONS IN OHIO AND NEVADA. ALSO, THE DRIVERS WERE REQUIRED TO REPORT THEIR PROGRESS EVERY FOUR (4) HOURS. THIS WAS ACCOMPLISHED BY PHONE CALLS TO THEIR DISPATCHER WHO IN TURN CALLED THE MAIN GUARD STATION AT THE U.S. DEPARTMENT OF ENERGY, NEVADA OPERATIONS OFFICE, IN LAS VEGAS, NEVADA. WHEN THE DRIVERS STOPPED FOR FUEL OR MEALS ONE PERSON HAD TO REMAIN WITH THE UNIT AT ALL TIMES IN ORDER TO MAINTAIN SURVEILLANCE OVER THE LOAD. THE NORMAL

TRANSIT TIME BETWEEN TURKEY POINT AND BATTELLE LABS IN OHIO WAS APPROXIMATELY EIGHTEEN (18) HOURS AND BETWEEN TURKEY POINT AND THE NEVADA TEST SITE, FORTY-NINE (49) TO FIFTY-ONE (51) HOURS.

DURING THE PRE-SHIPMENT DISCUSSIONS, IT WAS DETERMINED THAT DOE WOULD MEET OR SURPASS THE EXISTING PUBLIC PROTECTION STANDARDS GOVERNING THE SHIPMENT OF THE SPENT FUEL IN ORDER TO PROVIDE MAXIMUM SAFEGUARDS TO THE PUBLIC. ALTHOUGH THE ENTIRE SHIPPING OPERATION APPEARED TO PROCEED SMOOTHLY, THE FOLLOWING PROBLEMS OCCURRED AND WERE SUCCESSFULLY SOLVED.

1. CASK DECONTAMINATION WAS UNUSUALLY LENGTHY DURING THE FIRST SHIPMENTS BECAUSE OF WORK CREW SCHEDULING AND FAILURE TO USE "GOOD OLD SOAP AND WATER" TO WASH THE CASK IMMEDIATELY UPON REMOVAL FROM THE SPENT FUEL STORAGE POOL.

2. THE WORK CREW SCHEDULING PROBLEM CENTERED AROUND THE FOLLOWING TWO FACTORS:

   a. INITIALLY THE WORK CREW WAS NOT ASSIGNED AND DEDICATED TO THE CASK LOADING AND WAS OFTEN CALLED OUT TO PERFORM OTHER "PRIORITY WORK" AS DETERMINED BY PLANT MANAGEMENT.

   b. LOADING DELAYS CAUSED BY THE WORK CREW "BREAKS" RESULTED FROM (1) THE NECESSITY TO DRESS IN PROTECTIVE CLOTHING WHEN ENTERING THE RADIOLOGICAL CONTROL AREA (RCA) AND (2) THE NECESSITY TO

REMOVE THE POSSIBLY CONTAMINATED CLOTHING BEFORE BEING ALLOWED TO EXIT THE RCA. THE ADDITION OF 20 TO 30 MINUTES REQUIRED FOR DRESSING AND UNDRESSING TO ENTER OR LEAVE THE RCA GENERALLY RESULTED IN A BREAK OF 35 TO 45 MINUTES. THIS MUCH TIME AWAY FROM THE CASK LOADING PROCESS USUALLY REQUIRED ADDITIONAL WORK, SUCH AS REPEATED DECONTAMINATION BECAUSE OF THE CONTAMINATED STORAGE POOL WATER HAVING DRIED ON THE SURFACE OF THE CASK.

3. BECAUSE OF THE REQUIREMENTS FOR DOE-CLEARED DRIVERS, THE REPLACEMENT OF A DRIVER AT ANY TIME WAS NEVER SIMPLE. IN SOME INSTANCES, AS MUCH AS SEVENTY-TWO (72) HOURS WERE REQUIRED TO REPLACE A DRIVER. THIS CAUSED THE SHIPPING REPRESENTATIVES TO REMAIN IN THE TURKEY POINT AREA UNTIL A NEW DRIVER ARRIVED BEFORE DISPATCHING THE SHIPMENT.

4. THERE WAS TIME LOST BECAUSE OF DAMAGES TO THE TRANSPORT TRACTOR/TRAILER. CRACKED WELDS HAD TO BE REPAIRED, BENT WHEELS REPLACED, AND TEARS IN THE PERSONNEL BARRIER SCREEN MENDED. THE MINOR DAMAGES WERE UNDOUBTEDLY CAUSED BY 12G ROAD SHOCKS (12 X 52K = 624,000). BECAUSE OF THE DAMAGES, CAREFUL INSPECTIONS OF THE TRACTORS AND TRAILERS WERE MADE AT THE FLORIDA, BATTELLE AND NTS LOCATIONS PRIOR TO RELEASING THE UNITS FOR TRANSIT. ON AT LEAST ONE OCCASION, TEMPORARY TRACTOR/TRAILER REPAIRS WERE ACCOMPLISHED AT NTS IN ORDER FOR THE TRACTOR/TRAILER TO BE DRIVEN TO LAS VEGAS WHERE PERMANENT REPAIRS WERE MADE.

5. ROUTE CHANGES ALSO AFFECTED DELIVERY SCHEDULES AND WERE CAUSED BY INCLEMENT WEATHER AND CERTAIN STATES THAT PROHIBITED THE MOVEMENT OF SPENT FUEL ON THEIR HIGHWAYS.

PRIOR TO THE ARRIVAL OF THE SPENT FUEL SHIPMENTS AT THE NEVADA TEST SITE, DRY RUNS WERE CONDUCTED TO ASSURE THAT ALL PERSONS INVOLVED WERE AWARE OF THEIR PARTICULAR FUNCTIONS IN THE OFF-LOADING AND STORAGE PROCESS. WHEN THE SHIPMENTS ACTUALLY ARRIVED AT THE MAIN GATE OF THE NEVADA TEST SITE, THEY WERE RADIOLOGICALLY MONITORED BEFORE BEING TRANSPORTED TO THE NEVADA RESEARCH AND DEVELOPMENT AREA FOR UNLOADING. UNLOADING WAS ACCOMPLISHED BY BACKING THE TRACTOR AND TRAILER-MOUNTED CASK INTO THE HOT BAY FACILITY, WHICH IS THE LARGEST KNOWN OF ITS KIND IN THE WORLD. THE DIMENSIONS OF THIS FACILITY ARE 140 FEET IN LENGTH, 66 FEET IN WIDTH, AND 74 FEET IN HEIGHT. A 40-TON CEILING-MOUNTED CRANE, WITH REMOTE CONTROL CAPABILITIES, ROTATED AND ELEVATED THE CASK TO A VERTICAL POSITION FOR UNLOADING FROM THE CASK INTO THE HOT BAY TRANSFER PIT. NUMEROUS MEASUREMENTS AND READINGS WERE TAKEN ON AND AROUND THE CASK PRIOR TO THE UNLOADING OF THE SPENT FUEL AND ITS PLACEMENT INTO THE LAG STORAGE PIT. DURING THE TWO-MONTH STORAGE PERIOD, MORE TESTS OF THE FUEL ASSEMBLIES WERE CONDUCTED AND FURTHER READINGS WERE COLLECTED FOR CHARACTERIZATION OF EACH ASSEMBLY. AT THE END OF THIS PERIOD, THE FUEL ASSEMBLY WAS READY TO BE TRANSFERRED TO ONE OF THE FOLLOWING THREE TYPES OF AVAILABLE STORAGE LOCATIONS:

1. ABOVEGROUND

2. SUB-SURFACE DRY WELL

3. AIR-COOLED, PASSIVE CIRCULATION

AFTER THE STORAGE LOCATION WAS DETERMINED, THE FUEL ASSEMBLIES WERE PREPARED FOR EMPLACEMENT AND TRANSFER OF THE FUEL ASSEMBLIES FROM THE LAG STORAGE PIT IN THE HOT BAY FOR THE SHALLOW DRY WELL TEST. THIS WAS ACCOMPLISHED BY AN EMPLACEMENT INSTALLATION VEHICLE (EIV), A MANNED CONTROL CAR AND AN L-3 LOCOMOTIVE.

TRANSPORT OF THE FUEL ASSEMBLIES TO THE CLIMAX SITE FROM THE NEVADA RESEARCH AND DEVELOPMENT AREA WAS ACCOMPLISHED BY SPECIALLY DESIGNED CASKS MOUNTED ON A TRACTOR-DRAWN TRAILER RIG. THE CASK CONTAINING A SPENT FUEL CANISTER WAS THEN POSITIONED OVER A 1400-FOOT-DEEP ACCESS HOLE AND THE SPENT FUEL CANISTER WAS LOWERED TO THE MINE STORAGE LEVEL 1400 FEET UNDERGROUND. A CASK MOUNTED ON A REMOTELY OPERATED RAIL-MOUNTED UNDERGROUND TRANSFER VEHICLE RECEIVED THE SPENT FUEL CANISTER AT THE MINE STORAGE LEVEL AND WAS USED TO PLACE THE FUEL ASSEMBLIES INSIDE STEEL-LINED HOLES IN THE FLOOR OF THE MINE STORAGE DRIFT. NUMEROUS EVALUATIONS ARE ONGOING AT BOTH LOCATIONS INVOLVING SPECIAL SPENT FUEL AND SOIL TEMPERATURE TESTS, AS WELL AS MONITORING THE RESPONSE OF GRANITE TO RADIATION.

UCRL-53702

Spent Fuel Test—Climax: An Evaluation of the Technical Feasibility of Geologic Storage of Spent Nuclear Fuel in Granite

Final Report

Compiled by:

W. C. Patrick

March 30, 1986

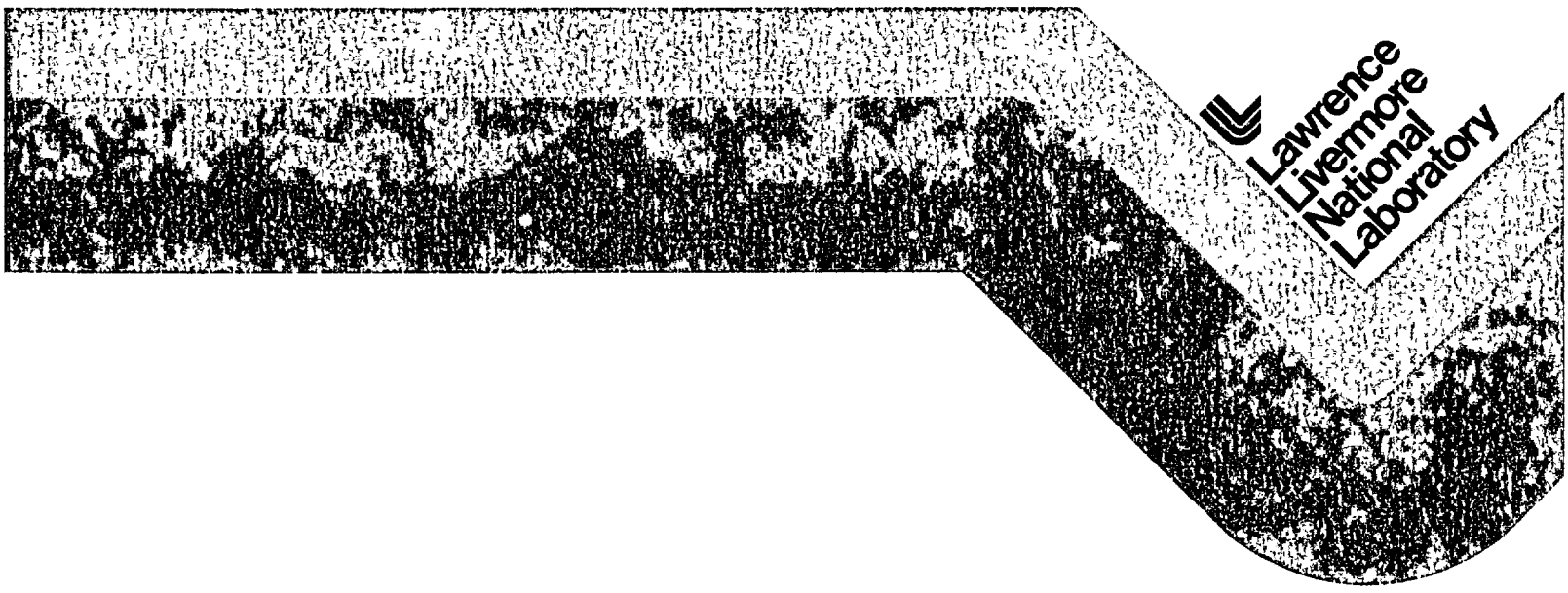

UCRL-53702

Spent Fuel Test—Climax: An Evaluation of the Technical Feasibility of Geologic Storage of Spent Nuclear Fuel in Granite

Final Report

Compiled by:

W. C. Patrick

March 30, 1986

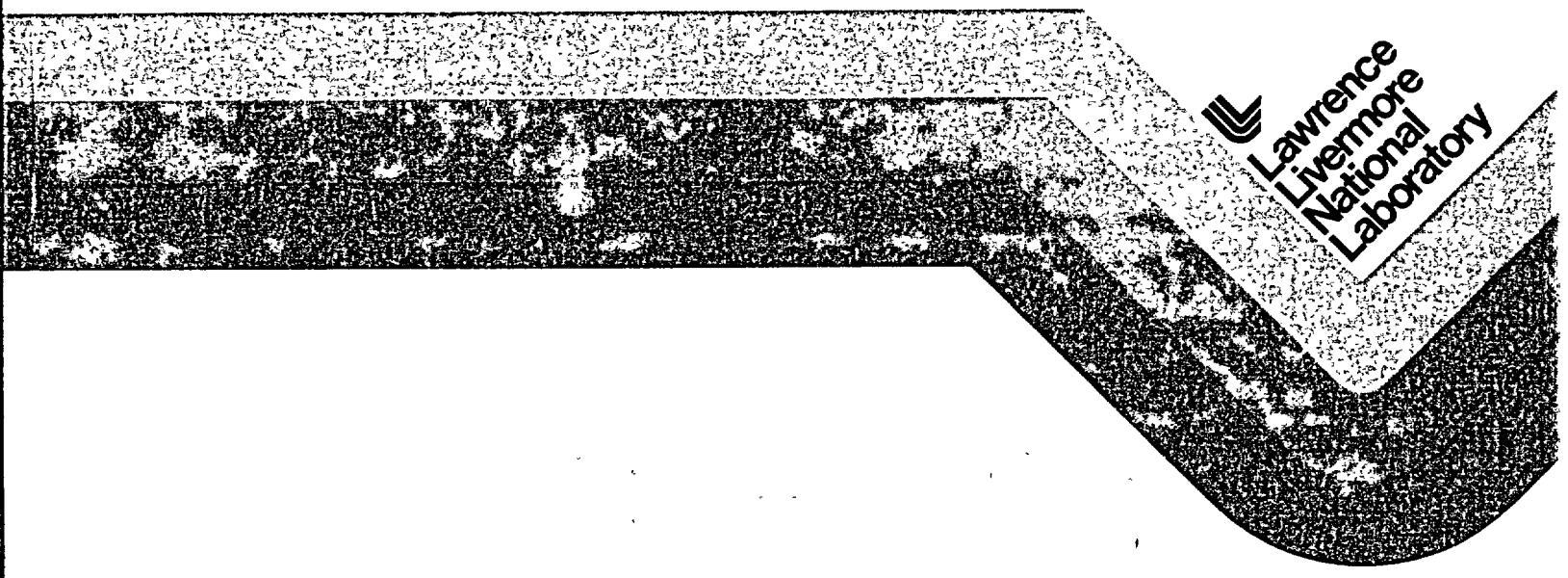

DISCLAIMER

Prepared by Nevada Nuclear Waste Storage Investigations (NNWSI) Project participants as part of the Civilian Radioactive Waste Management Program. The NNWSI Project is managed by the Waste Management Project Office of the U.S. Department of Energy, Nevada Operations Office. NNWSI Project work is sponsored by the Office of Geologic Repositories of the DOE Office of Civilian Radioactive Waste Management.

Work performed under the auspices of the U.S. Department of Energy by Lawrence Livermore National Laboratory under Contract W-7405-Eng-48.

UCRL-53702
Distribution Category UC-70

Spent Fuel Test—Climax: An Evaluation of the Technical Feasibility of Geologic Storage of Spent Nuclear Fuel in Granite

Final Report

Compiled by:

W. C. Patrick

Manuscript date: March 30, 1986

LAWRENCE LIVERMORE NATIONAL LABORATORY
University of California • Livermore, California • 94550

Available from National Technical Information Service • U S Department of Commerce
5285 Port Royal Road • Springfield, VA 22161 • A06 • (Microfiche A01)

Foreword and Acknowledgments

From the development of the test concept in January 1978 to the writing of this final report, the Spent Fuel Test—Climax (SFT—C) has spanned 8 years and involved hundreds of scientists, engineers, and craftsmen in many organizations. During that time, those of us associated with the project had the pleasure of witnessing the successful achievement of all the engineering and scientific objectives of the test. Perhaps more importantly, we saw an increased public awareness of the need for nuclear energy and for a means of safely and reliably disposing of the associated wastes. Some 10,000 people from all walks of life throughout the U.S. and 22 foreign countries visited the test facility. Most went away with a more objective view of nuclear waste disposal than when they arrived.

Because the SFT—C was officially completed in FY 1985 and only very limited funding remains to finish up the remaining reports, it was not possible to assemble a complete team to write this report. Instead, it was assembled and edited by one person, but builds heavily on the FY 1983 project interim report in several technical areas. Although the responsibility for the material presented here rests with the author, the important contributions of the following people are acknowledged: L. Ballou, T. Butkovich, R. Carlson, W. Durham, H. Ganow, G. Hage, E. Majer, D. Montan, R. Nyholm, N. Rector, F.J. Ryerson, H. Weiss, D. Wilder, and J. Yow, Jr.

Most of the scientists and engineers who worked on the SFT—C have published formal reports and journal articles, providing a lasting record of their efforts. However, many others filled roles vital to the success of the project, but that did not lend themselves to public documentation. Although it is not possible to properly acknowledge the contributions of each of these participants, those individuals and organizations whose efforts were keys to the success of the project are recognized here.

The SFT—C was funded as part of the U.S. Department of Energy (DOE) Nevada Nuclear Waste Storage Investigations (NNWSI) Project. Originally part of the National Waste Terminal Storage Program, it was conducted under the auspices of the Office of Civilian Radioactive Waste Management following passage of the Nuclear Waste Policy Act of 1982, which went into effect in January 1983. When the SFT—C was initiated, the DOE Project Manager was Robert Nelson. Beginning in June of 1982, Dr. Donald Vieth served as Manager of the Waste Management Project Office (WMPO) in Nevada. Mr. Mitch Kunich was WMPO's cognizant engineer and was intimately involved in all aspects of the SFT—C throughout the development and execution of the test.

Facility engineering and construction were the responsibility of Holmes and Narver (general architect and engineering), Fenix and Scisson (architect and engineering services for mining and drilling), and Reynolds Electrical and Engineering Company (REECo) (construction). Special acknowledgment is extended to the late G.W. Adair, who served as superintendent throughout the construction and during the early storage phase, and to the REECo crew who provided continuous subsurface access and experimental support far beyond the normal requirements. Members of this crew included (at various times): L. Ala, J. Campbell, L. Cheney, D. Daffer, G. Frye, C. Halstead, and G. Medina. Appreciation is also extended to H. Allen, T. Clapp, D. Hansen, R. Murphy, and W. Smyth who provided special drilling support for stress measurements and geological characterization.

Spent fuel encapsulation was accomplished at the engine maintenance, assembly, and disassembly (EMAD) facility with a highly skilled Westinghouse team managed by D.C. Durrill. T. Cross was the project engineer with key responsibility for all hardware provided by Westinghouse. The accomplishments of his team were essential in preparing nuclear waste for emplacement less than two years from the date of authorization of the SFT—C. C. Balmgren coordinated and was the principal contributor to the test Safety Assessment Document.

A large suite of instrumentation was critical to the successful achievement of the technical objectives of the test. EG&G-Las Vegas personnel filled a vital role in this area. Laboratory calibrations and recommendations regarding transducer selection were provided by R. Noyes and J. Pelles. In the field, B. Bailey, D. Jackson, W. Webb, and R. Seivert provided support for instrument installation, calibration, troubleshooting, and remedial actions.

Several colleagues at LLNL deserve special recognition as well, including: M. Mayr in construction management and coordination; R. Hasbrouck in control systems for spent-fuel handling; J. Duncan, P. House, and G. Wright in development of the spent-fuel handling system; W. Brough, R. Nyholm, N. Rector and R. Stager in data acquisition system and instrumentation support; the late N. Cotter, M. Higuera, W. Richardson, and L. Rogers in data processing; J. Button as Operations Coordinator

throughout the spent-fuel emplacement and exchange operations; T. Moran, K. Raschke, T. Roy, and T. Straume in Health and Safety; and J. Beiriger, P. Burklund, T. Gates, R. Neurath, D. Peifer, J. Scarafiotti, F. Schumacher, and B. Sellick for electronics and mechanical technican support.

From test concept to final report, overall technical guidance for the SFT—C has been provided by L. Ramspott. His insights and direction during the active phase of test development and execution, and his patience during the period of preparing final reports is gratefully acknowledged. I also extend my thanks and special recognition to L. Ballou. As Task Director for the SFT—C through April 1983, he was responsible for many of the engineering and test design concepts which led to the successful execution of the SFT—C, as reported here.

This manuscript represents uncountable hours of effort on the part of S. Gonzales. Her word processing skills, careful attention to details, and perseverance in working with the author are gratefully acknowledged. Editorial services were capably provided by M. Donohue and S. Stull, with help from B. Strack, P. Ayde, and S. Wander.

Finally I thank F. Coffman, IT Corporation, for allowing me to complete this report after joining his company.

Contents

Spent Fuel Test—Climax: An Evaluation of the Technical Feasibility of Geologic Storage of Spent Nuclear Fuel in Granite

Final Report

Abstract

The Spent Fuel Test—Climax (SFT—C) was recently conducted to demonstrate the feasibility of deep geologic storage of spent nuclear fuel from commercial nuclear power reactors. Located 420 m below surface in the Climax stock granite on the Nevada Test Site, the test was conducted under the technical direction of the Lawrence Livermore National Laboratory (LLNL) as part of the Nevada Nuclear Waste Storage Investigations (NNWSI) Project for the U.S. Department of Energy (DOE). Eleven canisters of spent nuclear reactor fuel were emplaced, and six electrical simulators were energized in April-May 1980. When test data indicated that the test objectives were met during the 3-year storage phase, the spent-fuel canisters were retrieved and the thermal sources were de-energized in March-April 1983.

The SFT—C operational objective was met by demonstrating the feasibility of packaging, transporting, storing, and retrieving highly radioactive fuel assemblies in a safe and reliable manner. In addition to emplacement and retrieval operations, three exchanges of spent-fuel assemblies between the SFT—C and a surface storage facility, conducted during the storage phase, furthered this demonstration.

Technical objectives of the test led to development of a technical measurements program. To meet these objectives, nearly 1000 instruments and a computer-based data acquisition system were deployed. Geotechnical, seismological, and test status data were recorded on a continuing basis for the three-year storage phase and six-month monitored cool-down of the test.

This report summarizes the engineering and scientific endeavors which led to successful design and execution of the test. The design, fabrication, and construction of all facilities and handling systems are discussed, in the context of test objectives and a safety assessment. With regard to technical aspects of the test, our discussion progresses from site characterization and experiment design through data acquisition and analysis of test data in the context of design calculations.

1. Executive Summary

1.1 Introduction

The National Waste Terminal Storage (NWTS) Program was established in 1976 by the predecessor of the U.S. Department of Energy (DOE) to evaluate the feasibility of retrievable deep geologic storage of commercial nuclear reactor wastes. In September 1983 the NWTS became the Civilian Radioactive Waste

Management program. This large, multidisciplinary program plans to create an operational repository in the 1990s.

Although it was clear that a large-scale field test would be ideal for demonstrating essential technologies and revealing unexpected effects of waste emplacement, it was also evident that there would be few opportunities for such testing early in the program. Therefore, the Spent Fuel Test—Climax (SFT—C) was undertaken to demonstrate the feasibility of spent fuel handling and to address technical concerns related to granitic rocks.

Each chapter of the full report is summarized below. Please refer to the appropriate chapter for discussions of each subject and for specific references. The publication list at the end of this report lists all reports published on the SFT—C.

1.2 Background

The SFT—C was conducted under the technical direction of the Lawrence Livermore National Laboratory (LLNL) for the U.S. DOE. As part of the Nevada Nuclear Waste Storage Investigations, it was managed by the Nevada Operations Office of the DOE.

The SFT—C facility (shown in Fig. 1-1) was located 420 m below surface in the Climax stock granite. Facilities were constructed between June 1978 (when funding for the test was initiated) and April 18, 1980 (when spent-fuel emplacement began). Spent fuel was emplaced between April 18 and May 28, 1980, and retrieved between March 3 and April 6, 1983. Individual spent-fuel canisters were exchanged in January

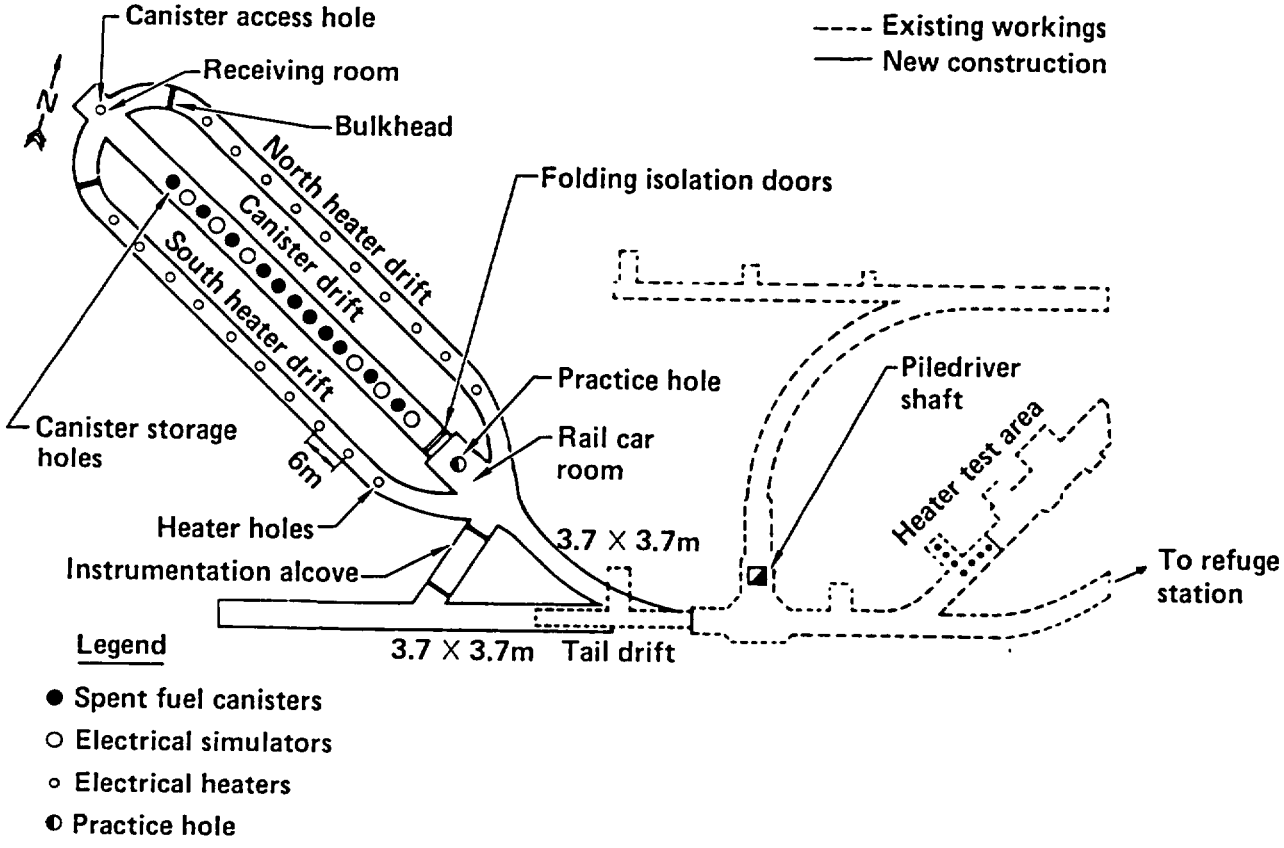

Figure 1-1. The SFT—C facility located 420 m below the surface in the Climax granite.

and October 1981 and August 1982. Post-test characterization followed retrieval of the spent fuel and was completed during 1985.

The operational objectives of the test were to demonstrate safe and reliable packaging, transport, short-term storage, and retrieval of spent nuclear reactor fuel. The storage period corresponds to spent-fuel ages of 2.5 to 5.5 years out of core (YOC).

A technical measurements program was implemented to acquire data for the ultimate qualification of granitic rock as a repository medium, to aid in the design of such a repository, and to predict its response in granitic rock. Numerous technical objectives were established at the beginning of the test, as presented in the technical concept report (see Ramspott et al., UCRL-52796, 1979). Our activities focused on these stated aims throughout the test.

We recorded data continuously on more than 900 computer channels during the three-year fuel storage phase and for six months following retrieval to record thermal and thermomechanical responses as the simulated repository environment cooled. Although most data were acquired through a central data acquisition system (DAS), periodic displacement measurements and radiation dosimetry data were acquired manually and processed independently of the DAS. Acoustic emissions data were also acquired independently.

1.3 Chapter Summaries

Chapters 2 through 18 are summarized below. Please refer to the full chapters for specific details.

1.3.1 Chapter 2. Test Objectives

Both operational and technical objectives guided the design, development, and execution of the SFT—C. The overall operational objective of the test was to evaluate the feasibility of safe and reliable short-term storage of spent reactor fuel assemblies at a plausible repository depth, and to retrieve the fuel assemblies afterward.

An underlying technical objective was to simulate the near-field thermal effects of a panel of a full-scale repository within a relatively small test volume. An additional technical objective was to evaluate the effects of heat alone and the combined effects of heat and radiation on the near-field canister environment and materials.

Although the highest priority of the SFT—C was a timely demonstration of spent-fuel handling, the test also addressed the ultimate qualification of granitic rocks for geologic disposal and the design of future repositories in granitic or other hard rocks. The focus of these objectives was to model and collect data on heat transfer, rock mechanical response, and radiation transport processes. Evaluating our ability to model such phenomena also became an important element of the SFT—C.

1.3.2 Chapter 3. Test Design

We designed the test by using a series of calculations of heat transfer, rock mechanical response, and radiation transport processes. To make the SFT—C demonstration meaningful and technically sound, we designed it to simulate the early, near-field history of a panel of a full-scale repository containing thousands of spent-fuel assemblies. A suite of increasingly sophisticated heat transfer calculations was the primary basis of the SFT—C facility design.

By emplacing a central linear array of spent-fuel assemblies and simulated assemblies and flanking that array with auxiliary heaters, we matched the thermal conditions of a conceptual repository within 4.5% in a central portion of the SFT—C. Thermal calculations also estimated the temperatures of fuel cladding, handling system hardware, and ventilation air.

We also calculated the response of the rock mass to excavating underground facilities, extensive heating, and cooling following retrieval of the spent-fuel assemblies. Most calculations were made with the assumption that the rock was a homogeneous, isotropic, linearly elastic material; however, we also incorporated dilatant and nondilatant joints in our estimates of excavation response to mining. Calculated rock responses were used to site instrumentation and later provided a basis for comparison with field data. As field-properties data became available, the laboratory values used in initial design calculations were revised. *In situ* stress measurements also replaced early estimates of the stress state.

We calculated radiation transport for two distinct purposes: to design acceptable radiation shielding and to determine the radiation dose to the granitic rock near the spent-fuel emplacement boreholes. Hand calculations of isotopic abundances, gamma energy spectra, and neutron attenuation test data established the shielding necessary to limit dose rates to 100 mrem/h at the surface of the shielding casks and 0.5 mrem/h at the storage drift floor. Monte Carlo simulation of the complex spent-fuel storage configuration was used to estimate doses and dose rates at various positions outward from the spent fuel assemblies. In addition, these calculations estimated the thermal contribution of gamma attenuation to be 40 W per canister.

1.3.3 Chapter 4. Site Characterization and Geologic Investigations

We studied the local structural geology and hydrology, measured the *in situ* state of stress, measured physical properties (*in situ* and in the laboratory), studied mineralogy and petrology of pre- and post-test cores obtained near the canister emplacement holes, and analyzed (by microfracture counts) potential drilling damage and radiation effects. We summarize below the more important observations.

Structural Geology. The Climax stock quartz monzonite (CSQM) in which the SFT—C was located is part of a two-component stock of Cretaceous age that intrudes Paleozoic carbonates and is partially overlain by Tertiary tuffs. We identified eight joint sets during mapping and core logging; three sets account for 80% of all joints mapped. An average frequency of three joints per metre produces a moderately fractured, blocky structure.

Geohydrology. Relatively low annual rainfall (150 to 200 mm), high evapotranspiration, and sparse overlying sediment contribute to low infiltration of water into the stock, which is exposed at the surface above the test facility. The zone of total saturation appears to occur at about 975 m above mean sea level (MSL), about 145 m below the test horizon.

***In Situ* Stress.** In the north and south heater drift pillars, the maximum principal stress (sigma 1) is essentially vertical, the intermediate principal stress (sigma 2) is horizontal and aligned parallel to the long axes of the pillars, and the least principal stress (sigma 3) is parallel to the pillar width. "Free field" state-of-stress measurements indicate that the maximum principal stress is oriented toward the east-northeast and is nearly horizontal, the intermediate principal stress is nearly vertical, and the least principal stress is nearly horizontal and oriented north-northwest. These results are consistent with both the conclusions of previous investigators and the motions of active faults at the Nevada Test Site (NTS). The maximum secondary principal stress levels measured in boreholes ISS-9 and ISS-10 (located at and above the facility horizon) apparently differ systematically. The observed difference does not appear to be related to any geologic structural anomaly.

Physical Properties. Laboratory measurements indicate that Young's modulus increases with confinement, decreases with increasing temperature, and is relatively unaffected by prior treatments of heat and stress. *In situ* deformation modulus apparently depends on prior heating and stress conditions. The average field modulus is about half that measured in the laboratory. The coefficient of thermal expansion increases substantially with temperature and decreases somewhat as confinement increases. Thermal conductivity and diffusivity decrease with increasing temperature and with decreasing confinement. *In situ* testing produced values of 3.1 W/m·K and 1.2 mm^2/s, respectively. *In situ* permeability was about 1 nD at ambient temperature, decreasing to 0.2 nD at 50 °C. No permanent change in gas permeability occurred as a result of heating and subsequent cooling.

Mineralogy and Petrology. The quartz monzonite is a porphyritic rock composed of a ground mass that is predominantly equant, subhedral grains of plagioclase, K-feldspar, quartz, and biotite; grains range from 0.5 to 2.0 mm in diameter. Modal percentages for the primary phases of quartz, plagioclase, and K-feldspar are 17.3 ± 2.1%, 32.8 ± 5.6%, and 31.2 ± 5.3%, respectively. Igneous accessory phases make up less than 3 vol%. The Climax record cores show significant chemical, petrographic, and modal variations. These variations result from both igneous and hydrothermal processes.

Radiation and Thermal Effects. No statistically significant changes in strength or Young's modulus were observed after intense laboratory irradiation of CSQM. Mineralogical and petrographical characteristics did not change significantly in samples obtained from nearby the spent-fuel storage boreholes or auxiliary heaters. The microfracture structure of Climax granite is highly heterogeneous on the scale of 0.1 to 10 mm, making it difficult—if not impossible—to discern damage produced by elevated stress, temperature, gamma irradiation, or combinations of the three. No statistically significant evidence of changes in microfracturing were observed to be produced by laboratory gamma irradiation.

Drilling Damage Effects. The damage induced by hammer-drilling the 0.61-m-diameter spent-fuel emplacement boreholes is limited to an annular ring less than 20-mm thick around the borehole.

1.3.4 Chapter 5. Site Development and Facility Construction

The PILEDRIVER shaft, headframe, and hoist system (shown in Fig. 5-2) provided access to the 420-m test level. Developed in the 1960s for testing nuclear weapons effects, this access was used to support a heater test known as Heater Test No. 1 before the SFT—C was authorized. After the shaft was internally refurbished, we drilled an additional 0.76-m-diameter shaft and lined it with a 0.51-m-outside-diameter steel pipe section, which was cemented in place. This canister access shaft allowed encapsulated spent-fuel assemblies to be moved between the surface and the underground. Two 3.4-m-cross section parallel drifts were driven about 70 m to connect drifts from the main shaft with the base of the canister access shaft. The floors of these drifts housed the auxiliary heaters during the heated phase of the SFT—C. After the heater drifts were built, the central canister storage drift was driven in two passes: a 4.0-m-high × 4.6-m-wide top heading and a 2.1-m × 4.6-m bench. Controlled blasting techniques were used to excavate some portions of this drift.

Subsurface outfitting included installing ground control measures, placing a reinforced concrete floor with embedded shielding pits and rails, drilling emplacement boreholes for spent-fuel and heater installations, and installing nearly 1000 instruments.

On the surface, construction included the ventilation and filtration system, the DAS trailer, power and water supplies, and the spent-fuel canister hoisting system.

1.3.5 Chapter 6. Spent-Fuel Characterization

The 13 spent-fuel assemblies used in the SFT—C came from the Florida Power and Light Co. Turkey Point Unit 3, a Westinghouse-design commercial pressurized water reactor. Hanford Engineering Development Laboratory and the Battelle Columbus Laboratory characterized the intact fuel assemblies and individual fuel rods. Their evaluation was as follows: The average length and cross-section width of the assemblies were 3.903 m (153.65 in.) and 211.1 mm (8.312 in.), respectively. The average weight of the assemblies was 663 kg (1459 lb). A combination of gas and wet sip testing indicated that no assemblies contained leaking rods. Visual inspections revealed no major anomalies (such as bulges, scars, or blisters) on the rods, although profilometry detected circumferential ridges as high as 0.076 mm (0.003 in.) at pellet interfaces.

In September 1979, a total neutron flux of 1.06×10^4 n/cm^2/s with an average energy of 1.4 MeV was measured and found to be distributed fairly symmetrically around the canister axial midplane. An average gamma flux of 9.11×10^4 R/h was determined. In March 1984, one year after fuel retrieval, the gamma dose rate was measured to be 2.33×10^4 R/h. ORIGEN2 calculations and a series of boiling-water calorimetries established the decay-power-generation curve for the spent-fuel assemblies. During the test, the heat-generation rate decreased from about 1500 to 600 W per canister.

1.3.6 Chapter 7. Spent-Fuel Handling System

Spent-fuel assemblies were shipped from the Turkey Point reactor to the engine maintenance, assembly, and disassembly (EMAD) facility in southeastern Nevada in truck-mounted, licensed, commercial shipping casks. Once the fuel assemblies were received and encapsulated, remote handling systems were used for all operations at NTS. Each assembly was encapsulated in a 356-mm- (14-in.-) outside diameter stainless steel canister that was sealed, evacuated, and backfilled with helium gas. An integral shield plug and grappling knob provided the necessary interface with the handling system.

The handling system had three major components: The surface transport vehicle (STV)—a special trailer with a rotatable shielding cask and a commercial tractor—was designed and developed to move the encapsulated spent fuel from EMAD to the SFT—C. Top and bottom gates permitted loading through the top at EMAD and unloading and loading through the bottom at the SFT— C. All functions were remotely controlled. The underground transfer vehicle (UTV)—a rail-mounted, remotely controlled shielding cask with an onboard jib crane—received the spent-fuel canisters underground and emplaced or retrieved them from the individual storage boreholes. A canister-handling system—a specially designed wire-line hoist with control and braking subsystems—lowered and raised the spent-fuel between the STV and the UTV. An automatically actuated brake travelled with the spent-fuel canister for protection in the event of a hoist

or cable failure. Control systems and closed-circuit television permitted remote operations with no risk of excess radiation exposure to personnel.

1.3.7 Chapter 8. Safety Assessment

The conduct of the SFT—C required that a safety assessment document (SAD) be prepared. A similar document was also developed to cover supporting operations at the EMAD facility. The SAD showed that no unacceptable radiological or nonradiological consequences to site personnel, the public, nor the environment would result from normal operations, abnormal operations, or postulated accidents. Calculations showed that nuclear criticality could not occur for any postulated fuel configuration, even with flooding.

1.3.8 Chapter 9. Selection, Deployment, and Performance of Instruments

Nearly 1000 instruments were deployed and operated for 3.5 years to monitor the temperatures of rock, air, and metallic components of the test; displacements and stress changes in the rock mass; radiation dose to personnel and to the rock; thermal energy input; characteristics of the ventilation airstream; and the operational status of the test. Careful selection, installation, calibration, and maintenance of these instruments allowed acquisition of about 15.3×10^6 high-quality data points.

Our studies show that currently available continuous air monitor (CAM) and remote area monitor (RAM) systems adequately monitor radiation safety in an underground environment. However, long-term gamma radiation dosimetry techniques were augmented by short-term thermoluminesence dosimetry (TLD) measurements.

Properly sheathed, commercially available RTDs, thermocouples, and thermistors provide reliable, accurate, long-term temperature data. Moisture-balance and energy-removal calculations were found to require better calibrations of flowmeters than are commonly available. In addition, systematic changes in watt transducer calibrations suggest a need for periodic calibrations if accuracies better than 5% are needed.

Available vibrating-wire stressmeters have been failure-prone in the past and do not provide data with an accuracy better than about $\pm$ 50%. The several types of rock displacement gauges functioned reliably and accurately with one exception: Linear potentiometers failed early in the test, resulting in the loss of near-field rock displacement data.

1.3.9 Chapter 10. Data Acquisition and Management Systems

A dual HP1000 disk-based DAS was developed to control instrument scanning, to provide preliminary data conversion, and to generate remote alarms if the data were outside of anticipated limits. The DAS performed all functions from acquiring analog signals through digitizing and archiving the raw data records on magnetic tape for subsequent detailed conversion by the data management system (DMS).

The DAS functioned accurately and reliably throughout the 3.5-year storage and cool-down phases. System statistics show that system availability averaged about 96% (functionally disabled index was 4%), providing about 15.3×10^6 data points during the test. The accuracy of dc voltage measurements was maintained within $\pm 4\,\mu$V. The accuracy of four-wire resistance measurements was occasionally outside the anticipated ± 0.0092-Ω envelope because of periodic digital voltmeter failures.

In addition to several utility functions, the DMS included a binary reading and screening code, a conversion code with algorithms for incorporating individual calibrations and temperature compensation, and a set of file manipulation codes for organizing the raw and converted data files into individual files that contain all data for each instrument. This latter feature allowed easy access to the data for plotting. DMS statistics indicate that of the 15.3×10^6 points recorded by the DAS, 8.7×10^6 were retained, processed, and archived for analysis. An additional 6.3×10^6 data points from radiation monitors and test status monitors were valid but not retained. Only 2.5×10^5 points (1.6% of the total) were discarded as invalid.

1.3.10 Chapter 11. Spent-Fuel Handling Experience

Spent-fuel handling was at the heart of the SFT—C, which had as its main goal the demonstration of the feasibility of safe and reliable transport, storage, and retrieval of spent nuclear fuel. Operating procedures, administrative controls, and personnel training contributed to attaining this objective.

Eleven encapsulated spent-fuel assemblies were stored at the SFT—C between April 18, 1980, and May 28, 1980, at a rate of about two per week. To maintain a state of readiness for both personnel and equipment, we exchanged single spent-fuel assemblies between the SFT—C and EMAD three times: January 12 to 14, 1981; October 26 to 28, 1981; and August 16 to 18, 1982. Between March 3 and April 6, 1983, all 11 assemblies were retrieved and returned to temporary storage at the EMAD. These operations showed that spent fuel can be safely handled with available technologies.

Total radiation exposure to operating personnel was 0.4 person-rem. Although the highest exposure was 10 mrem per handling operation, the average was about 30% of this value. Neutron exposure was greater than gamma exposure. Expressed relative to the energy generated while the spent fuel was in the reactor, the normalized dose commitment at the SFT—C was 0.002 person-rem/MW•y (electric), a small fraction of the 1 to 4 person-rem/MW•y (electric) received during power plant operations.

1.3.11 Chapter 12. Thermal Sources

Three principal sources deposited energy into the rock mass during the SFT—C: spent-fuel assemblies, electrical simulators, and auxiliary heaters. Facility lighting also contributed to the input energy.

These thermal sources were monitored during the test to ascertain their energy input for use in thermal and thermomechanical calculations of SFT—C response. Measurements show that total thermal energy input to the SFT—C was 1041 MW•h during the 3-year storage phase, with 19 MW•h added during post-retrieval activities. The input energy partition was 25.3% from the 11 spent fuel assemblies, 14.2% from the 6 electrical simulators, 57.7% from the 20 auxiliary heaters, and 2.8% from the facility lights. Electrical sources of heat, associated controllers, and instrumentation were very reliable.

1.3.12 Chapter 13. Heat Transfer Analyses and Measurements

Measured temperatures were compared with the heat transfer calculations described briefly in Chapter 3, with the following observations and conclusions. The intended SFT—C simulation of emplacing thousands of spent-fuel assemblies in a hypothetical repository was successful. Throughout the test, measured temperatures in the vicinity of the spent-fuel storage boreholes were within 3°C of those calculated at the axial midplane of the heat sources. Measured temperatures were somewhat higher than calculated near the top and somewhat lower than calculated near the bottom of the heat sources. Comparison of measured and calculated temperatures throughout the approximately 10,000 m^3 instrumented volume indicates very good agreement. Pairwise plots of measured and calculated temperature increases may be fit by straight lines with near-unity slopes and near-zero intercepts. Associated mean-square errors are generally about 2°C, only slightly greater than the 1.1°C ISA special limits of error for the thermocouples. Analytical and finite-difference models of the finite-length geometry of the SFT—C produced marked improvements in the level of agreement between data and calculations near the ends of the test array, where the infinite-length assumption of the early models is no longer valid. Temperature-measuring instruments functioned accurately and reliably during the test, as confirmed by calibrations.

1.3.13 Chapter 14. Ventilation System Analyses and Measurements

We documented the energy removed from the SFT—C by the ventilation system by measuring inlet and outlet air temperatures, dewpoints, and air flowrates for the three drifts. These measurement systems functioned reliably. The ventilation system removed a total of 148 MW•h during the spent-fuel storage phase of the test. Of this, 76.7% was removed as sensible heat and 23.3% as latent heat of vaporization. About 20 tonnes of water were removed from the facility each year in the ventilation airstream.

Attempts to calculate energy removed by the ventilation system were marginally successful. After trying a variety of values for the pertinent parameters, we found that good agreement between measured and calculated rock temperatures was achieved only by calculating with an energy-removal rate much higher than that measured.

1.3.14 Chapter 15. Radiation Transport Calculations and Measurements

The radiation dose calculations described in Chapter 3 form the basis for comparison with data measured during the test. In addition to personnel dosimetry and areal radiation monitoring, we also instrumented the rock near selected spent-fuel storage boreholes. The latter measurements used optical-grade

LiF dosimeters at the borehole wall and at positions 200 and 360 mm into the rock. Neutron dosimeter foils were also incorporated with these measurement packages. The RAM and CAM areal monitors performed well but exhibited drift that required periodic adjustment. The fade characteristics and temperature sensitivity of the LiF dosimeters required that they be augmented with short-term $MgBO_4$ and CaF_2 TLDs. The Monte Carlo radiation transport calculations were generally more accurate than the measurements. However, generally good agreement was observed, particularly with the short-term dosimeters.

Radon-thoron concentrations in the air gradually increased from 1×10^{-10} to about 6×10^{-10} Ci/m^3 as the rock mass was heated. The log of concentration was found to increase nearly linearly with decrease in ventilation airflow rate. As noted in Chapter 11, measurements of radiation doses to man indicate that minor whole-body doses were received during spent-fuel handling operations and that no whole-body dose above background was received during spent-fuel storage. Very low finger doses were recorded for technicians who installed thermocouples on the emplaced canisters.

1.3.15 Chapter 16. Rock Mechanical Response Calculations and Measurements

Calculations were made and data were obtained for each phase of the SFT—C: excavation, heating, and post-retrieval cooling. The calculations described briefly in Chapter 3 are the basis for comparisons with data. The response of rock near underground openings to the excavation process was dominated by the behavior of joints. This behavior has not been adequately modeled by either homogeneous, isotropic, elastic formulations or by two-dimensional models, which include joints with either dilatant or nondilatant behavior. The rock-mass response during extensive heating was calculated quite well by the linearly elastic formulations, provided that measured *in situ* stress values and proper field deformation properties were incorporated in the model. Accurate calculation of temperature changes is essential for good rock-response results. Because commonly available codes do not incorporate all heat-flow features of interest, we found it necessary to simulate such processes as thermal radiation and ventilation by means of "effective" conductive properties.

Most displacement instrumentation performed accurately and reliably during the test. Stress-change instrumentation failed, causing loss of all early data. In addition, near-field extensometer potentiometers malfunctioned, producing loss of early data near the emplaced spent-fuel assemblies.

Rock response to post-retrieval cool-down was calculated to be very small. The heated phase instruments were augmented during cooling by instruments designed and fabricated to monitor displacements within selected canister emplacement holes after spent-fuel was retrieved.

1.3.16 Chapter 17. Acoustic Emission and Wave Propagation Monitoring

We studied acoustic emissions (AE) and wave propagation to improve our understanding of the rock mass response to heating and to determine whether these techniques could reliably monitor changes in a full-scale repository. Continuous AE monitoring began about three months before spent-fuel emplacement and continued through the post-retrieval cooling phase. About six months after spent-fuel emplacement, we installed wave propagation instruments. Data were acquired and processed with an automated seismic processor (ASP).

The frequency of occurrence of AE is directly related to changes in rate of energy deposition to the rock mass. Adjustments to heater power levels and emplacement or retrieval of heat sources (such as spent-fuel assemblies) produce rapid increases in AE that decrease to background levels within a few days. Analyses of AE data indicate small-scale shear displacement or fracturing on the order of 0.01 to 0.05 mm per event, with source dimensions of several centimeters. Changes in the ratio of S- to P-wave amplitudes recorded over path lengths of several meters qualitatively agree with temperature changes in the rock mass. These changes are hypothesized to result from fracture closure. No measurable variations in P- and S-wave velocities occurred during the monitoring period.

1.3.17 Chapter 18. Metallurgical Investigations

We conducted metallurgical analyses to examine failures in emplacement borehole liner welds and in Superinvar connecting rods from borehole extensometers and to examine corrosion of a spent-fuel canister and thermocouple sheathing. Inadequate weld penetration caused at least one emplacement borehole liner to leak at the connection of the bottom plate and the pipe section. The stainless steel canister stored

within the leaky liner showed no evidence of general or localized corrosion even though it withstood temperatures of about 95°C and radiation dose rates of 10^4 rad/h while immersed in Climax stock ground water for at least eight months.

Superinvar connecting rods corrosion-cracked when in contact with Climax ground water at temperatures near 55°C. Thermocouple sheathing corroded in two cases where the thermocouples were erroneously sheathed in stainless steel rather than Inconel 600, as specified.

2. Design Criteria and Objectives

This chapter outlines the objectives that focused the design of the SFT—C and test equipment and facilities. The overall objective was twofold: to evaluate the feasibility of safe and reliable short-term storage of spent reactor fuel assemblies at a plausible repository depth in a typical granitic rock and to retrieve the fuel afterwards (Ramspott et al., 1979). An additional objective was to evaluate the difference—if any—between the effects of an actual radioactive waste source and an electrically heated simulator.

2.1 General Design Criteria

To achieve these objectives, we specified five general design criteria for the test:

1. Create a storage drift geometry reasonably similar to that expected for a spent-fuel repository. Toward that end, deploy supplementary heat sources to simulate the thermal effects within a large repository.
2. Include enough electrical simulator canisters to evaluate the effects of heat alone and heat in combination with ionizing radiation.
3. Develop spent-fuel handling systems compatible with test conditions to allow retrieval at any time during the test.
4. Meet appropriate industrial and radiation safety standards.
5. Allow access to the test facilities for operational, public awareness, and educational purposes.

These criteria were sufficient to define the major features of the test, including the three-drift array, the number of spent-fuel and simulator canisters, the data acquisition system with remote alarming capability, conservative radiation shielding, and remote operation of handling equipment.

2.2 Technical and Scientific Objectives

Although a timely engineering demonstration was the highest priority, the SFT—C had technical and scientific objectives as well. Because the test involved the largest-scale heating of a hard rock medium to date for a test of this type and was the first *in situ* exposure of crystalline rock to spent fuel, we had the opportunity to collect technical data on the suitability of granitic rock as a medium for deep geologic disposal of high-level reactor waste. We also gathered information useful for designing future repositories in hard rocks and predicting their response to exposure to reactor waste. Our specific objectives were to:

- Analyze displacements and stress changes in the rock that forms the pillars between the central and side drifts; these displacements resulted from mechanical disturbance when the central drift was mined.
- Assess the validity of our calculational models for mechanical and thermomechanical effects.
- Measure the temperature and radiation dose in the close-in heated zone to infer both the total power level of the spent-fuel assemblies and the proportion of that power transported out of the canisters by nuclear radiation, as opposed to thermal processes. Similarly, measure both the heat removed by ventilation and the thermal field (both close-in and intermediate) and compare our findings with calculational models.
- Evaluate displacement and stress instrumentation under simulated repository conditions.
- Measure displacement and stress effects in the intermediate heated zone; these displacements were caused by the thermal disturbance of the spent fuel and heaters. Also, assess the relative effect of existing fractures on rock response by duplicating all mechanical measurements in regions that were either fractured or relatively unfractured, and by directly instrumenting selected, prominent geologic fractures.

3. Test Design*

Although physical simulation is well-established in other engineering fields, it had never been tried in nuclear waste management until the SFT—C. The associated design techniques and supporting calculations are the topics of this chapter. Heat transfer, rock mechanical response, and radiation transport calculations were used in designing the experiment.

3.1 Test Concept

The SFT—C was planned as a generic test of deep geological storage of spent nuclear fuel from commercial power reactors (Ramspott et al., 1979). To make this test meaningful and technically sound, we designed it to simulate the near-field thermal history of a repository containing thousands of spent-fuel assemblies. As described below, we accomplished this by modeling a large panel of a full-scale repository and comparing the temperature distributions generated by this calculation with those generated by similar calculations of possible design geometries. The thermal conditions in a 15-×-15-m section of the array matched the conditions of the modeled repository within 4.5%.

3.2 Heat Transfer Calculations

Heat transfer calculations were used at all stages of design, from conceptual to as-built. The purpose, general formulation, and pertinent results of each calculation that supported design, construction, operation, and subsequent evaluation of the SFT—C are described here (also see Montan and Patrick, 1981 and 1986).

3.2.1 Preliminary Design Calculations

The model repository that formed the basis of the SFT—C design comprised many long, parallel drifts on 15-m centers. Spent-fuel assemblies with an initial power level of 2 kW were placed on 3-m centers in the 5-m-wide drifts. Using this geometry, we obtained an initial areal loading density of 190 kW/acre, which had been reported previously in preconceptual repository designs (Kibbe and Boch, 1978).

We simulated this geometry using analytical calculations and the following parameters:

k = 3.0 W/m·K, thermal conductivity,
κ = 1.25 mm²/s, thermal diffusivity,
Q = 2 kW, power level at 2.5 years out of core,
L = 3.66 m, length of heat sources.

Calculations were made for both a 300- × 300-m array containing 2000 spent-fuel assemblies and a 600- × 600-m array containing 8000 canisters.

The characteristics of the spent fuel were chosen to match those of the Westinghouse pressurized water reactor fuel from Turkey Point Unit #3 (see Chapter 6). These assemblies, which were 0.21 × 0.21 m in cross section by 3.66 m long, had an anticipated fuel loading of 448 kg with 2.56% ^{235}U and a burnup of 28,000 MW·d/MTU. The preliminary power estimates were later shown to be somewhat higher than actual but were satisfactory for purposes of design.

Figure 3-1 shows the resulting temperature rises associated with emplacement of spent fuel at 2.5, 5, and 10 YOC. The figure clearly shows that the early-time thermal peak of 2.5 YOC fuel is somewhat higher than the later peaks of older fuels. Thus, a test using spent fuel 2.5 YOC allows an assessment of maximum (or slight over-test) thermal conditions within a few years as opposed to a few decades, as would be the case for the older fuels.

After considerable study involving not only thermal effects but rock mechanical, mining, and operational considerations as well, a design evolved for the SFT—C. The heat transfer aspects of the design were developed by considering how the curve in Fig. 3-1 could be approximated in a relatively small-scale test. Figure 3-2 shows that emplacement of a single canister would produce a thermal pulse of insufficient magnitude and duration. Adding canisters to form a linear array increased the peak temperature and the duration was extended by means of auxiliary heat sources in two parallel drifts.

*Contributed by W. C. Patrick

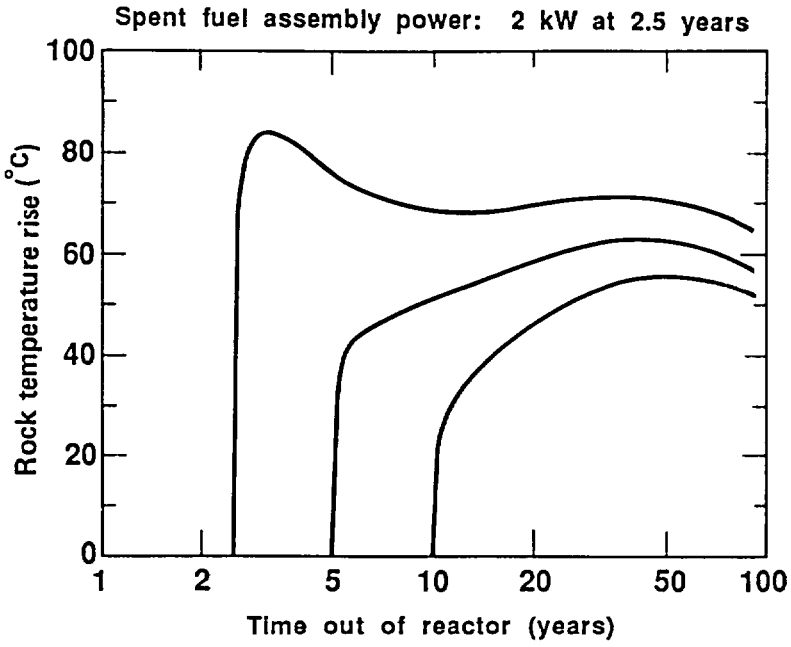

Figure 3-1. Temperature history of rock surface at fuel assembly midpoint in center hole of hypothetical spent-fuel repository (after Montan and Patrick, 1981).

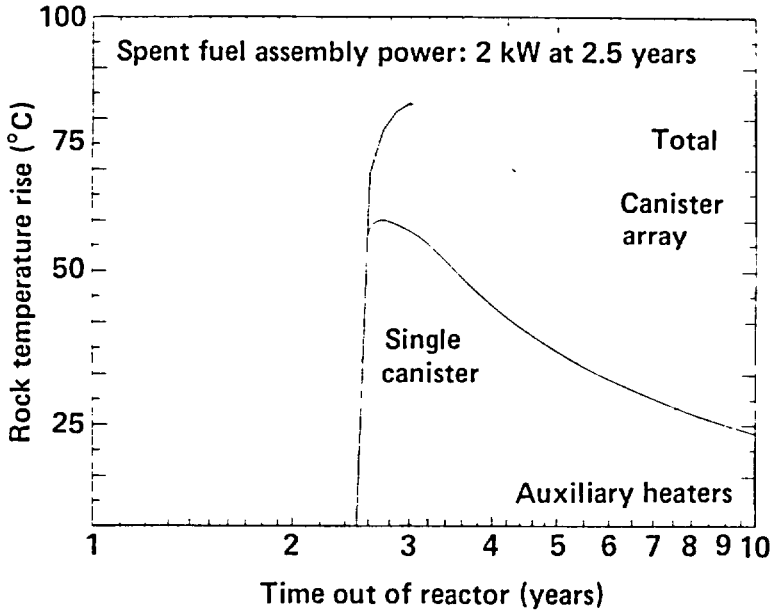

Figure 3-2. Calculated temperature on the storage-hole wall at canister midplane of 17-canister storage array (after Montan and Patrick, 1981).

The resulting SFT—C test geometry consisted of a linear array of 17 heat sources—11 spent-fuel assemblies and 6 electrical simulators on 3-m centers and 10 auxiliary heaters on 6-m centers in each of two parallel drifts positioned on 10-m centers from the central drifts (Fig. 3-3). The resulting temperature histories of the model repository and SFT—C design were almost indistinguishable (Fig 3-4).

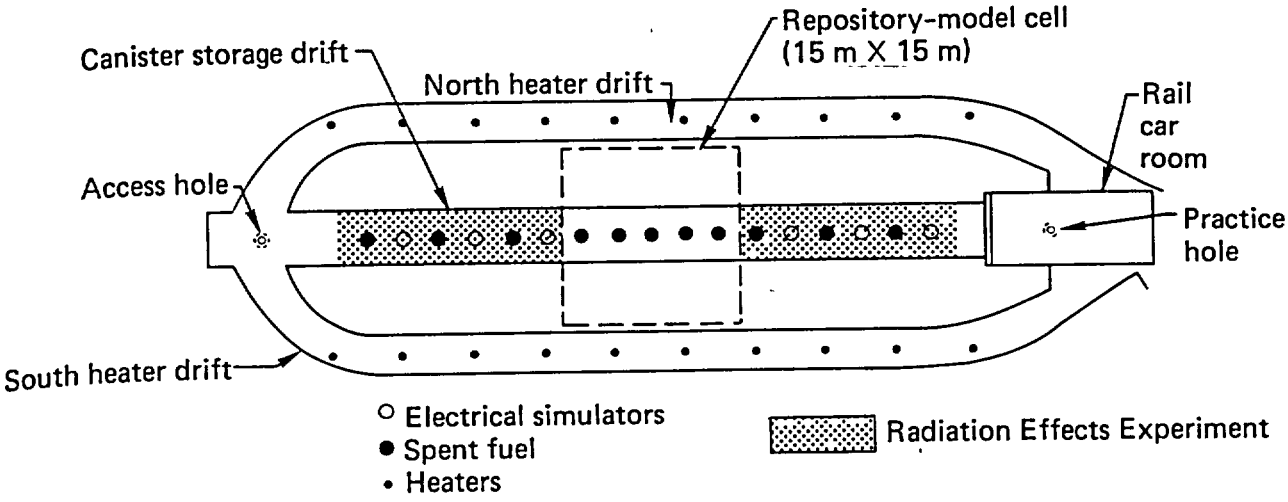

Figure 3-3. Plan view of the Spent Fuel Test—Climax.

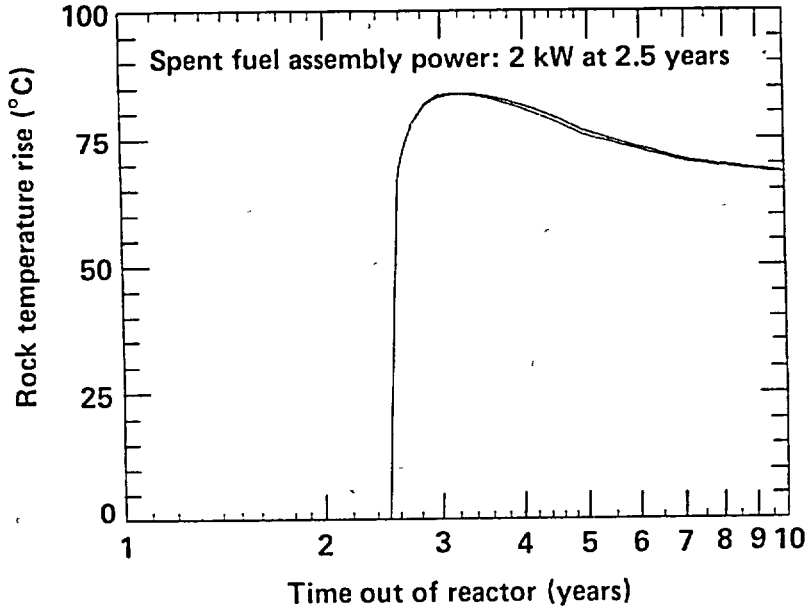

Figure 3-4. Temperature histories for model repository and SFT—C (after Montan and Patrick, 1981).

3.2.2 Detailed Design Calculations

The TRUMP finite difference code (Edwards, 1972) was used to address the complexities of ventilation as well as radiative, convective, and conductive heat transfer. These calculations also permitted us to assess the temperatures of operational concern, such as those of rails, air, and the shield plugs of the spent-fuel canisters (Montan and Patrick, 1981).

To perform the detailed design calculations, a unit cell approach was taken. This cell contained one canister and was bounded by two parallel vertical planes perpendicular to the drifts and spaced halfway between the canisters. The four-fold axis of symmetry through the canister centerline provided two additional planes of symmetry that reduced the calculational mesh to one-fourth of the unit cell.

The mesh used in these calculations contained three basic regions (Fig. 3-5). The innermost Region III was 20 m wide × 40 m high and was divided into 1600 zones to provide the required spacial resolution.

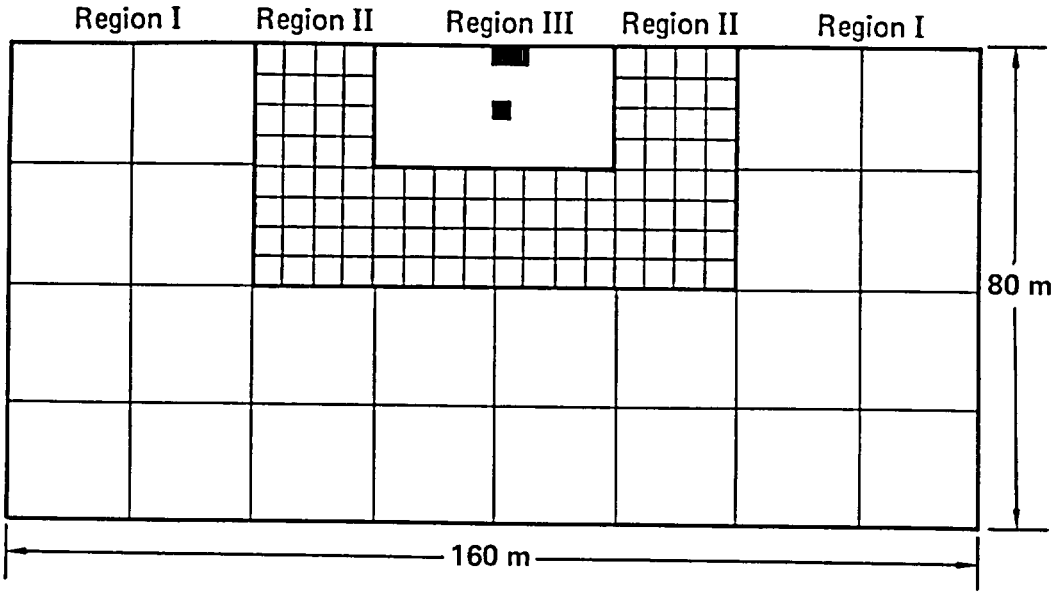

Figure 3-5. Schematic vertical section of mesh used in two-dimensional TRUMP calculations (after Montan and Patrick, 1981).

Region II, consisting of 96 zones measuring 5 × 5 m, and Region I, consisting of 24 zones measuring 20 × 20 m, were added to give an overall mesh size of 80 m × 160 m with an associated thermal time constant of about 120 years. The thickness of the zones is 1.5 m: one-half the canister spacing. In the regions comprising the drifts, the regular zoning was replaced with single zones representing air. In addition, 50-mm-thick zones of rock or concrete, as appropriate, were placed in the drift surface to obtain accurate surface temperatures for radiation and convection calculations.

Accurate representation of the canister environment required that relatively large, two-dimensional blocks near the heat sources be replaced with a finer, three-dimensional mesh. To accomplish this, the 50 zones beneath the floor of the canister drift were replaced to a depth of 10 m with 150 zones measuring 0.5 × 1.0 × 0.5 m each. The 54 zones comprising the 1.5-×-6.0-×-1.5 m-volume whose midplane coincides with that of the canister were in turn replaced by 486 zones measuring 1/6 × 1.0 × 1/6 m. Finally, the six corner zones were removed and the surrounding 18 zones were reduced in size, leaving the 305-mm-radius hole in which to place the canister and steel liner. The 230-mm-radius liner base was represented by 12 zones varying in height from 0.2 to 0.5 m. The canister was represented by 11 zones, seven of which represented the active heat source of the spent-fuel assembly or electrical simulator.

Heat transfer from the canister to the liner and from the liner to the emplacement borehole wall was modeled as radiative and convective with emittances of 0.4 for the outer canister and inner liner surface and 0.9 for the outer liner and rock wall surfaces. Zero-volume zones were placed on the rock surfaces in the borehole to give correct temperatures for the radiative transport calculation. Additional zones were provided to model other details of the test geometry (Montan and Patrick, 1981).

The auxiliary heaters in the side drifts were removed far enough from the principal areas of interest so that they were modeled in two dimensions. In this representation, these cylindrical heat sources were "smeared out" so that they were, in effect, strip sources.

An example of the types of detailed calculational results used in the test design is given in Fig 3-6. Further discussion is provided by Montan and Patrick (1981).

A specific design concern was that the temperature of the spent-fuel cladding not exceed 380°C. To calculate the canister skin temperature that would drive the cladding-temperature calculation, we considered radiative transport across the rock/liner and liner/canister air gaps. Conductive and convective processes were not modeled, so the resulting temperatures were conservative in the sense that they were higher than would actually occur.

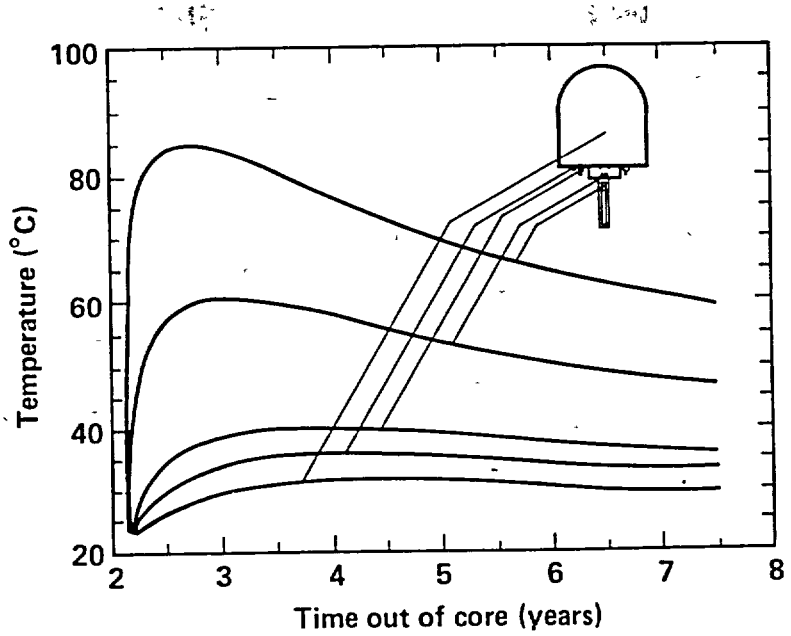

Figure 3-6. Three-dimensional TRUMP code calculations of temperature vs time at indicated locations in storage drift (ventilation effects included) (after Montan and Patrick, 1981).

Using a relaxation technique for steady-state heat transfer, we performed a sensitivity analysis for a range of all important parameters (Montan and Patrick, 1981). Only for an extreme case of canister power increased to 2.5 kW, no conductance in the helium fill gas, and degraded thermal properties around the canister did temperatures reach 383°C, slightly in excess of the design limit. Based on these calculations, we judged that the cladding integrity would not be jeopardized during the test.

3.2.3 As-Built Calculations

Using the model described above and revised thermal properties, power tables, and ventilation rates, we performed heat transfer calculations for the completed SFT—C and published the results before the test commenced. As presented by Montan and Patrick (1981), the results of these calculations were the basis of the early-time comparisons of calculated and measured temperatures throughout the test array (Carlson et al., 1980, Patrick et al., 1981, 1982, 1983).

These calculational results were post-processed in two basic formats: temperature histories at selected points and cross sections of temperature contours at selected times. Examples of the high quality of comparison are provided in Figs. 3-7 and 3-8. Calculated and measured temperatures differ at most by a few degrees Celsius.

3.2.4 Test Completion Calculation

When we determined that a 3-year test provided enough time to achieve the goals of the SFT—C, we began calculations to determine the required duration of the post-retrieval cooling period. Ballou et al. (1982) documented the rationale and supporting thermal calculations that were used to establish the test completion plan and schedule.

The calculational geometry, associated mesh, material properties, and energy deposition from the spent fuel, electrical simulators, and auxiliary heaters were identical to those used in the as-built calculations discussed above. To obtain the maximum cooling rate, the ventilating capacity of the storage-phase fans (Chapter 5) was directed through the canister storage drift, and the construction-phase Sutorbilt blower capacity was partitioned between the two heater drifts. As a result, a planned 2.83 m^3/s (6000 cfm) was provided to each drift.

The calculations showed that temperatures dropped rapidly at positions near the thermal sources, bringing temperatures down to about 35°C after only 6 months of cooling (Fig. 3-9). Furthermore, we

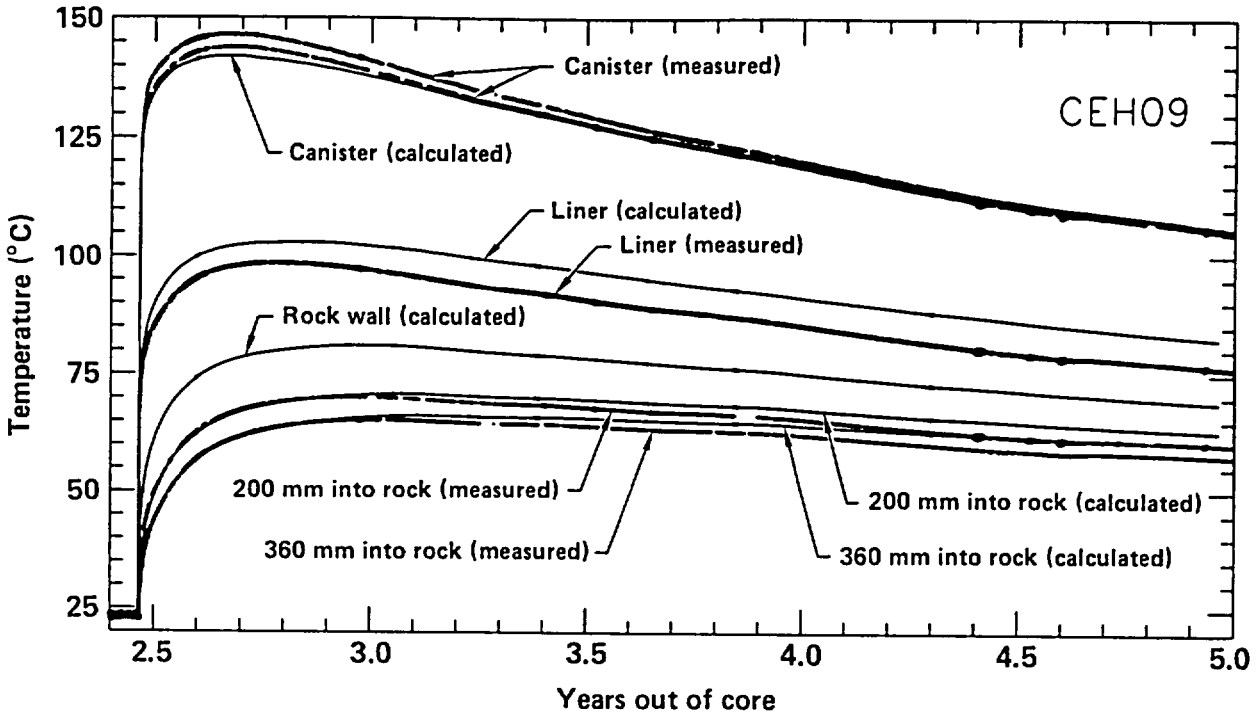

Figure 3-7. Calculated and measured temperature histories at various radial locations at axial midplane of CEH09 (as-built calculation).

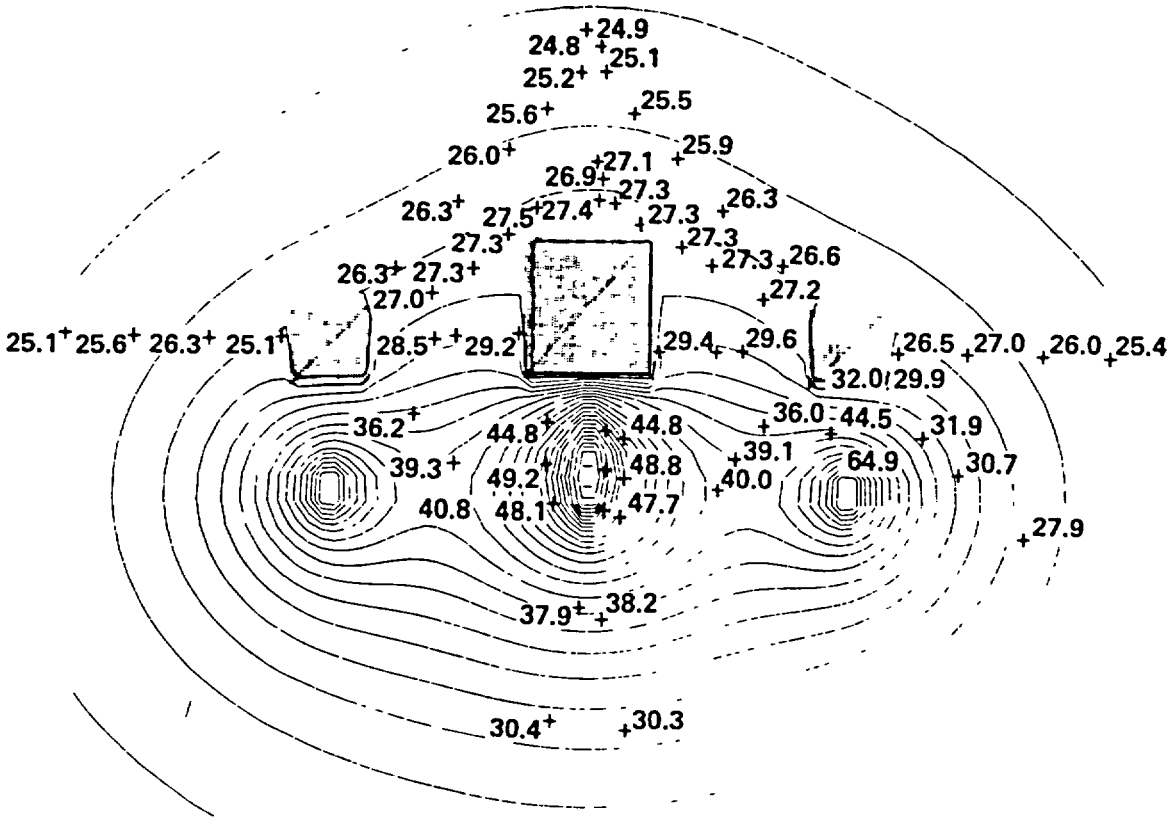

Figure 3-8. Comparison of measured temperatures with TRUMP-calculated temperature contours at 3.5 YOC at station 2+83 (first solid contour at 24°C, contour interval at 2°C).

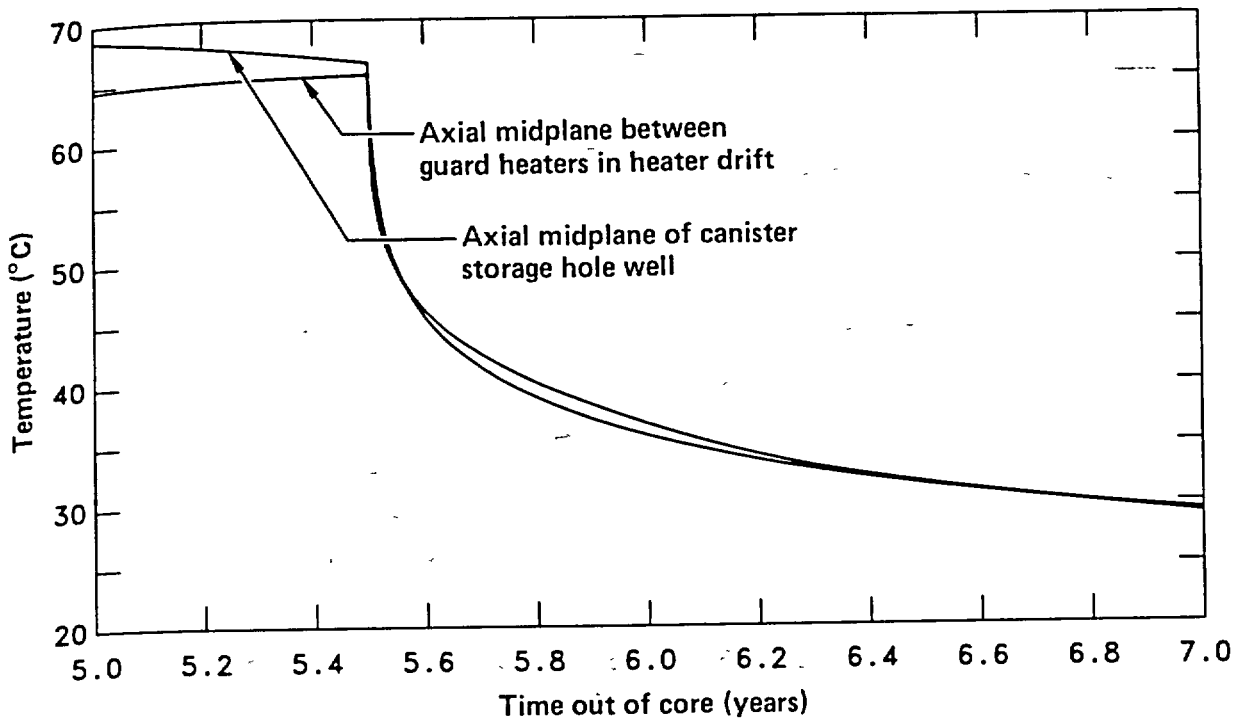

Figure 3-9. Temperature histories near thermal sources resulting from fuel retrieval (after Ballou et al., 1982).

found that an additional year of cooling would only lower the temperature another 5 to 7°C. Expressed another way, about 70% of all the temperature change that will ever occur in returning to ambient temperature, occurs during the first 6 months.

Farther from the heat sources, the rates of cooling were much slower, as expected (Fig. 3-10). The 4 to 5°C temperature changes during the first 6 months represent only 20 to 40% of the temperature differential with respect to ambient.

The overall effects of cooling are seen most clearly by comparing temperature contours at a cross-section through the middle of the SFT—C. Figures 3-11 and 3-12 show the calculated temperatures after 3 years of heating and following a 6-month post-retrieval cooling period, respectively. Since additional cooling was seen to be very slow, we adopted a 6-month planned cooling phase.

3.2.5 Post-Test Calculations

After all test data were acquired and the SFT—C was completed, we performed a final series of calculations using the best-available thermal properties, power tables, and ventilation parameters. In addition, ranges of values of the more important parameters were used to complete the series of eight post-test calculations (Patrick and Montan, 1986). All these calculations used the finite-difference mesh described above. Table 3-1 summarizes the pertinent input parameters and conditions used in these calculations.

Calculation number (CN) 1148 used the thermal properties, ventilation flowrate, ambient rock temperature, constant inlet air temperature, and convection coefficient that were selected before heated-phase testing began. This is the pretest as-built calculation reported by Montan and Patrick (1981).

For CN 1194, we used a somewhat higher ambient rock temperature and drove the ventilation model with the measured inlet air temperature history. We also included cooling of the rock mass by ventilation during construction of the SFT—C. As a result, temperatures near the drifts were cooler than the 24.7°C ambient, undisturbed temperature.

The next two modifications examined the effects of errors or variations in thermal conductivity on the quality of the results. CN 1195 and CN 1196 used rock mass conductivities of 3.42 and 6.22 W/m·K, respectively. CN 1199 treated possible decreases in thermal conductivity of the rock and concrete adjacent to the

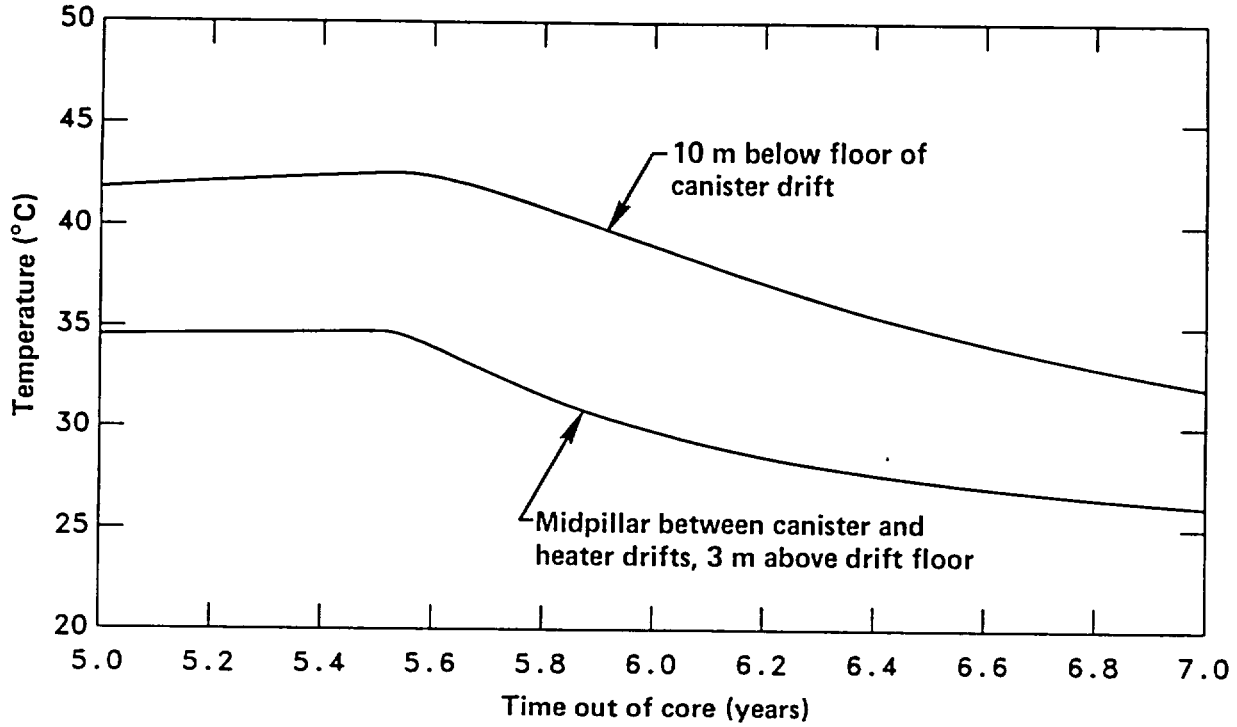

Figure 3-10. Temperature histories at intermediate locations resulting from fuel retrieval (after Ballou et al., 1982).

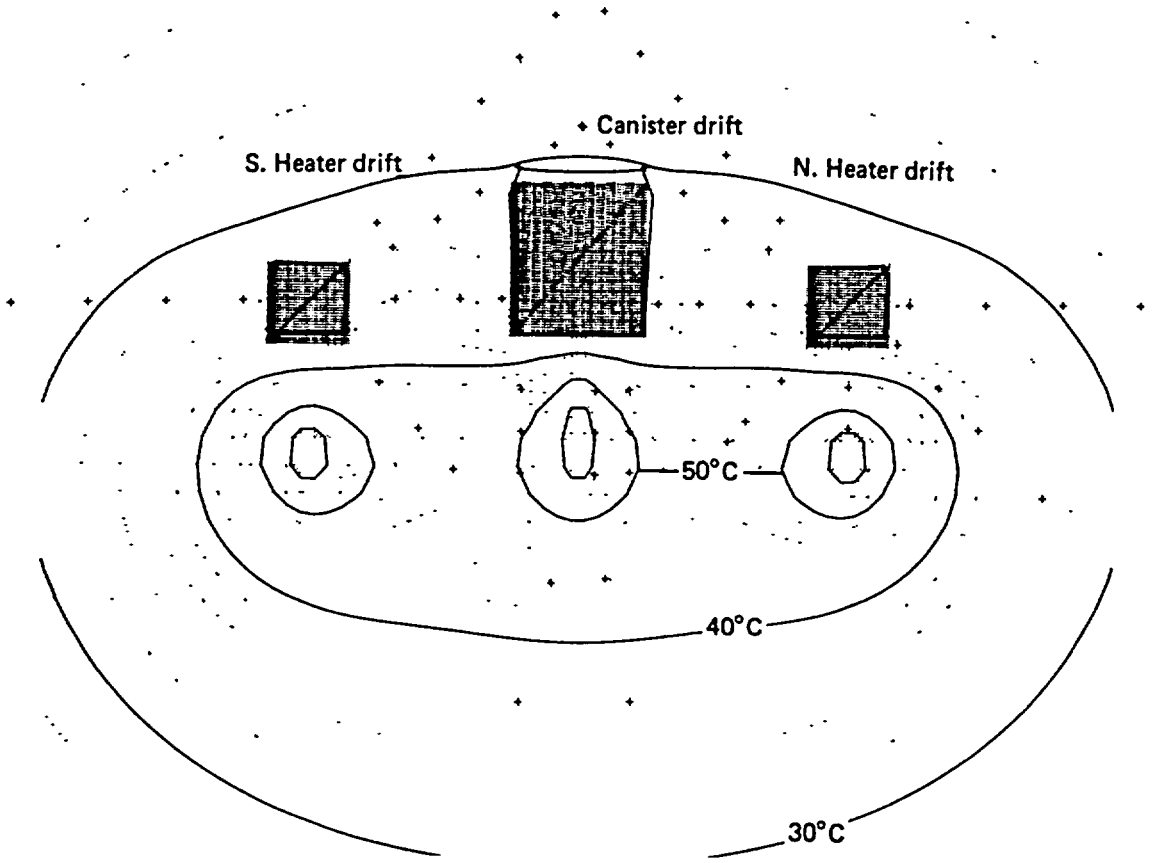

Figure 3-11. Contours of calculated temperatures at a fuel age of 5.5 years out of core, prior to spent-fuel retrieval (+ denotes thermocouple location) (after Ballou, et al., 1982).

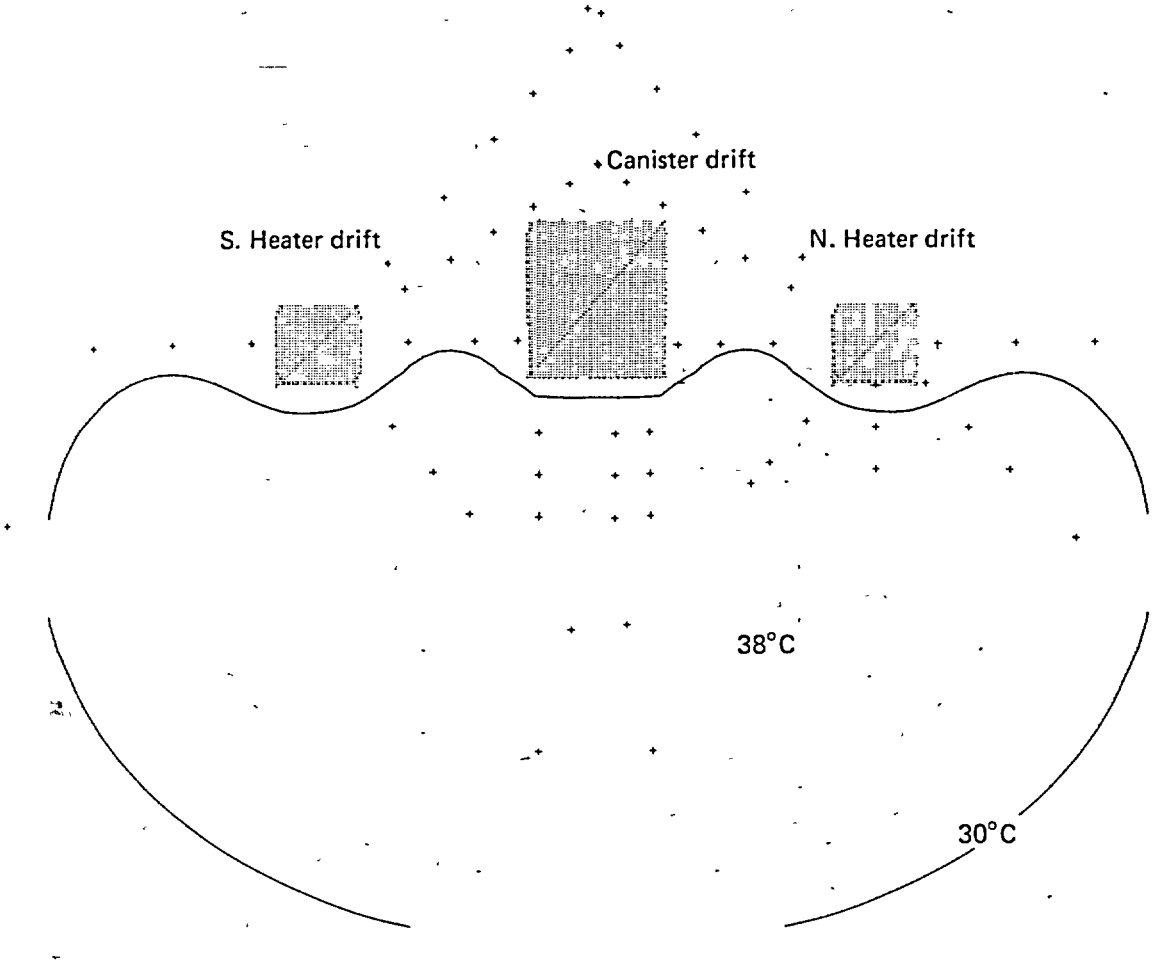

Figure 3-12. Contours of calculated temperatures at a fuel age of 6.0 years out of core, 0.5 years after spent-fuel retrieval (+ denotes thermocouple location) (after Ballou et al., 1982).

Table 3-1. Summary input parameters and conditions used in post-test thermal calculations (after Montan and Patrick, 1986).

Parameter	Calculation number[a]					
	1148	1194	1196	1197	1200	1201
k $\left(\frac{W}{m \cdot K}\right)$	3.11	3.11	6.22	3.11	3.11	3.11
C $\left(\frac{J}{Kg \cdot K}\right)$	930	930	930	930	930	1860
Ventilation[b] $\left(\frac{m^3}{s \cdot m}\right)$	0.026	0.026	0.026	0.006	0.026	0.026
Amb. rock temp (°C)	23	24.7	24.7	24.7	24.7	24.7
Inlet air temp	23°C	Meas.	Meas.	Meas.	Meas.	Meas.
Nusselt number[c]	$0.13\,R_a^{1/3}$	$0.13\,R_a^{1/3}$	$0.13\,R_a^{1/3}$	$0.13\,R_a^{1/3}$	$0.065\,R_a^{1/3}$	$0.13\,R_a^{1/3}$

[a] For 1195, k = 3.42 W/m·k; otherwise, it is like 1194. For 1199, low k is used for the walls and floor; otherwise, it is like 1194.

[b] In the model, ventilation flowrate is normalized per unit length in the direction of flow.

[c] Representation of the convection coefficient.

underground openings. (Such decreases could occur as a result of excavation-induced fracturing of the rock.) All other conditions and properties were the same as CN 1194.

The effects of changes in ventilation flowrate were examined in CN 1197. When preliminary calculations showed that the results were relatively insensitive to changes in flow rate, we introduced a four-fold reduction to examine the effect. The convective transfer of heat to the ventilation airstream was examined in CN 1200 by reducing the convection coefficient by a factor of two. Finally, the mass heat capacity was increased by a factor of two in CN 1201 to determine the sensitivity of results to this property.

Montan and Patrick (1986) discuss the effects of each of these variations on the level of agreement between data and calculational results. In addition, they present the results of fully three-dimensional finite-length models of the SFT—C. Both finite-difference and analytical solutions to the finite-length models are presented. Calculation 1194 is the basis of most of the analyses presented in Chapters 13 and 14.

3.3 Rock Mechanical Response Calculations

Several finite-element calculations were made to help select instrumentation types and locations and to estimate the response of the rock mass to excavation, heating, and subsequent cooling. The purpose and general formulation of each calculation are described here.

3.3.1 Preliminary Design Calculations

To determine the appropriate locations, orientations, and dynamic ranges of stress and displacement instrumentation, and to estimate the response of the rock mass, we performed scoping calculations (Ramspott et al., 1979, and Butkovich, 1980). Excavation response was calculated using the ADINA finite-element code (Bathe, 1978). For thermomechanical calculations, this code was coupled to the companion ADINAT heat transfer code (Bathe, 1977).

The unit cell modeled in the excavation response calculations was a 1-m-thick section transverse to the axis of the drifts. Because of symmetry, only half the unit cell was modeled. For these scoping calculations, the rock was assumed to be isotropic, linearly elastic, and homogeneous with an elastic modulus of 47.6 GPa and a Poisson's ratio of 0.2. The vertical stress was taken as the weight of the overburden, and the horizontal stress was assigned a magnitude of 0.8 times the vertical stress.

Scoping calculations for thermomechanical response used the same basic mesh, with the addition of a decaying 2-kW heat source to simulate the spent fuel and 1.6-kW auxiliary heaters energized at 3.5 months after spent-fuel emplacement. The thermal properties were the same as for the preliminary thermal design calculations. In addition, we used a thermal expansion coefficient of $8 \times 10^{-6}/°C$.

Although these calculations were quite simplistic, they were adequate for design purposes and for selecting instrumentation types and locations.

3.3.2 As-Built Calculations

Once the SFT—C was constructed, considerably better input data were available for use in the as-built design calculations, which we used to make comparisons with the rock mechanical response data, both during mining and during the heated phase of the test. Among the input data that changed were: the spent-fuel power table, the auxiliary heater power schedule, the rock deformation modulus, and the *in situ* stress.

The calculational mesh (Fig. 3-13) was based on the as-built dimensions and emplacement configurations (Table 3-2). The material properties used in the calculations are shown in Table 3-3. To include the properties of the zone of rock damaged by blasting during excavation of the facility, it was necessary to redesign the mesh, allowing for a 0.5-m-wide element group surrounding the excavations. The deformation moduli given here are markedly different from those used in the scoping calculations. Furthermore, limited *in situ* stress data (Ellis and Magner, 1982) led us to use a horizontal-to-vertical stress ratio of 1.2 instead of 0.8.

To accurately simulate the thermal radiation and ventilation process that would be operative in the drifts, Butkovich and Montan (1980) developed "pseudoproperties" for the air in the drifts. Heat removal was simulated by linking the central node of each drift to an outside node, the temperature of which was constant at the anticipated inlet air temperature. Because this linkage was a temperature-dependent convection coefficient, the heat removal rate was temperature-dependent (Table 3-4).

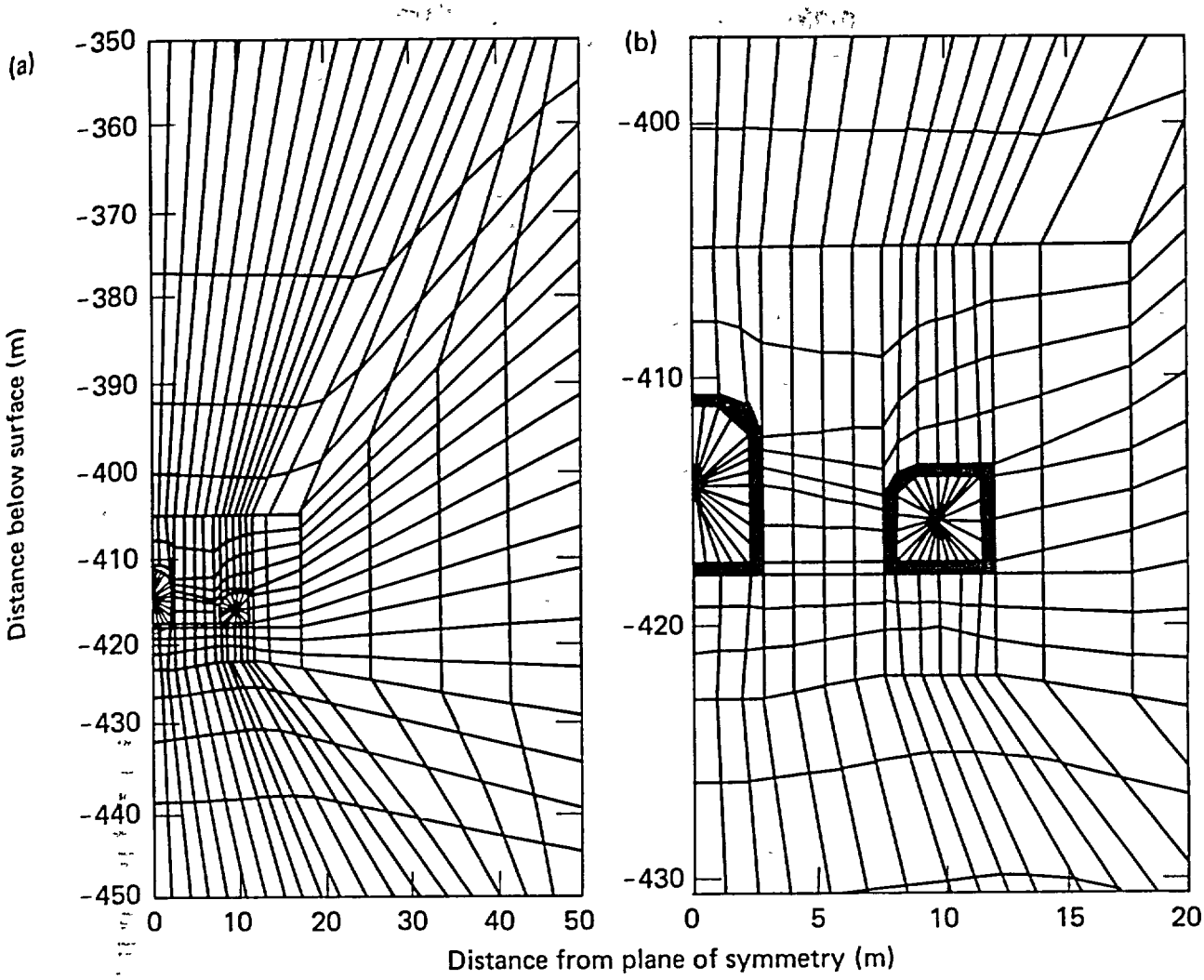

Figure 3-13. Finite-element mesh used with as-built mining and thermomechanical calculations (after Butkovich, 1981).

Table 3-2. Distances and dimensions used in ADINA and ADINAT calculations (after Butkovich, 1981a).

Spent-fuel drift	**Distances and dimensions**
Floor position	417.58 m below surface
	1.74 m above top of canister
Cross section	4.58′ × 6.25-m domed roof
Heater drift	
Floor position	417.58 m below surface
	2.66 m above top of heater
Cross section	3.35′ × 3.55-m rounded corner
Spent-fuel canisters and electrical simulators	
Spacing	3 m on center
Length	3.66 m
Electrical resistance heaters	
Spacing	6 m on center
Length	1.83 m

Table 3-3. Values of Climax stock granite and air properties used in calculations (after Butkovich, 1981a).

Climax stock granite	Values
Heat capacity[a]	930 J/kg·K
Thermal Conductivity (°C)	
0	3.1679 W/m·K
23	3.1104 W/m·K
477	2.1104 W/m·K
Thermal expansion coefficient (°C)	
0	10×10^{-6} K^{-1}
23	10×10^{-6} K^{-1}
40	8.9×10^{-6} K^{-1}
80	7.4×10^{-6} K^{-1}
125	8.0×10^{-6} K^{-1}
175	9.6×10^{-6} K^{-1}
225	12.7×10^{-6} K^{-1}
Elastic modulus	
Field	
Explosive-damaged region	13 GPa
Rock mass	27 GPa
Laboratory	
Rock samples	48 GPa
Poisson's ratio:	
Field	
Rock mass	0.25
Damaged zone	0.35
Laboratory	
Rock samples	0.21
Air[b]	
Density	1 kg/m^3
Heat capacity	1000 J/kg·K
Thermal conductivity	0.03 W/m·K

[a] Derived from diffusivity measurements.

[b] Used to derive input values shown in Table 3-4.

Table 3-4. Values of drift material properties derived to simulate radiation and ventilation with ADINAT (after Butkovich, 1981a).

Properties	Values
Thermal conductivity	
Spent-fuel drift	70 W/m·K
Heater drift	40 W/m·K
Volumetric heat capacity	8×10^4 J/m^3·K
Convection coefficient (H)	
ΔT (K)	H(W/m^2·K)
0	0
0.272	4.5
0.445	5.0
0.903	5.5
1.878	6.0
4.074	6.5
9.427	7.0
24.042	7.5

Table 3-5. Variation in power level in electrical-resistance heaters (after Butkovich, 1981a).

Time since emplacement (yr)	Date	Power level (kW)
0	6 May 1980	0
0.14	27 June 1980	1.850
0.16	2 July 1980	0.925
0.60	17 December 1980	1.300
1.46	8 March 1982	1.400

The decay curve (Fig. 3-14) and auxiliary heater power table (Table 3-5) were also notably different from those used in the scoping calculations. The peak spent-fuel power was 1,530 W, and the auxiliary heaters were designed to operate at several different power levels during the test.

The results of the as-built calculations formed the basis for several comparisons with measured rock displacements and stress changes. In general, the as-built calculations simulated the heated-phase response quite well (Patrick et al., 1982, 1983, 1984). The response to excavation was not reproduced by the calculation because, in the pillars, the calculation and data differed in sign (Fig. 3-15), leading to a further calculational effort and analysis.

3.3.3 Analysis of the Climax Mine-By

Wilder and Patrick (1980) provided an initial analysis and presentation of the mine-by data in the context of calculations. They established that the major joints and faults significantly influenced rock response. The regions of the rock mass that exhibited the larger discrepancies between measured and calculated displacements coincided with regions containing major geologic discontinuities.

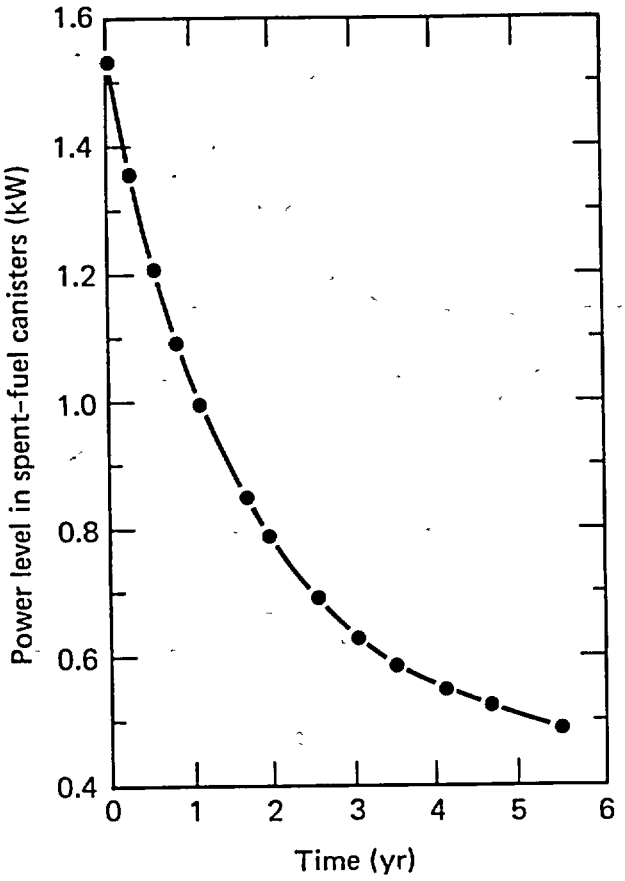

Figure 3-14. Spent-fuel decay curve used in ADINAT calculations (after Butkovich, 1981a).

Because of the poor agreement between measured and calculated rock responses to excavation, further analyses were undertaken. Calculations by Schrauf and Board (1979) using the finite-element code TWODI and the boundary element code DIG produced results that were consistent with ADINA and, hence, inconsistent with the measurements. Heuze, Butkovich, and Peterson (1981) used Heuze's JPLAXD finite-element code. Developed specifically for analysis of structures in rock, this code contains a library of solid and joint elements that can exhibit strain softening and dilatancy in the post-peak region of stress-strain response.

The JPLAXD code incorporates discrete geological discontinuities as well as strain-softening and dilatancy behaviors, which the earlier ADINA code did not. Other features were also different, including field-measured rock mass modulus and *in situ* state of stress, field-scale Poisson's ratio derived from stress measurements (Chapter 4), and a parametric variation in the ratio of horizontal to vertical stress between 0.5 and 3.5.

Both jointed and unjointed models were used for these calculations; the former models used dilatant and nondilatant joint behaviors. The jointed meshes for the two heavily instrumented sections of the excavation are shown in Figs. 3-16 and 3-17. Because JPLAXD is a two-dimensional formulation, it was necessary to treat features that were 10 to 30 degrees from parallel as though they were parallel to the axis of the drifts (Chapter 4).

The initial properties of intact rock and joints used in these calculations are given in Tables 3-6 and 3-7, respectively. As rock displacements progressed during excavation, these material properties were automatically adjusted by JPLAXD in accordance with the assigned constitutive laws for the respective materials. Because no *in situ* strength data were available, Heuze adopted the minimum values of the shear-strength parameters that would provide stable excavations.

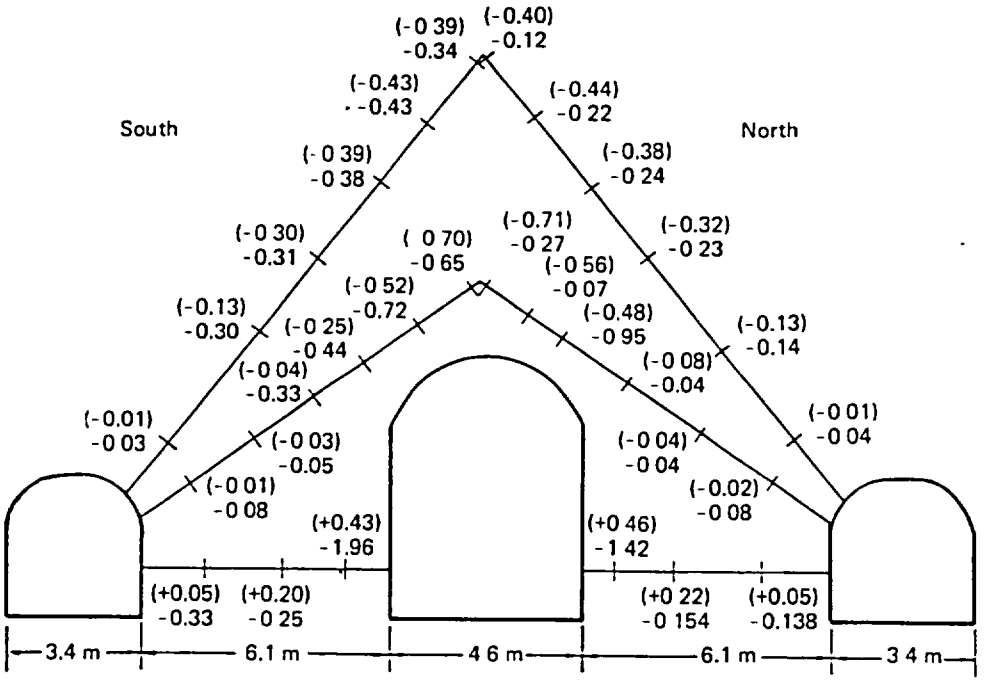

(a) Station 2+83

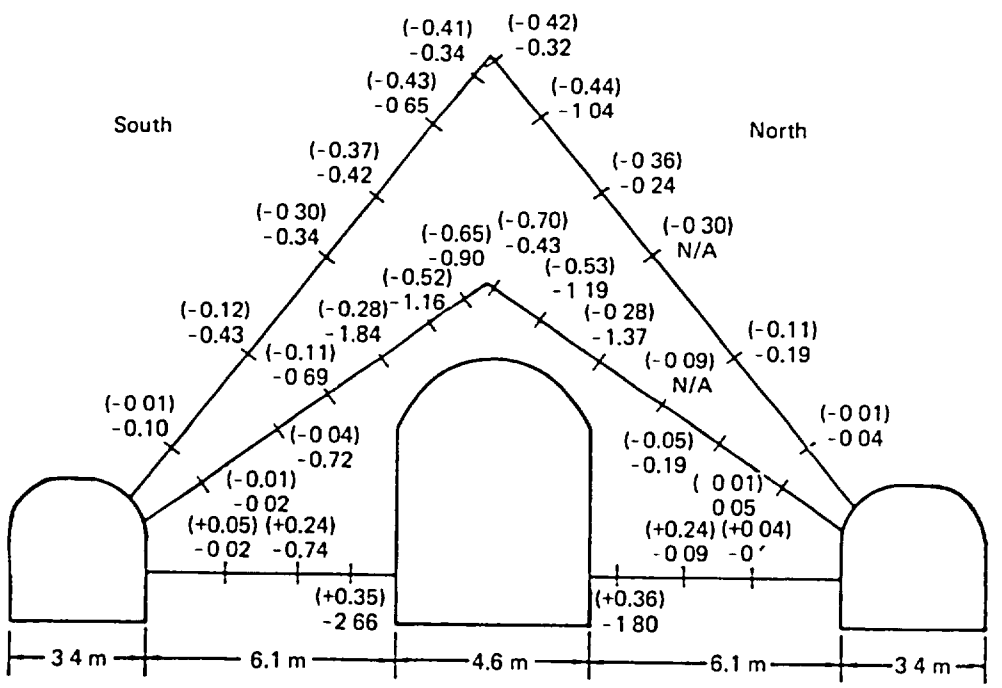

(b) Station 3+45

Figure 3-15. Comparison of observed and (ADINA-calculated) displacements (mm) during Mine-by.[2] Minus sign indicates shortening; plus sign indicates lengthening (after Heuze, Butkovich, and Peterson, 1981).

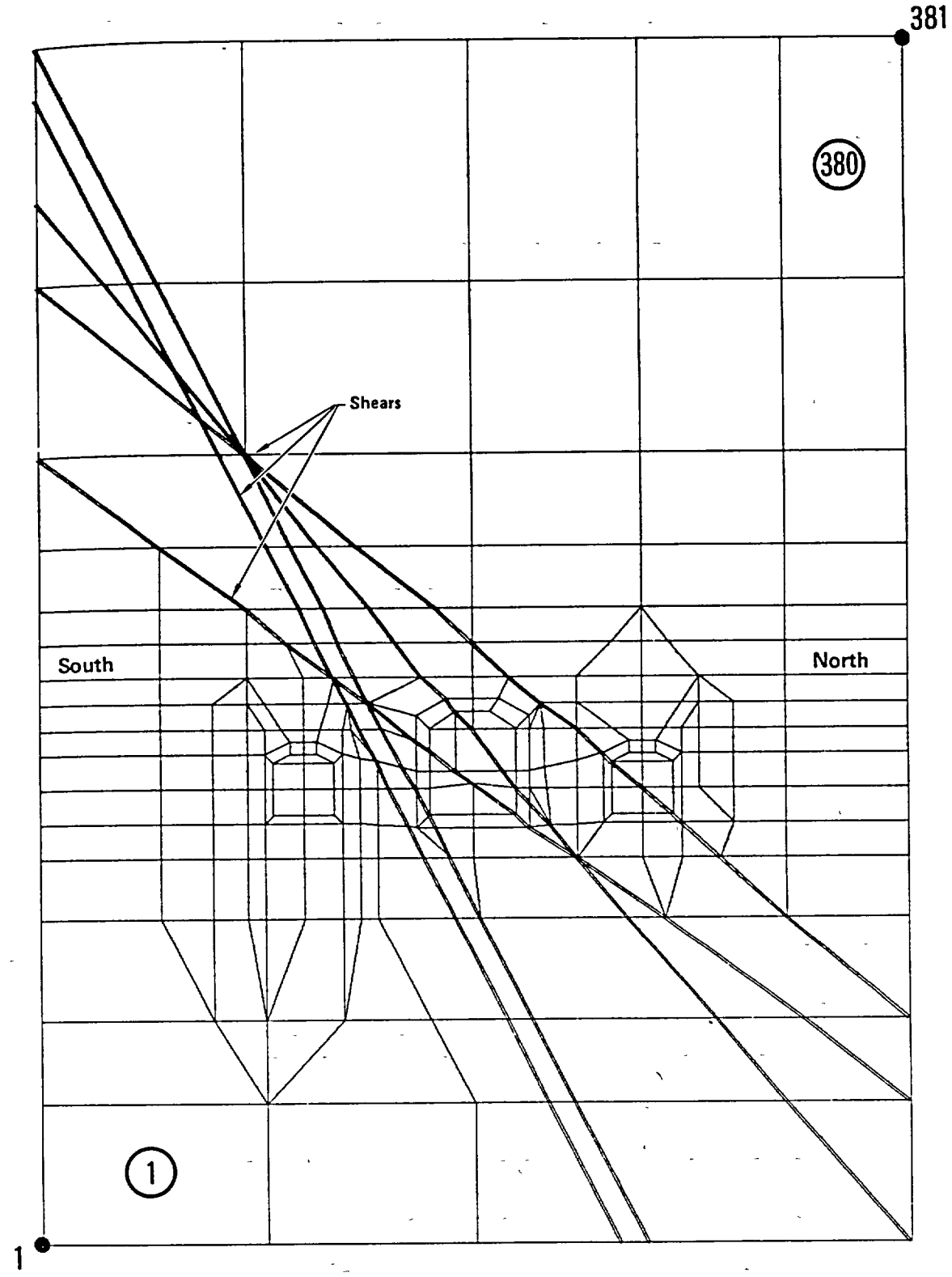

Figure 3-16. Jointed mesh of the SFT—C caverns at station 2+83 (381 nodes, 380 elements, after Heuze, Butkovich, and Peterson, 1981).

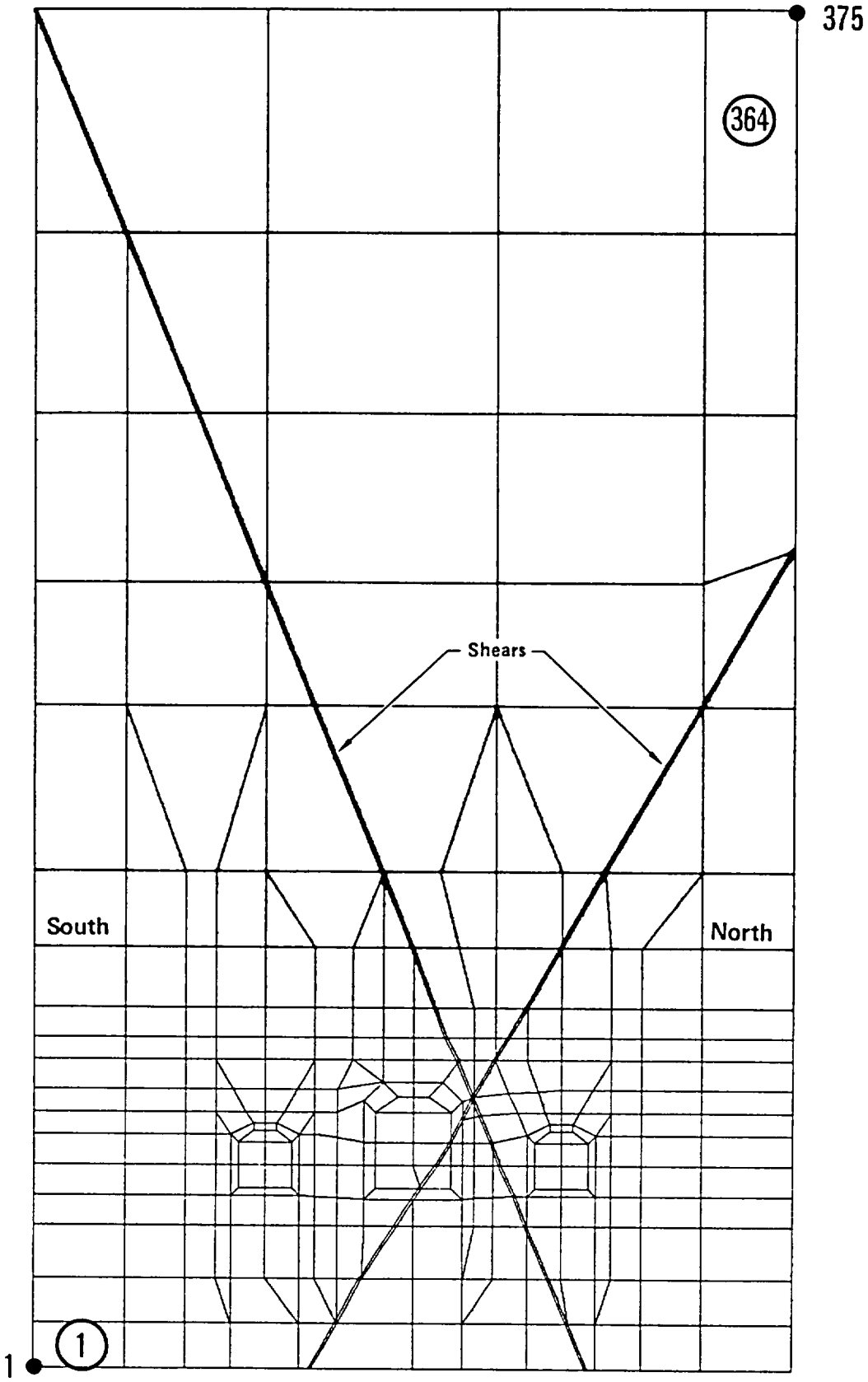

Figure 3-17. Jointed mesh of the SFT—C caverns at station 3+45 (375 nodes, 364 elements, after Heuze, Butkovich, and Peterson, 1981).

Table 3-6. Initial values of rock properties used for JPLAXD calculations (after Heuze, Butkovich, and Peterson, 1981).

Property	Intact rock	Damaged rock[a]	Excavated rock[b]
Mass density	2.65	2.65	10^{-2}
Modulus (GPa)	30	10	10^{-2}
Poisson's ratio	0.25	0.35	0.25
Peak cohesion (MPa)	7	3.5	10^{10}
Residual cohesion (MPa)	0	0	10^{10}
Peak friction (deg)	60	45	0
Residual friction (deg)	45	45	0
Tensile strength (MPa)	10	2.7	10^{10}

[a] Damaged rock surrounds the drifts to a depth of 0.5 to 1 m.

[b] The excavated rock is made very light and soft, but strong to bypass the failure criterion routines.

Table 3-7. Initial values of joint properties used for JPLAXD calculations (after Heuze, Butkovich, and Peterson, 1981).

Property	Joint in intact rock	Joint in damaged rock	Excavated joint
Normal stiffness (MPa/m)	10^5	10^5	10^{-3}
Shear stiffness (MPa/m)	2700	2700	10^{-4}
Maximum closure (m)	2.10^{-3}	2.10^{-3}	200
Peak cohesion intercept (MPa)[a]	5	5	0
Peak cohesion[a]	0	0	0
Initial dilation angle (deg)[a]	10	10	0
Critical normal stress (MPa)[a]	30	30	10^{10}
Tensile strength (MPa)	0	0	10^{10}
Residual friction (deg)[a]	40	25	0

[a] See Heuze, Butkovich, and Peterson (1981) for derivation.

The results of Heuze, Butkovich, and Peterson (1981) are summarized for nondilatant models in Figs. 3-18 and 3-19, and in Fig. 3-20 for dilatant joint models. In general, the JPLAXD-calculated displacements are larger than those calculated by ADINA for the inclined instrument locations. At some locations, the JPLAXD results are opposite in sign from the ADINA results and the measured displacement. Although JPLAXD did calculate that vertical stresses decreased in some locations within the pillars, the average vertical stress increased. The measured narrowing across the pillar was not observed in the calculations.

Taken in total, the agreement between measured and calculated displacements was poorer for JPLAXD than for ADINA. The former differed from measured values by more than a factor of two in 87% of the cases for inclined instruments and 100% of the cases for horizontal instruments. The latter differed from measured values by more than a factor of two in 56% of the cases for inclined instruments and 100% of the cases for horizontal instruments. The JPLAXD stress-change results were clearly better than the ADINA results because they showed the measured stress decreases as excavation progressed.

Although Heuze, Butkovich, and Peterson (1981) concluded that the instrumentation was probably in error, other researchers who have reviewed the data and calculations reached a different conclusion. Cook (1983) has shown that all the data, while highly variable, are statistically consistent, leading him to conclude that it was unlikely that instrumentation errors caused the unusual pillar narrowing. Even so, to date the observed displacements have not been successfully modeled. Scoping studies of the permanent displacements resulting from nearby detonation of high explosives indicates that this mechanism could be responsible for the observed displacements (Butkovich, 1985). Because of the limited capability of such

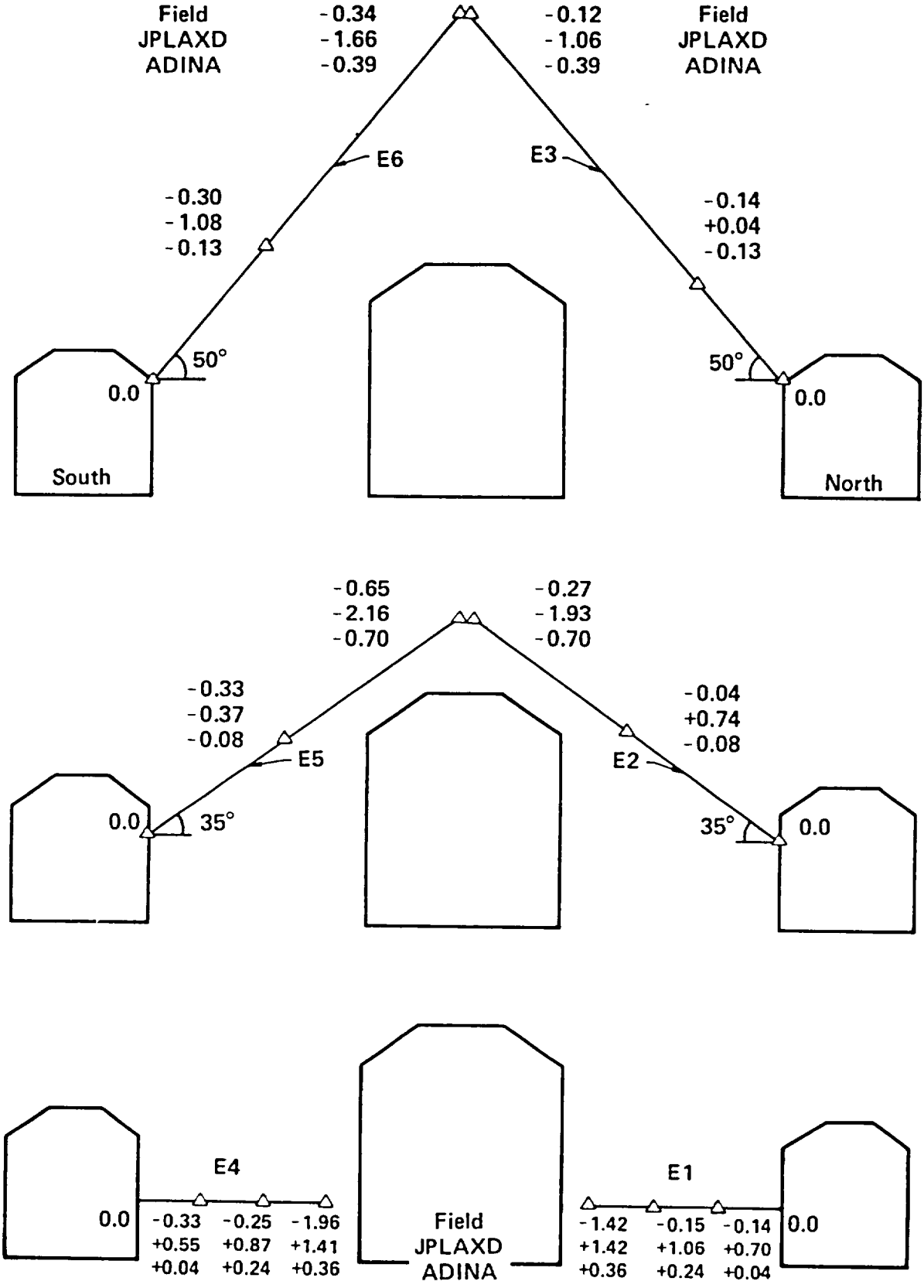

Figure 3-18. Comparison of field observations with JPLAXD and ADINA calculations, for the relative movements of MPE anchors during the mine-by (mm). Station 2+83, non-dilatant joints (after Heuze, Butkovich, and Peterson, 1981).

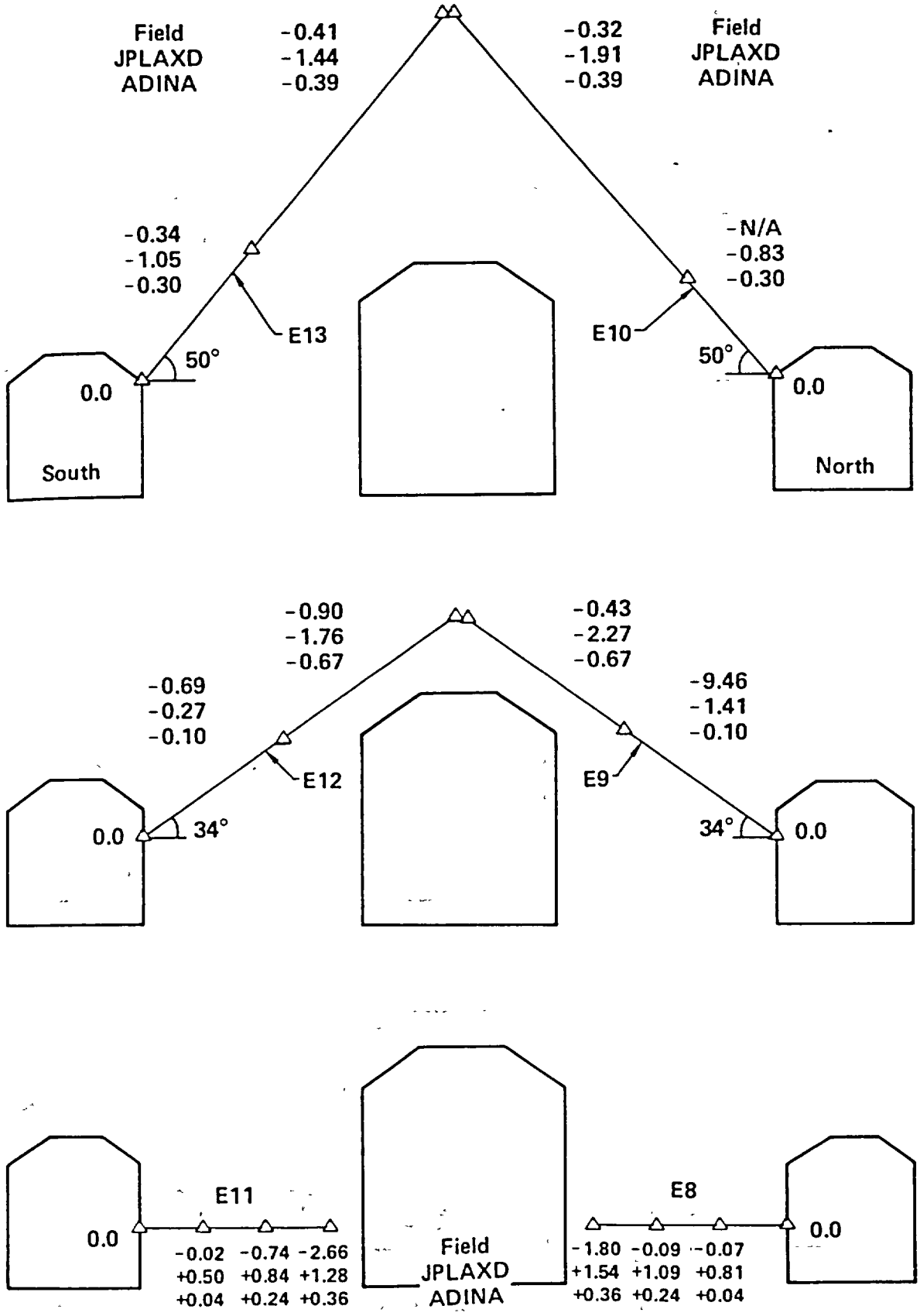

Figure 3-19. Comparison of field observations with JPLAXD and ADINA calculations for the relative movements of MPE anchors during the mine-by (mm) (after Heuze, Butkovich, and Peterson, 1981).

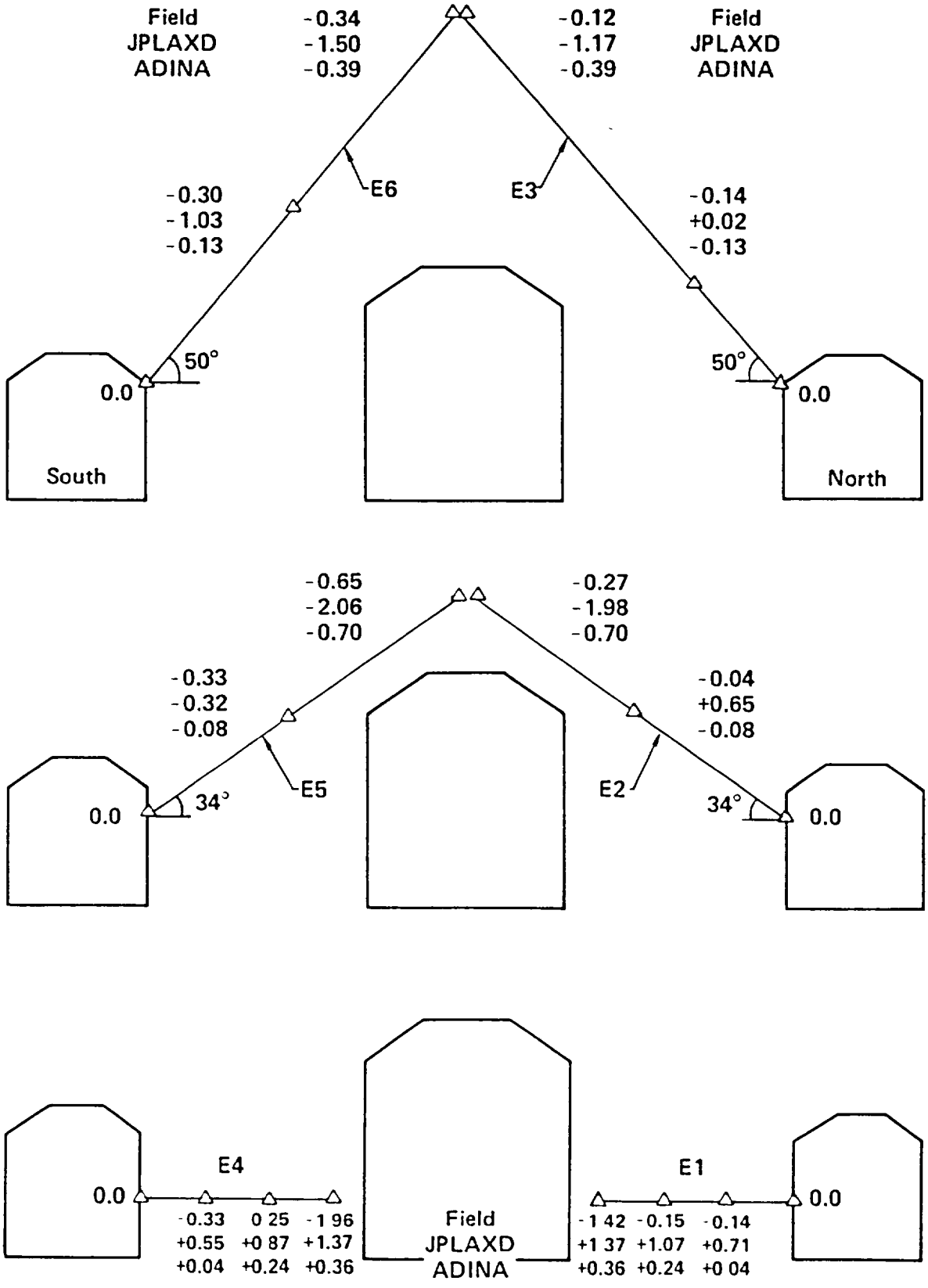

Figure 3-20. Comparison to field observations with JPLAXD and ADINA calculations for the relative movements of MPE anchors during the mine-by (mm). Station 2+83, dilatant joints (after Heuze, Butkovich, and Peterson, 1981).

codes to calculate the geometry and because of the large number of explosive charges used in the excavation, definitive results have not been produced.

3.3.4 Effects of Boundary Conditions

To confirm the adequacy of the mesh sizes used in the ADINA as-built thermomechanical calculations and to evaluate differences between plane strain and plane stress boundary assumptions, Butkovich (1982) performed an additional series of calculations for three cases:

- The effect of mesh loading on three progressively larger meshes.
- The difference in results from plane strain and plane stress boundary conditions.
- The effect of isothermal boundaries on a small mesh and a significantly larger mesh.

To study these effects, he developed an "onion skin" mesh consisting of a 40- by 80-m inner core of 274 eight-node isoparametric elements, a second layer of 52 eight-node elements that enlarged the mesh to 55 × 110 m, and a third layer of 56 eight-node elements that enlarged the mesh to 70 × 140 m (Fig. 3-21). The effective mesh sizes were twice these dimensions because of the vertical plane of symmetry through the center of the unit cell.

The rock mass heat transfer and mechanical parameters, auxiliary heater power table, spent-fuel decay curve, and other features of the calculation were essentially the same as were used in the as-built thermomechanical analyses (Butkovich, 1981a and 1982).

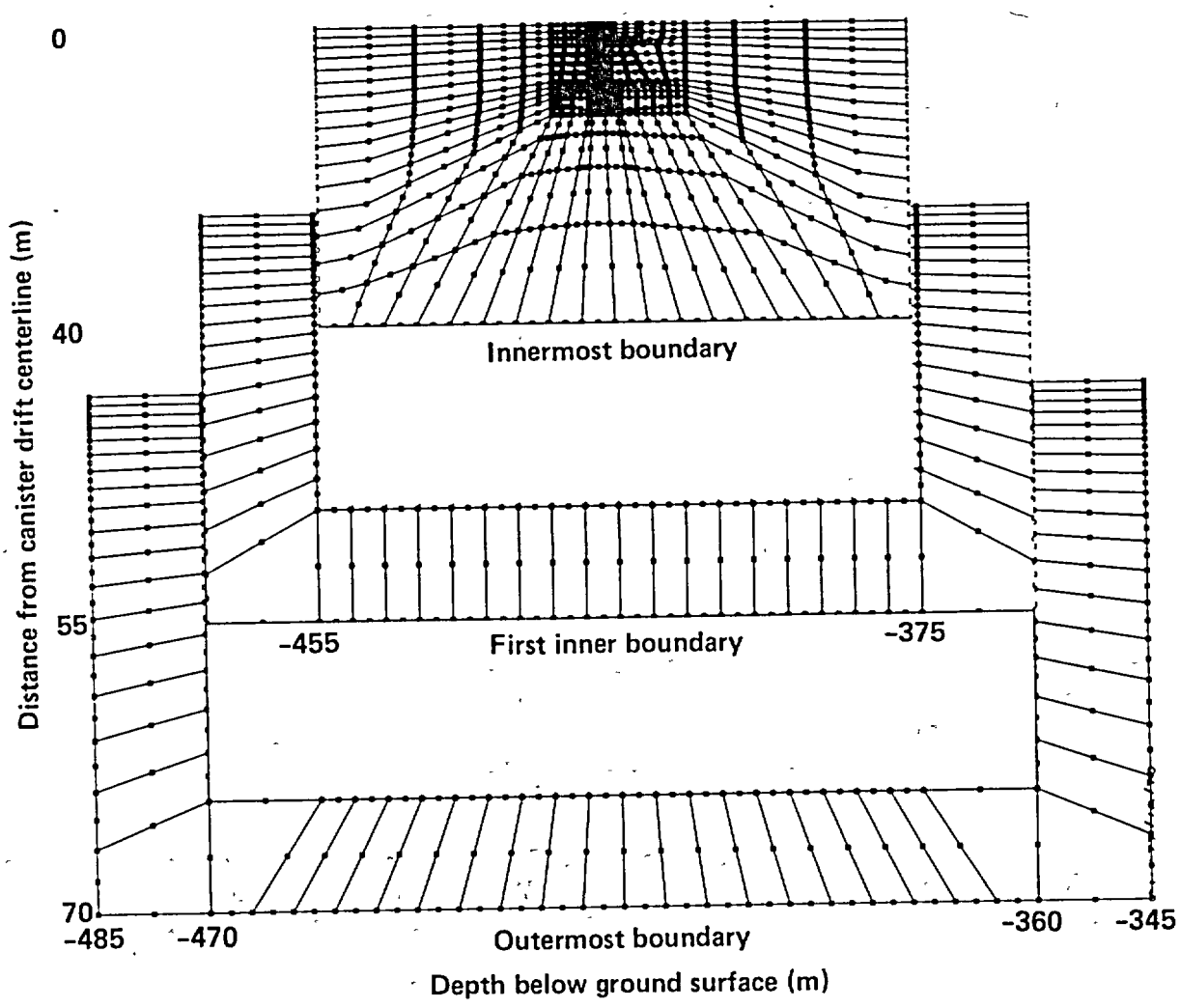

Figure 3-21. Mesh construction allows layers to be peeled off like onion skins (boundary coordinates in meters) (after Butkovich, 1982).

The three mesh sizes produced essentially identical displacements at all times. This confirms that the smallest mesh, which was identical in size and similarly zoned to the as-built mesh, was adequate for the duration of heating simulated.

The plane strain calculations commonly used do not allow out-of-plane motion. As a result, out-of-plane stresses are generated that are dependent upon the material properties and the state of stress in the other two directions. Because these out-of-plane stresses were not the same as were measured *in situ*, a plane stress (zero out-of-plane stress) calculation was conducted. At the locations compared, stress changes were 5 to 10% greater for the plane stress calculation. Similar variations were seen in calculated displacements. Because the actual out-of-plane stress value is intermediate between the plane strain and plane stress values, we judged it unlikely that the effect would significantly influence the quality of comparision between data and calculations.

The position of the isothermal boundary could affect the accuracy of the calculation because this boundary condition acts as a heat sink. This study showed that whether the isothermal boundary condition was located at the innermost or outermost boundary, differences did not exceed 1°C at the end of a 5 year simulated heating phase, and did not exceed 1/4°C after 3 years of heating, the actual duration for the SFT—C. The resulting thermomechanical responses were insignificantly different.

3.3.5 Test Completion Calculations

When we determined that a 3-year test duration was sufficient to achieve the goals of the SFT—C, calculations were undertaken to determine the required duration of the post-retrieval cooling period. Ballou et al. (1982) documented the rationale and supporting thermomechanical calculations, which were used in establishing the project test completion plan and associated schedule.

The geometry, associated calculational mesh, material properties, and input energy tables were the same as were used in the as-built calculations.

Because the structural response of the SFT—C to cooling is a direct result of temperature changes, we found that the thermomechanical response mirrored that of the thermal response discussed in Sec. 3.2.4. Stress changes and displacements occurred very rapidly near the thermal sources and relatively slowly elsewhere (Figs. 3-22 and 3-23). Using the effects after 1.5 years of cooling as a basis, we found that after 6 months:

- 50% of the stress change would have occurred at locations in the pillars.
- 70% of the stress change would have occurred at positions 1 m from the canister emplacement boreholes.
- 75% of the horizontal and 60% of the vertical closure would have occurred in the canister drift.
- All stress changes and displacements would be very small; a few MPa and a few tenths of mm, respectively.

Although the total stress changes and displacements were seen to be small after 6 months of cooling, the rates were also small. Because very long cooling times would be required to obtain easily measureable effects, we retained the planned 6-month cooling period that we had originally adopted on the basis of the thermal calculations.

3.3.6 Post-Test Thermomechanical Calculations

After all test data were acquired and the SFT—C was completed, a final series of thermomechanical calculations was performed using the best available material properties, test conditions, and energy deposition and removal rates (Butkovich and Patrick, 1985). The structural analysis portion of the calculation was driven with nodal point thermal histories that closely approximated the multipoint temperature measurements. The mesh used was identical to the one used for the as-built and post-test calculations discussed above.

Comparison of measured temperatures with ADINAT-calculated nodal-point temperatures revealed that they differed by as much as 5°C (Patrick et al., 1982). When further attempts to improve the level of agreement were unsuccessful, we used a different approach. Because the purpose of the ADINAT calculation was to produce the correct temperature change with which the thermomechanical calculation would be driven, we arbitrarily varied the convection coefficient (which controls the rate of heat removal by the ventilation airstream) until we obtained good agreement between measured and calculated temperatures.

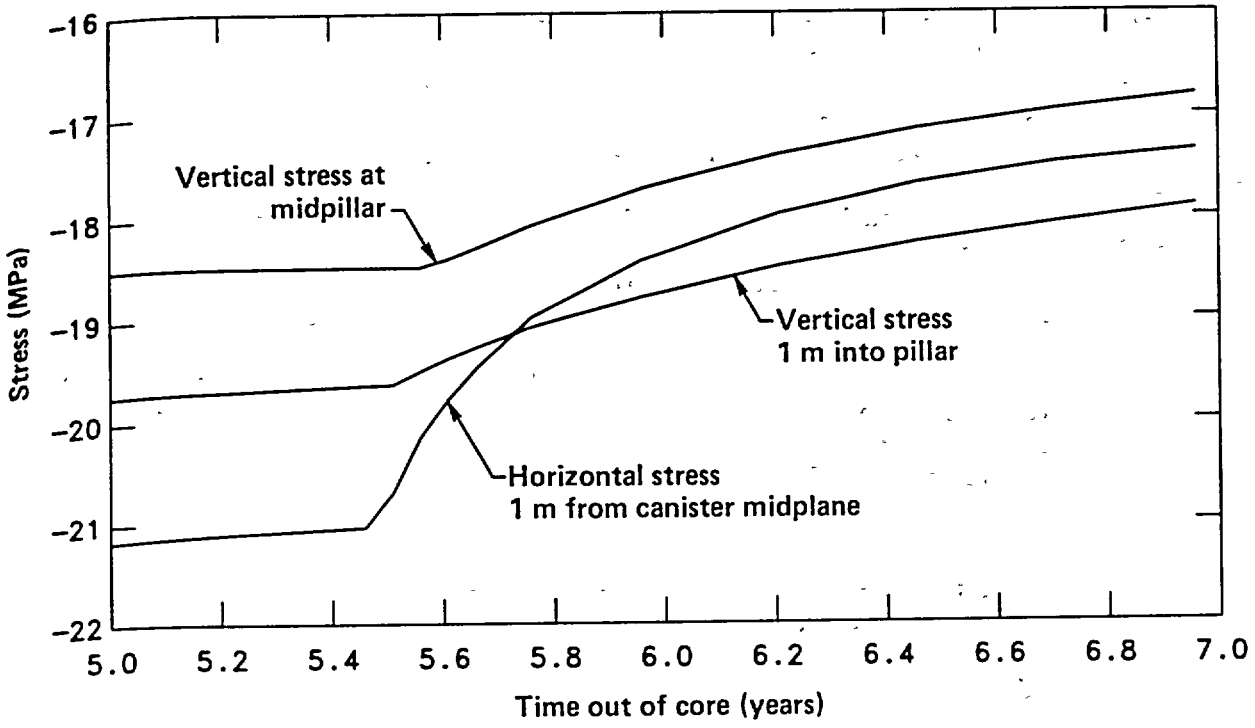

Figure 3-22. Stress changes resulting from fuel retrieval at selected locations (after Ballou et al., 1982).

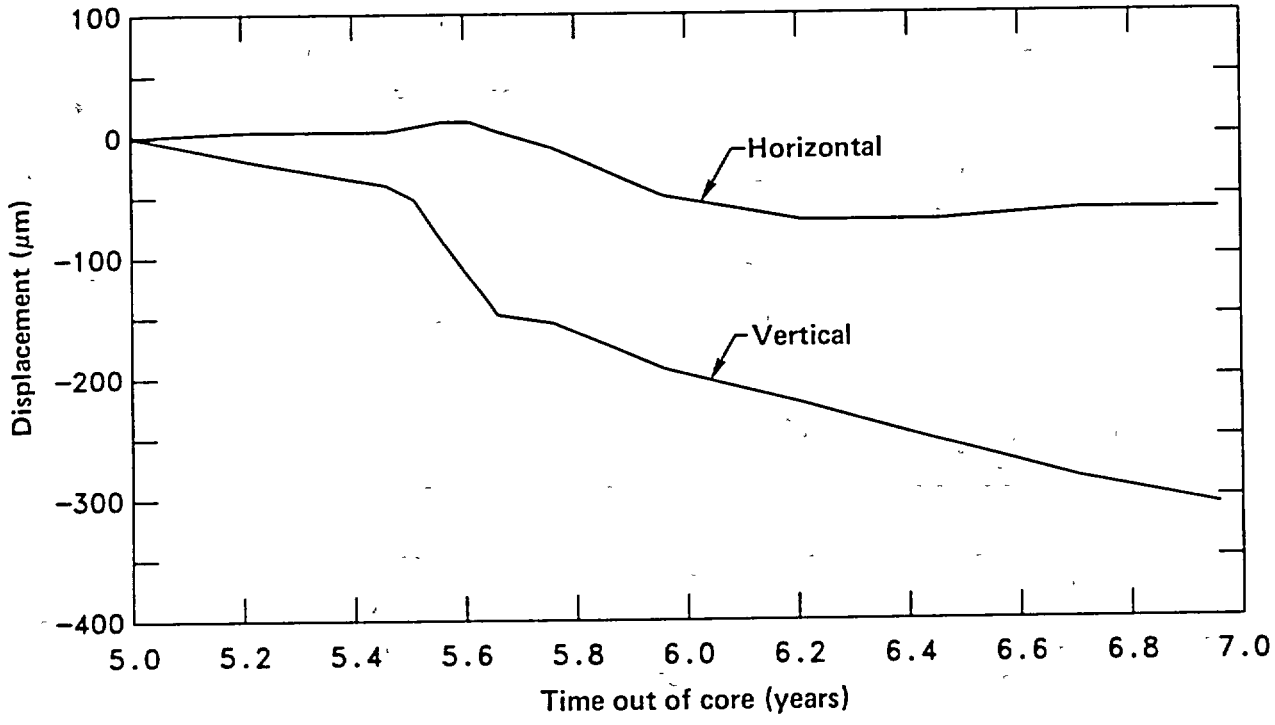

Figure 3-23. Displacements across canister drift due to fuel retrieval (plus values of displacement denote closure) (after Ballou, et al., 1982).

As indicated in Fig. 3-24, agreement between measured and calculated temperatures was very good. After 0.5 year of heating, the least squares slope through a cross-plot of measured vs calculated temperature rises is near unity and $R^2 = 0.98$. Furthermore, the mean square error (RM) of 0.81°C is less than the ISA special limits of error for the thermocouples (1.1°C). We consider this exceptionally good agreement, considering that the positions of the thermocouples were not coincident with nodal points in the finite-element mesh used to calculate temperatures.

Three sets of mesh loadings and deformation moduli were used in the post-test calculations (Table 3-8). These were selected from *in situ* stress measurements by Ellis and Magner (1982) and Creveling et al. (1984) and *in situ* modulus measurements by Heuze et al. (1981) and Patrick, Yow, and Axelrod (1985) to represent our best estimate of these parameters and estimates chosen to represent extreme conditions on either side of this estimate.

Several comparisons were made between measured and calculated stresses and displacements. These comparisions, which considered the accuracies of the instruments used to obtain the measurements, led to the conclusion that Calculation 2 provided the best agreement with the data. It forms the basis of the comparisions and discussions provided in Chapter 16.

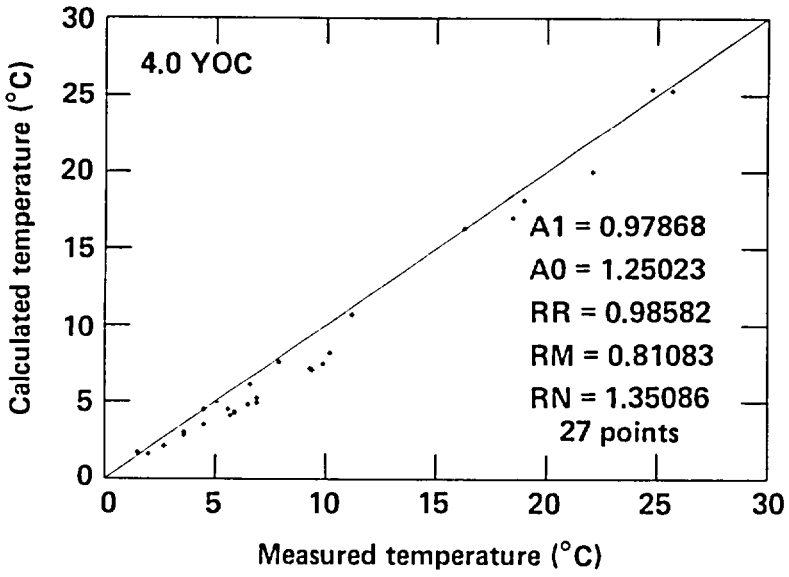

Figure 3-24. Comparison of measured and calculated temperatures (after Butkovich and Patrick, 1985).

Table 3-8. Elastic properties and mesh loadings used for three thermomechanical calculations (after Butkovich and Patrick, 1985).

Property of parameter	Calculation number		
	1	2	3
Rock mass modulus (GPa)	27	38	38
Rock mass Poisson's ratio	0.25	0.25	0.25
Damaged zone modulus (GPa)	13	19	19
Damaged zone Poisson's ratio	0.35	0.35	0.35
Vertical mesh loading[a] (MPa)	6.21	6.21	12.60
Horizontal-to-vertical stress ratio	1.2	1.2	0.98

[a] Vertical mesh loading based on *in situ* stresses measured at mid-rib. A value of 7.89 MPa was used in calculations 1 and 2, and a value of 14.28 MPa was used in Calculation 3.

3.4 Radiation Transport Calculations

Radiation transport calculations were conducted to assist in the design of shielding and to determine the radiation dose to the rock in the vicinity of the canister emplacement boreholes.

3.4.1 Shielding Calculations

Radiation shielding calculations were used to establish design dimensions for transport casks, remote handling hardware, and the spent-fuel storage geometry (Raschke et al., 1983). The two principal design assumptions were:

- Total spent-fuel burnup of 33,000 MW•d/MTU.
- Age of spent fuel 2 years out of reactor core.

We established the design goal that dose rates be less than 100 mrem/h at contact with the transport casks and less than 0.5 mrem/h at the canister drift floor.

The required gamma ray shielding was calculated using the isotopic abundances, the gamma energy spectra, and the assumptions. Since neutron attenuation factors are less well known, shielding requirements were determined experimentally from the attenuation of ^{252}Cf fission neutrons by iron.

A 330-mm-thick (13-in.) shield was determined to satisfy the design goal of 100 mrem/h at the surface of the transport casks of both the surface transport vehicle and underground transfer vehicle (Chapter 7). A 305 mm (12-in.) thick shield plug was determined to provide sufficient primary shielding in the storage configuration and additional concrete shielding lowered the radiation dose rate to background levels in the canister storage drift.

Table 3-9 indicates the level of agreement between measured and calculated radiation doses reported by Raschke et al. (1983). The authors attributed the observed differences to:

1. The spent-fuel assemblies actually used were 2.45 rather than 2.0 years out of core.
2. The spent-fuel assemblies actually used had burnups of 28,000 rather than 33,000 MW•d/MTU.
3. The shielding calculations were based on higher than actual source dose rates.
4. Careful machining of parts reduced radiation streaming pathways.

Because each of these differences would decrease the calculated dose rates, they would also decrease the observed differences between calculated and measured values.

3.4.2 Radiation Dose Around Emplacement Holes

Because one of the objectives of the SFT—C was to evaluate the effects of radiation on the granite, it was necessary to calculate the dose to the rock surrounding the canister emplacement boreholes. Wilcox and Van Konynenburg (1981) used the MORSE-L Monte Carlo code to determine dose rates and cumulative doses in the materials surrounding the spent-fuel assemblies. These calculations, together with *in situ* measurements and spent-fuel characterization studies, were used to establish the dose rates and doses discussed in Chapter 15.

Characteristics of Spent Fuel. The Turkey Point Unit #3 spent-fuel assemblies modelled in the radiation transport calculations had the characteristics described in Chapter 6. Wilcox and Van Konynenburg (1981) cited the four most significant gamma-emitting nuclide pairs shown in Table 3-10, which were included in the calculations with gamma-ray yields from Lederer and Shirley, 1978 (Table 3-11). Using the

Table 3-9. Total (gamma and neutron) radiation dose rate calculations and measurements at selected locations (after Raschke et al., 1983).

Location	Radiation dose rates	
	Calculated (mrem/h)	Measured (mrem/h)
Surface of transfer casks	105	90
Canister shield plug	36	5
Thermocouple tubes and shield plug interfaces	152	Not measured
Canister drift floor above shield plug	0.5	<0.1
Truck cab of surface transfer vehicle	3	<1

Table 3-10. Significant gamma emitters in the spent-fuel assemblies (after Wilcox and Van Konynenburg, 1981).

Nuclide	Concentration at 740 days (gram-atoms)	Half-life	Activity at 2.45 yoc (Ci)
$^{106}Ru-^{106}Rh$	0.1575	366.5 d	4.18×10^4
^{134}Cs	0.1595	2.062 y	2.40×10^4
$^{137}Cs-^{137}Ba$	3.202	30.17 y	3.76×10^4
$^{144}Ce-^{144}Pr$	0.1516	284.5 d	4.77×10^4

Table 3-11. Gamma ray yields of the significant gamma emitters in the spent-fuel assemblies (after Wilcox and Van Konynenburg, 1981).

Nuclide	Energy (meV)	Gammas/disintegration
$^{106}Ru-^{106}Rh$	0.5118	0.19
	0.6163	0.0082
	0.6221	0.098
	0.8738	0.0045
	1.0507	0.016
	1.128	0.0042
	1.562	0.0017
^{134}Cs	0.4753	0.01465
	0.5632	0.0838
	0.5693	0.1543
	0.6047	0.9756
	0.7958	0.8544
	0.8019	0.0873
	1.0386	0.0100
	1.1679	0.01805
	1.3651	0.0304
	1.4005	0.0008
$^{137}Cs-^{137}Ba$	0.6616	0.850
$^{144}Ce-^{144}Pr$	0.0801	0.0113
	0.1335	0.111
	0.6965	0.0133
	1.4891	0.0029
	2.1856	0.0075

results of ^{137}Cs gamma scans performed by Davis (1980), the axial source strength distribution was estimated (Fig. 3-25). Since the neutron dose contribution was known to be small relative to the gamma dose, no attempt was made to accurately estimate the neutron source strength.

Calculational Geometry. The actual spent-fuel emplacement geometry was approximated for purposes of the calculation (Fig. 3-26). The exact geometry of the upper shield plug was simplified, the hemispherical bottom of the canister was treated as flat, and the helium fill gas was considered a vacuum. Because water could possibly enter the liner borehole annulus, calculations were made for each material. Clay, a potential backfill material, was also treated as a liner/borehole annular fill.

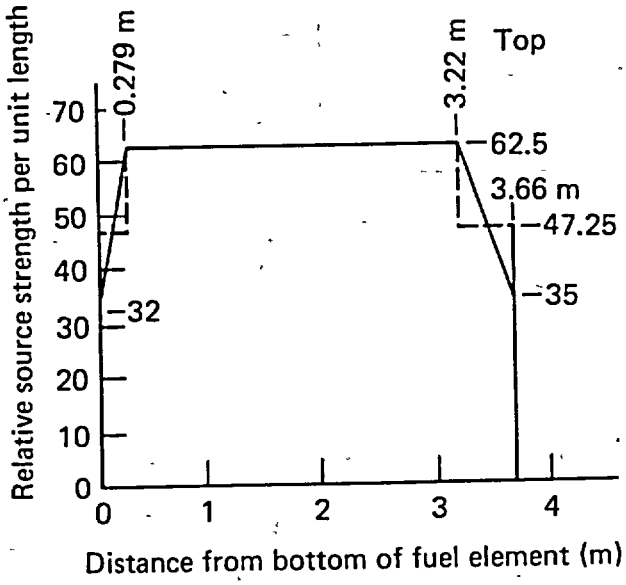

Figure 3-25. Axial gamma source distribution (dotted lines show the configuration used in the computer simulation, after Wilcox and Van Konynenburg, 1981).

Wilcox and Van Konynenburg (1981) used the Monte Carlo code because of the following complicating factors:

- The uranium content of the spent fuel results in self-absorption with several scattering collisions before the average gamma ray reaches the borehole wall.
- Gamma ray transport out of the fuel is complicated by the nonuniform geometry, which causes variations in flux with angular position.
- The nonuniform geometry causes streaming out the top and bottom ends of the fuel assembly.
- The transmission properties of the media vary greatly over the energy ranges of emitted gamma rays and neutrons.
- Many of the fluxes of interest are at interfaces between materials where simpler hand calculations give inaccurate results.

The MORSE-L Monte Carlo Code (Wilcox, 1972) used LLNL's L-Division gamma library (Wilcox, 1973) to track the scattering history of photons until their energies fell below 150 keV, at which energy they were assumed to be totally absorbed.

A series of gamma calculations was made for each of the four dominant nuclide pairs. The neutron component and coupled neutron-gamma problems were also solved to determine neutron dose rates and secondary gamma dose rates.

Results. The results of the MORSE-L calculations showed that the neutron dose was negligible in comparison to the gamma dose, as anticipated. Within the central 2.44 m of the 3.66-m-long assemblies, the dose to granite was found to be uniform within the uncertainty of the calculations.

Radiation-absorbed dose rates and total doses for the four liner/borehole/backfill options are shown in Figs. 3-27 and 3-28, respectively. These results are largely as expected: the decrease in dose rate with distance into the rock is essentially linear on a semilog plot, and the decrease in dose rate within the liner/borehole gap is dependent on the density of the fill material.

These calculations were also used to estimate the thermal contribution of the gamma ray attenuation. Fitting the dose rate by a function of the form $Ae^{-\mu r}/r$ and integrating over the volume of granite from the borehole outward to infinity, Wilcox and Van Konynenburg (1981) calculated a contribution of 40 W, less than 3% of the total heat output.

In Chapter 15 the results of these calculations are compared with the actual radiation dose and dose rates measured in the field.

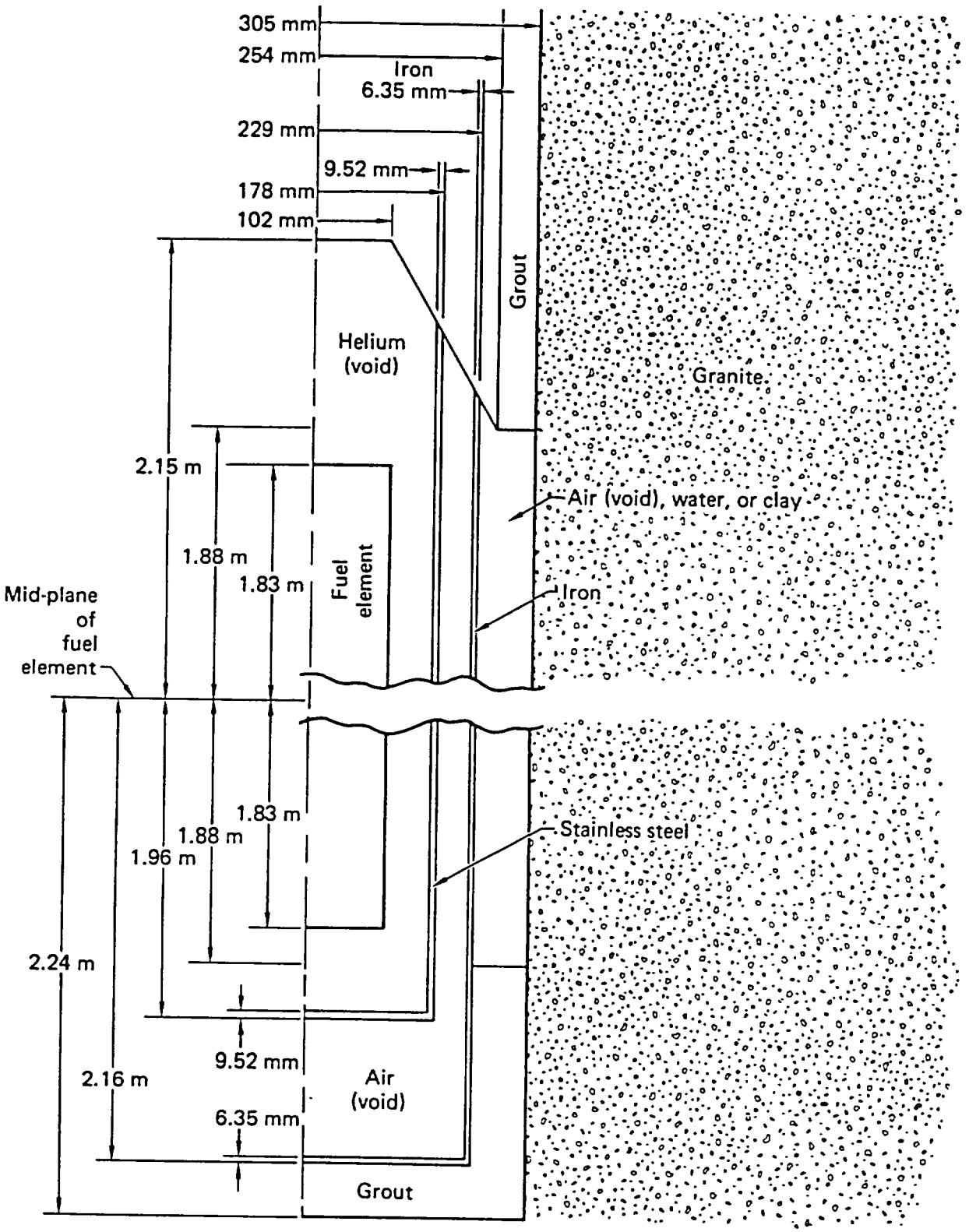

Figure 3-26. Approximate geometry of spent-fuel emplacement. Calculations assumed voids rather than air or helium in the actual case; this substitution is indicated by the "void" in parentheses in the figure (after Wilcox and Van Konynenburg, 1981). Treated as flat, and the helium fill gas was considered a vacuum. Because there was a possibility of water entering the liner borehole annulus, calculations were made for each material. Clay, a potential backfill material, was also treated as a liner/borehole annular fill.

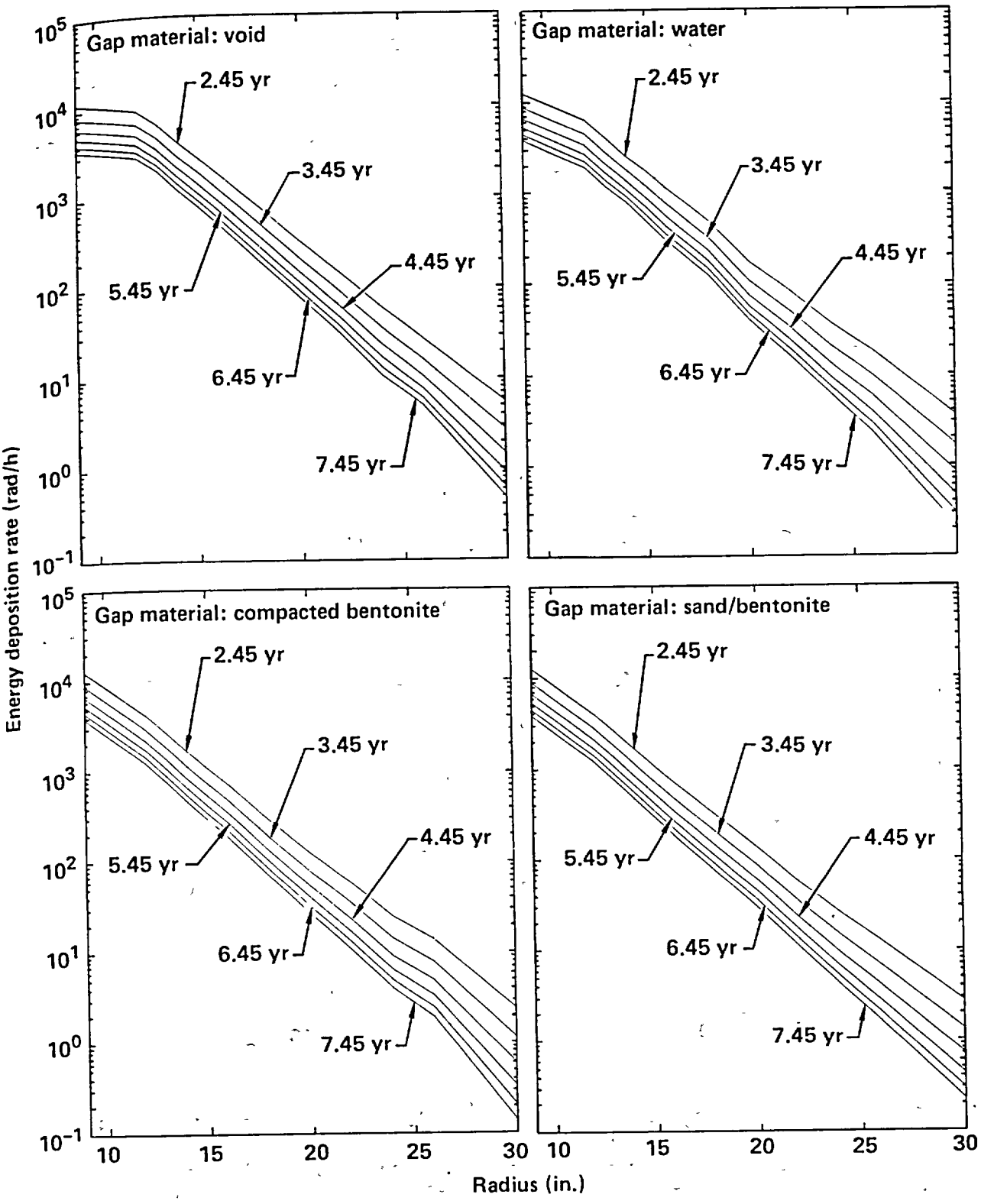

Figure 3-27. The absorbed dose rate (rad/h to granite) outside the iron liner as a function of radius from the center line of the fuel assembly. The values plotted are averages over the central 2.44 m (8 ft) of the fuel assembly. The gap between the liner and the granite was assumed to be VOID, or filled with WATER or COMPACTED BENTONITE or a SAND/BENTONITE mixture, as shown in the legends of the plots. The parameter is time elapsed since discharge of fuel from reactor (after Wilcox and Van Konynenburg, 1981).

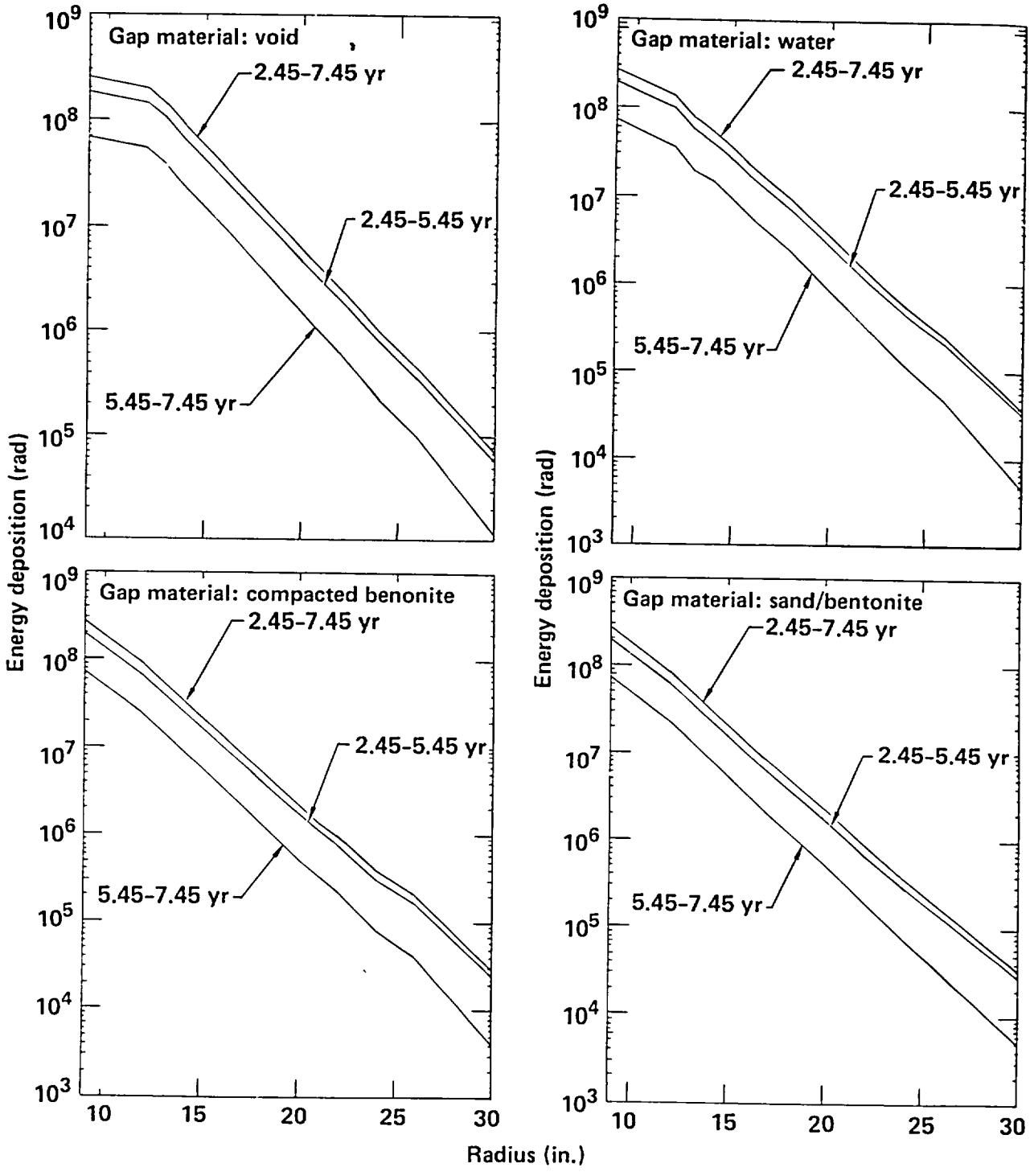

Figure 3-28. The absorbed dose rate (rad/h to granite) outside the iron liner as a function of radius from the center line of the fuel assembly. The values plotted are averages over the central 2.44 m (8 ft) of the fuel assembly. The gap between the liner and the granite was assumed to be VOID, or filled with WATER or COMPACTED BENTONITE or a SAND/BENTONITE mixture, as shown in the legends of the plots. The parameter is time period after discharge of fuel from reactor (after Wilcox and Van Konynenburg, 1981).

4. Site Characterization and Geologic Investigations

Several different investigations were undertaken to determine the pertinent mechanical, thermal, thermomechanical, and hydrological properties of the Climax Stock Quartz Monzonite (CSQM) in which the SFT—C was conducted. We also measured *in situ* stresses and studied the thermal and radiological effects on selected material properties and on the mineralogy and petrology of the CSQM.

4.1 Structural Geology*

Many reports have been written on the structural geology of the Climax stock. Although studies by Maldonado (1977), Allingham and Zietz (1962), Barnes and Poole (1968), and Houser and Poole (1960) predate the SFT—C, the works of Connolly (1982), Thorpe (1984), Wilder and Yow (1981), Wilder, Yow, and Thorpe (1982), and Yow and Wilder (1983) were done in direct support of the test. Most of these investigations have been synthesized and analyzed by Wilder and Yow (1984), whose work is the basis of the summary given here.

There were three main reasons for studying the structural geology at the SFT—C:

- To provide data on geologic structure relevant to facility design and safety considerations.
- To help select the types and locations of rock-response instrumentation.
- To identify and characterize geological features for incorporation in rock-response models.

4.1.1 Characterization Techniques

The previously cited literature gave us an initial understanding of the structural geology of the CSQM. Exploratory drilling conducted before underground excavation provided a means to assess the rock mass for large geological features that could adversely affect the stability of the facility (Fig. 4-1).

As excavation progressed, we conducted reconnaissance mapping of the ribs and roof, followed by more detailed mapping that included the drift floor. Wilder and Yow (1982) reported the details of the mapping techniques and data. Joint alteration studies were also conducted to assess the chronology of the dominant fracture sets (Connolly, 1981).

We conducted reconnaissance mapping on the surface to determine the continuity of geological structure with depth, and to attempt to identify surface expressions of faults observed underground. These studies relied upon surface outcroppings, six trenches across the Boundary fault, and a nearby borrow pit as data sources.

4.1.2 Regional Geology

The NTS is located in the Basin and Range Province of southern Nevada, within the miogeosynclinal belt of the Cordilleran geosyncline. More than 11,300 m (37,000 ft) of marine sediments accumulated in this area during the Precambrian and Paleozoic eras (Ekren et al., 1968). The regional geology is expressed as complexly folded and faulted Paleozoic sedimentary rocks overlain by Tertiary tuffs and lavas. Valleys are typically filled with Tertiary and Quaternary alluviums.

These rocks and related fault structures identified by Barnes and Poole (1968) are shown in Fig. 4-2. Also shown is the Climax stock, one of three plutons formed during the Mesozoic era. Maldonado (1981) considers the Climax and Twin Ridge stocks to be diapiric extensions of the same deep-seated crystalline body.

Following an episode of post-intrusion erosion, Tertiary volcanic activity deposited several hundreds of meters of rhyolitic ash-flow and ash-fall tuffs as well as some rhyolite lavas and basalts on the NTS area. These have since eroded, exposing the Climax stock at the surface.

4.1.3 Local Geology

Located in the northeastern corner of the NTS, the Climax stock outcrops over an area of about 4 km^2 (Fig. 4-3). Geophysical evidence indicates that the stock expands conically downward to an area of 100 km^2 at several kilometers depth (Allingham and Zietz, 1962). Recent geophysical studies by Orkild (1983) have revised the details of this model but support the concept of conical expansion with depth.

*Contributed by W. C. Patrick.

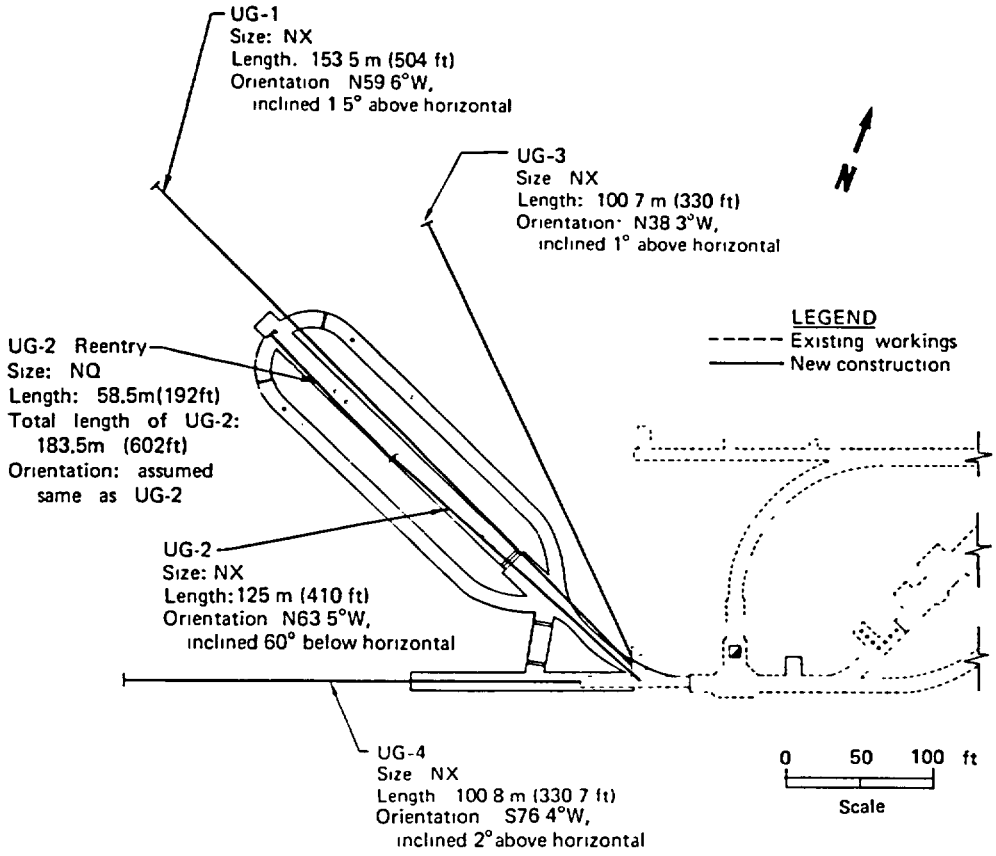

Figure 4-1. Exploratory boreholes.

The stock consists of a granodiorite unit to the north and a slightly younger quartz monzonite unit to the south and east. Houser and Poole (1961) indicate that the contact between the units is very steep or vertical. The SFT—C is located completely within the quartz monzonite unit, at least 65 m from the contact at its nearest approach (Connolly, 1981).

The average modal analysis of the intrusives is provided in Table 4-1. Pink alkali feldspar phenocrysts up to 150 mm long are scattered throughout the light- to medium-gray holocrystalline porphyritic groundmass. The major mineral constituents occur as follows:

- Quartz as anhedral grains from 0.25 to 5 mm.
- Plagioclase as euhedral to subhedral grains from 0.25 to 3.5 mm.
- Orthoclase as anhedral grains from 0.15 to 3 mm and as pink euhedral phenocrysts from 10 to 150 mm in length.
- Biotite as subhedral grains averaging 1.5 mm.

4.1.4 Area Faults

The high-angle Tippinip Fault, located just west of the stock (Fig. 4-3), has been cited by Orkild (1983) as a possible magma path during intrusion.

As its name implies, the Boundary Fault forms the contact between the stock and the valley fill alluvium to the southeast. At its northeast end it merges with the Butte Fault, and its southwest end may intersect the Tippinip Fault. The Boundary and Yucca Faults may also merge near the southeastern boundary of the stock.

Maldonado (1977), Orkild (1983), and Knauss (1981) have investigated the complex interrelationships among these faults. The reader is referred to these sources or to Wilder and Yow (1984) for a summary of their findings.

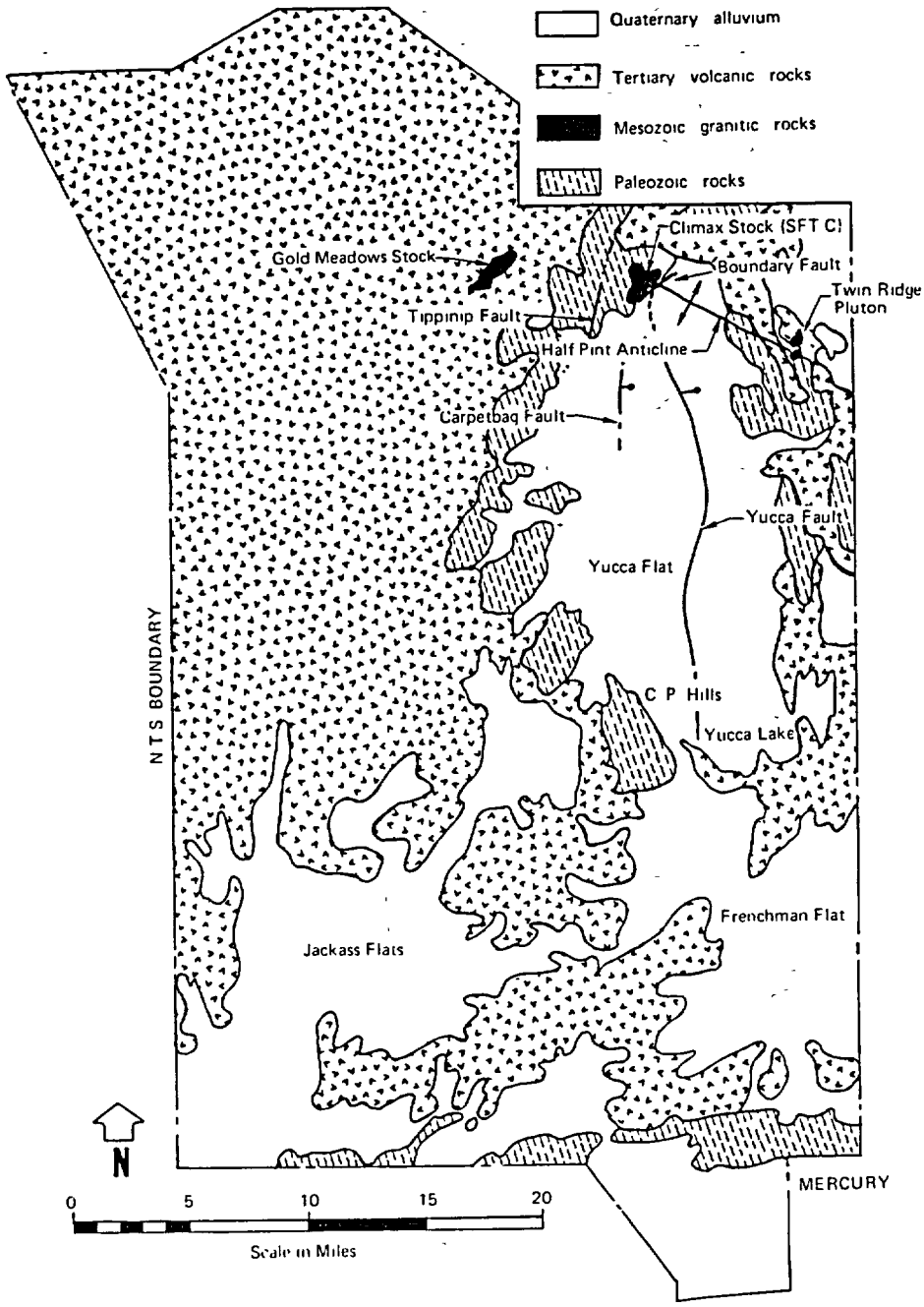

Figure 4-2. NTS geology.

4.1.5 Subsurface Geological Features

During underground fracture mapping for the SFT—C, eight joint sets were identified. Wilder and Yow (1984) numbered these joint sets in chronological order of formation rather than in abundance, as is often done. Even so, they are discussed here in order of prominence because this aspect is more important to our understanding of the structural ability and response of the SFT—C. Orientation and frequency data are provided for each set in Table 4-2. An equal area lower hemisphere pole plot of the fracture data is provided in Fig. 4-4.

The mineralization and alteration characteristics of these joints are provided in Table 4-3. Pervasive wall-rock alteration and joint infilling contributed to easy identification of joint set 2. The clay and calcite

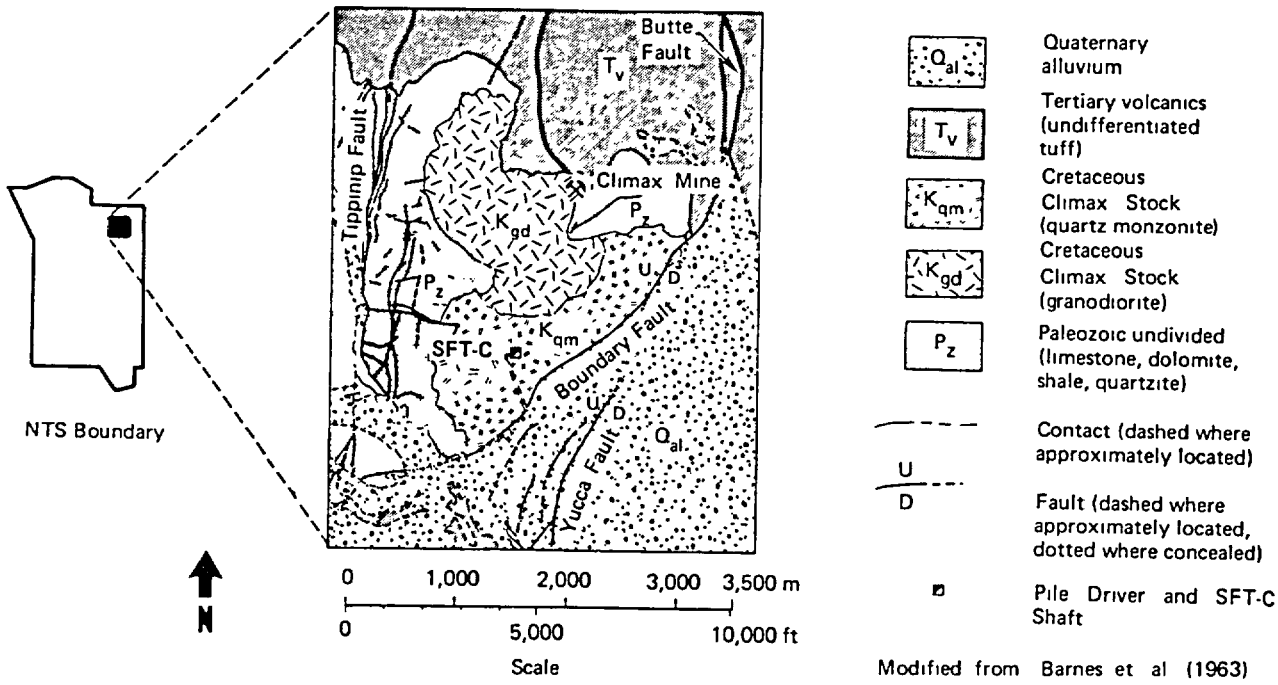

Figure 4-3. Climax geology map.

Table 4-1. Average modal analyses for rock of the Climax stock (after Houser and Poole, 1961).

Essential minerals[a]	Volume (%) of minerals	
	Granodiorite	Quartz monzonite
Quartz	28	28
Potassium and/or sodium feldspar	16	25
Plagioclase	45	40
Biotite	9	6

[a] Accessory minerals (mainly apatite, sphene, opaque iron oxides, and zircon), which together constitute 1 to 2% of the rock, are not reported here.

Table 4-2. Joint sets identified during mapping of the SFT—C (after Wilder and Yow, 1984).

Joint set (in chronological order of formation)	Orientation	Frequency of occurrence (as percent of total number of joints)
1	N59°E–39°NW	0.4
2	N44°W–20°NE	23
3	N2°W–vertical	2
4	N24°W–vertical	23
5	N59°W–vertical	35
6	N82°W–vertical	5
7	N46°E–80°SE	8
8	N33°E–78°SE	4

infillings were treated by Wilder and Yow (1984) as indicators that the joints were open to groundwater flow, at least in the geologic past.

In addition to these joints, three sets of shears were identified, oriented N40°W-85°NE, N55°E-80°SE, and N53°W-85°NE (Fig. 4-5). A fault zone extending from the receiving room nearly 20 m down the drifts is also noted in Fig. 4-5. Initially identified as a single feature in the north heater drift where it is a 2- to 3-m-thick (6- to 10-ft) fracture zone with a 0.3- to 0.4-m-thick (12- to 16-in.) clay-gouge-filled zone, it was later related to other fault traces. Although these latter traces appear to be minor where exposed, the variable character of the Receiving Room fault suggests that this appearance may be deceptive. This conclusion is based on exploratory borehole UG-1 (Fig. 4-1), which perforated the Receiving Room fault but did not detect the significance of the feature as expressed in the north heater drift.

Core Logging Data Analysis. Wilder and Yow (1984) used several methods of presenting and analyzing the fracture data obtained from core logs. One of the more informative presentations is a histogram of fracture spacings. Figure 4-6 displays histograms for the four exploratory boreholes and a "composite"

Table 4-3. Mineralization and alteration characteristics of the eight joint sets identified during the SFT—C (after Wilder and Yow, 1984).[a]

	Joint set							
	1	2	3	4	5	6	7	8
Mineralization								
Quartz	A	A	P	—	—	A	NB	NB
Calcite	P	A	P	A	A	A	P	—
Chlorite	P	P	—	—	—	—	—	—
Clay	—	P	P	—	—	P	A	P
Pyrite	A	A	P	NB	NB	—	P	m
Iron staining	P	P	P	—	NB	P	P	P
Alteration								
Albitization	P	A	—	—	—	P	m	—
Bleaching	A	A	P	—	NB	—	P	—
Altered feldspar	A	A	—	—	—	—	NB	NB
Healed/filled	A	A	P	NB	—	—	—	NB
Saussuritization	A	A	—	—	—	—	—	—
Sericite	—	A	NB	—	—	—	P	—
Shearing	—	m(NB)	—	NB	A(NB)	m	NB	—

[a] A = abundant, P = present, m = minor, NB = in nearby fractures that are not specifically part of the set, and — = not present.

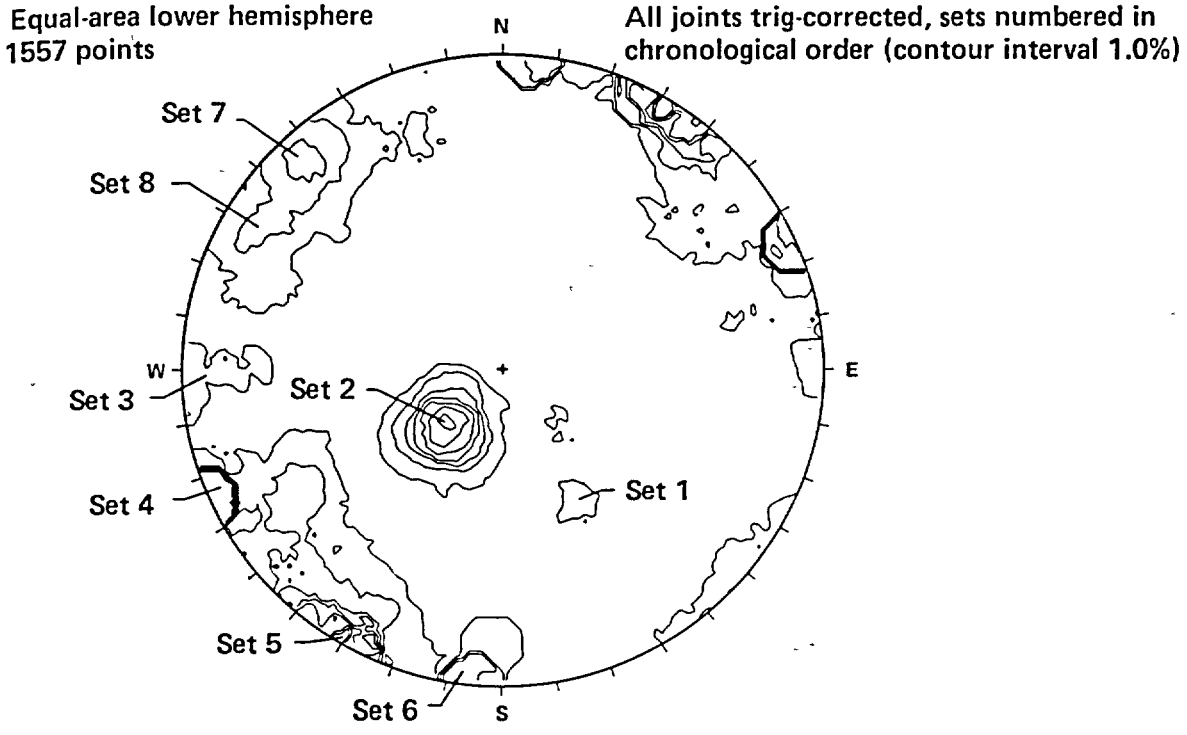

Figure 4-4. Joint sets identified during mapping of the SFT—C (after Wilder and Yow, 1984).

comprising four boreholes oriented vertically downward. Data for each segment of these boreholes are displayed in Table 4-4. The composite was prepared to provide a similar length of hole (and number of fractures) as was available for the exploratory boreholes.

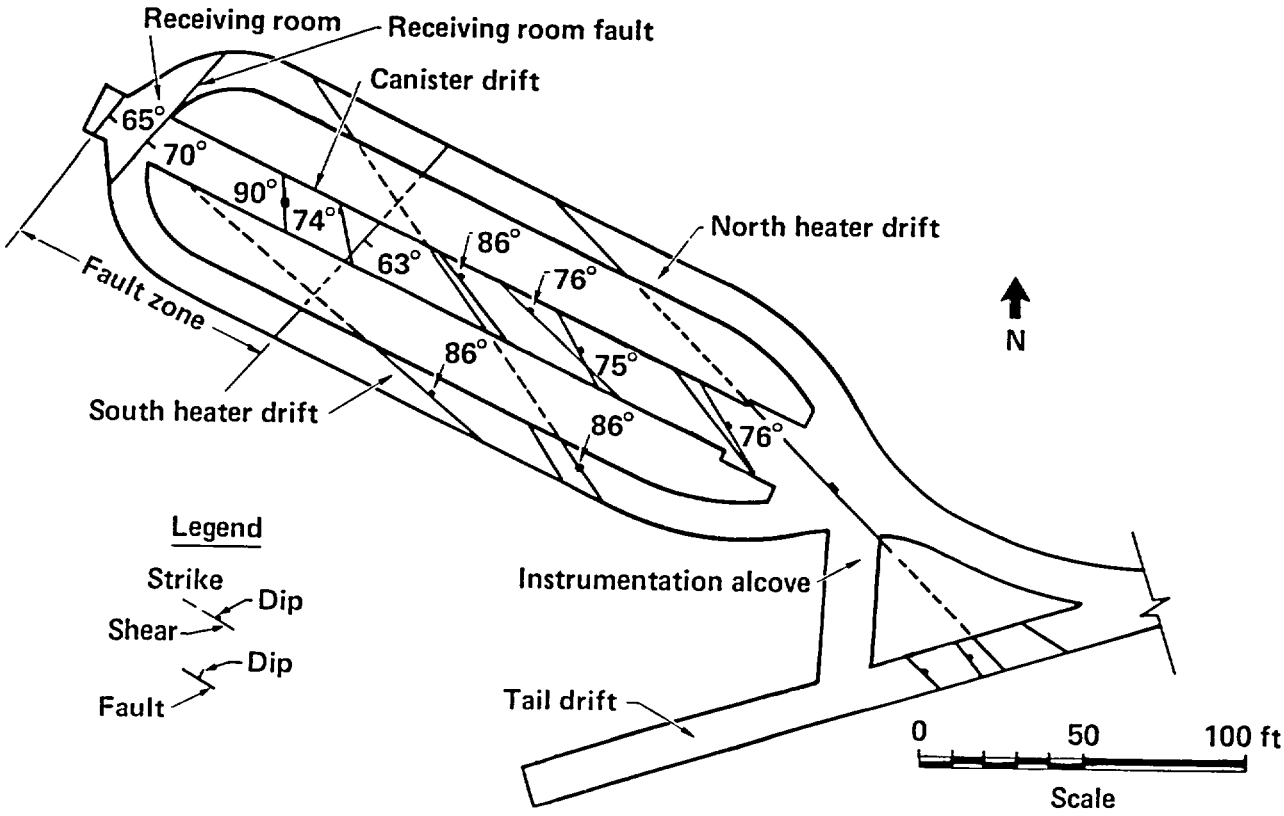

Figure 4-5. Shears and faults in the SFT—C drifts (after Wilder and Yow, 1984).

Table 4-4. Tallies of natural fractures in SFT—C exploratory holes (after Wilder and Yow, 1984).

Hole/ orientation	Segment	Length (ft)	Number of fractures	Average fracture spacing (ft)
UG-1	1	150.0	92	1.6
N59.6°W	2	150.0	103	1.5
+1.5° incline	3	150.0	152	1.0
	1+2+3	450.0	347	1.3
UG-2	1	150.0	68	2.2
N63.5°W	2	150.0	105	1.4
−60° incline	1+2	300.0	173	1.7
UG-3	1	150.0	96	1.6
N38.3°W	2	150	108	1.4
+1.0° incline	1+2	300.0	204	1.5
UG-4	1	150.0	100	1.5
S76.4°W	2	150.0	129	1.2
+2.0° incline	1+2	300.0	229	1.3
GxE	1	178.6	119	1.5
Composite vertical				

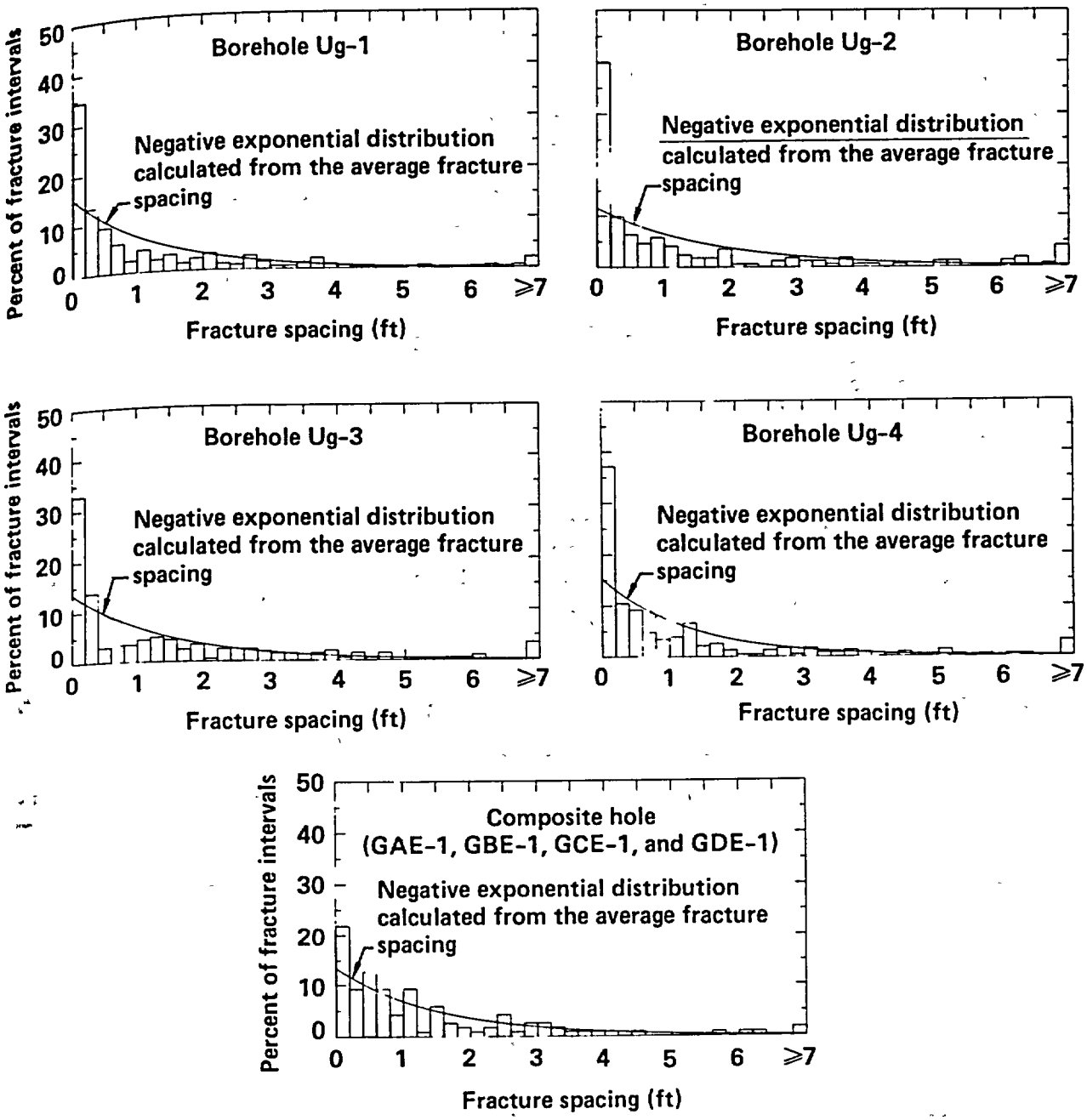

Figure 4-6. Spacing distribution of open fractures in selected boreholes (after Wilder and Yow, 1984).

Although a casual inspection of these curves indicates a reasonable fit to the data, detailed analysis revealed that this was not the case. The prominent spike at very small spacings and the absence of a monotonic decline in frequency with increasing spacing suggests that these histograms represent composites of two or more joint populations. This is consistent with our understanding of the numbers of joint sets identified in mapping. Further analyses are provided by Wilder and Yow (1984).

Mapping Data Analysis. Wilder and Yow (1984) recognized that both "blind zones" and trace length biases exist as a result of using scanline techniques to map excavation surfaces. Bias introduced by differences in fracture trace lengths has been discussed by LaPointe and Hudson (1981) but could not be treated in this study because fracture length data were typically not collected.

Two methods were considered for treating the effects of blind zones, which, according to Goodman (1976), occur when the orientation of a geological feature is within 20° of that of the mapped surface. The first method introduces a trigonometric correction to the number of mapped fractures N by dividing this number by the sine of the angle A between the normal to the feature and the normal to the mapped surface. That is, $N_{kC} = N/\sin(A)$. To be correctly applied, the joint must be a member of a set; otherwise the apparent frequency of occurrence of truly random joints will increase.

A second approach is to compensate for one blind zone by adding in the results of mapping on another surface with a different blind zone. Because such mapping surfaces are typically not the same length, the respective data-set frequencies must be normalized to a common length. For such additive adjustments to be legitimate, all data sets must come from the same population.

Wilder and Yow (1984) used both techniques, with a further subdividing of all data and only data mapped on surfaces oriented N61°W. Because complete orientation data were not available for all of the 2578 discontinuities mapped, at most 1820 could be treated in these analyses. The frequency of occurrence of certain mineralogical characteristics of these features is provided in Table 4-5, and the numbers and spacings of joints mapped on the drift ribs are provided in Table 4-6. Detailed analyses of these data are presented by Wilder and Yow (1984). In addition, the data base was published by Yow (1984) and is available to the technical community for further analysis.

4.1.6 Chronology of Fractures

By studying the structural interrelationships and the petrology of alteration products, Wilder and Yow (1984) were able to postulate the history and genesis of the observed fracture sets. These studies rely heavily on the work of Connolly (1982). Based on these studies and an assumption that fracture orientations at the time of formation were normal to the least principal stress, they postulated the stress-path history depicted in Fig. 4-7.

Table 4-5. Results of different analytical approaches, showing the percentage of discontinuities with certain characteristics recorded during the SFT—C (after Wilder and Yow, 1984).

Discontinuity characteristics	Discontinuities (%) based on			
	All mapping data	N61°W mapping data	Additive correction of N61°W and N7°E data	Trigonometric correction of N61°W data
Mineralogy				
Albite alteration	8	8	7	7
Bleaching	5	4	3	3
Calcite	34	31	27	33
Chlorite	3	2	3	1
Clay	4	4	11	4
Feldspar (misc.) alteration	1	1	1	1
Iron oxide stains	4	4	4	4
Pyrite	32	29	25	23
Saussuritization	2	1	1	1
Sericite	9	10	9	7
Quartz	29	28	21	23
Joint characteristics				
Healed	5	3	3	3
Truncated	22	2.4	19	22
Master (truncating)	6	7	5	6
Total number of fractures				
All joints	1820	1120	1648	1557
Shears	97	40	124	80

Table 4-6. Number of joints mapped on ribs trending N61°W (after Wilder and Yow, 1984).[a]

Drift	Stations	Number of joints	Joint spacing (ft)
North heater	2 + 30 to 2 + 81	176	0.58
	2 + 81 to 3 + 32	111	0.92
	3 + 32 to 3 + 83	160	0.64
Canister	2 + 00 to 2 + 50	127	0.79
	2 + 50 to 3 + 00	61	1.64
	3 + 00 to 3 + 50	68	1.47
	3 + 50 to 4 + 00	110	0.91
South heater	2 + 30 to 2 + 81	133	0.77
	2 + 81 to 3 + 32	115	0.88
	3 + 32 to 3 + 83	121	0.84

[a] Tallies were taken from both ribs in a given drift between stations listed. Therefore, mapped lengths were twice the differences between the station designators. The canister drift floor was excluded. Both healed and open joints were tallied.

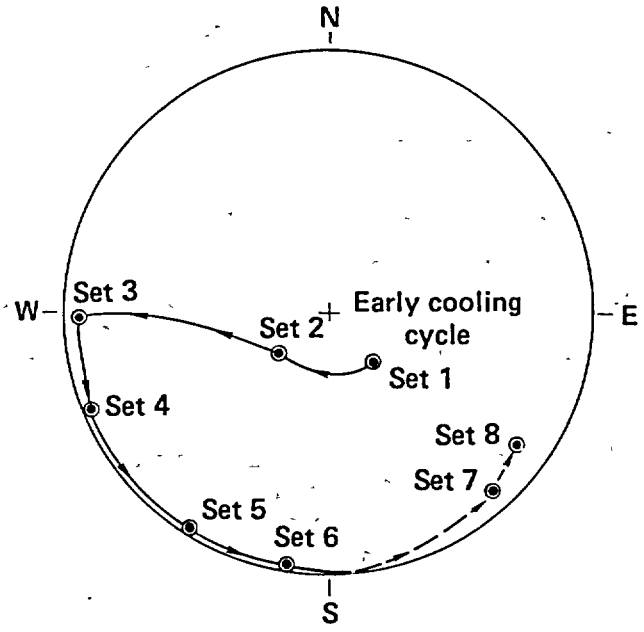

Figure 4-7. Orientation with time of the least principal stress in the Climax stock (after Wilder and Yow, 1984).

4.2 Geohydrology*

Because the SFT—C was conducted above the regional water table and was planned to be of short duration, relatively few hydrological investigations were conducted. Studies were undertaken to summarize anticipated hydrological conditions and to determine the depth of the zone of total saturation beneath the test facility.

4.2.1 Physiography

The ground-surface elevation above the Climax stock varies from about 1500 m near the southern edge to about 1800 m to the north. Located between Yucca Flat and the Pahute and Ranier Mesas, elevations drop steeply to the southeast and rise to the north and west to over 2100 m (Fig. 4-2).

With an average annual rainfall of 150–200 mm, the local climate produces vegetation common to desert environments. While rainfall in the valleys range from 80 to 150 mm, the mesas and ridges experience up to 250 mm (Winograd and Thordarson, 1975).

Borg et al. (1976) concluded that precipitation may exceed evapotranspiration in the uplands during the winter periods. It is doubtful that precipitation exceeds evapotranspiration in the valleys. The typically thin overlying unconsolidated materials immediately above the stock are believed to provide opportunity for infiltration (Murray, 1981).

4.2.2 Regional Hydrology

Both Winograd and Thordarson (1975) and Borg et al. (1976) describe the geohydrology of the NTS where test drilling has shown at least five intermontane basins connected by groundwater movement in the deep Paleozoic carbonate strata.

Three of the 10 main geohydrolic units have major influence on the hydrology of the Climax stock. These are the lower carbonate aquifer, the lower clastic aquitard, and the upper clastic aquitard (Murray,

*Contributed by W. C. Patrick.

1981). Although transmissivities of the Paleozoic carbonates range from 12 to 12,000 m^2/day, the clastic rocks have transmissivities of less than 12 m^2/day.

The general directions of groundwater movement are noted in Fig. 4-8. As suggested by Borg et al. (1976), there appears to be a groundwater divide running approximately north-south between the stock and Pahute Mesa to the west.

4.2.3 Geohydrology of the SFT—C Site

Previous investigators had identified many zones of perched water in and around the stock, but the zone of total saturation had not been identified when site characterization began (Fig. 4-9 and Table 4-7). Although local seeps occur where water-bearing fractures intersect the underground openings, the stock is unsaturated at the 1120-m elevation above mean sea level (MSL) of the SFT—C (Fig. 4-10). Previously published data and recent water level measurements in an exploratory borehole indicate that the top of the zone of saturation exists at an elevation of about 975 m, or about 145 m below the test level (Murray, 1981).

To the southeast, the stock is in fault contact with Paleozoic carbonates where water levels vary from 1100 to 1200 m above MSL in the northeast to 800 to 900 m above MSL in the southwest (Fig. 4-11). Since the stock is of low permeability (except where faults and shear zones are present), the water level was inferred to be somewhat higher in the stock than in the higher permeability carbonates.

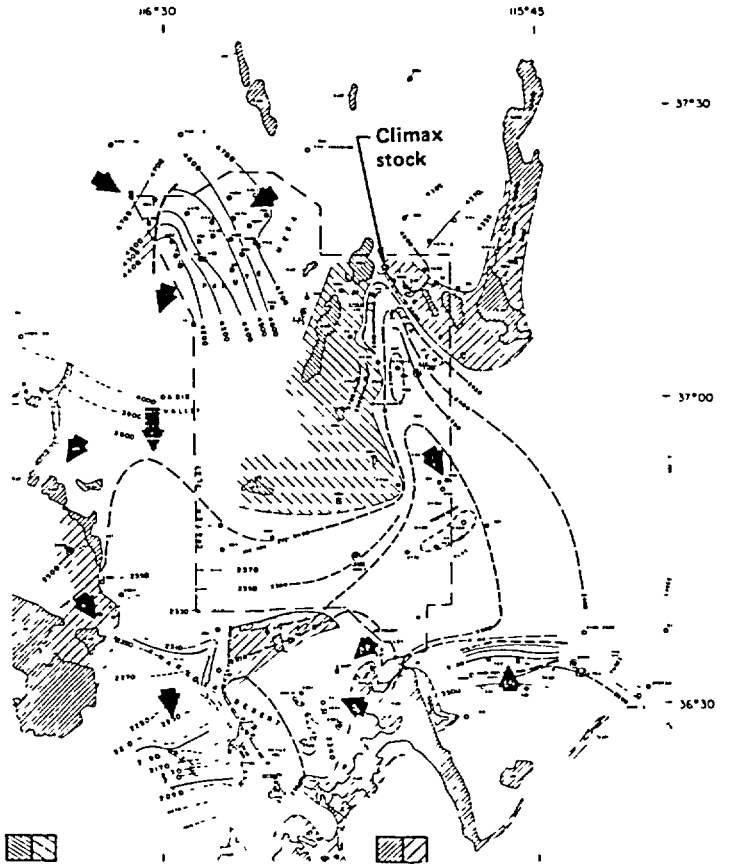

Figure 4-8. Potentiometric contours (Nevada Test Site and vicinity) are dashed where inferred and given in feet above MSL (from Winograd and Thordarson, 1975).

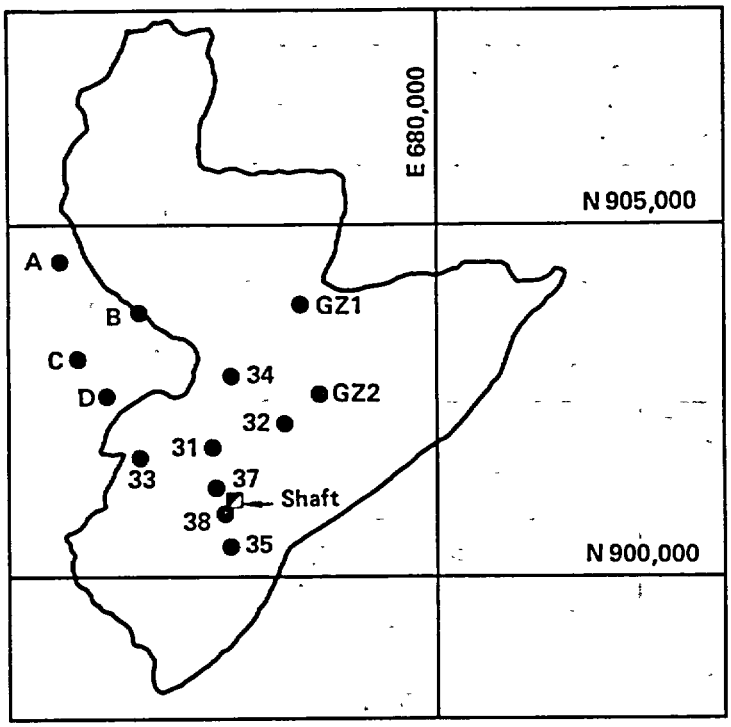

Figure 4-9. Vertical borehole locations in the Climax stock (after Murray, 1981).

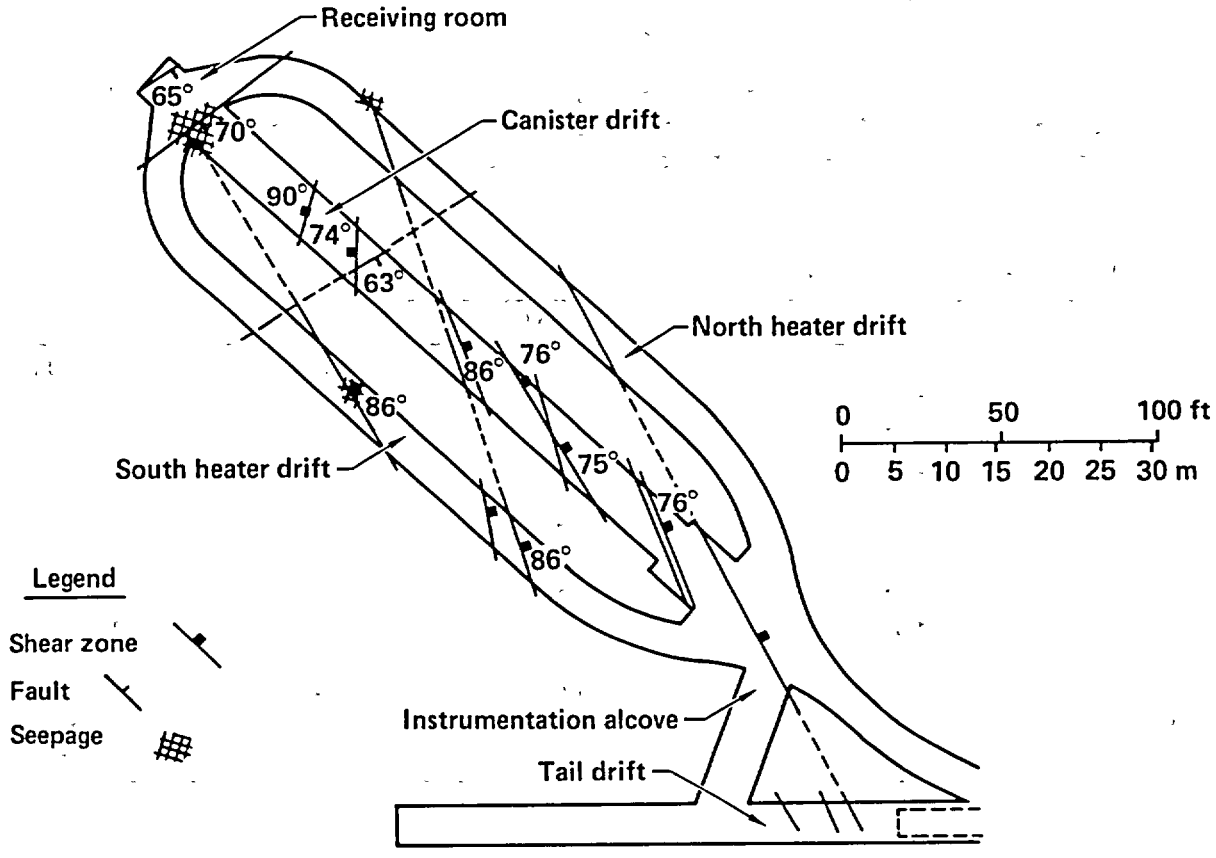

Figure 4-10. Location of seepage zones in the SFT—C (after Wilder and Patrick, 1980).

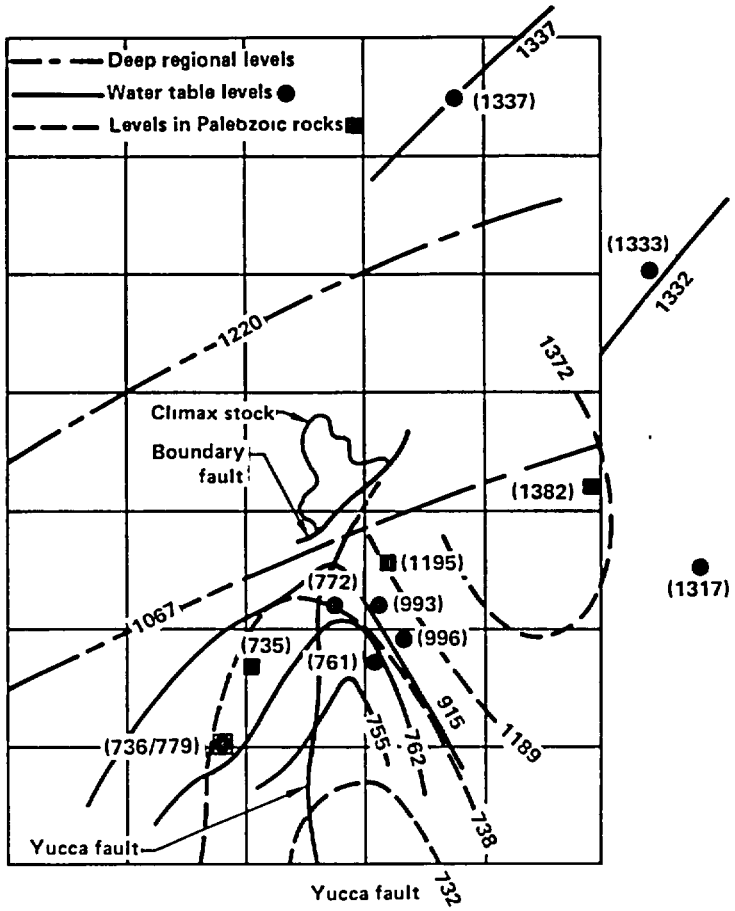

Figure 4-11. Potentiometric levels surrounding the Climax stock in metres above MSL. Numbers in parentheses indicate measured water levels. Where two numbers are separated by a slash, the first refers to the Paleozoic rocks; the second is the water table in the Cenozoic rocks (after Murray, 1981).

Table 4-7. Vertical boreholes in the Climax stock and vicinity (after Murray, 1981).

Borehole[a]	Ground surface elevation[b] (m)	Hole depth (m)	Water level[b] (m)	Comments
A	1674	362	1387	Perched water
B	1599	60	1549	Perched water
C	1621	298	1475	Perched water
D	1588	115	1486	Perched water
31	1559	366	1502	Perched water
32	1548	277	1418	Perched water
33	1571	301	—	Dry
34	1571	301	1363	Perched water
35	1519	246	1494	Perched water
37	1543	508	—	Dry
38	1536	610	—	May be dry
GZ-1	1590	549	—	Unknown
GZ-2	1550	549	—	Unknown

[a] See Fig. 4-9.

[b] Referenced to MSL.

An existing exploratory borehole (UG-02) was deepened to probe for the water level inferred from measurements in the carbonates. After extending the borehole to 960 m above MSL, a series of water level measurements was made (Fig. 4-12, Table 4-8).

Once the water level in UG-02 stabilized, bailing tests were performed to determine the recovery characteristics of the water levels. Analysis of the bailer test data indicated a permeability of about 10^{-5} D. The rising trend of the hydrograph (~0.25 m/mo) was apparently caused by recharge of the well through a pervasive fracture system. These data (together with the inferred water level of 800 to 1200 m above MSL)

Table 4-8. Water levels in exploratory borehole UG-02 (after Murray, 1981).[a]

Date	Time	Water level (m above MSL)	Comments
09/12/80	—	—	Drilling ended
10/14/80	1200	977.7	—
11/06/80	1200	974.5	—
11/19/81	1200	974.0	—
02/18/81	1017	974.6	—
02/18/81	1528	973.2	Bailer Test 1
03/04/81	1000	974.9	—
03/25/81	1035	974.9	—
03/25/81	1520	973.8	Bailer Test 2
03/27/81	1000	974.6	—
03/27/81	1137	973.1	Bailer Test 3
03/30/81	0900	974.3	—
04/01/81	1300	974.7	—
04/09/81	1300	975.1	—
05/07/81	1200	975.4	New probe on water level indicator

[a] UG-02 is a 76-mm-diam (3-in.) cored borehole.

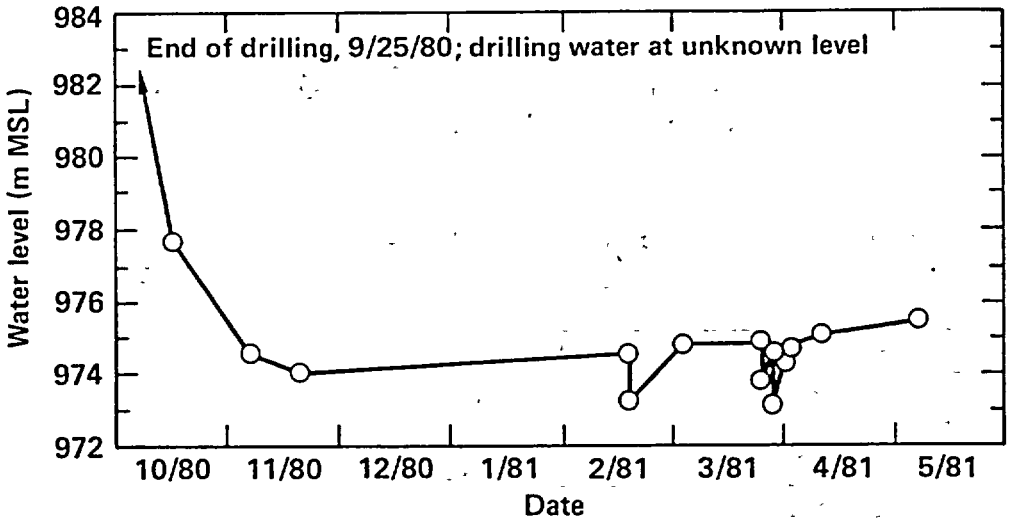

Figure 4-12. Water-level hydrograph for exploratory borehole UG-02 (after Murray, 1981).

indicate that the local zone of saturation is about 975 m above MSL. Further discussion of the data and the geohydrology of the stock and surrounding formations is provided by Murray (1981).

4.3 Summary of *In Situ* Stress Measurements*

The *in situ* state of stress is one of the most important parameters in determining the response of a rock mass to excavation and heating. As discussed in Chapter 3, we found substantial differences in calculational results when the ratio of horizontal-to-vertical stress was changed from 0.8 to 1.2. To obtain information on the *in situ* state of stress and its spacial variations, we undertook three series of measurements at the SFT—C. Each is discussed in turn here.

4.3.1 Pretest Measurements

Following excavation of the heater drifts, Ellis and Magner (1982) conducted *in situ* stress measurements under contract to LLNL. These measurements were obtained in three boreholes drilled outward and downward from the south heater drift of the SFT—C (Table 4-9). A U.S. Bureau of Mines (USBM) borehole deformation gauge was used for these overcoring measurements. One borehole (ISS-2) provided a stress profile outward from the drifts, and two additional boreholes completed the strain-relief rosette.

The magnitudes and orientations of the three principal stresses determined from measurements in these boreholes are shown in Table 4-10. It is interesting to note that the vertical stress component calculated from these values is 7.92 MPa, about 73% of the 10.9-MPa value calculated from the weight of overburden.

Since these boreholes were only 5.5 to 7.5 m long (4.8 to 6.5 m from the rib) and the drift had a 3.4 cross section, it is possible that the measurements were not within the "free field." Ellis and Magner (1982) report that the last three secondary stress measurements in ISS-2 appear to be in a different block of rock than the previous measurements.

Despite these cautions, we proceeded to use these data in the as-built thermomechanical calculations (Chapter 3) because at the time we felt they were superior to values one might calculate from depth of overburden and Poisson's effect. This judgment was vindicated by an extensive series of post-test measurements.

4.3.2 Undercoring Measurements

As part of a general investigation of the *in situ* geomechanics of the SFT—C, Heuze et al. (1981) obtained undercoring measurements on the surfaces of the north and south heater drifts. These values were obtained by measuring the response of a rosette of six metal reference pins when a central section of core was removed.

Two sets of measurements, one in the roof of each heater drift, provided the drift-surface stresses shown in Table 4-11. These were judged to be reasonably consistent with the horizontal "free-field" stresses of 9.2 and 4.2 MPa calculated by Heuze et al. (1981).

Table 4-9. Location and configuration of the *in situ* stress borehole used by Ellis and Magner (1982).

Designator	Bearing[a]	Inclination[b]	Total depth (m)
ISS-1A	N29°E	−76.5°	6.1
ISS-2	S59°W	+3.0°	5.5
ISS-3	S01°E	+3.0°	7.5

[a] South heater drift bearing was N61°W.

[b] Negative is below horizontal.

Table 4-10. Pretest *in situ* stress determinations (after Ellis and Magner, 1982).

Component	Magnitude (MPa)	Bearing[a]	Inclination[b]
σ_1(max)	11.56	N56°E	−29°
σ_2	7.13	N26°E	+57°
σ_3(min)	2.75	N43°W	−14°

[a] South heater drift bearing was N61°W.

[b] Negative is below horizontal.

*Contributed by H C. Ganow and W C Patrick.

Table 4-11. Undercore measurements of drift-surface stresses.

Measurement	Component	Magnitude (MPa)[a]	Bearing
Undercore 2	Min.	1.3	N56°W
	Max.	11.0	N34°E
Undercore 6	Min.	3.8	N79°W
	Max.	7.1	N11°E

[a] Positive is compression.

4.3.3 Post-Test Measurements

After spent fuel was retrieved from the SFT—C, we conducted many *in situ* stress measurements to determine the *in situ* stress states within two distinct regions of the facility. The first of these areas includes the two fairly long pillars located between the central canister drift and the north and south heater drifts (Fig. 4-13). In these pillars, four fairly short test borings designated ISS-4 through ISS-7 were drilled to measure stress profiles. The second measurement area was located in relatively virgin rock that was reached by drilling test boreholes outward from the south heater drift (ISS-8) and from the tail drift extension (ISS-9, ISS-10, and ISS-11), as shown in Fig. 4-13. Tests in these boreholes were intended to measure the free-field state of stress that existed before the rock mass was excavated and heated. In addition, borehole ISS-8 was used to obtain a profile of stresses outward from the SFT—C facility.

Two different types of stress relief or "overcoring" measurement instruments were used during this study: the U.S. Bureau of Mines (USBM) gauge and the Commonwealth Scientific and Industrial Research Organization (CSIRO) gauge. Both were modified to include a thermistor heat-sensing element through which we were able to directly measure ambient rock temperature at the actual test location. Standard test procedures were also extensively modified to maintain, to the extent possible, a constant temperature during each overcoring measurement.

Foundation Sciences, Inc. (FSI), supplied the USBM and CSIRO gauges, calibration and readout apparatus, and various support equipment for these measurements, along with three staff members, who assisted LLNL personnel in conducting these tests. The data presented here are summarized from Creveling et al. (1984), which contains details of the measurements.

Test Methods. Both the USBM and CSIRO gauges use strain relief by overcoring to measure the magnitude and orientation of the stress regime. During the test, one of the gauges is inserted in a nominally EX size (38-mm-diameter) borehole and is coaxially overcored with a nominally 150-mm-diameter (6-in.) core barrel. These gauges measure changes in the size and shape of the central borehole. After the overcoring is complete, the recovered core is tested in a hydraulic "biaxial" test cell to obtain data used to calculate a Young's modulus. This modulus value is in turn used to calculate the rock stresses at the test location.

The USBM and CSIRO gauges are fundamentally different in the manner in which they measure borehole deformation. The USBM gauge uses six strain-gauged beriflium-copper cantilevers mounted so that they measure three equally spaced borehole diameters in a single transverse plane (Fig. 4-14). This reusable instrument cannot measure borehole axial deformation and therefore cannot measure all the strain components necessary to determine the complete state of stress. The information obtained is sufficient to derive two secondary principal stresses (P and Q) that exist perpendicular to the borehole axis. These values are combined with measurements obtained in at least two other nonparallel boreholes to obtain directions and magnitudes for the true principal stresses.

The CSIRO gauge consists of nine variously oriented electrical-resistance-type strain gauges encased in a thin plastic cylinder (Fig. 4-15). This unit is then irretrievably bonded to the borehole wall using a special epoxy-based adhesive. The nine strain gauges are arranged such that they measure all three principal strain components, which allows, using the modulus value and thin-walled cylinder theory, a direct calculation of the principal stresses. Clearly, a very high quality gauge-to-borehole bond is required if one is to measure correct strain relief values with this gauge.

For tests within the induced thermal field at the Climax stock, the USBM gauge probes were modified to include thermistors for direct temperature measurement, and all CSIRO gauges were modified during

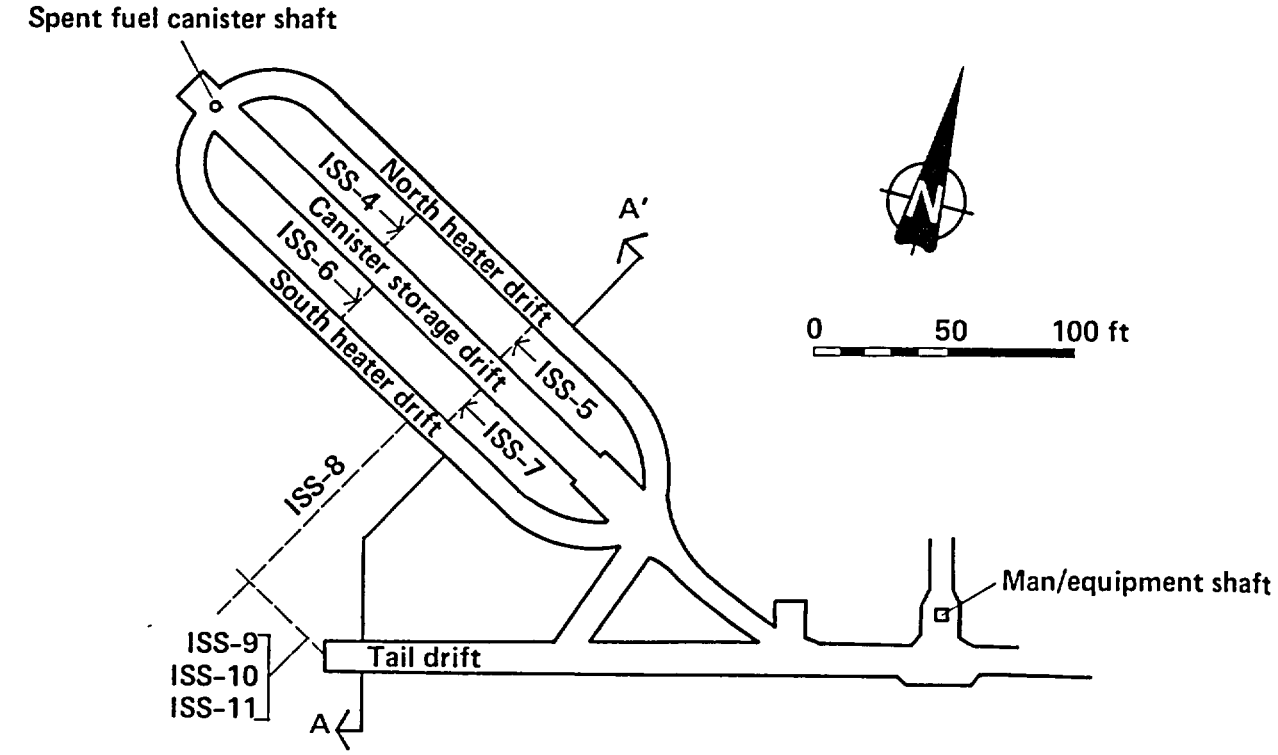

Note: ISS-10 is inclined upward about 45°.
ISS-11 is inclined downward about 45°.
Both are on the same bearing as ISS-9.
Other boreholes horizontal.

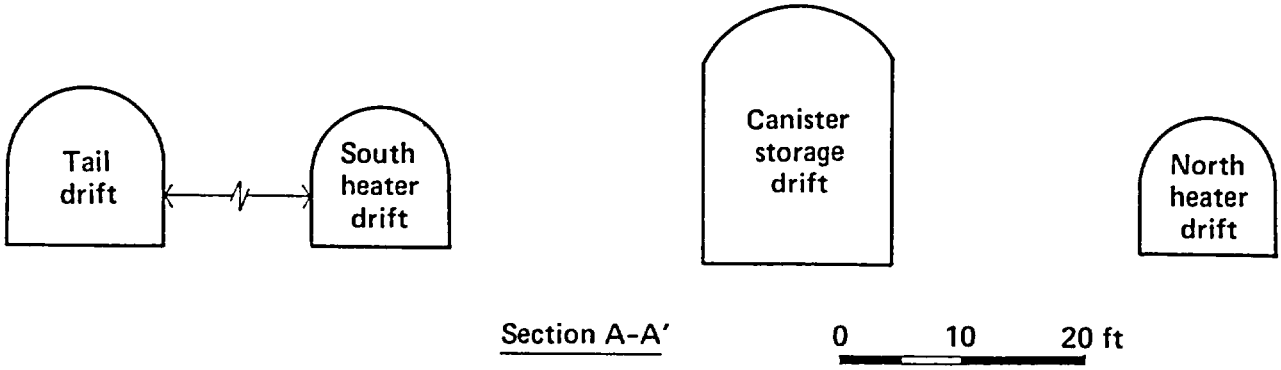

Figure 4-13. Map and section views of the Spent Fuel Test site showing the locations of the *in situ* state of stress measurement boreholes ISS-4 through ISS-11 (after Creveling et al., 1984).

manufacture to include a similar thermistor within the unit's plastic shell. Both types of devices required electrical cables with additional conductors for the thermistor signal. Following gauge insertion and thermal equilibration, the temperature value measured was used as a reference for adjusting the initial drilling water temperature. During actual overcoring, cold run-of-mine water was added to the circulating water to compensate for the thermal energy deposited in the rock by the drilling process. Following the test, the circulating water was warmed by electrical heaters to reestablish the same initial temperature. The total strain relief values obtained after thermal equilibration were the ones used to calculate the secondary or true principal state of stress values, as appropriate.

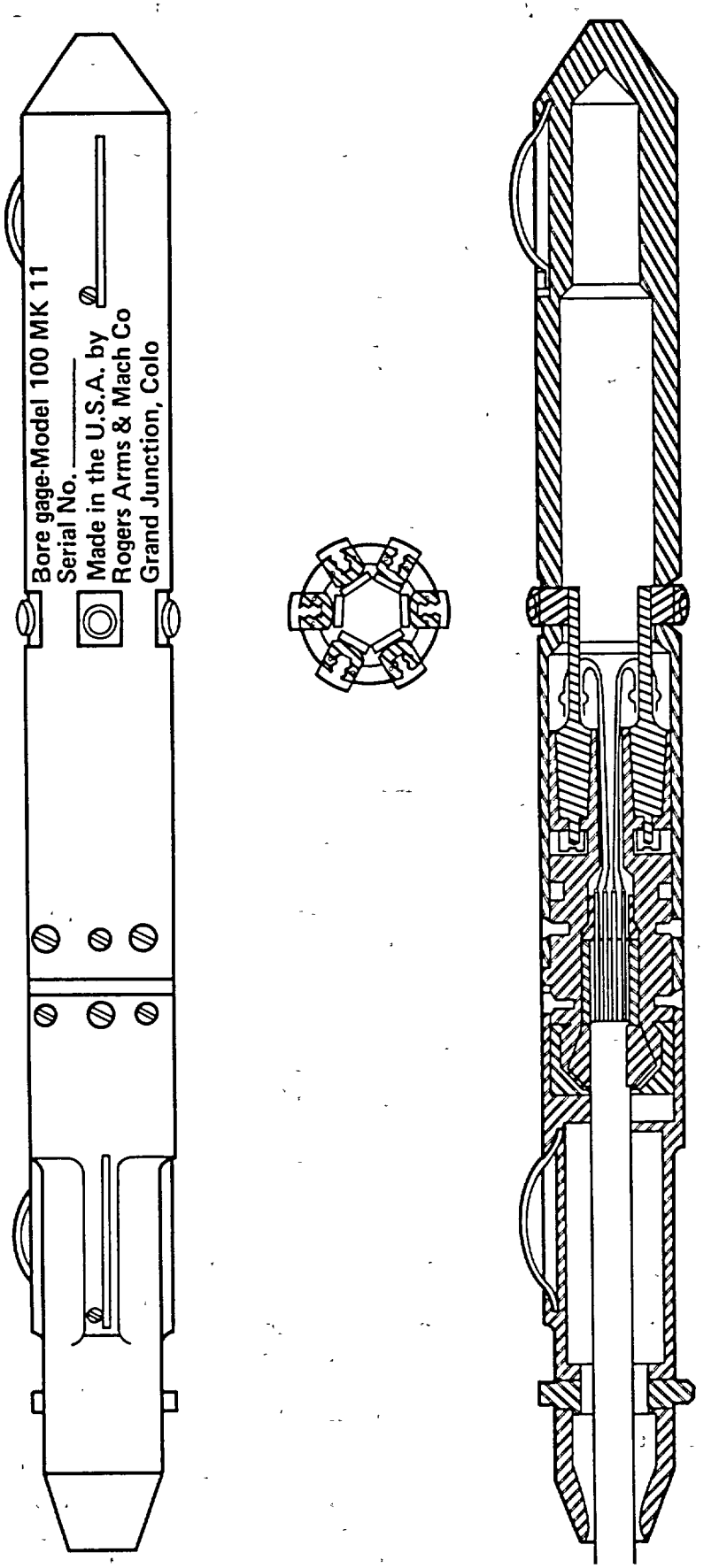

Figure 4-14. Three views of the modern reverse case U.S. Bureau of Mines Borehole Deformation Gauge (modified after drawing by Rogers Arms and Machine Co.).

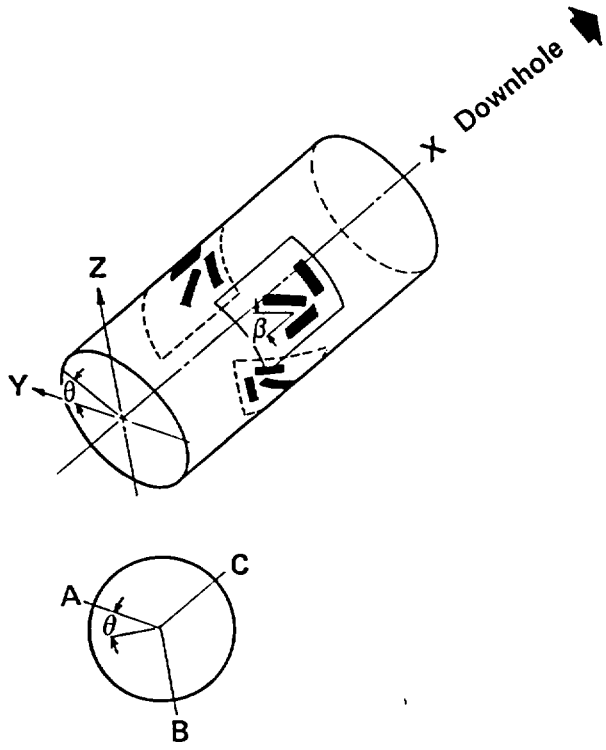

	A	B	C
θ	30°	270°	150°
β	0°90°45°	45°90°135°	0°90°45°

Figure 4-15. Oblique view showing the orientations of the nine electrical strain gauge elements of the CSIRO thin walled borehole deformation gauge (after Worotnicki and Walton, 1979).

Pillar Stress Measurements. Four test boreholes, designated ISS-4 through ISS-7, were drilled through and perpendicular to the two long, slender, rock pillars that separate the central canister drift from the north and south heater drifts (Fig. 4-13). Fifteen USBM and three CSIRO gauge tests were successfully conducted in these boreholes. The purpose of these tests was to:

- Determine the magnitudes and orientations of the secondary principal stresses (USBM gauge) and total principal stresses (CSIRO gauge).
- Observe the stress distribution along the boreholes with respect to the heater drift and canister drift ribs.
- Determine whether the USBM and CSIRO gauges yield similar values for these stresses.

The results of these tests are shown in Figs. 4-16, 4-17, and 4-18 which are taken from the report by Creveling et al. (1984). Figure 4-16 shows the magnitude of the major "P" and minor "Q" secondary principal stresses (those stresses that exist in a plane perpendicular to the borehole axis) from USBM gauge tests. These values are calculated assuming that no axial deformation occurred during overcoring. Synthetic (back-calculated) secondary principal stresses are also shown for the three CSIRO gauge tests. These data generally indicate that the P-value ranges from about 1900 to 500 psi, and that maximum values are located near the inner heater drift ribs and decrease to a minimum at the canister drift ribs. The Q-value ranges from about 700 to -200 psi (tension) and shows a similar, although weaker, trend.

Figure 4-17 shows these same data plotted in a graphical form along the borehole such that both their orientations and relative magnitudes can be studied. Recall that the P and Q stresses actually exist in a plane transverse to the borehole and are portrayed as though one were looking into the borehole collar.

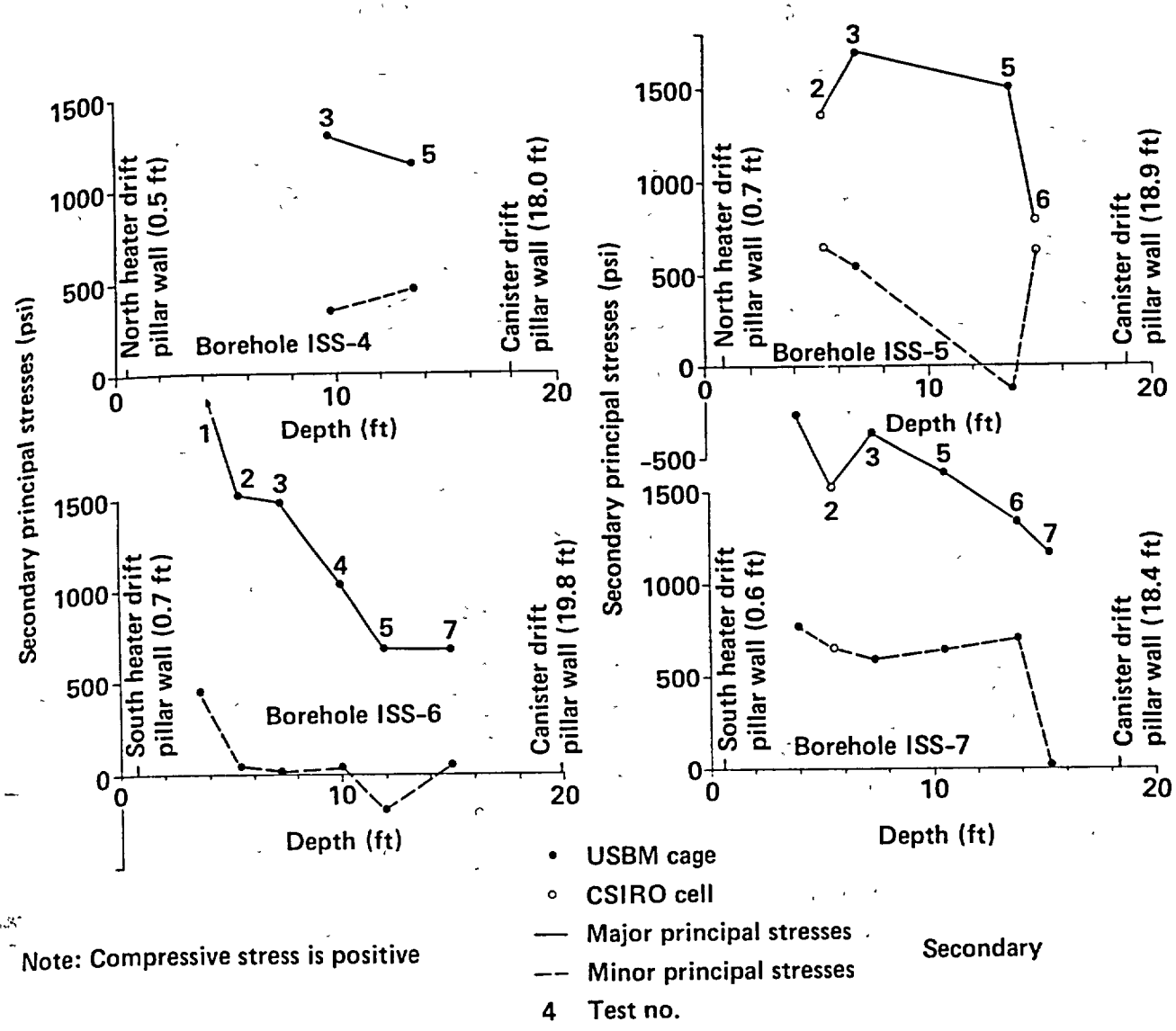

Figure 4-16. Secondary principal stress values of P and Q vs borehole depth for both USBM gauge and CSIRO gauge pillar stress measurements in boreholes ISS-4, ISS-5, ISS-6, and ISS-7 (after Creveling et al., 1984).

From these diagrams, it is clear that the maximum secondary stress is nominally within 20 to 30 degrees of vertical; therefore, Q is nearly horizontal. In general, the data between the boreholes are quite similar in form, with the possible exception of tests 1, 2, and 3 in ISS-6. These measurements are quite consistently inclined to the northwest, which, in itself, suggests they are correct. This orientation change may reflect the influence of nearby prominent joints and shears (Wilder and Yow, 1981).

The orientations of the principal stresses obtained from the CSIRO tests in pillar boreholes are shown in the upper-hemisphere polar steronet plot in Fig. 4-18. These data generally confirm the previous statements and, along with the tabulated stress magnitudes, provide additional information. The maximum principal stress (sigma 1) is systematically inclined toward the north-northeast. The intermediate principal stress (sigma 2) is nearly horizontal and aligned parallel to the pillar axis, and the least principal stress (sigma 3) is also essentially horizontal and oriented parallel to the minimum pillar width. These findings are quite consistent with the long, thin geometry of the pillars.

Free-Field Stress Measurements. Four boreholes, designed ISS-8 through ISS-11, were drilled into a relatively undisturbed portion of the stock from the tail drift extension and south heater drift (Fig. 4-13)

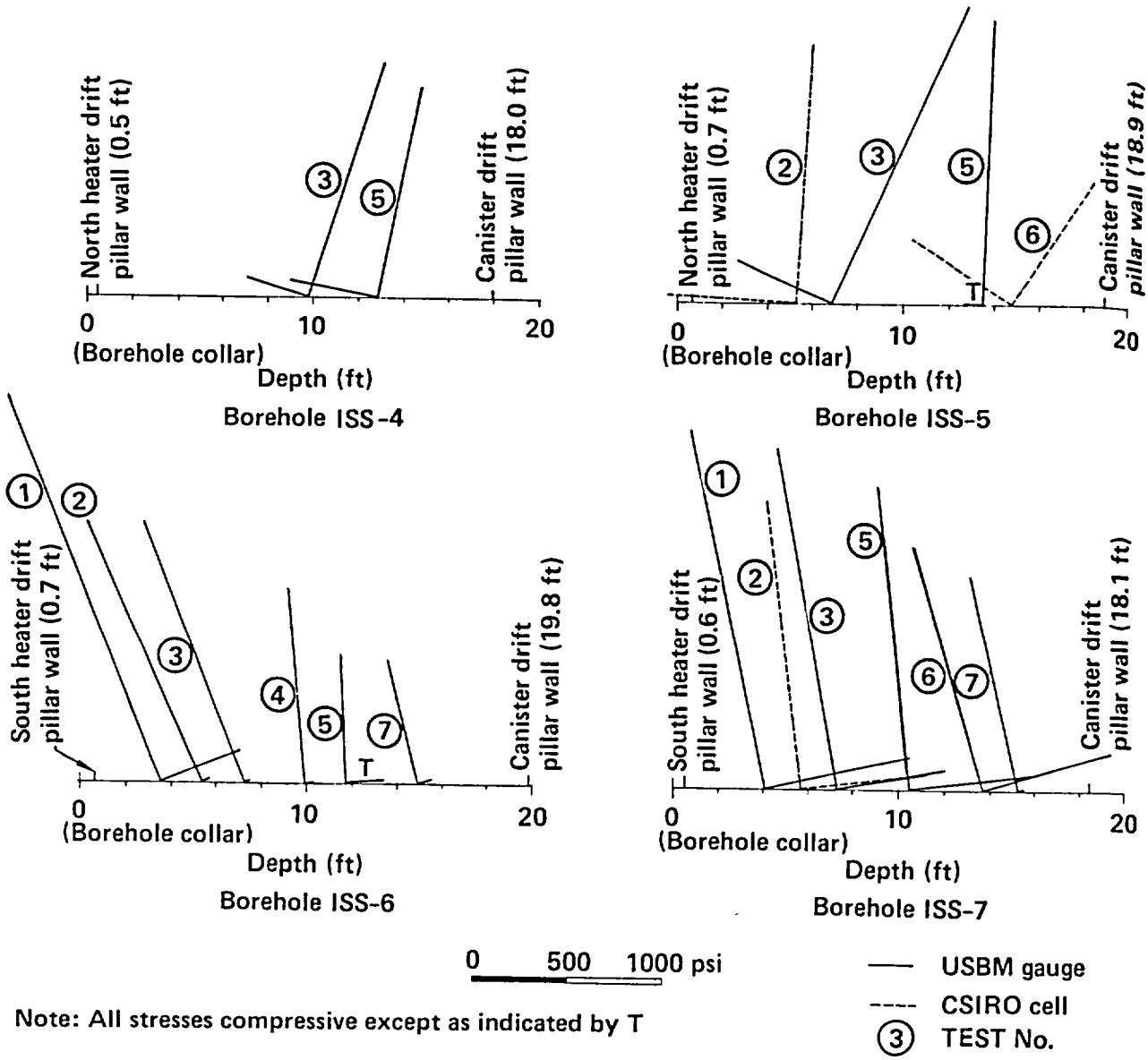

Figure 4-17. Secondary principal stress orientations of P and Q vs borehole depth for both USBM gauge and CSIRO gauge pillar stress measurements in boreholes ISS-4, ISS-5, ISS-6, and ISS-7 (after Creveling et al., 1984).

with the intent of measuring the existing free-field state of stress before excavation began. Many of the experimental objectives were the same as for the pillar study, but we also need to (1) measure the stress distribution in an outer heater drift rib for a significant distance into the virgin rock; and (2) perform an independent check on the CSIRO gauge results, using USBM gauge data from various combinations of boreholes ISS-8, ISS-9, ISS-10, and ISS-11.

Twenty-eight USBM gauge tests and 22 CSIRO gauge tests were successfully conducted in these four boreholes. Figure 4-19 shows the major P and minor Q secondary principal stresses for borehole ISS-8. It appears that the magnitudes of stresses measured by USBM and CSIRO methods agree reasonably well. The major secondary stress (P) ranges from about 800 to 1700 psi, and increases gradually away from the rib (0- to 30-ft region). Both P and Q values fall to a very low 700 and 500 psi, respectively, in the 40- to 45-ft depth range, and there is no obvious explanation for this change. The P value then increases from 900 to

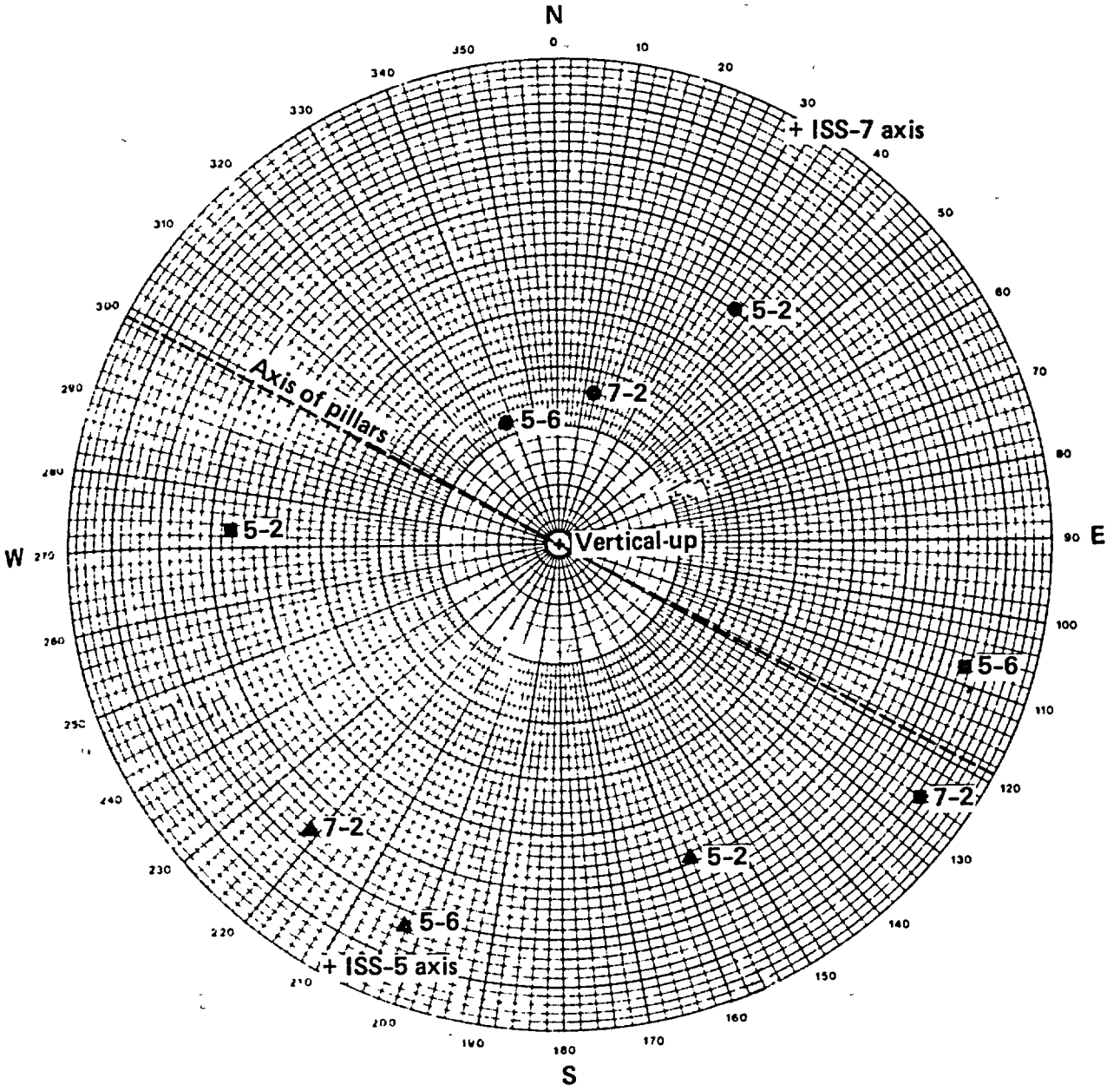

Principal stresses (psi)

Test No.	Depth (ft)	● σ_1	■ σ_2	▲ σ_3
ISS-5-2	5.3	2,290	836	433
ISS-5-6	14.8	822	674	-294
ISS-7-2	5.5	1,838	668	254

Note: Compressive stress positive

Figure 4-18. Polar stereonet plot showing the principal stress orientations obtained from three CSIRO gauge measurements made in boreholes ISS-5 and ISS-7 (after Creveling et al., 1984).

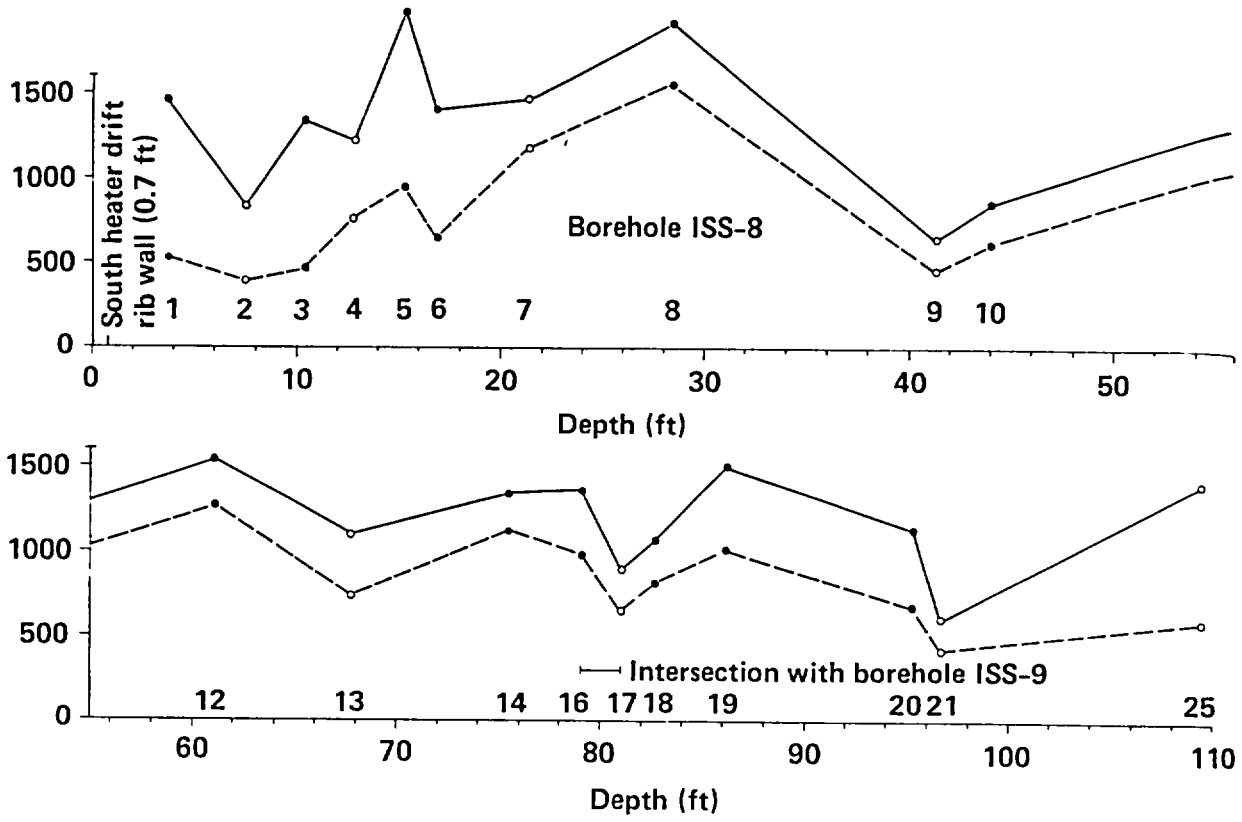

Figure 4-19. Secondary principal stress values of P and Q vs borehole depth for both USBM gauge and CSIRO gauge measurements in boreholes ISS-8 (after Creveling et al., 1984).

1600 psi for the remainder of the borehole. The stress differential is maximum for those tests in the 0- to 30-ft region, as well as at CSIRO Test No. 25, located at the very end of the borehole. The latter may be an anomaly, however.

Figure 4-20 shows the P and Q stress orientations. The maximum secondary stress tends to be oriented nearly vertical in the 0- to 30-ft portion of ISS-8, which is probably a result of its relatively close proximity to the drifts. Beyond this region, P tends to be highly inclined, reflecting the influence of the true free-field state of stress.

As shown in Fig. 4-13, boreholes ISS-9 and ISS-10 were drilled along the same bearing and inclined upward 4 and 46 degrees, respectively, and borehole ISS-11 was on the same bearing but inclined downward about 45 degrees. Secondary principal stress magnitude data and orientation data are shown in Fig. 4-21 and Figs. 4-22 and 4-23, respectively. In ISS-9, the stress values appear relatively constant along the borehole length except for test pair numbers 7 and 8. Nominally, the P and Q stress values are 700 to 1100 psi and 400 to 700 psi, respectively. However, in ISS-10, the P value is consistently higher at 1300 to 2100 psi, and the P-to-Q stress differential is larger. Although the presence of a shear zone has been suggested as the cause of this disparity, careful examination of the core from both ISS-9 and ISS-10 does not support

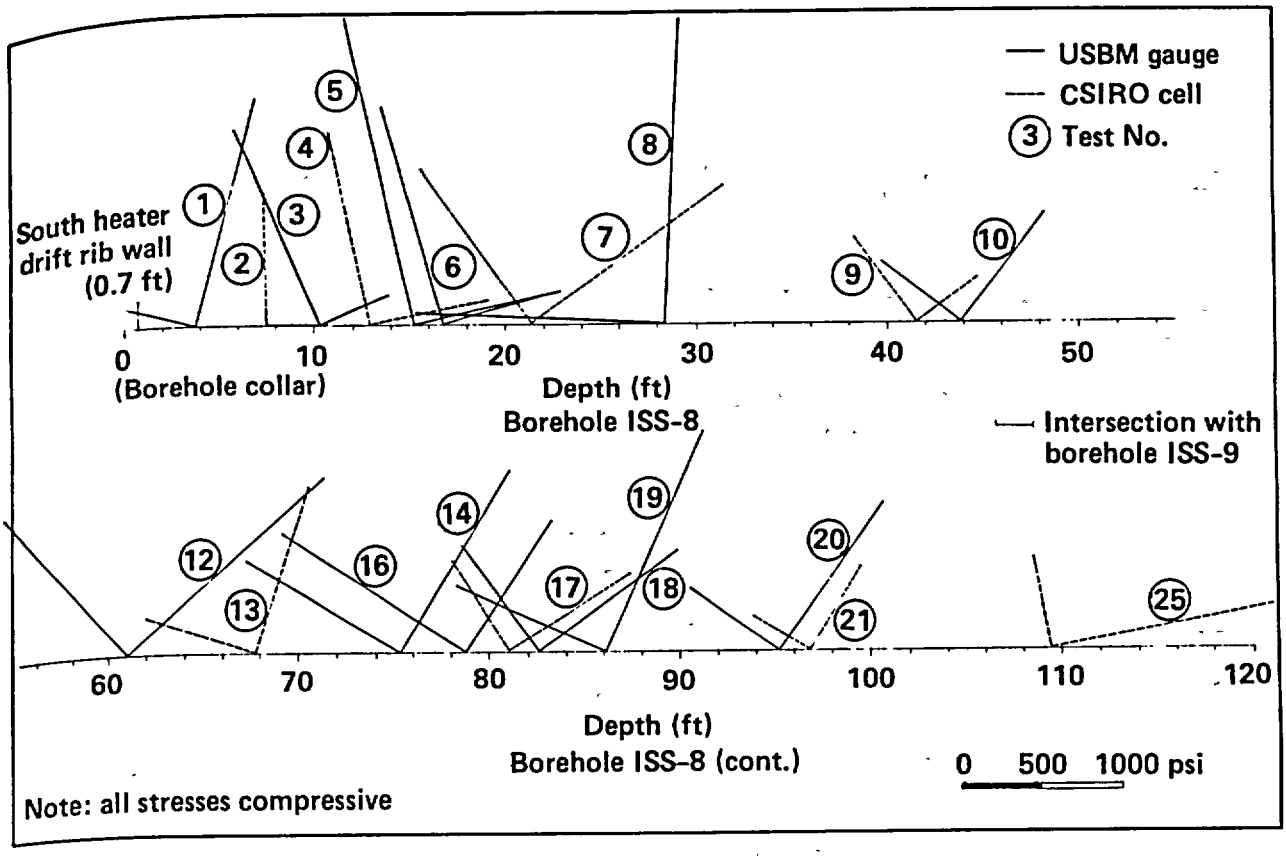

Figure 4-20. Secondary principal stress orientations of P and Q vs borehole depth for both USBM gauge and CSIRO gauge measurements in borehole ISS-8 (after Creveling et al., 1984).

this interpretation. In ISS-11, we see a fairly consistent increase in the major secondary stress with depth. Although this trend is also evident to a depth of 85 ft for the minor stress, a rapid decrease is noted at greater depths.

Figures 4-24 and 4-25 are upper-hemisphere polar steronet plots of the average principal stress orientations from CSIRO gauge tests in ISS-8 through ISS-11 and the principal stress orientations calculated from USBM gauge tests in various combinations of these four boreholes. Note that these combinations give considerably different results—a natural consequence of obtaining the data from three separate, usually diverging boreholes in a spacially varying stress field. The combination of ISS 8, 9, and 10 is considered to most represent conditions at the depth of the SFT—C. The maximum principal stress (sigma 1) values tend to cluster at about N70°E, with a plunge of 20 to 30 degrees to the northeast. The intermediate and least principal stress (sigmas 2 and 3) values alternate from nearly horizontal and trending to the northwest to nearly vertical. This is because they tend to be more nearly equal in magnitude. It is interesting to note that the maximum stress orientation of N70°E is reasonably consistent with Carr's (1974) estimate of N40°E. Also, Wilder and Yow (1984) and Zoback and Zoback (1980) estimate that the least principal horizontal stress is oriented about N45°W, which compares with the N30°W calculated from these data.

4.3.4 Conclusions

The following conclusions are offered with regard to this study.

1. Acceptable results were obtained from both the USBM and CSIRO gauges, and the experimental objectives were achieved. The CSIRO gauge results appear to be consistently about 30% lower than values obtained with the USBM gauge.

2. In the north and south heater drift pillars, the maximum principal stress (sigma 1) is essentially vertical, the intermediate principal stress (sigma 2) is horizontal and aligned parallel to the long axes of the

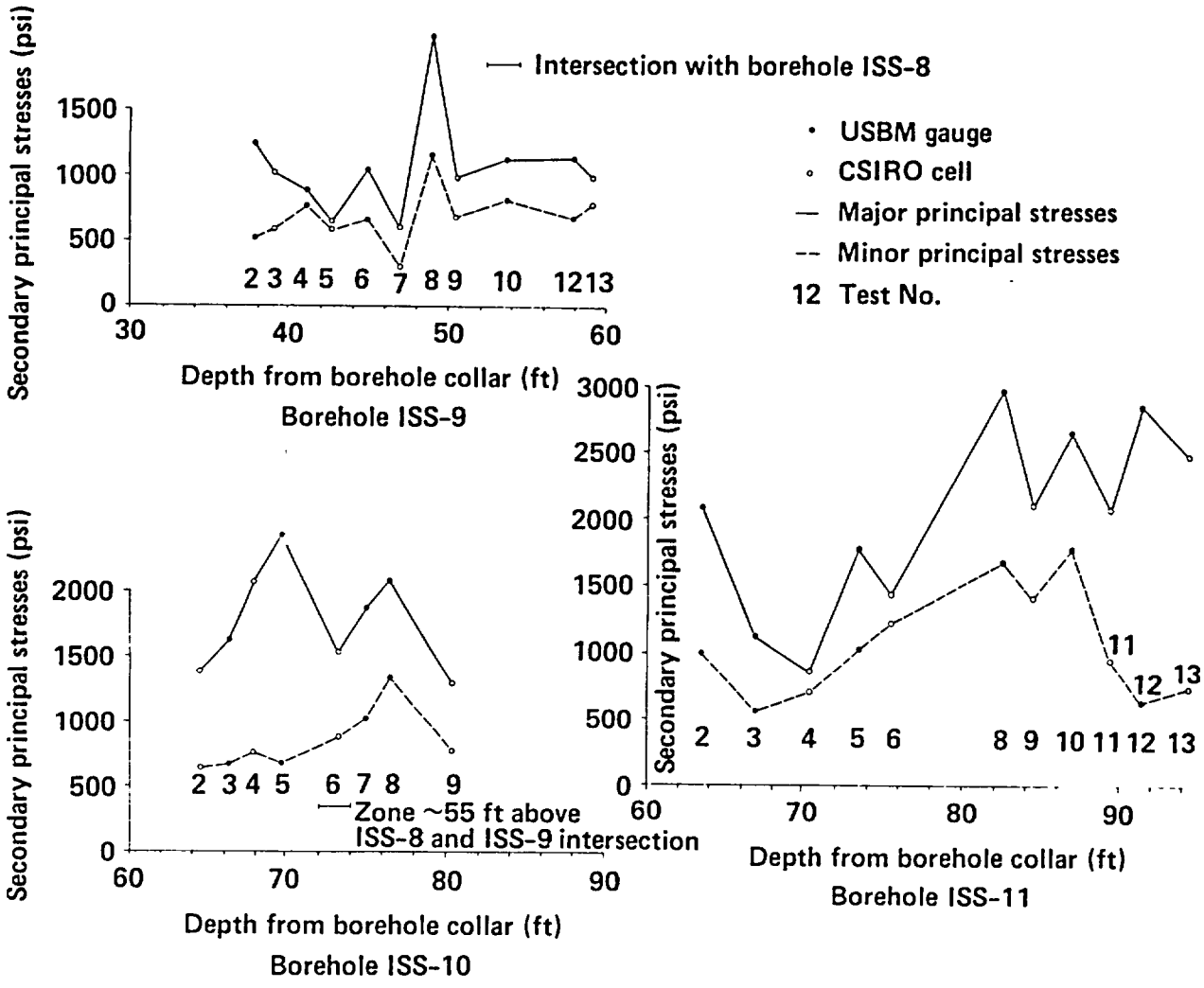

Figure 4-21. Secondary principal stress values of P and Q vs borehole depth for both USBM gauge and CSIRO gauge measurements in boreholes ISS-9, ISS-10, ISS-11 (after Creveling et al., 1984).

pillars, and the least principal stress (sigma 3) is parallel to the pillar width. These results are consistent with the long, thin geometry of the pillars.

3. The "free-field" state of stress measurements indicate that the maximum principal stress is oriented toward the east-northeast and is nearly horizontal, the intermediate principal stress is nearly vertical, and the nearly horizontal least principal stress is oriented north-northwest. These results are consistent with the conclusions of previous investigators and motions of active faults at the NTS.

4.4 Physical Properties Measurements*

Both laboratory and *in situ* measurements were undertaken to determine mechanical, thermal, and thermomechanical properties for use in calculations that formed the basis for design (Chapter 3) and subsequent comparisons with data obtained during the test (Chapters 13, 14, and 16). The effects of heat and ionizing radiation on selected properties are discussed in Section 4.6. The transport of heat and the resulting thermomechanical response of a rock mass are controlled in large part by the physical properties of the rock mass. Among the properties important to heat transport are the thermal conductivity, diffusivity, and

*Contributed by W C. Patrick.

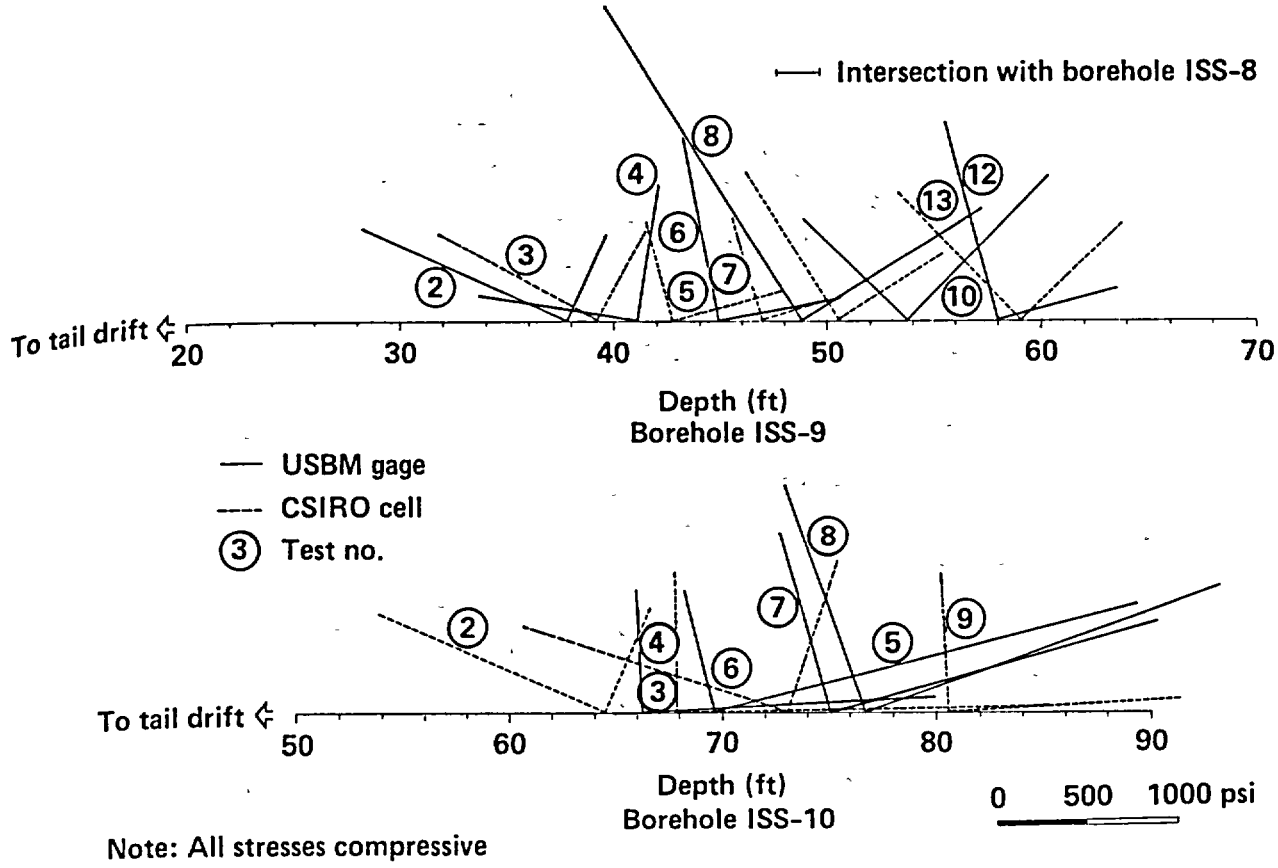

Figure 4-22. Secondary principal stress orientations of P and Q vs borehole depth for both USBM gauge and CSIRO gauge measurements in borehole ISS-9 and ISS-10 (after Creveling et al., 1984).

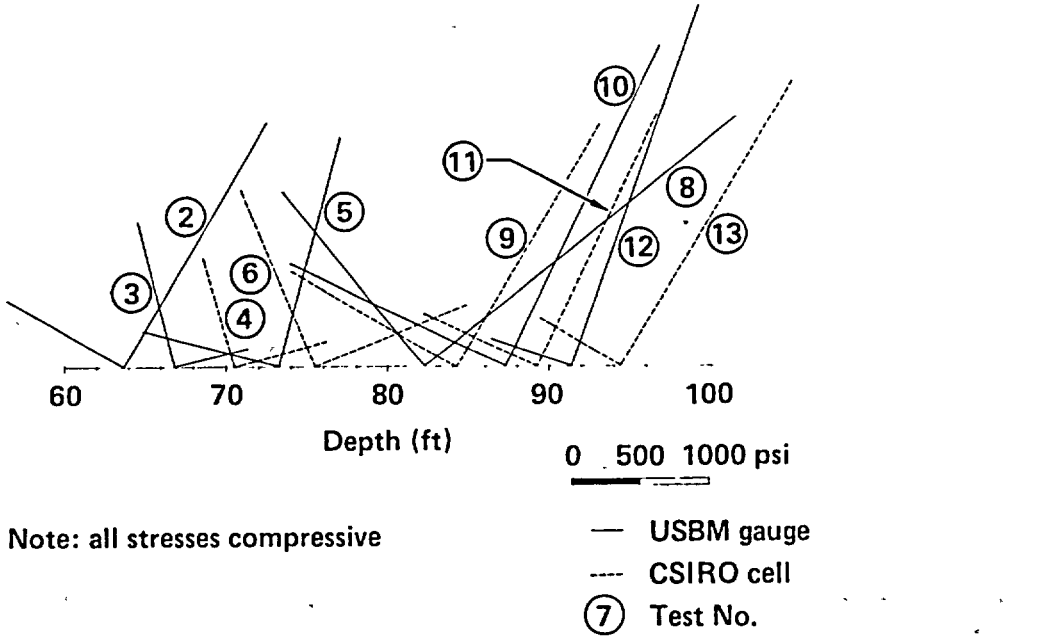

Figure 4-23. Secondary principal stress orientations of P and Q vs borehole depth for both USBM gauge and CSIRO gauge measurements in borehole ISS-9, ISS-10, and ISS-11 (after Creveling et al., 1984).

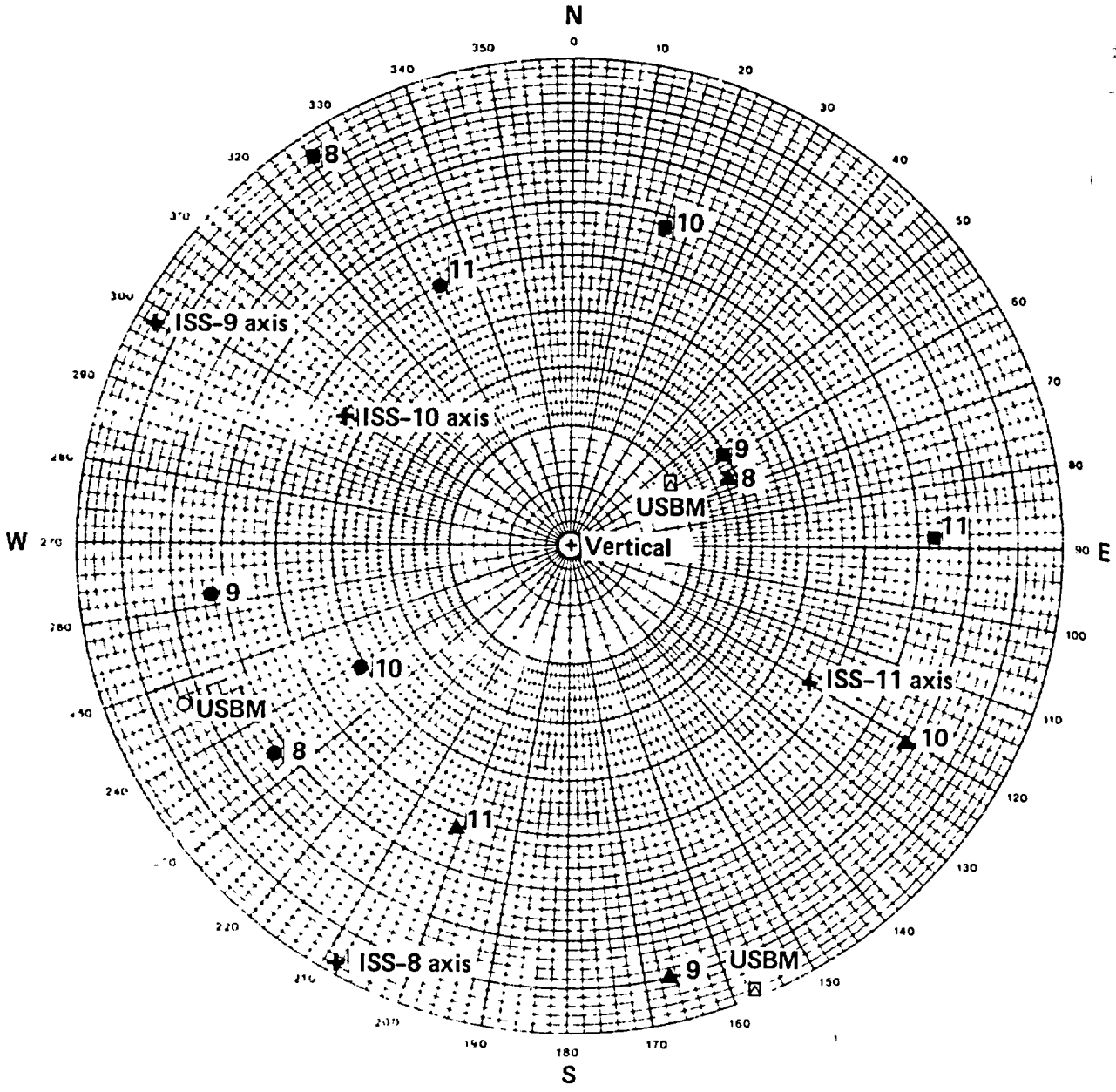

Borehole No.	Principal stress (psi) ● σ_1	■ σ_2	▲ σ_3
ISS-8*	1,390	918	652
ISS-9**	1,153	617	472
ISS-10**	1,907	1,384	686
USBM***	1,795	1,081	714

* Solution from all CSIRO cell tests beyond depth 60 ft
** Solution from all CSIRO cell tests in
*** Solution from boreholes ISS-8, 9, 10

Figure 4-24. Polar stereonet plot showing principal stress orientations obtained from CSIRO gauge measurements; and principal stresses calculated from USBM gauge measurements in boreholes ISS-8, ISS- 9, and ISS-10 (after Creveling et al., 1984).

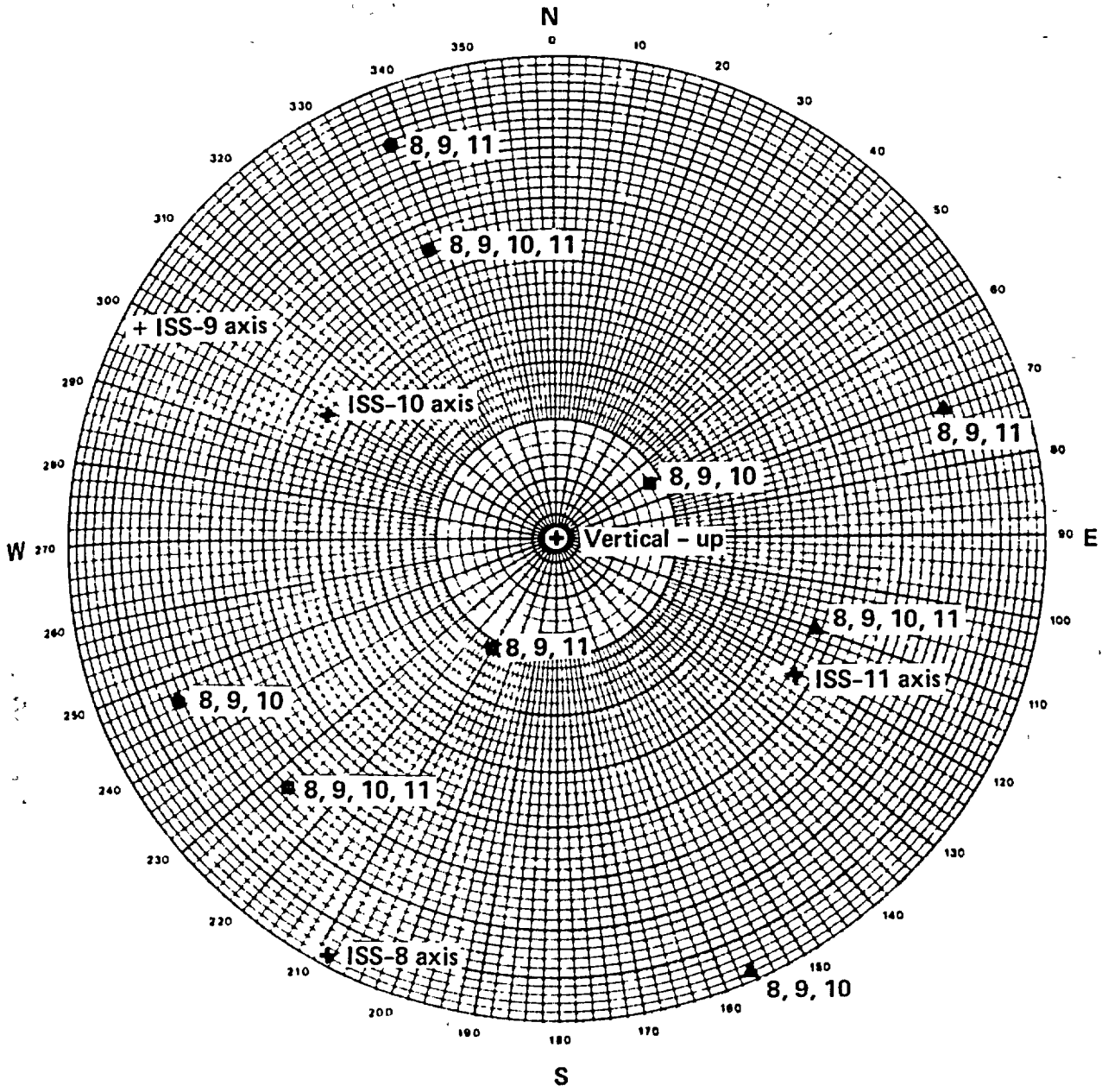

Borehole combinations	Principal stresses (psi) ● σ_1	■ σ_2	▲ σ_3
ISS-8, 9, 10	1,795	1,081	714
ISS-8, 9, 11	1,844	1,287	557
ISS-8, 9, 10, 11	1,654	1,195	992

Note: All stresses compressive

Borehole ISS-8 includes all USMB gage tests beyond 60-ft depth.

Borehole ISS-8 includes all USMB gauge tests beyond 60-ft depth.

Figure 4-25. USBM Gage Principal stressses, boreholes ISS-8, ISS-9, ISS-10, and ISS-11 (after Creveling et al., 1984).

density. For thermomechanical response, the "stiffness" of the rock (usually expressed in terms of its response to loading and reported as Young's modulus, shear modulus, and Poisson's ratio), thermal expansivity, and measures of strength (including a failure envelope) are important. If the rock mass is jointed or fractured, the pertinent shear and normal stiffnesses and related strength parameters must also be known.

Complicating factors in expressing these properties are:

- Temperature and pressure dependence.
- Effects of sampling disturbances.
- "Scale effects" resulting from sample inhomogeneities.
- Sampling biases that tend to eliminate weaker, softer materials, often during the drilling process.

As a result, we elected to conduct both laboratory and *in situ* tests to determine the pertinent rock properties. The former were effectively used to examine pressure and temperature dependences whereas the latter were used to determine the field-scale values of selected properties.

4.4.1 Laboratory Studies of Thermomechanical Properties

Some of the earliest physical properties data for the SFT—C were obtained by Pratt, Lingle, and Schrauf (1979). The resulting data are summarized in Table 4-12. While the 76-mm-diameter cores "G-1" and "G-2" were obtained from exploratory borings in the region where the SFT—C was later constructed (Chapter 3), the "large core" (143-mm) was obtained from the floor of an alcove in which an earlier *in situ* heater test was performed (Sec. 4.4.4).

These data display several interesting trends: First, there seems to be relatively minor variability in properties at a given set of conditions, typically no more than 10%. Second, strength increases with confinement, which is fairly common. Third, there appears to be little effect (at least no monotonic change) of confining pressure on Young's modulus. Fourth, the effect of confining pressure on Poisson's ratio is unclear—it appears to increase for the smaller cores and decrease for the large core.

Page and Heard (1981) later studied in detail the effects of temperature and pressure on selected properties. Young's modulus was seen to increase fairly consistently with increases in confining pressure and decrease with increasing temperature (Fig. 4-26). Similar effects were observed in the bulk modulus (Fig. 4-27).

The same study, which also summarized the earlier work of Heard (1980), indicated that porosity and permeability decrease with increasing confining pressure and increase with increasing temperature (Fig. 4-28).

Preliminary studies by Heard (1980) indicated that the coefficient of expansion of the CSQM was not a simple function of pressure or temperature. Page and Heard (1981) extended these studies to provide the

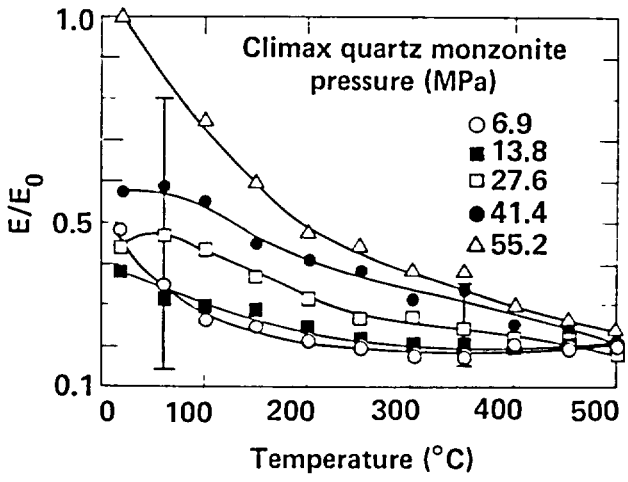

Figure 4-26. Normalized Young's modulus (E/E_0) vs temperature for Climax quartz monzonite. The error bars represent 1 std dev of the 9-sample population, which averages ±7% at 10 °C, ranging to ±40% at 350 °C. Estimated std dev for E/E_0 of a uniform population is ±10% at 19 °C, and ±6% at 350 °C (after Page and Heard, 1981).

Table 4-12. Summary of laboratory thermomechanical properties of Climax stock quartz monzonite (after Pratt et al., 1979).

Thermomechanical properties	Sample source		
	G-1 core	G-2 core	Large core
Physical Properties			
Dry bulk density (g/cm³)		2.635 ± 0.036	
Grain density (g/cm³)		2.723 ± 0.027	
Total porosity (%)		3.2 ± 0.7	
Permeability (μD)	0.12	0.10	
Mechanical properties			
Compressive strength (GPa)			
@ σ_3 = 0 MPa	0.20 ± 0.03	0.20 ± 0.03	
@ σ_3 = 3.4 MPa			0.275 ± 0.007
@ σ_3 = 6.9 MPa			0.282 ± 0.044
@ σ_3 = 10.3 MPa			0.337 ± 0.027
@ σ_3 = 20.7 MPa			0.452 ± 0.016
@ σ_3 = 41.4 MPa			0.569 ± 0.032
Young's Modulus (GPa)			
@ σ_3 = 0 MPa	48 ± 5	51 ± 5	
@ σ_3 = 3.4 MPa			66.7 ± 5.9
@ σ_3 = 6.9 MPa			54.4 ± 5.1
@ σ_3 = 10.3 MPa			61.8 ± 7.0
@ σ_3 = 20.7 MPa			63.7 ± 6.4
@ σ_3 = 41.4 MPa			66 8 ± 1.9
Dynamic	82.8	73.3	67.2 ± 3.9
Poisson's ratio			
@ σ_3 = 0 MPa	0.21 ± 0.02	0.22 ± 0.22	
@ σ_3 = 3.4 MPa			0.35 ± 0.02
@ σ_3 = 6.9 MPa			0.27 ± 0.06
@ σ_3 = 10.3 MPa			0.31 ± 0.05
@ σ_3 = 20.7 MPa			0.31 ± 0.05
@ σ_3 = 41.4 MPa	0.240	0.253	0.248 ± 0.012
Bulk modulus (GPa)			
Dynamic	53.2	49.4	44.5 ± 4.4
Ultrasonic velocities (km/s)			
P-wave	6.058	5.767	5.501 ± 0.208
S-wave	3.541	3.317	3.185 ± 0.080
Tensile strength (MPa)[a]	16 ± 2	14 ± 2	

[a] Brazilian test.

data shown in Fig. 4-29. Although there are no exceptions, the increase in α with increasing temperature and the decrease with increasing pressure are quite consistent. The curve labelled "calculated" indicates the theoretical coefficient based on the expansivity of the individual mineral constituents and their relative proportions of the cores tested. Note that the measured values are consistently substantially higher than those of the crack-free model.

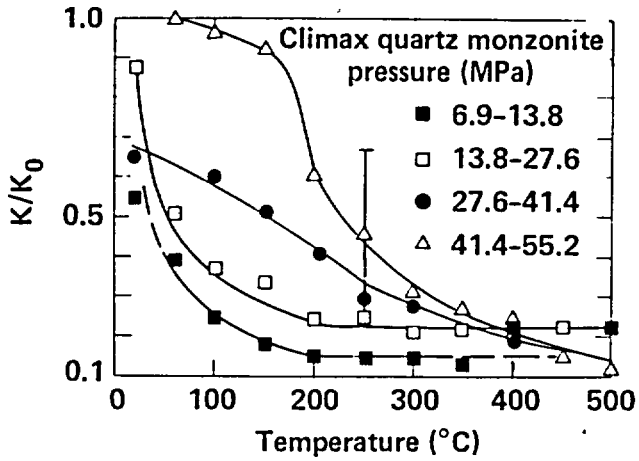

Figure 4-27. Normalized bulk modulus (K/K_o) vs temperature for Climax quartz monzonite. The error bar represents 1 std dev of the 9-sample population, which averages ±50%. Estimated std dev for K/K_o of a uniform population is ±10% at 19 °C, ranging down to ±6% at 250 °C (after Page and Heard, 1981).

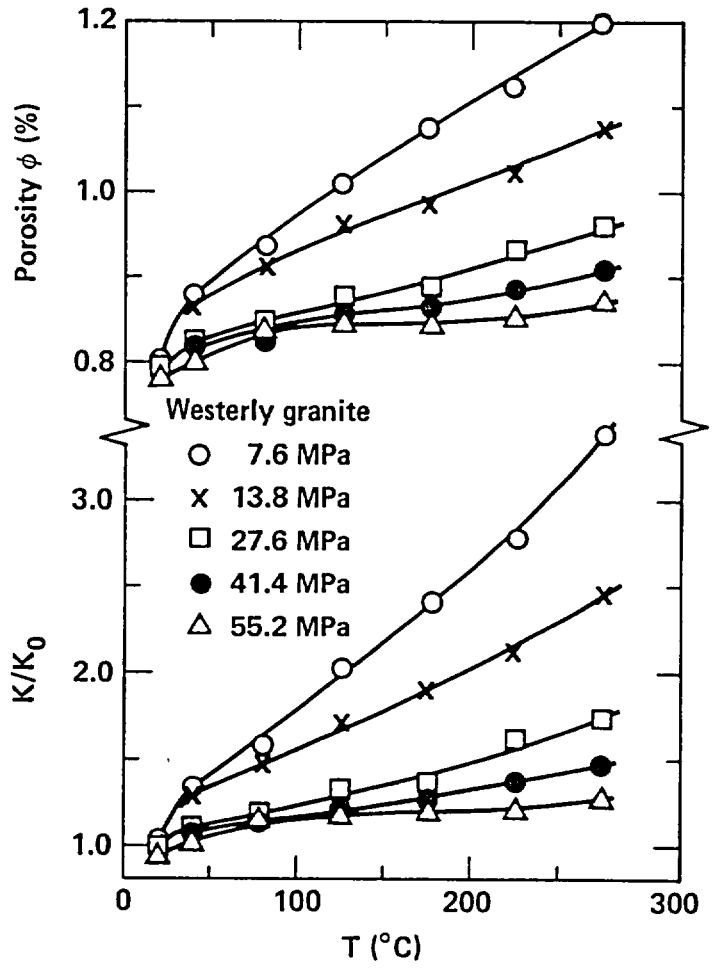

Figure 4-28. Calculated porosity (A) and normalized permeability (calculated) K/K_o, (B) at 5 pressures vs temperature for Climax quartz monzonite (after Page and Heard, 1981).

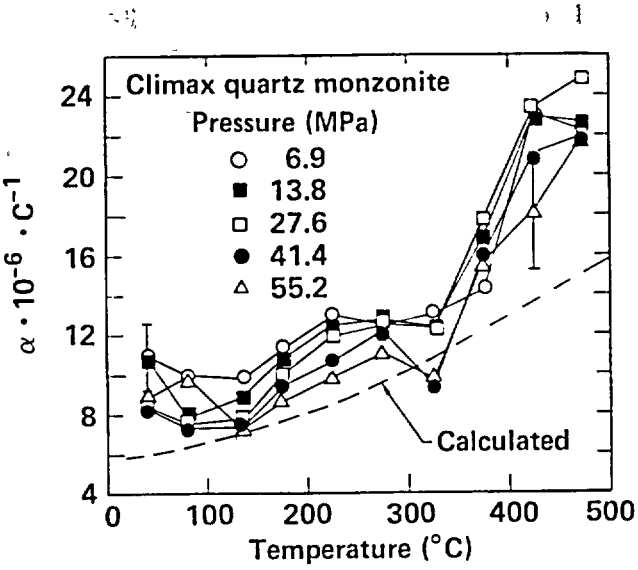

Figure 4-29. Coefficient of thermal linear expansion at five pressures vs temperature for the Climax quartz monzonite. The error bars represent 1 std dev of the 9-sample population which averages ±15%. Estimated std dev of a uniform population is ±2% (after Page and Heard, 1981).

The observed relationships are consistent with the generally accepted model for the material: a solid containing microfractures whose behavior is altered by the generation of new microfractures with increasing temperature. Because microfractures neither open and extend as much nor form as easily at higher pressures, increasing pressure tends to result in properties that are nearer their intrinsic values.

4.4.2 Laboratory Studies of Thermal Properties

The previously cited studies of Pratt, Lingle, and Schrauf also provided thermal properties for use in early calculations (Table 4-13). These studies were extended by Durham and Abey (1981) and Durham (1982) to establish the temperature and pressure dependence of thermal conductivity and diffusivity.

The latter study also examines the effect of preconditioning the samples at selected combinations of temperature and pressure.

Durham and Abey's data (1981) show the expected increase with pressure (Fig. 4-30) and decrease with temperature (Fig. 4-31) of the thermal conductivity. These effects are essentially monotonic but nonlinear. Durham (1982) subsequently showed a similar temperature effect on diffusivity (Fig. 4-32) and confirmed the previously observed effects on conductivity, even after preconditioning (Fig. 4-33). His study concluded that:

- Thermal conductivity of CSQM is 2.75 ± 0.25 W/m•K at 313 K and 3 MPa confining pressure, and increases nearly linearly with pressure.
- Thermal conductivity decreases in the temperature range of 373 to 523 K (at all pressures) approximately as 1/T. A slower rate of decrease is observed at lower temperatures.
- Conditioning at temperatures as high as 473 K has no discernable effect on room-temperature properties.
- Thermal diffusivity is 1.25 ± 0.4 × 10^{-6} m^2/s at 300 K and 50 MPa. Variations with temperature and pressure are proportional to those observed in conductivity.

4.4.3 Field Studies of Mechanical Properties

Six different techniques were used to estimate *in situ* deformability (Heuze et al., 1981). The means and ranges of moduli, together with selected laboratory values, are displayed in Fig. 4-34. As indicated, four of the techniques provided similar estimates; the mean was 26 GPa. An estimate of the laboratory deformability was 70 GPa, yielding a ratio of field-to-laboratory deformability of 0.37, which is about average for jointed hard rocks such as the Climax stock (Heuze, 1980). Heuze estimated the rock mass Poisson's ratio

Table 4-13. Summary of laboratory thermal properties of Climax stock quartz monzonite (after Pratt et al., 1979).

Properties	Sample source		
	G-1 core	G-2 core	Large core
Conductivity (W/m·°C)			
vs pressure*	3.6	3.7	
vs temperature			2.92 @ 25°C 2.76 @ 100°C 1.95 @ 200°C

* Not pressure-dependent in the range from 0 to 34.5 MPa.

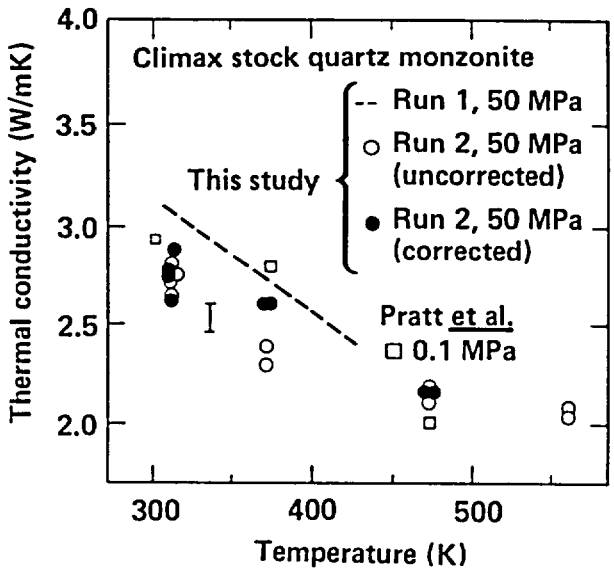

Figure 4-30. Thermal conductivity vs pressure at 313 K for CSQM Run 2, corrected (solid symbols). Also shown are the uncorrected data, open symbols (after Durham and Abey, 1981).

at 0.246 on the basis of stress undercore measurements and an assumption of plane strain conditions (Sec. 4.3). This study also detected an effect of excavation that caused the modulus within 0.5 m of the drifts to be about one-half the value elsewhere.

Two of the field techniques gave estimates close to those observed in the laboratory. As explained by Heuze et al. (1981), the "modified NX jack" of de la Cruz gave high estimates because of the presence of fractures. These fractures were located such that the friction strain gauges employed in the jack experienced anomalously low strain, causing the calculated modulus to increase. In addition, petite sismique modulus estimates agreed quite well with laboratory values. It was not until several years later that Zucca (1984) was able to repeat the petite sismique measurements and determine that there are fundamental problems with the technique and, further, that transducer (receiver) and source problems occurred during the previous study.

With source and receiver problems resolved or mitigated, Zucca produced a dominant shear-wave frequency of 480 Hz, substantially below the 1100-Hz value reported by Heuze et al. (1981). As a result, the estimate of deformability decreased by more than a factor of 3 to about 15 GPa. More importantly, he concluded that since the recorded signals were source- and distance-dependent (and, hence, not solely a result of intrinsic rock properties), the petite sismique technique cannot be used with any confidence until further research resolves these dependencies.

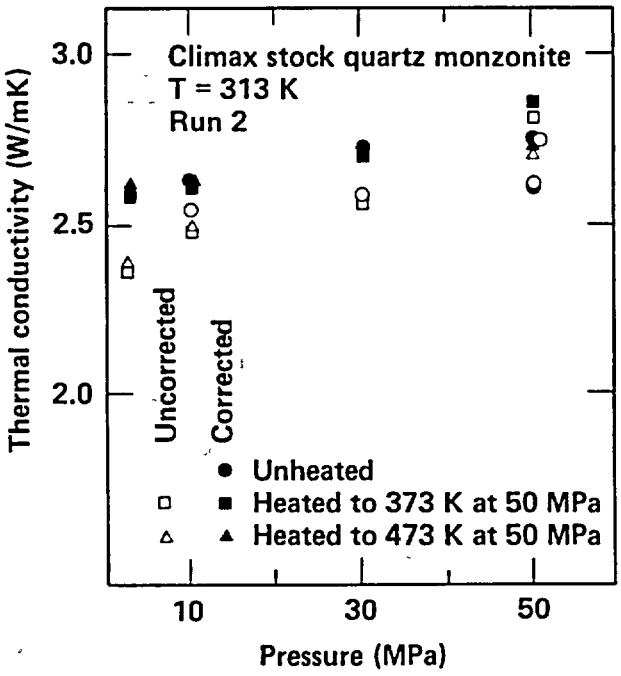

Figure 4-31. Thermal conductivity vs temperature at 50 MPa for CSQM Run 2, corrected and uncorrected. Dashed line is uncorrected data from Run 1. Error bar indicates precision of data from this study (after Durham and Abey, 1981).

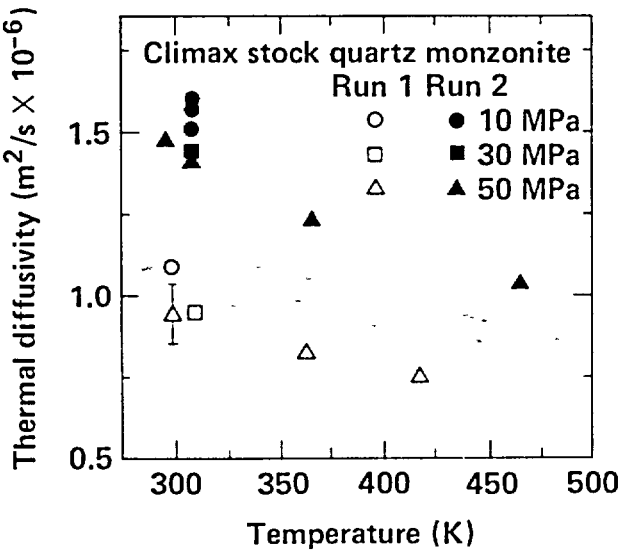

Figure 4-32. Thermal diffusivity vs temperature for various pressures for Runs 1 and 2 (after Durham, 1982).

Zucca (1984) also determined the dynamic moduli of the rock in the vicinity of the SFT—C by means of *in situ* compression- and shear-wave velocity measurements. He used distributions of these velocities to estimate the deformation modulus and Poisson's ratio (± 1 std dev) as 61 ± 16 GPa and 0.28 ± 0.08, respectively.

After spent fuel was retrieved from the SFT—C, Patrick, Yow, and Axelrod (1985) conducted extensive *in situ* deformability measurements using an NX borehole jack to determine the effects of heating on the

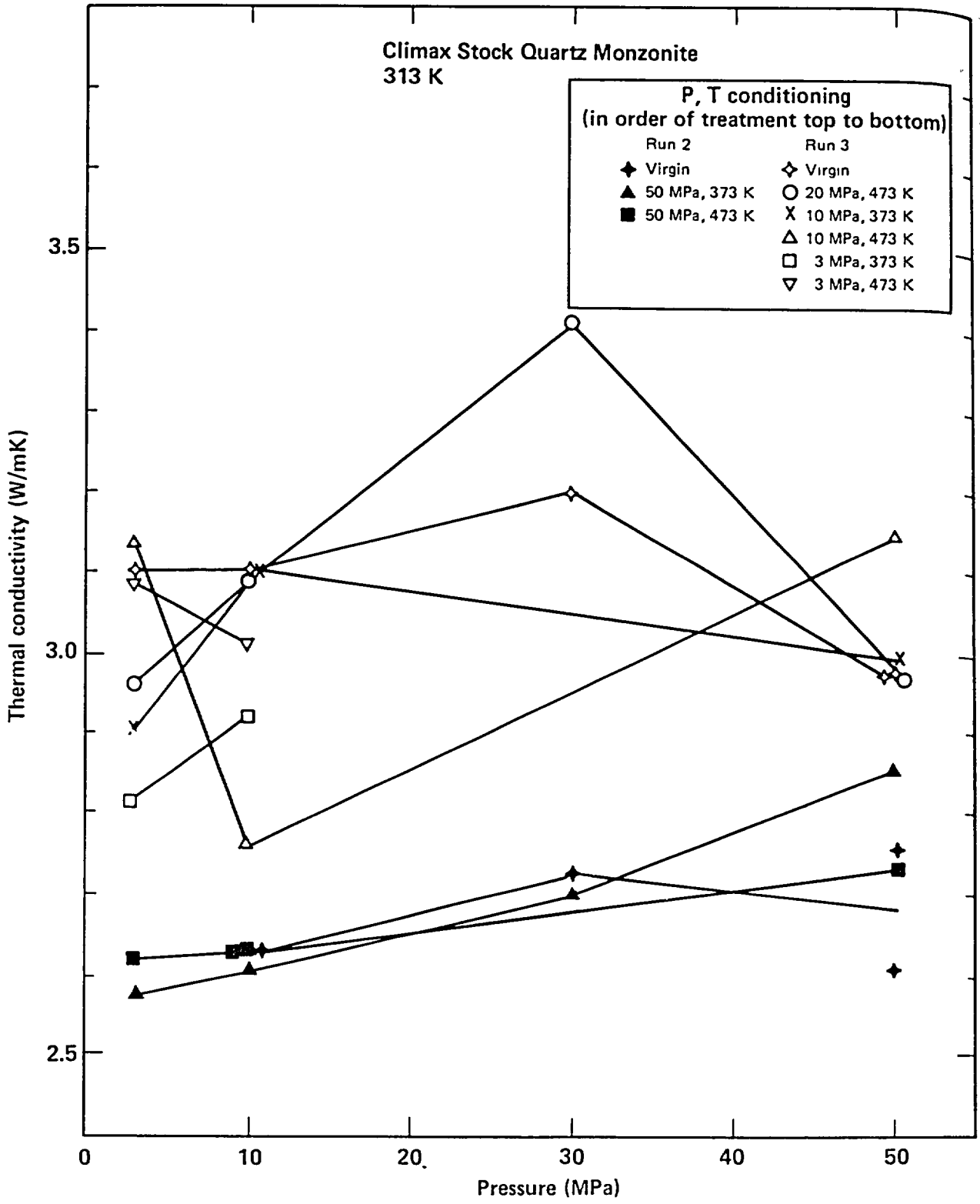

Figure 4-33. Thermal conductivity vs pressure at 313 K for Runs 2 and 3 showing a lack of effect due to thermal cycling (after Durham, 1982).

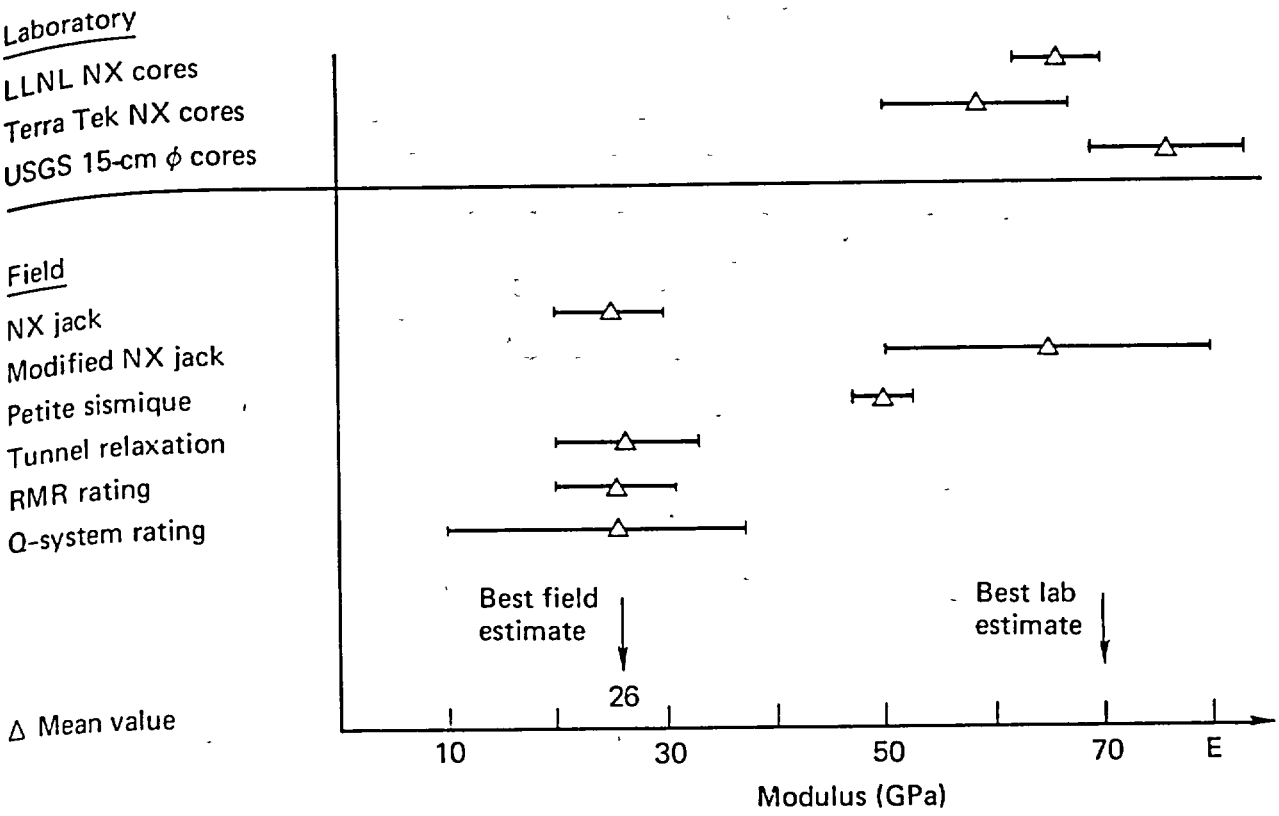

Figure 4-34. Multiple estimates of laboratory and field modulus for Climax granite (after Heuze et al., 1981).

rock mass modulus. To examine this effect, 41 preheat and 63 post-heat modulus values were compared. All these measurements were obtained from four NX (76-mm diameter) boreholes located in the pillars between the drifts of the SFT—C facility (Fig. 4-35). The preheat values were obtained by reanalyzing data from Heuze et al. (1981) to include the new scaling factor developed by Heuze and Amadei (1984). Post-heat measurements were made in the same boreholes.

In addition to heat, the following factors were found to influence the value of modulus: position within the borehole, location within the facility (borehole location), and loading direction. Linear statistical models were used to analyze the data for these effects. Table 4-14 lists the "intercept" terms associated with the statistical models developed for data from boreholes MBI07N, MBI07S, and MBI14S. Figure 4-36 provides an example of how these general equations represent the data subsets.

These intercepts represent the mean moduli observed at the pillar center. Because modulus decreases in both directions toward the ribs, the data were pooled and the locations of measurements were referenced with respect to "distance from centerline." A pooled slope of −7.00 GPa/m expresses this decrease in modulus from pillar center.

From Table 4-14, we conclude the following:

- Preheat modulus is strongly anisotropic with the vertical about 10.7 GPa less than horizontal.
- Post-heat modulus is also anisotropic, but vertical values now exceed horizontal by about 9.8 GPa.
- Heating produced substantial increases in modulus values obtained under vertical loading, probably as a result of heat-induced stress increases.
- Heating effects on the modulus under horizontal loading are equivocal.

Similar statistical models for deformation modulus were developed using data from other individual boreholes or groups of boreholes (Patrick, Axelrod, and Yow, 1985). The reader is referred to their work for further discussion of spacial and thermal effects on the nearly 250 measurements obtained at the SFT—C.

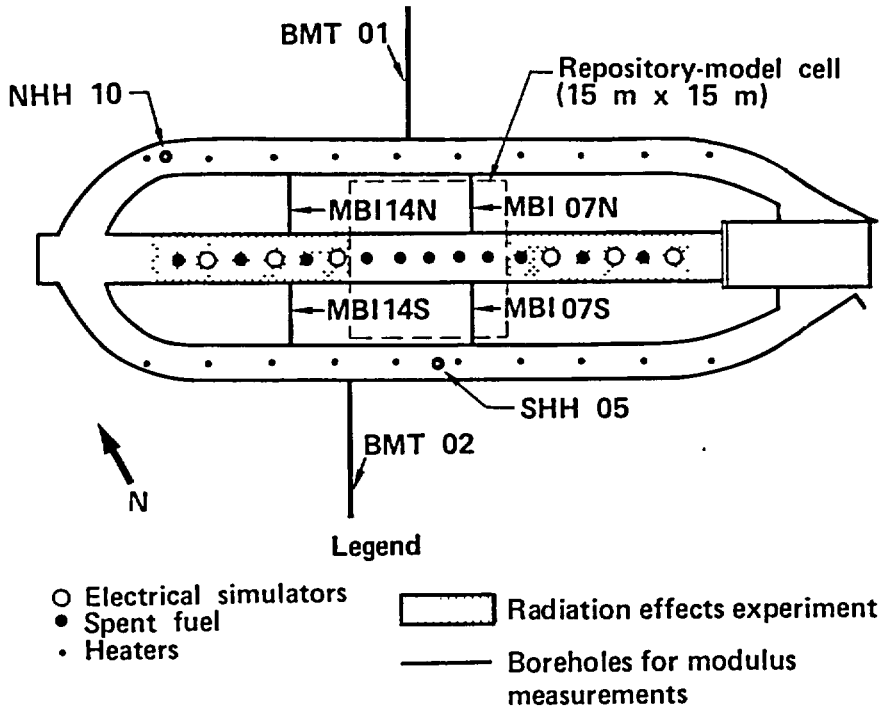

Figure 4-35. Plan view of Spent Fuel Test—Climax facility showing location of thermal sources, principal experiments, and boreholes (after Patrick, Yow, and Axelrod, 1985).

Table 4-14. Intercept coefficients calculated using a 12-term general linear model for deformation modulus, in GPa (after Patrick, Yow, and Axelrod, 1985).

	North pillar		South pillar	
Time of measurement	Vertical loading	Horizontal loading	Vertical loading	Horizontal loading
Preheating	46.5	57.2	26.3	37.0
Post-heating	62.7	52.9	54.6	44.8

4.4.4 Field Studies of Thermal Properties

Before the SFT—C was authorized, a relatively large-scale heater test was conducted at the Climax stock to determine the *in situ* thermal properties and gas permeability of the rock mass (Montan and Bradkin), 1984). The geometry of Heater Test No. 1 and its location relative to the shaft used to access the SFT—C are shown in Figs. 4-37 and 4-38. The alignment of the two heaters and instrument arrays was selected to facilitate determination of anisotropy with respect to heat transfer and permeability.

Montan and Bradkin (1984) analyzed the test thermal data by varying the thermal conductivity and diffusivity values in a model for conductive heat transfer, which treated the heaters as a set of point sources with appropriate source strengths. Based on a sensitivity study in which conductivity, diffusivity, and thermocouple location were varied, they estimate the conductivity and diffusivity values to be about 3.1 W/m·K and 1.2 mm^2/s, respectively (Fig. 4-39). Durham's (1982) comparable laboratory values of these properties are 2.75 ± 0.25 W/m·K and 1.25 ± 0.4 mm^2/s, respectively. Although Durham's mean conductivity appears to be substantially lower than the field value, Fig. 4-33 reveals that his data cluster near 2.6 W/m·K for one sample and 3.0 W/m·K for the other. Given the known heterogeneity of the CSQM and the

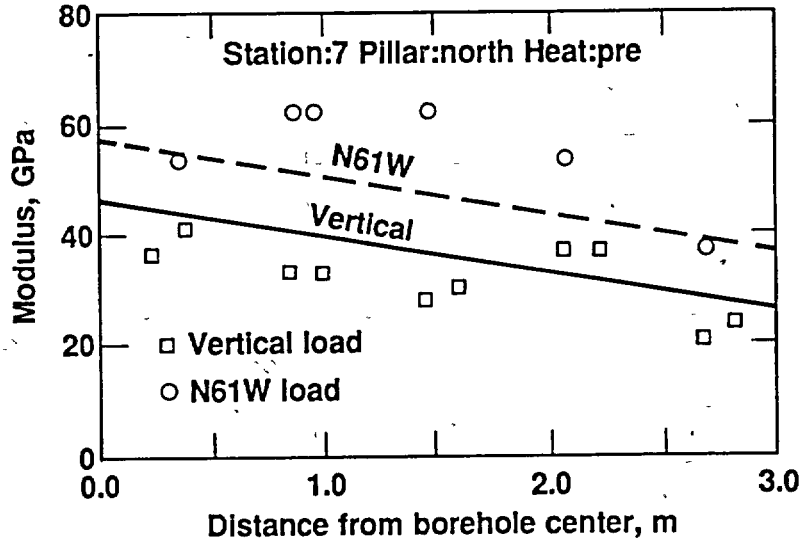

Figure 4-36. Typical example of relationship between borehole modulus value and distance from pillar center. The slope and intercepts of the lines were developed from a 12-term general linear model (after Patrick, Yow, and Axelrod, 1985).

laboratory sample size, Montan and Bradkin (1984) concluded that their *in situ* measurements are a more accurate reflection of the average rock properties.

4.4.5 Field Studies of Permeability

Gas permeability measurements were also made as an integral part of Heater Test No. 1. Permeability tests were conducted during periods of relatively stable borehole temperatures (Fig. 4-40).

Data analysis was based on Jaeger's (1956) solution for cooling a heated infinite cylinder and used Morrison's (1972) technique for "linearizing" this inherently nonlinear problem of porous flow of a compressible gas. Details of this analysis and related data reduction techniques are provided by Montan and Bradkin (1984).

Table 4-15 summarizes the average permeabilities measured during Heater Test No. 1. Included are the porosities, temperatures, and root-mean-square residuals resulting from the curve fitting. Ambient-temperature permeability was about 1 nD, decreasing to 0.2 nD at 50 °C above ambient. At higher temperatures, they reported that the permeability was too small to measure with the techniques used. Upon cooling, the permeability returned to near its initial value, implying that no permanent change occurred in this property.

4.5 Mineralogical and Petrological Studies of Climax Pretest Cores*

This section presents mineralogical and petrological data from the characterization of samples from the 17 canister core holes (CCH 1-17) by Ryerson and Qualheim (1983). These cores were obtained from just inside the perimeter of emplacement holes that were subsequently hammer-drilled to 0.61 m in diameter and loaded with either spent-fuel assemblies (hole numbers 1, 3, 5, 7–12, 14, 16) or electrical simulators (hole numbers 2, 4, 6, 13, 15, 17) (Chapter 12 and Ramspott et al., 1981). The purpose of this investigation was to provide a data base of mineralogical compositions, assemblages, and modal proportions from pretest samples to compare with a similar data base obtained from post-test samples. The post-test core samples were obtained from just outside the perimeter of the canister emplacement holes directly adjacent (along a radius) to the pretest core. This allowed us to determine whether any mineralogical changes occurred during the course of the test. The close proximity of the pre- and post-test cores also allowed us to

*Contributed by F. J. Ryerson.

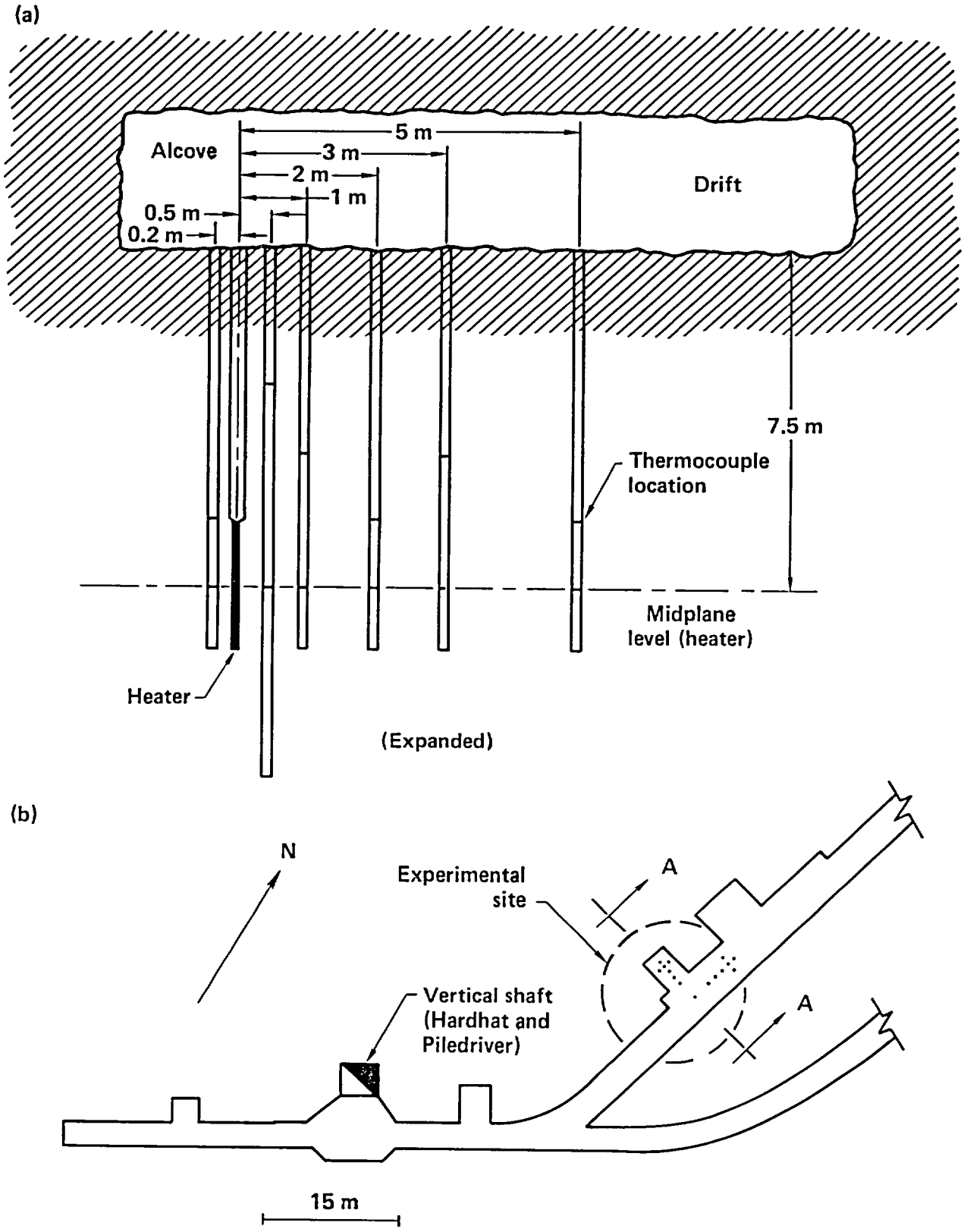

Figure 4-37. (a) Vertical cross section and (b) plot plan of Heater Test No. 1 (after Montan and Bradkin, 1984).

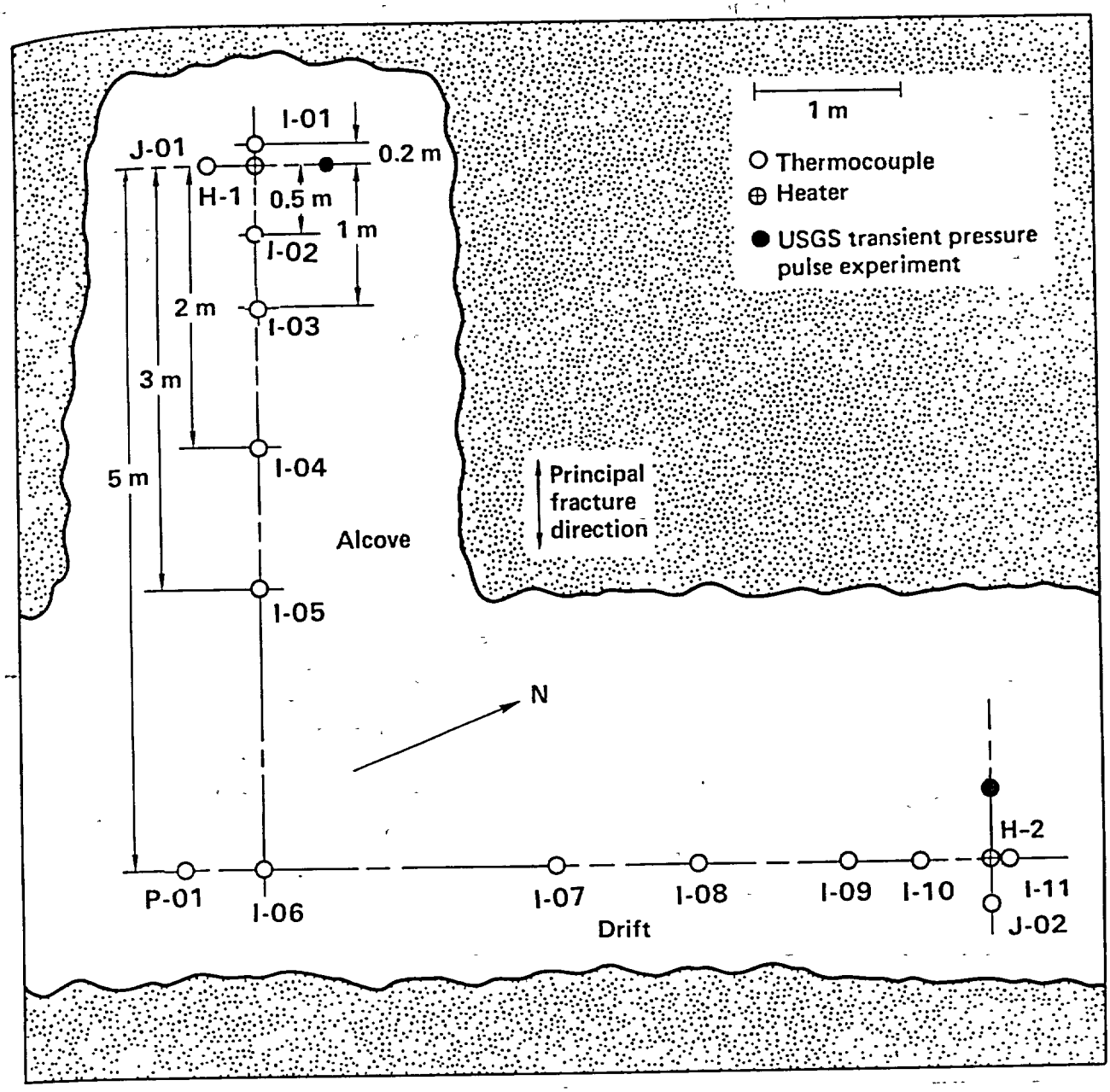

Figure 4-38. Heater test layout (after Montan and Bradkin, 1984).

assess the possible migration of materials produced as a result of the stored spent-fuel assemblies, electrical simulators, and/or the presence of alteration-generated materials along the various types of fractures in the quartz monzonite. The effects of spent-fuel assemblies vs electrical simulators were also investigated (Sec. 4.6).

4.5.1 Sample Selection

A reference line was drawn longitudinally along the recovered core to measure distances along the core and to determine the relative orientations of fractures for logging and sample selection. The location and orientation of all fractures and alteration zones in the 17 core samples were recorded at NTS. Using these core logs, 0.3- to 0.6-m sections of core were selected using the following criteria:

1. Top of core.
2. Bottom of core.

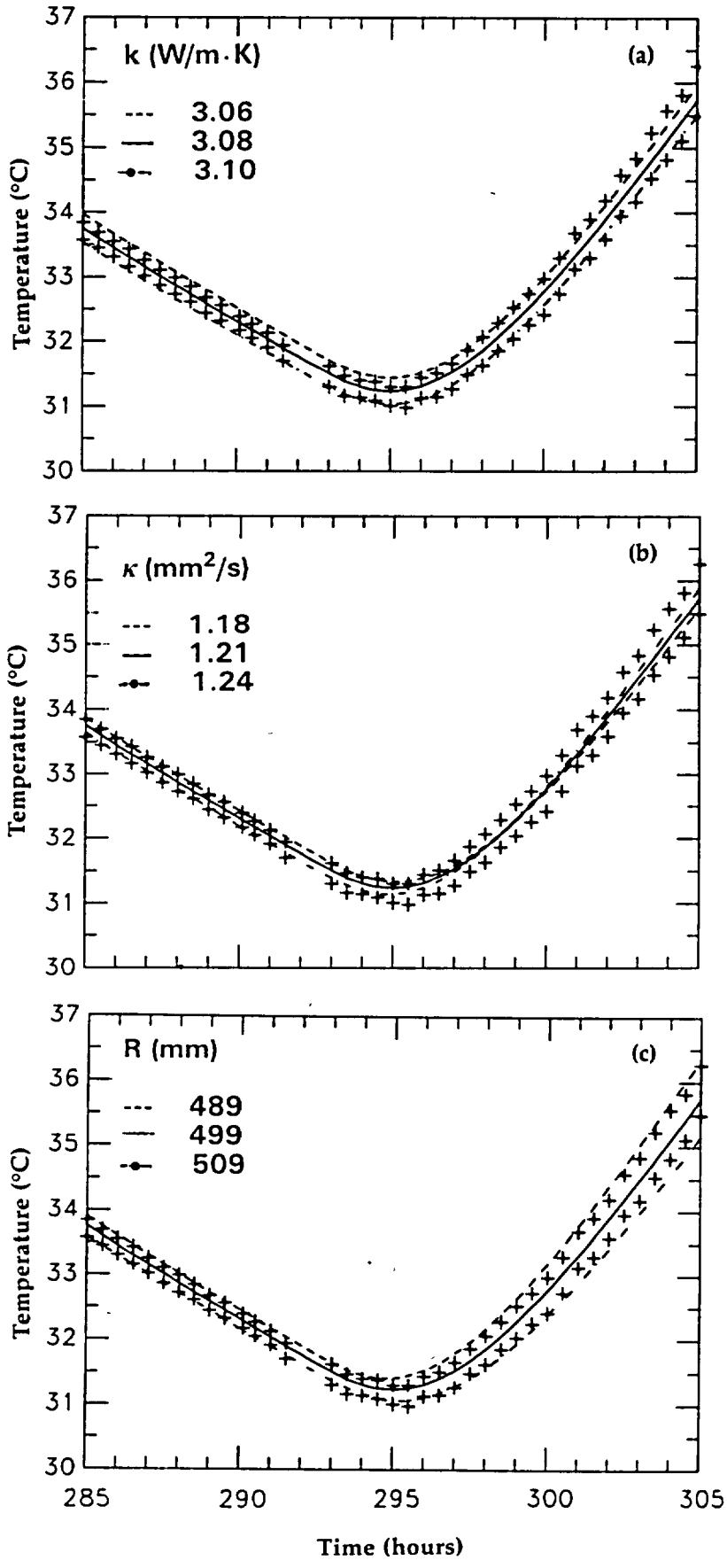

Figure 4-39a. Measured and calculated data for 20-h time span from two midplane thermocouples in hole I-02, showing sensitivity with respect to conductivity. Here κ = 1.21 mm^2/s and R = 499 mm (after Montan and Bradkin, 1984).

Figure 4-39b. Measured and calculated data for 20-h time span from two midplane thermocouples in hole I-02, showing sensitivity with respect to diffusivity. Here k = 3.08 W/m·K and R = 499 mm (after Montan and Bradkin, 1984).

Figure 4-39c. Measured and calculated data for 20-h time span from two midplane thermocouples in hole U-02 showing sensitivity with respect to distance. Here k = 3.08 W/m·K and κ = 1.21 mm^2/s (after Montan and Bradkin, 1984).

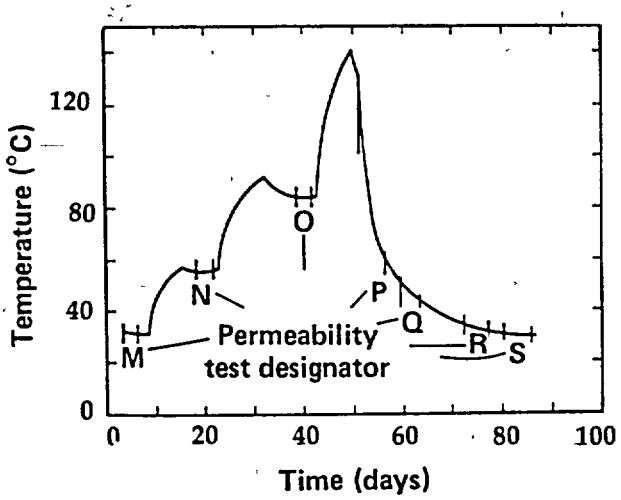

Figure 4-40. Temperature history of permeability test at 0.4 m from heater (after Montan and Bradkin, 1984).

Table 4-15. Permeability test results (see Fig. 4-40 for test sequence designator) (after Montan and Bradkin, 1984).

Borehole designator	Distance (m)[a]	M		N		O		P		Q		R		S		Perm., k, nD	Porosity, ϕ
H-2	0.0	b	b	b	b	1.09	0.0071	b	b	PF		PF		PF			
		32.4	0.016	290.9	0.049	419.3	0.082	85.0	0.261								
J-02	0.4	0.40	0.0028	0.15	0.0010	b	b	PF		PF		PF		PF		Temp., t, °C	Residual error, psi
		32.3	0.007	51.2	0.009	74.3	0.015										
I-09	0.73	0.62	0.0047	0.13	0.0103	b	b	0.070	0.0029	0.93	0.0011	1.08	00018	NI			
		32.4	0.007	43.6	0.007	59.4	0.014	70.9	0.060	46.8	0.009	36.4	0.008				
I-10	0.37	1.19	0.0031	0.24	0.0053	b	b	b	b	0.78	0.0013	1.16	0.0009	NI			
		32.4	0.007	53.4	0.017	78.4	0.062	80.8	0.043	47.7	0.008	36.6	0.009				
I-11	0.4	0.69	0.0001	0.13	0.0012	b	b	b	b	1.03	0.0025	1.27	0.0013	1.31	0.0010		
		32.3	0.009	51.3	0.018	74.1	0.067	78.8	0.077	47.5	0.008	36.5	0.007	33.7	0.009		
I-06	4.92	NI		NI		NI		NI		NI		NI		0.88	0.0013		
														28.7	0.010		
P-01	5.23	NI		NI		NI		NI		NI		NI		1.67	0.0001		
														28.2	0.015		

[a] Distance to test borehole measured from centerline of heater borehole.

[b] No meaningful result. Negative permeability and porosity calculated.

NI = not instrumented.

PF = packer failure.

3. Sample representing (as closely as possible) "fresh" unaltered rock free of fractures, i.e., "bulk sample."

4. Samples encompassing all the different types of alteration that could be described in hand specimen (it turns out that much of the sampling was redundant).

Criteria 1–3 were fulfilled for each hole; criterion 4 was only applied to holes of specific interest. The core sections were then shipped to LLNL for further selection.

After selecting the desired sample areas, a disk of the section cut perpendicular to the reference line was removed from the core. This disk was then cut in half parallel to the reference line, one piece was retained at LLNL while the other was used to prepare polished thin sections.

4.5.2 Petrography

Petrography and Modal Analysis. All thin sections were observed in plane and cross polarized, transmitted light to determine mineral assemblages and textures. Several samples were then point-counted (2000 point modes) in transmitted light to determine modal abundances. The samples selected for modal analysis were:

1. All samples from CCH-1.
2. The "bulk sample" from each hole.

Samples from group (1) were used to demonstrate the variation in modal abundances in a specific hole as a result of alteration and vein injection. The group (2) samples were chosen as "fresh" rock. Modal variations among these samples should, therefore, demonstrate the range of modal abundances in unaltered rock as a function of position along the canister drift.

Unaltered Rock. The quartz monzonite is a porphyritic rock composed of a groundmass comprising predominantly equant, subhedral grains of plagioclose, K-feldspar, quartz, and biotite ranging in size from 0.5 to 2.0 mm in diameter. Igneous accessory phases (titanite, allanite, zircon, and apatite) are below 3 vol %.

Vein Mineralogy. Two distinctly different types of mineral assemblages are found in the veins within the canister drift region. The first vein, henceforth referred to as "barren," is composed of quartz with or without pyrite. Alteration zones adjacent to the barren veins are typically thin (< 5 mm) and lack intense secondary mineralization. In particular, calcite is never found in these alteration zones.

The second vein assemblage is composed of quartz, calcite, pyrite, and apatite. It may also contain grains of muscovite, K-feldspar, and intensely altered plagioclase. The alteration zones adjacent to these "fertile" veins can be as large as 2 cm in width, and often show intense alteration.

Alteration of Plagioclase. Plagioclase from the Climax stock is almost always altered to some combination of muscovite, epidote, and calcite (Table 4-16). The most common assemblages are plagioclase and muscovite (B) and plagioclase, muscovite and calcite (C), which are found in 43% and 35% of the sample areas, respectively. The alteration phases generally have irregular outlines, although muscovite is often present as fan-shaped aggregates. The percentage of plagioclase converted in a single grain can range from 0 to 75 vol %, and the distribution of converted and unconverted plagioclase is sporadic, although greater conversion is noted near veins.

It should also be noted that the plagioclase alteration assemblages can be correlated with the vein mineral assemblage about which they are localized. Assemblages B and D (from Table 4-16) are usually found adjacent to "barren" veins, whereas assemblages C and E are found adjacent to "fertile" veins.

Alteration of Biotite. The alteration of biotite in these samples is extremely complex and makes any classification scheme quite difficult. The secondary phases found on biotite include chlorite, muscovite, epidote, titanite, rutile, calcite, and pyrite. In any particular sample, the number of phases found on biotite

Table 4-16. Mineral assemblages formed during the alteration of plagioclase (after Ryerson and Qualheim, 1983).

Assemblage designator	Principle assemblage components	No. of regions
A	Pc	10
B	Pc, Mu	55
C	Pc, Mu, Cc	45
D	Pc, Mu, Ep	8
E	Pc, Mu, Ep, Cc	11

may vary. For instance, one biotite grain may include only chlorite, whereas an adjacent grain contains chlorite and epidote. Our classification scheme is based on the maximum number of phases found on biotite rather than on the most frequent assemblage. The variability and, in some cases, large number of phases may be related to variability in the pore fluid composition during alteration and/or the variability in cation transport paths within the rocks.

A large variety of alteration assemblages is found on biotite (Table 4-17). The most common of these are (a) biotite and chlorite; (b) biotite, chlorite and epidote, and (c) chlorite, muscovite, epidote, and titanite, which are found in 23%, 20%, and 13% of the samples classified, respectively.

The alteration assemblages in Table 4-17 record a progressive loss of iron and magnesium from the biotite sites. This is first seen by the replacement of biotite by chlorite. Further depletion of iron and magnesium results in the complete disappearance of biotite, which often produces symplectic intergrowths of muscovite and chlorite that include scattered anhedral grains of epidote or titanite and/or rutile needles. Eventually, even chlorite may disappear, leaving assemblages that are predominantly muscovite. An additional feature of the biotite-free samples is the presence of calcite after biotite. The calcite commonly appears along cleavage traces in chlorite or muscovite, but may also be found as anhedral grains with these phases.

Modal Analyses. Results of modal analyses for CCH-1 samples and "bulk samples" from each of the 17 CCHs are presented in volume percent and were obtained from 2000 point modes. Percentages of key phases have been plotted against sample position in Figs. 4-41 and 4-42.

Table 4-17. Mineral assemblages formed during the alteration of biotite (after Ryerson and Qualheim, 1983).

Assemblage designator	Principle assemblage components	No. of regions
1	Bt	0
2	Bt, Chl	30
3	Bt, Chl, Mu	1
4	Bt, Chl, Ep	26
5	Bt, Chl, Tn	2
6	Bt, Chl, Mu, Ep	1
7	Bt, Chl, Ep, Tn	5
8	Bt, Chl, Mu, Tn, Ru	1
9	Bt, Chl, Mu, Ep, Tn	2
10	Bt, Chl, Ep, Tn, Ru	1
11	Bt, Chl, Mu, Ep, Tn, Ru	2
12	Chl, Mu, Tn	6
13	Chl, Ep, Tn	4
14	Chl, Mu, Ep, Tn	17
15	Chl, Mu, Tn, Cc	2
16	Chl, Mu, Tn, Ru	3
17	Chl, Mu, Ru, Cc	4
18	Chl, Ep, Tn, Ru	1
19	Chl, Mu, Ep, Tn, Cc	3
20	Chl, Mu, Ep, Tn, Ru	4
21	Chl, Mu, Ep, Ru, Cc	3
22	Chl, Mu, Tn, Ru, Cc	4
23	Chl, Mu, Ep, Tn, Ru, Cc	1
24	Mu, Tn	4
25	Mu, Ep, Tn, Cc	2

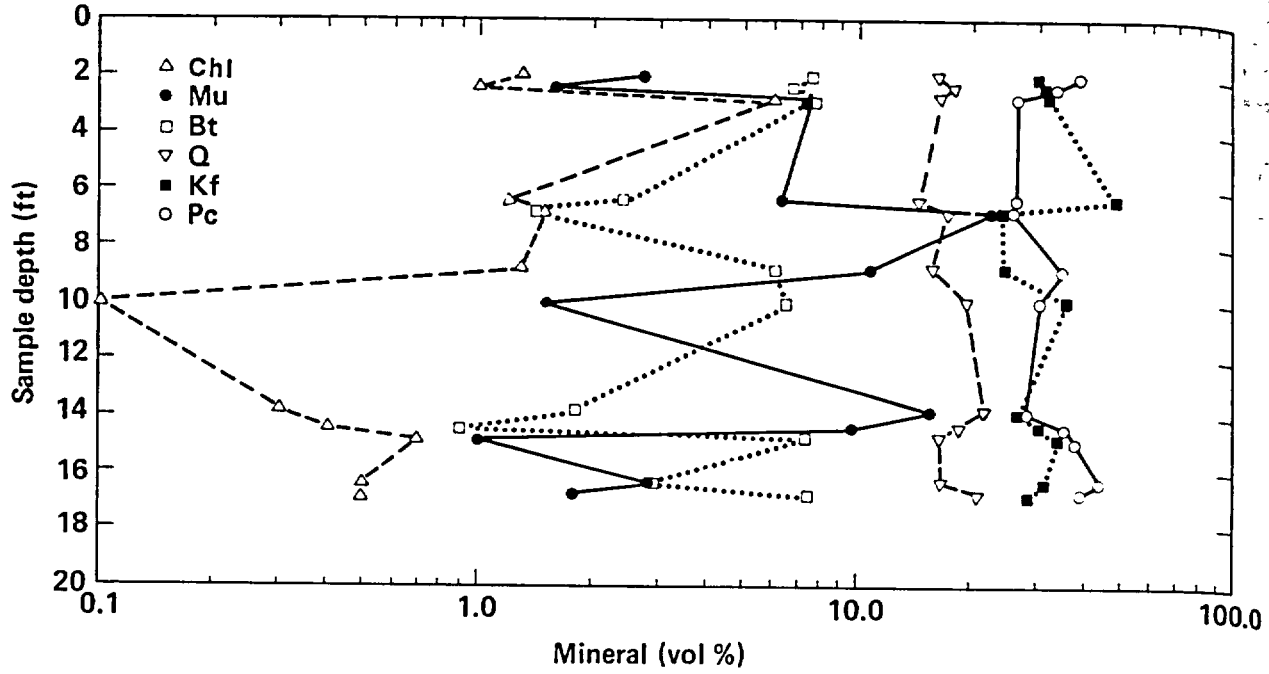

Figure 4-41. Modal abundances of major minerals from CCH1 samples plotted vs depth in sample core (after Ryerson and Qualheim, 1983).

Modal analyses for the CCH-1 were obtained from the entire thin section regardless of any sample heterogeneity. Material from veins, alteration zones, and unaltered regions was all weighted equally so that we could document sample variability on this scale. Modal percentages for the primary phases—quartz, plagioclase, and K-feldspar—are fairly constant, with average modal volumes of 17.3% ± 2.1%, 32.8% ± 5.6% and 31.2% ± 5.3%, respectively. The variation of 1 std dev for plagioclase and K-feldspar is similar in spite of the much more pronounced alteration of plagioclase. Biotite is also a primary phase, but displays a much larger percent variation than do the felsic phases. The average biotite volume is 4.9% ± 2.7%. The higher variability in biotite abundance is consistent with textural variability demonstrated earlier for biotite alteration.

Muscovite, chlorite, epidote, clinozoisite, titanite, and pyrite are present as secondary minerals. Their secondary origin is reflected in much larger variations in their modal abundance (Fig. 4-41), and results from both variabilty in alteration down CCH-1 and the presence or absence of veins that carried the hydrothermal solutions.

The modal abundances for the bulk samples are shown in Fig. 4-42. Of the primary phases, only plagioclase appears to be significantly higher in the fresh bulk samples than in the variably altered samples from CCH-1: 42.8% vs 32.8%, respectively. This is consistent with the observation that plagioclase is the only felsic phase that undergoes significant alteration.

The modal volumes of the secondary phases are as variable in the "bulk samples" as in those from CCH-1 (Fig. 4-42). However, the variation in average volumes of secondary phases in the bulk samples is less.

4.5.3 Mineral Chemistry

Microprobe Analysis. Ryerson and Qualheim (1983) obtained microprobe analyses in both automated and interactive modes by using a 2-μm × 2-μm rastered beam at 15 na sample current (measured in a Faraday cup), with an accelerating voltage of 15 kV. The totally automated analyses were undertaken to objectively determine the frequency of K-feldspar and plagioclase compositions within selected samples. In this mode, 300 analyses were obtained along a grid covering the sample surface. The interactive analysis required the operator to select specific analysis points to determine the compositions of alteration phases that are normally low in the mode.

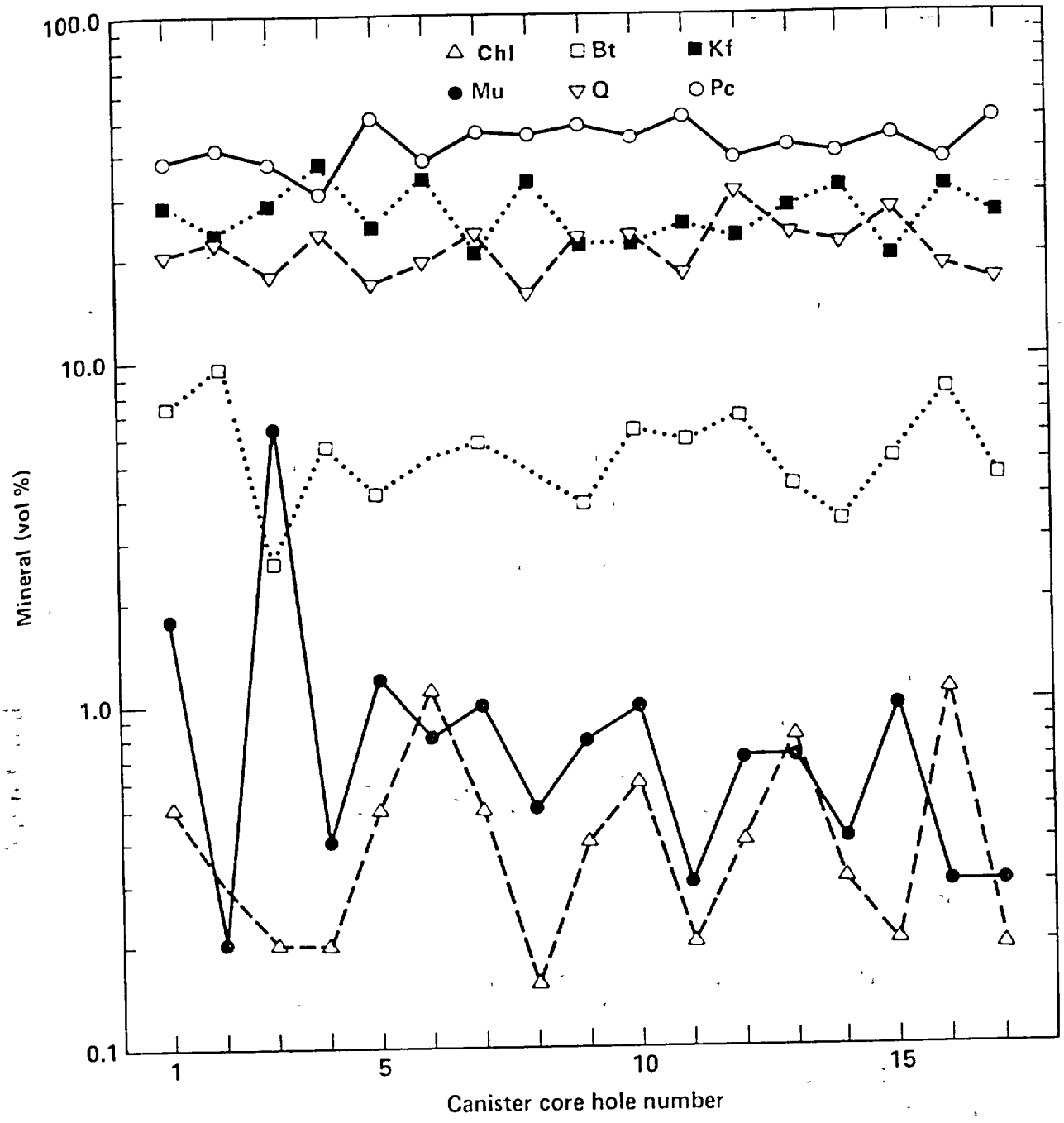

Figure 4-42. Modal abundance of major minerals from "bulk samples" plotted versus canister core hole number (after Ryerson and Qualheim, 1983).

Primary Phases. The major igneous phases are quartz, plagioclase, K-feldspar, and biotite. Analyses obtained in the interactive mode are presented in Ryerson and Qualheim (1983). In addition to interactive analysis, feldspar analyses were also obtained by automated step-scan traverses to objectively determine the extent of zoning and average feldspar compositions.

Histograms of feldspar analyses obtained from step-scan traverses indicate that the K-feldspar analyses vary between Or_{80} and Or_{98} with only occasional analyses falling at lower Or concentrations (Fig. 4-43). The average analysis is Or_{89}, and shows very little variation from sample to sample. These values agree quite well with those obtained during the interactive analyses. The K-feldspars show very little alteration,

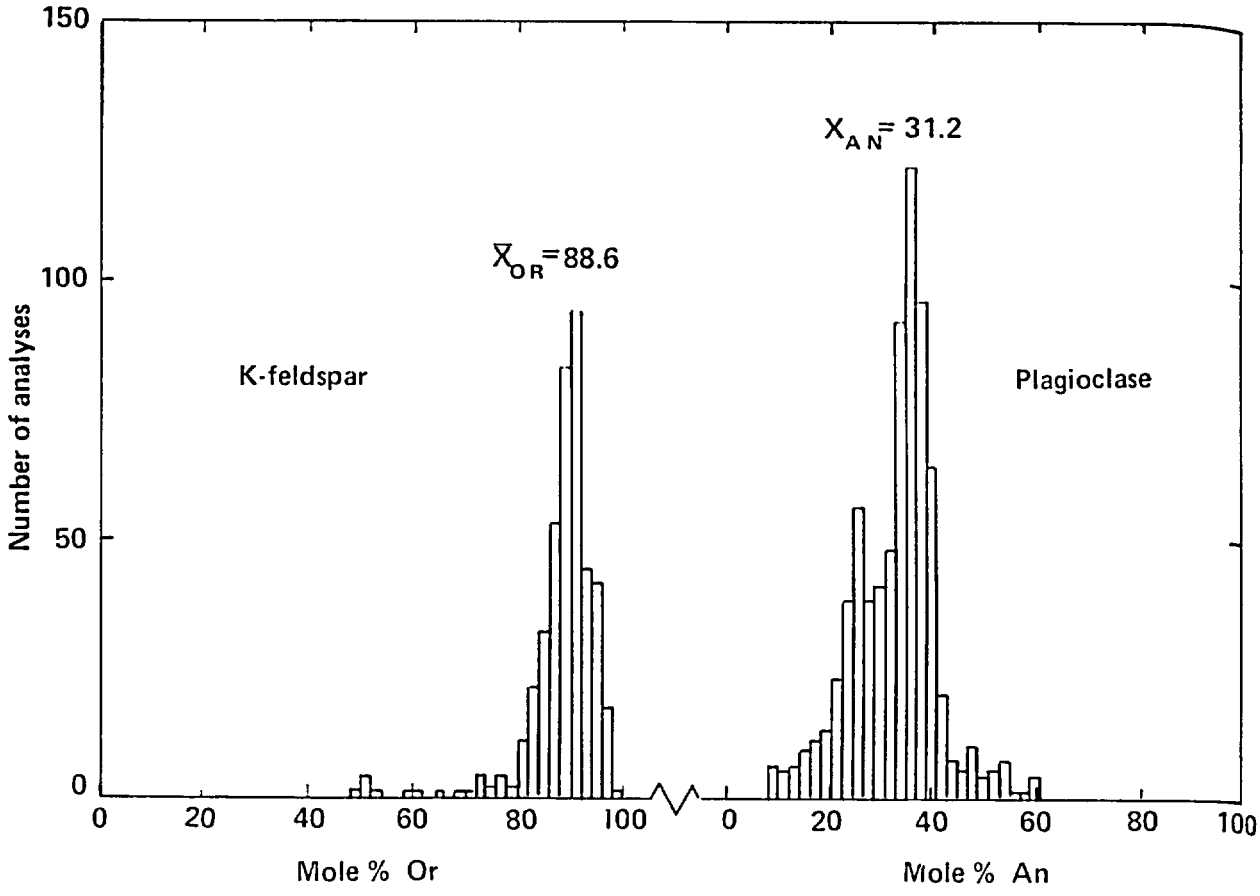

Figure 4-43. Number of feldspar analyses from "bulk" samples plotted vs feldspar composition. Analyses were obtained in step-scan mode (after Ryerson and Qualheim, 1983).

so that the variation must be due to a combination of primary igneous zoning coupled with subsolidus reequilibration.

The majority of the plagioclase compositions fall between An_{20} and An_{50}, with the average at An_{31} (Fig. 4-43). In contrast to the K-feldspar analyses, comparisons of the plagioclase analyses collected in automated and interactive analyses show an important difference. The interactive analyses focused upon plagioclase grains containing significant amounts of secondary phases. This group of analyses contains significantly more analyses in the range from An_{20} to An_0 than do those obtained in the automated step-scan traverses, indicating incongruent plagioclase alteration. The albite end member is conserved during hydrothermal alteration, while the anorthite component is preferentially dissolved and transported from the plagioclase site.

The biotite analyses can be represented by the formula

$$K[Ti_{0.2}(Fe,Mg)_{2.4}Al_{0.2}][Al_{1.2}Si_{2.8}]O_{10}(OH)_2 \quad .$$

The Mg/(Mg+Fe) ratio in these biotites lies between 0.50 and 0.68.

Secondary Phases. All data for secondary minerals were collected in an interactive mode. The muscovite compositions fall in the range approximated by the formula

$$K(Mg,Fe_{0.81}Al_{1.46})Al_{0.8}Si_{3.2}O_{10}(OH)_2\text{-}KAl_2(AlSi_3)O_{10}(OH)_2 \quad ,$$

with a range in Mg/(Mg+Fe)(atom) between 0 and 1.0. The muscovites found as pseudomorphs of biotites are generally enriched in MgO and FeO relative to those found on plagioclase. This most likely indicates

increased activities of the components on the biotite sites and also indicates that cation exchange equilibrium between plagioclase and biotite sites was not attained on even a thin-section scale during hydrothermal alteration.

Chlorite is found exclusively on biotite sites, and its composition is given by the formula $(Fe,Mg)_{4.4}Mn_{0.1\,0.2}Al_{2.6}Si_{2.7}O_{10}(OH)_2$. The range in Mg/(Mg+Fe) is between 0.42 and 0.74 and is slightly larger than the range for the primary biotite.

Mineral compositions and zoning patterns in the clinozoisite-epidote series are complex. The compositions are generally expressed by the formula $Ca_2(Al,Fe^{3+})_3Si_3O_{12}(OH)$. Generally, the "epidotes" found on biotite are more iron-rich than the "clinozoisites" found on plagioclase. The Al/(Al+Fe) in the epidotes ranges from 0.86-0.68, whereas that in the clinozoisites varies between 0.99 and 0.79.

For all practical purposes, the composition of pyrite can be assumed as FeS_2 and the composition of titanite as $CaTiSiO_5$. The calcite composition is given by the formula $Ca_{0.98}Mg_{0.01}Fe_{0.01}CO_3$.

4.5.4 Summary

The data presented here summarize documentation of the chemical, petrographic, and modal variations in core samples from the canister drift of the SFT—C and will serve as a data base for comparison with post-test samples (Ryerson and Qualheim, 1983). On a thin-section scale (3 × 5 mm), all of these properties vary significantly as a result of both igneous processes and hydrothermal alteration localized along fractures.

Variations due to primary igneous processes include zonation in plagioclase and K-feldspar within a particular section. The range and frequency of feldspar compositions have been documented through the use of an automated step-scanning procedure on an electron microprobe. Modal variations are primarily caused by either the presence or absence of quartz and K-feldspar phenocrysts.

Features due to hydrothermal alteration are highly variable both within a particular section as well as between samples. Alteration zones up to 2 cm wide are localized along veins. The actual assemblages of secondary phases can be quite variable from sample to sample and from grain to grain of primary mineral phases. The compositions of some secondary phases (muscovite and epidote) can vary between different primary-phase reaction sites, documenting gradients in chemical potentials of these components during hydrothermal alteration. The alteration assemblies also demonstrate that CO_2, S, and H_2O were added to the rock during hydrothermal alteration. The source of CO_2 is presumably the decarbonation of the carbonate country rock during the emplacement of the stock.

4.6 Radiation and Thermal Effects*

One of the principal objectives of the SFT—C was to evaluate the relative effects upon the rock of heat alone and in combination with ionizing radiation. To determine these effects, we studied changes in mechanical properties, microfracture development, and alteration of the mineralogy and petrology of the rock.

4.6.1 Effects on Mechanical Properties

Following Durham's (1982) discovery of an apparent degrading effect of gamma irradiation upon the mechanical strength and deformability of CSQM, additional laboratory work was undertaken to determine the validity of the effect and some of its details. The latter study used a statistical design and highly accurate and precise measuring techniques to provide a more definitive, less questionable result. Specific changes included:

- Rebuilding the test apparatus.
- Increasing the number of samples tested.
- Including samples of Westerly granite in the test matrix to provide a continuous calibration of the apparatus.

Experiment Design. For this experiment, a newly fabricated testing system consisted of a 100-ton reaction frame, a 50-ton hydraulic ram, redundant load cells above and below the sample, upper and lower platens between the load cells and the sample, and hardened steel caps between the load cells and the

*Contributed by W. B Durham, F. J. Ryerson, and W. C. Patrick.

frame (above) and ram (below). The lower platen included a hemispherical seal to improve column alignment. Shims of 0.01-mm-thick aluminum foil were used between the sample ends and the platens.

Sample material was obtained from borehole ISS-9 (Sec. 4.3). Of the 66 CSQM samples tested, 60 came from the 8.75- to 10.18-m interval and 6 came from the 16.70- to 16.89-m interval. The Westerly granite samples came from a single slab. Test cylinders 25.4 mm in diameter by 130 mm long were cored from the source rock and were cut to provide two matched 65-mm-long samples. With two exceptions, finished lengths were 63.50 ± 0.03 mm, and ends were parallel within 0.02 mm.

Statistical design techniques were used to establish the required sample size to detect a 10% change in strength and to establish the need for a "matched pair" analysis as used here. Both the selection of which member of a pair would be irradiated and the order of testing following treatment used a randomization technique (Durham et al., 1985).

Experimental Procedure. Gamma irradiation was accomplished in the ^{60}Co irradiation pool of the LLNL Standards and Calibration Laboratory. Calibration of the cell immediately following treatment of the samples showed the dose rate to be about 9.7 Gy/s (970 rad/s). Over the 11-day exposure, the samples received total doses of 9 ± 1 MGy (0.9×10^9 rad).

Based on a randomization procedure, the operator tested each specimen by loading it rapidly to 100 MPa and then loading it at a controlled strain rate of 1.5 to 4.0×10^{-6}/s until the rock failed. Data aquired by the HP3497A data aquisition system allowed us to calculate maximum stress, Young's modulus at strains above 0.1%, and Poisson's ratio at 0.1% longitudinal strain. Various diagnostic plots were also prepared.

Results. For the CSQM, Durham et al. (1985) found no significant change in the unconfined compressive strength. The calculated Student's t value of -0.864 indicates that differences between the unirradiated and irradiated values were not significantly different from zero. The experiment had a 90% chance of detecting a difference of 14 MPa at the 5% confidence level. In addition, no effect was found on the Young's modulus or Poisson's ratio. A Student's t value of -0.572 was calculated for the Westerly granite control samples. Here, too, there was no significant gamma irradiation effect.

4.6.2 Microfracture Analysis of Laboratory-Irradiated Climax Core

In addition, we examined the possible causes of the previously observed weakening effect in CSQM following heavy dosages of gamma irradiation. As noted above, Durham (1982) first detected this weakening effect, which has not been verified by additional testing (Durham et. al., 1985) nor, to our knowledge, has a similar phenomenon been observed in other silicate rocks. Our study was based on scanning electron microscope (SEM) examination of polished sections of Climax core. For the study, 10 identical test cores 63 mm long by 25 mm in diameter were prepared for unconfined compressive loading. Before testing, five of the cores were given a gamma ray dosage of about 10 MGy from a ^{60}Co source over a 9-day period, approximately the same irradiation treatment given in the study by Durham (1982). All 10 samples were then compressively loaded to 150 MPa (approximately 90% of the expected strength of irradiated samples), held at that stress level for 60 seconds, then unloaded and prepared for SEM examination (Beiriger and Durham, 1984).

Microfractures in rocks stand out rather clearly in an SEM image, and what Beiriger and Durham (1984) were hoping to observe was a difference in the crack structure between the two groups of test specimens. To be as quantitative and unbiased as reasonably possible, they used a crack measurement technique developed recently for measuring borehole wall damage induced by hammer-drilling at the SFT—C (Weed and Durham, 1983). The results are shown broken down by sample in Table 4-18 and by irradiation treatment in Table 4-19.

The most notable characteristic of the crack data in Tables 4-18 and 4-19 is the scatter. There is no detectable correlation between the measured crack parameters (areal density and average length) and irradiation treatment in stressed rock. In fact, based on a series of measurements on a single section of unirradiated, unstressed rock (Table 4-19), we have only weakly detected an effect on crack structure induced by the loading treatment itself.

These results are presented and discussed in greater detail by Beiriger and Durham (1984). Their principal conclusions were as follows:

1. The crack structure of Climax granite is highly heterogeneous on the scale of laboratory sections (0.1 to 10 mm). The underlying cause may be that grain sizes in the rock are heterogeneous, ranging in scale from 0.1 to 100 mm.

Table 4-18. Crack statistics by sample (after Beiriger and Durham, 1984).

Sample[a]	Number of cracks counted	Areal number density (mm^{-2})	Average length (μm)	Areal length density (mm/mm^2)
	18	85	52	4.41
2 (no γ)	31	177	14	2.47
	38	120	30	3.59
	45	157	30	4.70
3 (γ)	66	206	14	2.79
	20	81	32	2.64
	23	109	36	3.98
4 (no γ)	48	171	15	2.54
	51	182	26	4.67
	22	90	41	3.66
5 (γ)	49	124	14	1.74
	22	75	33	2.46
	12	57	35	1.99
6 (no γ)	64	214	12	2.47
	15	71	44	3.12
	25	119	36	4.27
7 (γ)	62	158	13	2.07
	30	107	38	4.01
	49	175	28	4.89
8 (no γ)	45	117	15	1.78
	14	67	29	1.95
	24	114	34	3.88
9 (γ)	46	131	16	2.15
	47	167	23	3.78
	18	86	30	2.53
10 (no γ)	71	285	16	4.44
	35	125	33	4.06

[a] Results are given for three independent traces across each sample, a middle scan, and two outer scans. The second number of each group gives the statistics for the middle scan. A subtle difference in SEM operating conditions existed for the middle scan.

2. Our microstructural measurements reveal no evidence that gamma irradiation lowers the compressive strength of the rock, although the resolution of the measurements is poor.

3. Improvements in the signal-to-noise ratio of the crack measurements in future experiments are not practical. Signal (i.e., damage) does not seem to be very sensitive to unconfined stress, except within a few percent of the failure stress, making a target stress difficult to attain in a rock with such a large variance in its fracture strength. Noise can be decreased only by increasing the quantity of measured values.

Table 4-19. Crack statistics by irradiation treatment (after Beiriger and Durham, 1984).

Sample treatment	Middle trace				Outer traces			
	Number counted	Areal density (mm^{-2})	Average length, $\bar{L}$ (μm)	$\overline{L/Area}$ (mm/mm^2)	Number counted	Areal density (mm^{-2})	$\bar{L}$ (μm)	$\overline{L/Area}$ (mm/mm^2)
No γ	223	149±153[a]	14±12	2.11±2.31	235	115±105	32±30	3.64±3.42
γ	259	190±178	14±13	2.71±2.64	273	113±100	32±33	3.61±3.15
Untreated, unstressed					54	91±91	36±47	3.24±3.16

[a] One standard deviation.

4.6.3 Effects on Mineralogy and Petrology

Mineralogical and petrological studies of post-test cores were conducted to determine and evaluate changes in these characteristics that may have resulted from the three-year episode of heating and irradiation (Ryerson and Beiriger, 1985). Data obtained from adjacent pretest samples provided the baseline for these comparisons (Sec. 4.5).

Sample Selection and Preparation. Post-test investigations focused on samples obtained from canister emplacement holes (CEH) 1, 3, 4, and 9. Although CEH01, 03, and 09 contained spent-fuel assemblies, CEH04 had housed an electrical simulator during the SFT—C. Furthermore, CEH01 contained water (Chapter 18); therefore, it provided the greatest opportunity for both hydrothermal and radiolytic effects to occur.

Samples were prepared from 140-mm-diameter post-test cores obtained by drilling longitudinally along the CEHs at such a radial distance that the wall of the hole was included in the sample. The azimuthal position was chosen to provide a sample adjacent to the pretest sample. The steps in the sampling are displayed in Fig. 4-44.

Analytical Techniques. Based on the results of pretest investigations, the post-test petrographic analyses were revised to eliminate counting of any phases greater than 4 mm in diameter. This was done to reduce the variability that results from the presence of phenocrysts, and was justified by the observation that natural hydrothermal alteration was concentrated in the groundmass rather than in phenocrysts. To permit a direct comparison between pre- and post-test petrology, Ryerson and Beiriger (1985) reanalyzed 13 CCH samples using this revised technique (Table 4-20). Microprobe analyses were conducted in the same manner as for pretest samples (Sec. 4.5).

Post-Test Results. The appearance of new phases in the post-test samples was the principal basis for detecting hydration and dehydration reactions and precipitation of new phases from solution. Most cation exchange processes were anticipated to be very slow at SFT—C conditions but could be detected as changes in mineral chemistry.

The post-test petrology detected no new phases in the samples studied. Furthermore, the identified alteration textures present in the post-test samples were identical to those identified in the pretest studies.

Although no penetrating chemical alteration was observed, we examined a film of fine-grained material that was apparently deposited on the surface of post-test core from CEH01. Since the phases identified by x-ray diffraction are the principal mineral constituents of the CSQM, Ryerson and Beiriger (1985) concluded that the film was simply rock flour from drilling. However, based on an earlier study of Climax groundwater chemistry (Isherwood et al., 1982), the possibility remains that some of the calcite identified was a chemical precipitate.

Modal analyses of the post-test samples are displayed in Table 4-21. Using Student's t test, they found no statistically significant difference between the pre- and post-test samples. Significant modal variations were found to exist between samples taken at a particular depth, but these variations did not display any particular trend with radial distance (Fig. 4-45).

Tables 4-22 and 4-23 display the mineral chemistry data of primary feldspar phases for pre- and post-test samples, respectively. There are no intra- or interhole variations in the feldspars, and no statistically significant changes in composition were observed. Biotite analyses show similar results, with the post-test compositions lying entirely within the range of the pretest analyses.

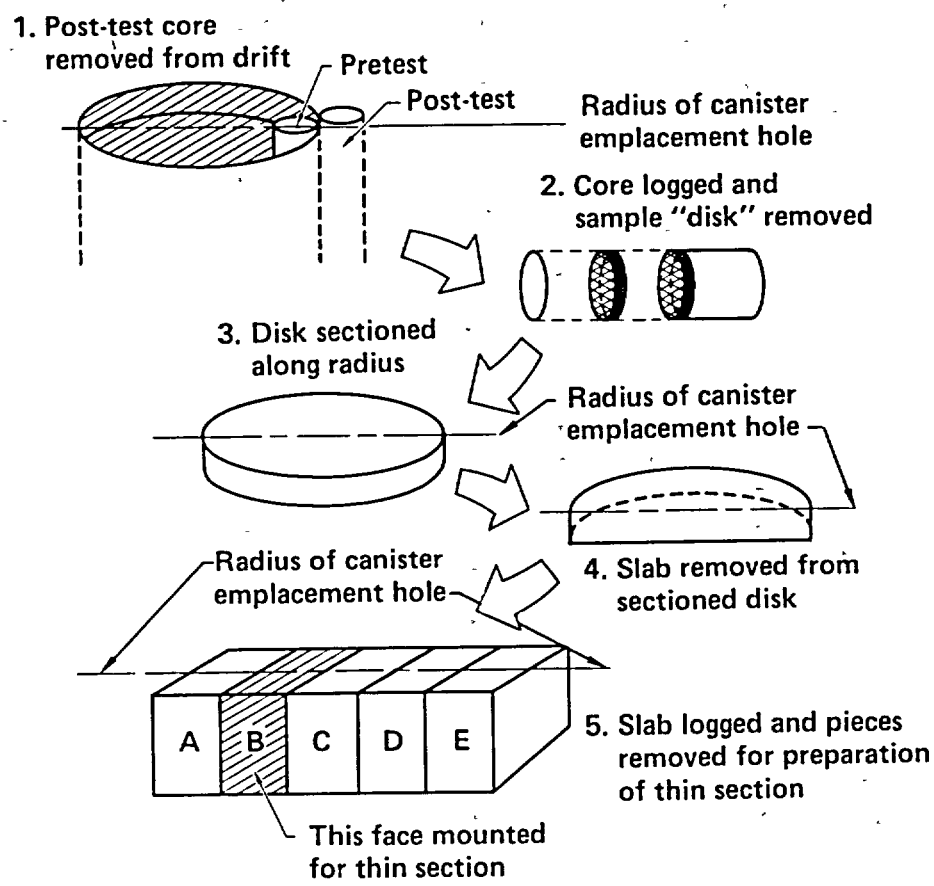

Figure 4-44. Location of post-test core samples with respect to the canister emplacement hole. Sample A is closest to the canister, and all samples are taken along a radius of the canister emplacement hole (after Ryerson and Beiriger, 1985).

Table 4-20. Modal distribution (vol %)[a] of pretest samples (after Ryerson and Beiriger, 1985).[b]

CCH Sample	Plag	Ksp	Q	Bt	Mu	Ch1	Czo+Ep	Ti	Ru	Mt	Py	ACC[c]
1	49.2	21.1	18.9	8.3	0.4	0.9	0.1	0.2	0	0.5	0.4	0
2	49.6	18.0	17.6	12.3	0.2	0.7	0.2	0	0	0.7	0.6	0.1
3	44.9	24.7	21.9	4.5	0.3	1.0	0.7	0.4	0	0.1	1.3	0.2
5	47.1	20.6	23.9	3.9	0.3	1.1	0.3	0.3	0	0	2.5	0
6	50.5	20.5	20.7	5.2	0.1	1.2	0.1	0.4	0	0.2	1.1	0
7	44.1	21.2	23.7	4.7	0.6	1.8	0.6	0.7	0	0.6	1.8	0.2
8	40.9	27.4	23.4	5.0	0	1.4	0.1	0.4	0	0	1.4	0
10	52.7	18.7	22.1	3.8	0	1.0	0.5	0	0	0	1.2	0
11	52.0	23.2	17.9	4.1	0.4	0.9	0.2	0.7	0	0	0.5	0.1
13	50.5	21.6	19.2	5.3	0	1.9	0	0.6	0	0.7	0.2	0
14	49.5	28.4	14.7	2.7	0.1	0.9	0.1	0.3	0	0	3.3	0
16	42.3	22.1	22.5	7.4	0.1	1.8	0.5	1.3	0	0.5	1.5	0
17	52.8	15.5	17.3	9.7	0.4	1.8	0	1.2	0	1.0	0.3	0
Avg	48.2	21.8	20.3	5.9	0.2	1.3	0.3	0.9	0	0.3	1.2	0.2
S.D.	4 0	3.6	2.9	2.7	0.2	0 4	0.2	1.6	0	0.3	0.9	0.5

[a] Phenocrysts greater than 4 mm in diameter were not counted.

[b] Samples represent "fresh" material without linear features, i.e., veins, alteration, etc.

[c] Allanite, apatite and zircon.

Table 4-21. Modal distribution (vol %)[a] of post-test samples (after Ryerson and Beirger, 1985).

CCH Sample	Plag	Ksp	Q	Bt	Mu	Chl	Czo-Ep	Ti	Ru	Mt	Py	ACC[b]
1-2.6A	48.2	17.8	21.0	3.2	4.9	1.3	1.6	0.8	0.1	0.1	1.0	0
1-2.6B	49.2	17.5	21.5	5.3	1.4	1.2	2.8	0.8	0	0	0.3	0
1-2.6C	52.2	19.4	18.4	2.9	1.2	2.4	2.6	0.2	0	0.6	0.1	0
1-2.6D	56.4	19.1	16.0	4.1	0.9	1.0	1.0	0.2	0.1	0.5	0.7	0
1-2.6E	55.2	17.5	16.0	4.3	1.2	1.6	2.5	0.7	0.1	0.7	0.1	0.1
Avg.	52.2	18.3	18.6	4.0	1.9	1.5	2.1	0.5	0.1	0.4	0.4	0
S.D.	3.6	0.9	2.6	1.0	1.7	0.5	0.8	0.3	0.1	0.3	0.4	0
1-15.0A	48.7	19.8	19.3	8.3	0.2	0.9	1.2	0.6	0	0.2	0.7	0.1
1-15.0B	54.4	17.4	15.3	9.2	0.3	1.5	0.6	0.3	0	0	0.9	0.1
1-15.0C	55.9	18.0	17.9	3.9	0.3	1.1	0.9	1.0	0	0	1.0	0
1-15.0D	55.5	18.0	15.5	6.8	0.7	1.6	0.7	0.5	0.2	0	0.4	0.1
1-15.0E	58.1	19.4	16.6	2.7	0.1	1.3	0.5	0.5	0	0.1	0.6	0.1
Avg.	54.5	18.5	16.9	6.2	0.3	1.3	0.8	0.6	0	0.1	0.7	0.1
S.D.	3.5	1.0	1.7	2.8	0.2	0.3	0.3	0.3	0	0.1	0.2	0.0
9-9.9A	48.3	18.2	21.9	8.7	0	1.2	0.7	0.4	0	0.4	0.1	0.1
9-9.9B	47.1	19.2	19.9	7.2	0.4	2.5	2.1	0.5	0.1	0.3	0.7	0
9-9.9C	50.4	17.1	22.9	3.2	0.6	1.4	1.8	0.8	0.5	0	1.3	0
9-9.9D	45.5	23.0	21.6	1.9	1.1	1.4	2.1	0.9	0	2.0	0.5	0
9-9.9E	53.4	18.3	17.7	3.9	0.3	1.7	2.5	0.6	0	1.3	0.3	0
Avg.	48.9	19.2	20.8	5.0	0.5	1.6	1.8	0.6	0.1	0.8	0.6	0
S.D.	3.1	2.3	2.0	2.9	0.4	0.5	0.7	0.2	0.2	0.8	0.5	0
Avg.[c]	51.6	18.5	18.5	4.3	0.4	1.4	1.1	0.6	0	0.1	0.6	0
S.D.	2.8	0.5	2.0	1.4	1.1	0.2	0.9	0.1	0.1	0.5	0.2	0.1

[a] Phenocryst greater than 4 mm in diameter were not counted.

[b] Allanite, apatite and zircon.

[c] All post-test data.

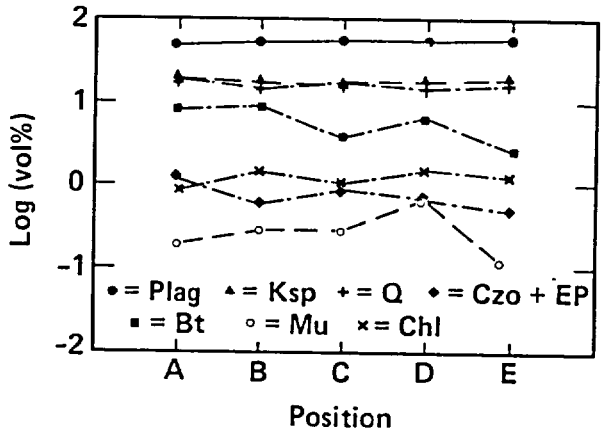

Figure 4-45. Modal data for CCH1-15.0 PT, showing vol% of mineral vs position with respect to the CEH (after Ryerson and Beiriger, 1985).

Table 4-22. Microprobe analyses of pretest feldspars. Numbers in parentheses are sample population sizes (after Ryerson and Beiriger, 1985).

Hole #	1	5	6	7	8	6	7	3	4	2	1	3	8
Depth	16.75	10.05	8.3	10.3	9.8	13.3	9.15	9.4	3.1	7.6	14.8	4.1	9.3
Plag[a]	33.03	31.63	31.19	31.94	31.79	33.19	33.17	32.45	30.17	38.53	31.24	34.04	34.40
S.D.	8.63	6.40	6.27	6.97	6.07	6.04	7.97	7.91	9.21	9.17	8.15	6.81	11.35
	(95)	(108)	(24)	(95)	(55)	(93)	(95)	(26)	(17)	(108)	(56)	(119)	(103)
K-feld[b]	90.71	85.65	87.97	89.02	80.92	88.74	88.88	88.62	86.22	87.73	88.93	89.15	86.70
S.D.	2.85	14.35	8.56	7.74	18.67	5.77	11.48	4.45	7.33	9.17	6.16	6.81	13.77

Average of all pretest analyses
Plagioclase[a] 32.61 ± 2.11
K-feldspar[b] 89.05 ± 2.85

[a] Mol% anorthite.
[b] Mol% K-feldspar.

Table 4-23. Microprobe analyses of post-test feldspars. Numbers in parentheses are sample population sizes (after Ryerson and Beiriger, 1985).

Hole No.	1	1	1	1	1	1	1	1	1	1	9	9	9	9	9
Depth(m)	7.25	7.25	7.25	7.25	7.25	17.0	17.0	17.0	17.0	17.0	9.9	9.9	9.9	9.9	9.9
Position	A	B	C	D	E	A	B	C	D	E	A	B	C	D	E
Plag[a]	33.11	30.59	30.64	32.13	33.09	30.83	32.45	31.93	32.14	32.29	34.92	33.74	30.93	29.62	32.74
S.D.	5.76	6.68	7.07	9.50	7.58	7.06	6.12	8.52	6.58	6.45	10.95	9.13	7.84	7.97	8.38
	(93)	(62)	(64)	(107)	(106)	(63)	(102)	(68)	(93)	(97)	(84)	(95)	(63)	(64)	(106)
K-feld[b]	86.85	87.12	90.39	84.52	88.67	89.91	89.61	91.63	86.40	87.45	86.55	89.28	88.08	89.82	89.32
S.D.	18.29	17.58	11.46	21.41	10.21	11.70	10.08	4.02	9.74	13.96	13.72	9.17	12.28	6.67	4.33

Average of all post-test samples
Plagioclase[a] 31.87 ± 1.44
K-feldspar[b] 89.8 ± 2.2

[a] Mol% anorthite.
[b] Mol% K-feldspar.

Analyses of the alteration phases confirm the lack of heating and irradiation effects on the CSQM. As displayed in Fig. 4-46(a)–(c), the post-test compositions of the alteration phases fall within the ranges of compositions observed in the pretest samples.

Conclusions. Since no mineralogical or petrological changes were observed for any samples, it follows that there was no significant difference between the effects of heat alone or heat in combination with ionizing radiation. Although this is an encouraging result for considering crystalline rocks for a full-scale repository, the limited time and range of conditions studied here must be recognized.

4.6.4 Physical and Chemical Changes Due to Heating

Beiriger et al. (1985) studied cores obtained from nearby auxiliary heaters at the SFT—C to evaluate possible changes in the microfracture characteristics and mineralogy of the CSQM.

Sample Selection and Preparation. To conduct this study, they obtained samples from nearby heaters designated NHH10 and SHH05. Pretest samples were obtained from the core retrieved to produce the heater boreholes. Post-test samples were obtained by drilling a 150-mm-diameter borehole tangent to each heater borehole and a parallel 76-mm-diameter borehole 0.76 m from each heater borehole. Maximum

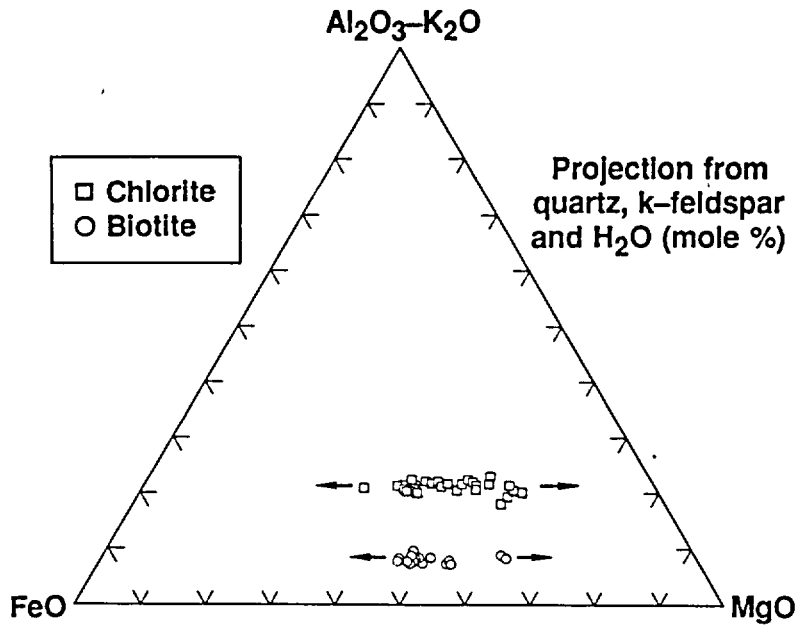

Figure 4-46a. Compositions of post-test chlorites and biotites projected from quartz, muscovite, and water. The symbols give post-test data; the range of pre-test data is shown by the arrows (after Ryerson and Beiriger, 1985).

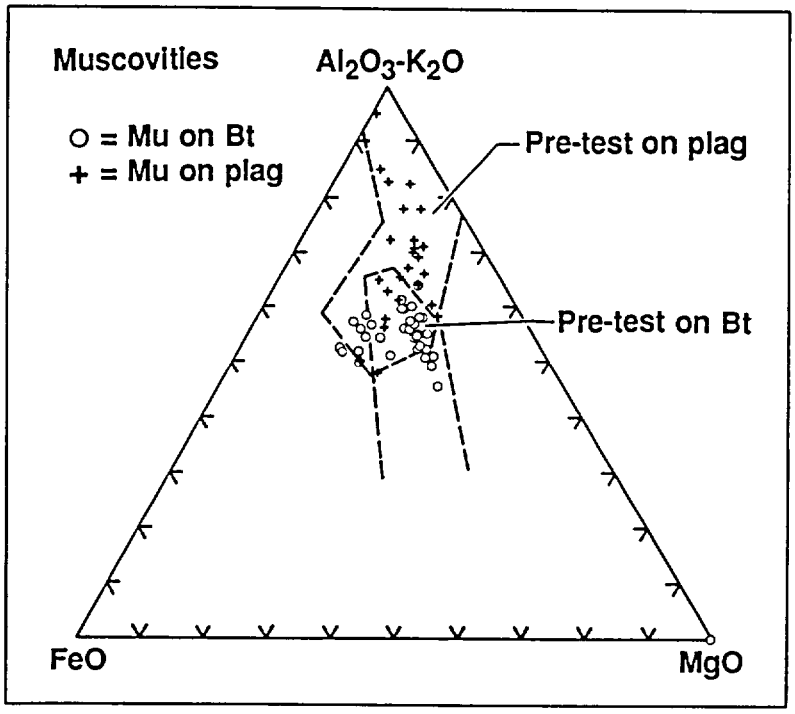

Figure 4-46b. Compositions of post-test muscovites projected from quartz and water. The open circle (o) represents muscovite found on biotite, and the plus (+) is muscovite found on plagioclase. The symbols give post-test data; the range of pre-test data is shown by the two outlined fields (after Ryerson and Beiriger, 1985).

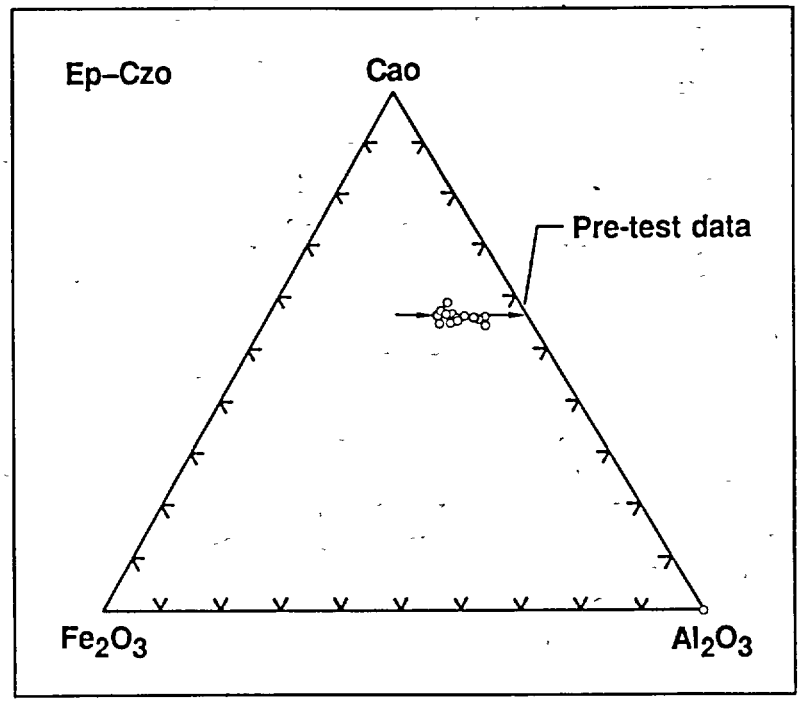

Figure 4-46c. **Compositions of post-test epidotes and clinozoisites projected from quartz and water. The symbols give post-test data; the range of pre-test data is shown by the arrows (after Ryerson and Beiriger, 1985).**

temperatures in these two positions were estimated to be near 350 and 80°C, respectively. The sampling depth was at the midheight of the heater.

Samples were prepared using a strict regimen similar to that described in Sec. 4.6.3. Facing pairs of sections were prepared for the SEM and optical microscopy studies. Crack counting techniques were as described by Durham et al. (1984), and included preselection of areas to be scanned to avoid operator biases associated with studying the more interesting areas. Microanalytical techniques were as described in Sec. 4.5.

Results. Three crack parameters were studied to detect a possible heating effect: areal number density, average crack length, and areal total length density. Although a significant difference in crack statistics was found between the NHH10 and SHH05 boreholes, there were no signficant differences between pre- and post-test cores. Furthermore, no change in fracture characteristics with radial distance was detected. The rock near NHH10 displayed about 25% more cracks per unit area with about 10% greater length than the rock near SHH05. This is believed to be related to the proximity of NHH10 to a major geological feature (Sec. 4.1).

Petrological studies showed no differences between the NHH10 and SHH05 cores. No new phases were found to have resulted from this episode of heating at temperatures near 350°C. The pre- and post-test samples were essentially identical, indicating that hydration, dehydration, and cation exchange mechanisms are too slow for a test of the intensity and duration of the SFT—C to produce measurable changes.

4.7 Drilling Damage Assessment*

To discriminate physical changes to rock induced by the waste storage canisters from damage induced by drilling the canister emplacement boreholes, Weed and Durham (1982) undertook an observational study of rock from the wall of an emplacement hole. Since the emplacement holes (610 mm in diameter) were hammer-drilled (Chapter 5)—a technique that requires that rock be broken up before it is removed—a

*Contributed by W. C. Patrick.

possibility exists that fractures generated by hammer-drilling extend into the wall rock around the hole. The importance of identifying drilling-induced damage was raised by the fact that the wall rock receives the most intense radiation and thermal energy from the canisters and was, therefore, the focus of attention when the canisters were removed (Sec. 4.6).

Weed and Durham examined rock from a section of 150-mm-diameter core that intersected, along its length, the edge of the practice canister emplacement hole CEH18. This core was obtained before thermal and radiation sources were introduced to the test area and thus served as a "control" for the studies of thermal and radiation effects. Several 25-mm-diameter sections were cut from the 150-mm core parallel to the hole axis at varying distances from the wall of the canister hole. These sections were polished and their surfaces examined for fractures and microfractures in the SEM. Several hundred fractures were photographically documented and quantified with the help of image analyzing hardware. Plots were then made of crack density and average fracture length as a function of distance from the wall of the emplacement hole. An example of the results is shown in Fig. 4-47.

As a general statement, the rock in the 150-mm-diameter core turned out not to contain a high density of fractures, so the noise level in the crack counting statistics was quite high. At most points in the core, the densities and length distributions of fractures could not be distinguished from background levels observed in rock far from the canister wall. The only 25-mm-diameter sections observed to contain abnormal fracture statistics were those that intersected the canister emplacement hole.

Therefore, the study concluded that the hammer-drilling of the canister emplacement holes changed the physical nature of the rock only within a thin annulus less than 20 mm thick around the emplacement hole, and that the physical change involved only a subtle increase in fracture density and length.

4.8 Radon Content*

Samples of CSQM were analyzed to determine the potential for radon exposures to underground workers. Concentrations of ^{222}Rn were determined to be about 2 pCi/g of CSQM.

The background radon concentrations in air averaged about 1.1×10^{-10} Ci/m^3 in the drifts and alcoves associated with the test (Ramspott et al., 1979). For practical purposes, the one "working level" limit imposed by 10CFR20 and 30CFR57 is equivalent to 1×10^{-7} Ci/m^3 of air. Thus, the background radon levels were a small percentage of the permissable limit. The effects of prolonged extensive heating and changes in ventilation on the radon concentration in air are discussed further in Chapter 15.

*Contributed by W. C. Patrick.

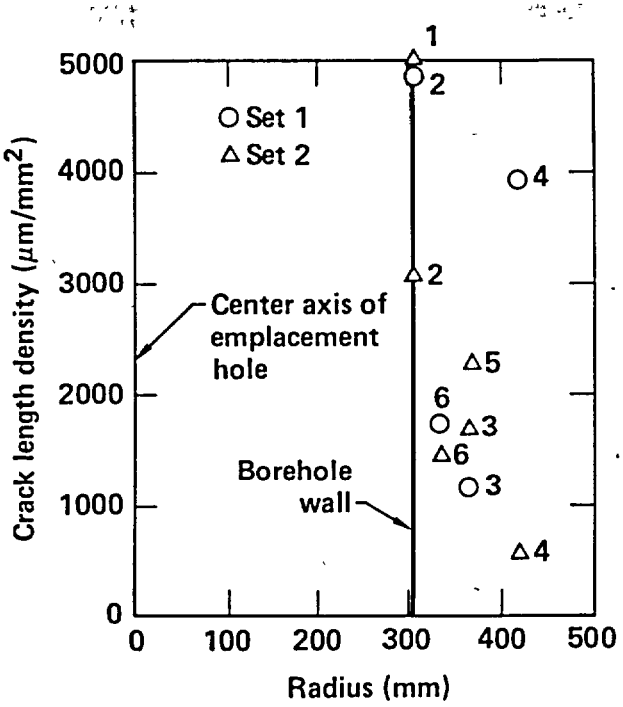

Figure 4-47. Example plot of crack length density vs radial distance from borehole wall; two independent sets of measurements were made (sets 1 and 2) on six specimens (numerals adjacent to data points indicate specimen numbers) (after Weed and Durham, 1982).

5. Site Development and Construction of the Facility*

Although an existing personnel and material shaft and associated surface plant were already in place at the SFT—C site, these facilities needed to be refurbished and the test area constructed. Necessary design, construction, and rehabilitation were initiated shortly after the SFT—C was authorized on June 2, 1978. Eleven spent-fuel assemblies were emplaced between April 18 and May 28, 1980, marking the completion of site development and construction activities.

5.1 Existing Facilities

Access to the 420-m (1400-ft) test level was provided by the PILEDRIVER underground nuclear test shaft and its associated headframe and hoist system (Figs. 5-1 and 5-2). Having these facilities already available shortened the development and construction time at the site and substantially reduced the cost of the test.

Beginning in the early 1960s, the Climax stock was host to nuclear weapons effects tests. To support these activities, a shaft was sunk 244 m for the HARD HAT underground nuclear test and was later deepened to the present level where the PILEDRIVER test was conducted. The shaft internals and surrounding rock were damaged during both of these tests.

In 1977 the shaft was again brought into service to provide access for Heater Test No. 1 (Montan and Bradkin, 1984), which was also conducted under the technical direction of LLNL. Repairs were limited to replacing damaged guides, installing a telephone messenger cable, and emplacing instrumentation cables in a 150-mm-diameter conduit.

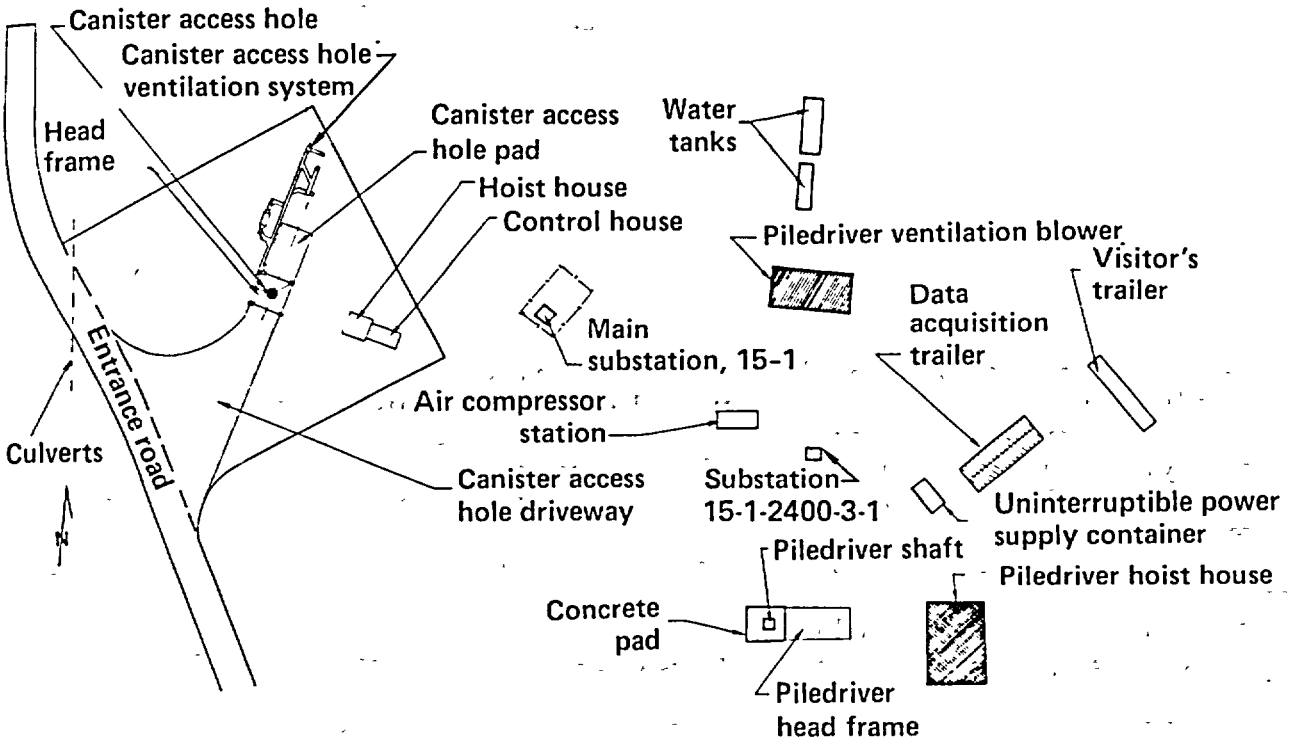

Figure 5-1. Surface area layout of the Climax site.

* Contributed by W. C. Patrick.

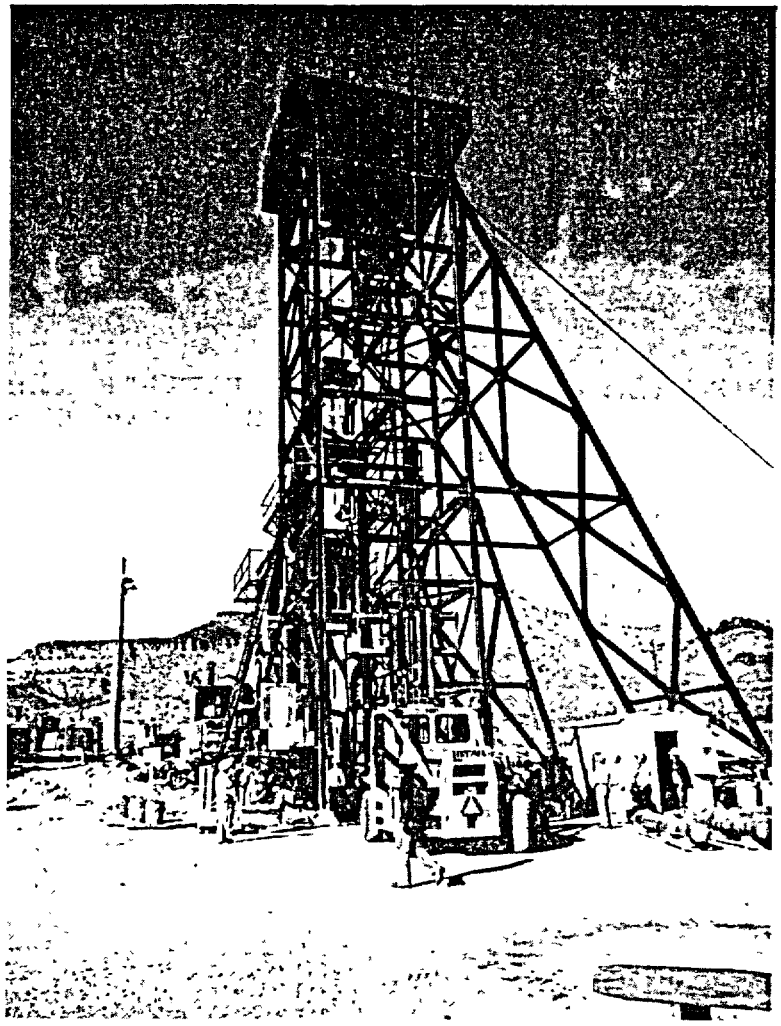

Figure 5-2. Piledriver head frame.

Divided into three compartments, the overall shaft dimensions are nominally 1.8 × 3.7 m (6 × 12 ft) (Fig. 5-3). A hoisting compartment 1.8 × 2.6 m (6 × 8.5 ft) accommodates materials, muck, personnel, and power and instrumentation cabling, and a ladderway 1.1 × 1.2 m (3.5 × 4-ft) is provided for emergency use in the event of power failure. The third compartment, which measures 0.6 × 1.1 m (2 × 3.5 ft), is the passageway for ventilation ducts and compressed air and water piping.

Once the SFT—C was authorized and funding was approved, major rebuilding of the shaft commenced, including:

- Replacement of elevator guides to accommodate heavy usage and high-speed mucking operations.
- Installation of new ladders and landings.
- Complete replacement of the twin 406-mm-diameter ventilation exhaust ducts, which were severely corroded.
- Inspection and replacement, as necessary, of wooden lagging between steel sets.
- Installation of a new 2400-V power and phone cables.

After refurbishment was completed, the shaft was ready to support the necessary underground construction activities.

The second major facility existing at the time the SFT—C was authorized was EMAD (Fig. 5-4). This large, shielded, highbay structure had been constructed to support a deep-space nuclear propulsion program and had since been idle. Relatively minor refurbishments and modifications brought EMAD to a

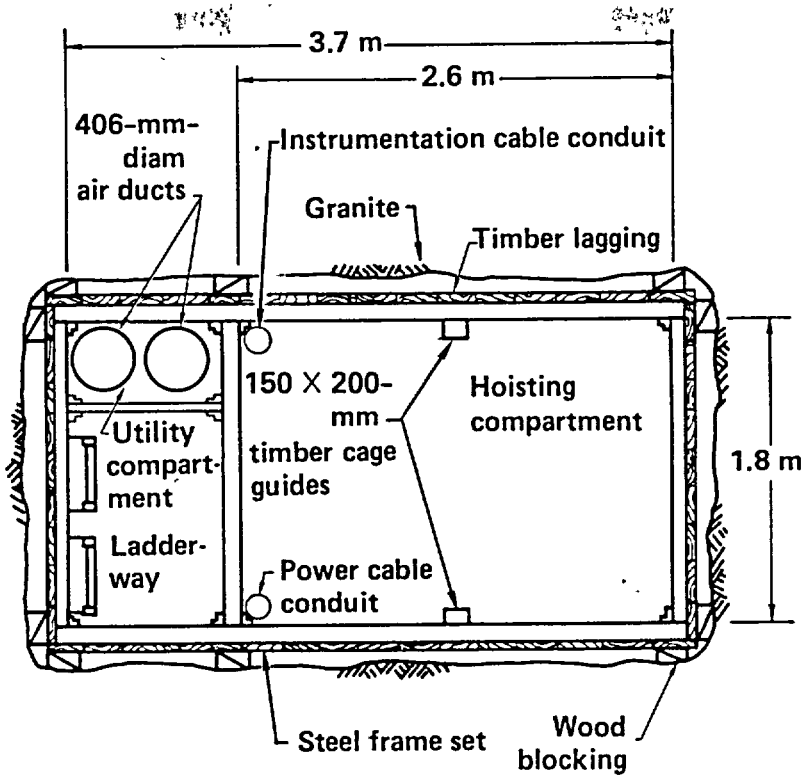

Figure 5-3. Plan view of Piledriver shaft.

state of readiness to receive, evaluate, and encapsulate intact spent-fuel assemblies for use in the SFT—C studies. These preparations are discussed further in NVO-198 and in Chapter 7 of this report.

5.2 Design and Construction Constraints

Several factors influenced the design and construction of the SFT—C facilities. As noted above, the availability of the PILEDRIVER and EMAD facilities produced significant cost and scheduling advantages. Likewise, they constrained the design and construction activities in the sense that they were unspecified subsystems within the larger system that was designed and constructed for the express purpose of executing the SFT—C.

The subsurface geology, *in situ* state of stress, and surface topography were used to establish the positions of the canister access shaft and underground workings. The three-drift complex was oriented N61°W to be roughly parallel and perpendicular to frequently encountered joint sets (Chapter 4). As a result, the drifts were also approximately aligned with the minimum principal stress. Although this alignment with respect to the fracture system produced somewhat irregular surfaces on the excavations because of overbreak, it resulted in a favorable position for the collar of the canister access shaft (Patrick and Mayr, 1981). Alternative orientations would have positioned the canister access shaft and headframe on steep hillsides or in a ravine.

The dimensions of the canister drift, as well as those of the railcar and receiving rooms, were selected as the minimum necessary for operation of the Underground Transfer Vehicle (UTV). The dimensions of the two heater drifts were the minimum necessary to permit mining and installation of heaters and instrumentation. The spacing between drifts was established by comparing thermal calculations of a full-scale repository with those of the proposed test geometry (Chapter 3).

The remaining constraints governed the sequence and method of excavation. Because alignment of the canister drift with respect to the canister access shaft was critical, the shaft was drilled before drift construction. After the location of the access shaft was determined by wireline surveying methods, the

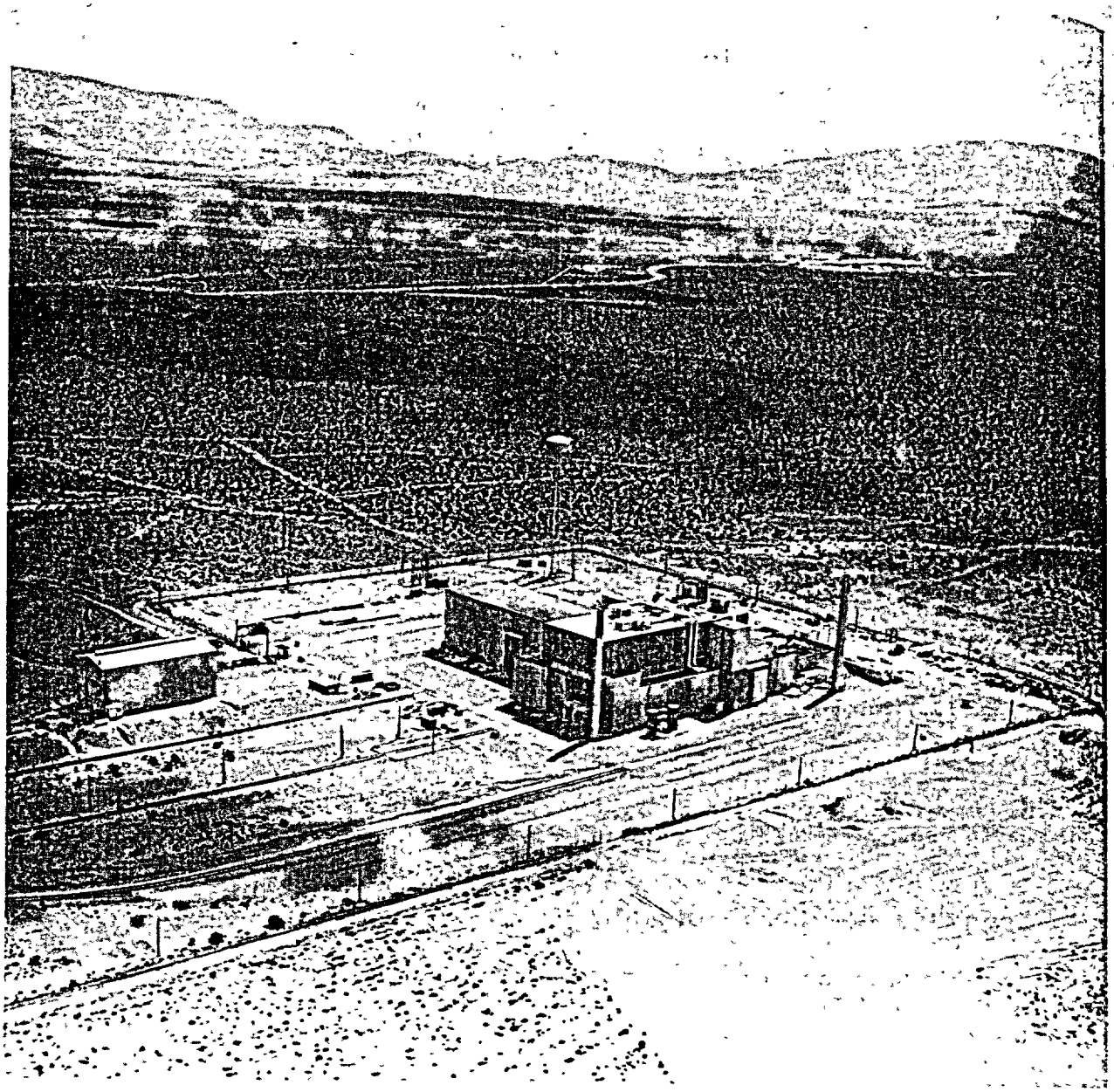

Figure 5-4. Aerial view of EMAD.

two heater drifts were driven to connect with it, thus confirming the location of the shaft. The canister drift alignment was then adjusted slightly and excavated. Conventional drill-and-blast excavation techniques were used in all but two short, instrumented sections where smooth-wall blasting techniques were specified.

5.3 Facility Description

The design and construction constraints described above and the construction activities described in Sec. 5.4 produced the underground structures shown in Figs. 5-5 and 5-6.

A 3.7-×-3.7-m access drift extends from the existing PILEDRIVER complex to the railcar room, which is 14.6 × 6 × 7.6 m high. Beyond this room, the 6.1-m-high × 4.6-m-wide canister storage drift extends 64 m

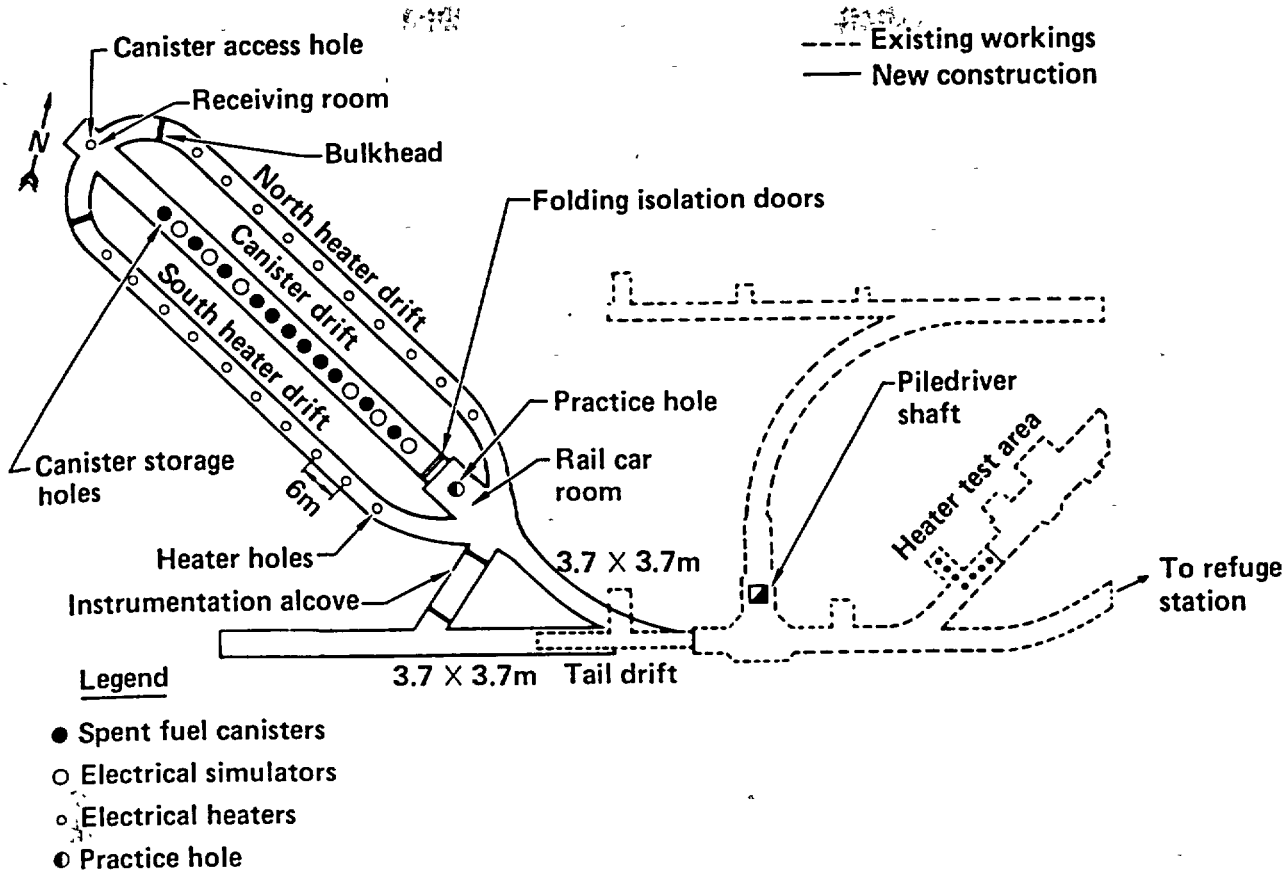

Figure 5-5. Climax site subsurface structures and facilities.

to the receiving room, which is located at the base of the 485-mm-inside diameter steel-lined canister access shaft.

A linear array of 17 storage holes is located on 3-m centers in the floor of the canister drift. Of these, 11 housed spent-fuel assemblies and 6 housed electrically heated simulators during the test. To accommodate personnel training and equipment evaluations, an additional hole with a dummy canister was provided in the railcar room. These 18 storage holes are identical: 610 mm in diameter by 5.2 m deep, with a 457-mm steel liner grouted in position at the top and bottom.

The north and south heater drifts on either side of the canister drift measure 3.4 × 3.4 m. As we indicated above, their 9.8- and 10.2-m spacings from center line of the canister drift resulted from adjustment of the planned drift alignment. Ten auxiliary electrical heaters were emplaced in small-diameter boreholes on 6-m centers in the floor of each of these drifts.

5.4 Facility Construction

Following refurbishment of the PILEDRIVER personnel and materials shaft, preparation and construction began on the hoist, headframe, and site.

5.4.1 Canister Access Shaft

The collar location of the canister access shaft, through which the encapsulated spent-fuel assemblies were lowered and raised, was selected based on surface topography and subsurface geological conditions. Its position 115 m (375 ft) northwest of the PILEDRIVER shaft (Fig. 5-1) is at a surface elevation of 1536 m (5040 ft) above MSL.

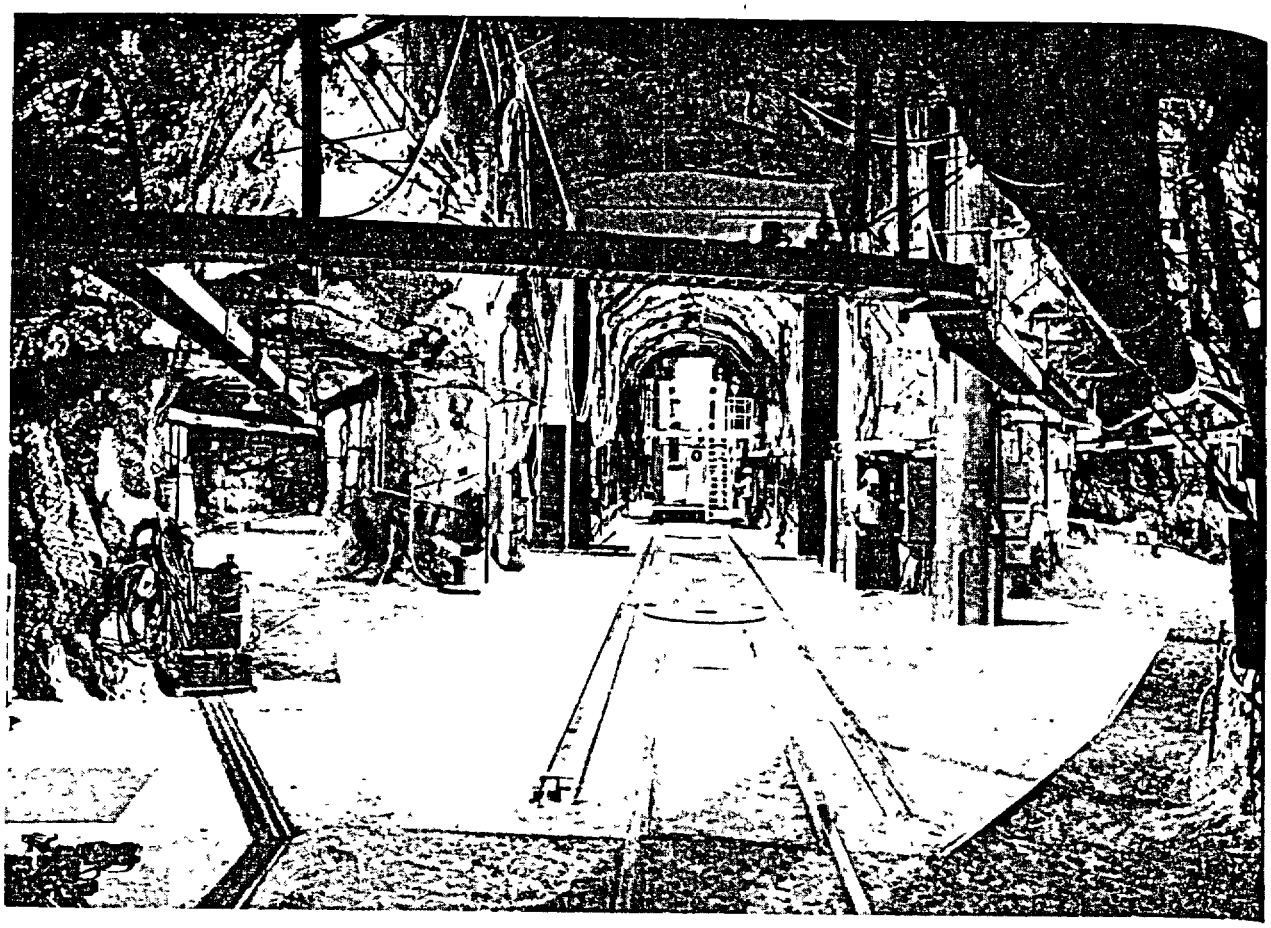

Figure 5-6. Panorama of Spent Fuel Test—Climax drifts.

Drilling of the 762-mm-diameter shaft was initiated in October 1978 using a tricone rotary bit with carbide button inserts. Although a number of collar weights and rotation speeds were tested, penetration was excessively slow (Table 5-1). After using this technique for 90 m, we rented an Ingersoll-Rand downhole hammer drill with an on-the-drill weight of about 7,000 kg and a rotation speed of about 2 rpm. As the table shows, substantial improvements were seen in the mean drilling rate (based on drilling time) and the effective drilling rate (based on total rig time). This method was used for all but the lower 14 m of the shaft, where the tricone bit was used because additional hammer-drill bits were unavailable.

Two directional surveys were conducted during the drilling operations: one when the shaft was at a depth of 90.5 m and one at a depth of 315 m. After total depth was reached, three directional logs were made with logging on both the up and down trips. The effective shot spacing was 1.5 m. Using a computer code previously developed at LLNL for post-shot drilling for underground nuclear testing, a total depth coordinate was calculated with a possible error circle of 150 mm. The shaft was line-of-sight to a depth of 305 m, and total shaft deviation was 4.92 m (1.2%).

After directional surveying was completed, the shaft was washed, bailed, and photographed, and density logs were taken. The 508-mm-outside diameter, 485-mm-inside diameter, 140-kg/m casing was then lowered and cemented into position. The Type A cement with 2% calcium chloride additive was pumped through two 50-mm diameter cementing lines.

Near the top of the shaft, the liner is slotted to provide a takeoff for ventilation air exhausted from the underground workings (Fig. 5-7). A pit was constructed to ensure that the Surface Transport Vehicle (STV) cask was aligned with the access shaft and to provide radiation shielding during transfer operations. The pit also incorporated hydraulic cylinders for emergency closing of the STV bottom gate (NVO-210, 1980). A similar shielding collar was also constructed at the base of the shaft.

Table 5-1. Drilling statistics for the canister-access shaft (after Patrick and Mayr, 1981).

Drilling parameter	Rotary tri cone		Hammerdrill (redrilling)	Hammerdrill (new drilling)
	Upper section	Lower section		
Distance drilled (m)	90.5	13.7	90.5	305
Rotating time (h)	381	68.0	37.5	201
Mean drilling rate (m/h)	0.24	0.20	2.4	1.5
Rig time (h)[a]	564	88.0	73.5	616
Mean effective drilling rate (m/h)	0.16	0.16	1.2	0.5

[a] Rig time is total time on the hole excluding approved work stoppages and logging time.

5.4.2 Underground Exploration

To confirm that the selected location was adequate for the purposes of the SFT—C and that no unexpected geological conditions would be encountered, four 76-mm-diameter (NX) exploratory borings were obtained with a Longyear 44 rig. All borings were collared near the end of the existing workings northwest of the PILEDRIVER shaft. Three boreholes were nearly horizontal and explored the regions north of, south of, and along the central axis of the canister drift, while the fourth probed the region below the proposed SFT—C (Chapter 4). A total of 480 m of drilling was done at an average rate of about 1 m/h, with about 99% core recovery. Cores were logged, photographed, and archived. Selected intervals were retained for subsequent testing.

5.4.3 Underground Excavation

Excavation was accomplished using drill-and-blast techniques to fragment the rock and a load-haul-dump (LHD) unit to move the rock to the PILEDRIVER hoisting station. The taildrift, alcove, access to the railcar room, and the two heater drifts were excavated using two Atlas-Copco 205 "Miniboomers" supported by an EIMCO 913 LHD.

After the heater drifts intersected the access shaft, thereby confirming its location, the canister storage drift was excavated. This was done in two passes. The top 4.0 × 4.6-m-wide heading was excavated using a shop-built drill jumbo with four Gardner-Denver 123 rotary percussion machines, again supported by the EIMCO 913 LHD. A Leroi airtrack was then used to drill the bench, enlarging the drift to 6.1 × 4.6 m wide. The Miniboomers and jacklegs were used to extend the taildrift, construct the alcove, trim the excavations, and enlarge the railcar and receiving rooms.

Several problems were encountered during underground development (Patrick and Mayr, 1981). A significant fraction of oversized material was produced, requiring secondary breakage. Primarily, this resulted from the geological fractures, which produced a blocky structure.

Many blast rounds failed to break to the full drilling depth. These "bootlegs" were attributed to the fact that the mining work force was more experienced in the weaker tuffs that are present in other tunnels at the NTS. Smooth-wall blasting results were not as good as anticipated for three reasons: drills were unable to be accurately positioned, stemming materials were not used, and delays were not properly patterned. And finally, overbreak in the floor of the canister drift was excessive because of the short vertical height of the benches. This problem was accentuated by the presence of a low-angle joint set that produced a sawtooth profile on the floor.

Excavation rates averaged about 2 m^3/h and ranged from a high of 3.6 m^3/h in the canister drift heading to 1.5 m^3/h in the canister drift bench. In comparison, low productivity mining methods typically average less than 2 m^3/h, whereas recent European tunneling rates in granite have been reported at 3.6 and 4.5 m^3/h for tunnel boring machine and for drill-and-blast methods, respectively.

Hercules "Unigel 65%" or DuPont "Tovex" were used in the main rounds, whereas Hercules "Hercosplit" or DuPont "Trimtex" were used in the perimeter holes. Explosive consumption varied widely, depending on drift dimensions, ranging from about 6 kg/m^3 for the heater drifts to 1.8 kg/m^3 for the canister drift bench, with an average of 5 kg/m^3.

Based on core logs and inspection of existing underground workings, it appeared that the excavations would remain open for extended periods with minimal ground control measures. Because there was little

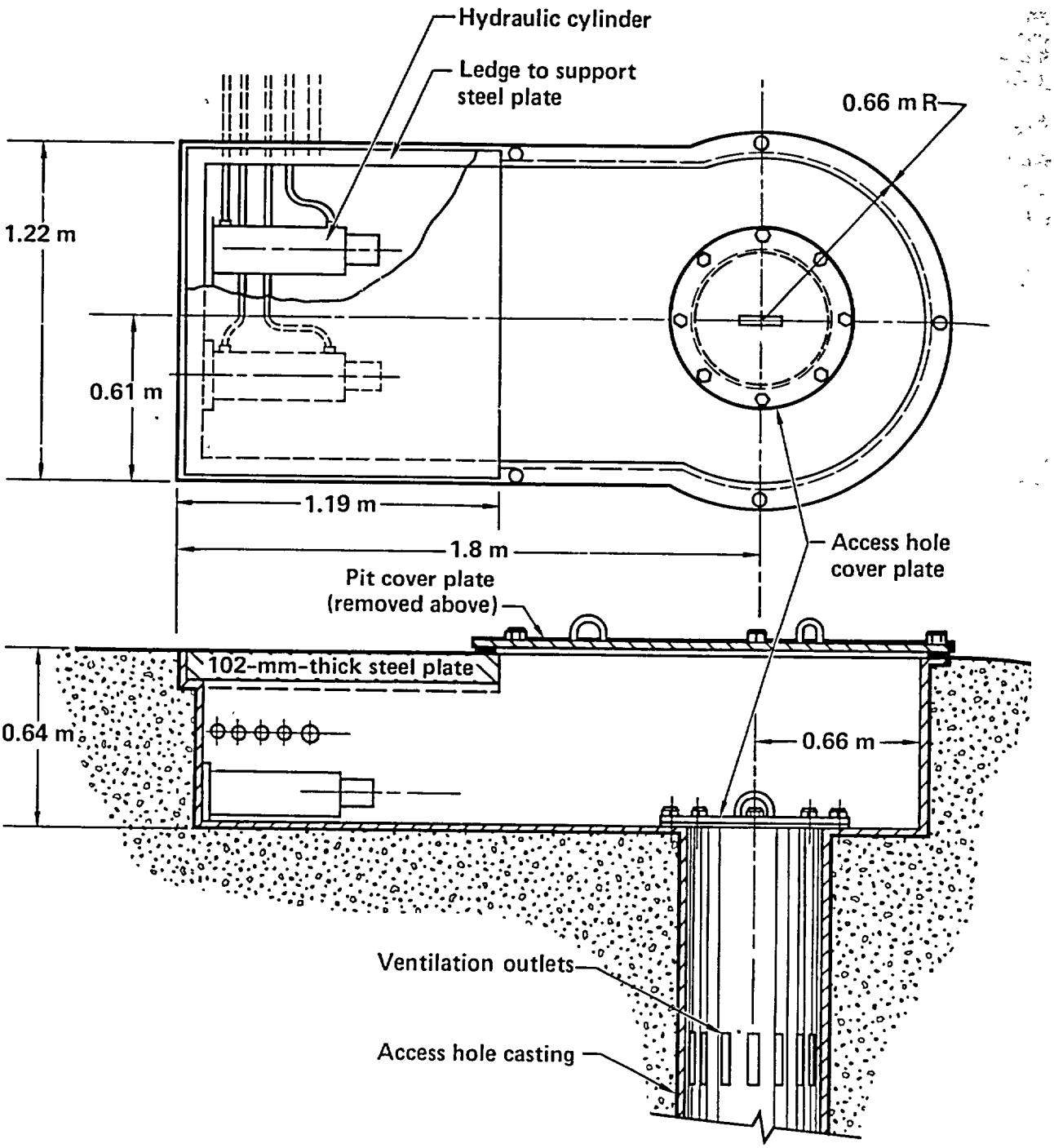

Figure 5-7. Canister access hole pit.

experience with stabilization of heated rooms, and because even minor rock falls could cause injury to workers, visitors, and instrumentation, more support was used than would be required for typical civil works in granitic rocks. Factors influencing the type and quantity of rock support included opening dimensions, local geology, and consideration of whether the support would carry external loads (such as a lifting fixture).

In the heater drifts, tail drift, and canister drift access, point-anchored resin bolts 1.8 m long by 19 mm in diameter or 2.4 m long by 22 mm in diameter with wire mesh was the principal ground support system.

A nominal 1.5-m spacing was used (Fig. 5-8). In the canister drift and receiving room, 3.6-m-long by 22-mm-diameter bolts were used partway down the ribs. Once again, wire mesh was used to secure loose rock fragments. The railcar room was supported with 4.1-m by 28-mm-diameter full-column grouted bolts with mesh in the crown as well as 2.4-m-long point-anchored bolts with mesh along the brow and ribs.

5.4.4 Subsurface Outfitting

After excavations were completed, the underground chambers were prepared for the test. The canister drift floor was completely cleaned, storage hole pits were formed from steel tubs, reinforcing steel was emplaced, rails for the UTV were positioned, and the concrete floor was constructed in two placements (Fig. 5-9).

Using a 610-mm-diameter downhole hammer drill mounted on a shop-built crawler unit, an outside contractor, New Jersey Drilling Company, drilled the 17 storage holes and the practice hole. Maximum penetration rates reached 2.3 m/h, with an average rate of 1.4 m/h including set-up time. Before the emplacement boreholes were drilled, a 76-mm-diameter (NX) core was obtained by drilling just inside the perimeter of each emplacement borehole. These cores provided baseline information for subsequent thermal and radiation effects studies (Chapter 4).

The 610-mm-diameter boreholes were cased with 508-mm outside diameter carbon steel pipe sections. Grouting at the upper and lower sections provided radiation shielding and held the liners in position.

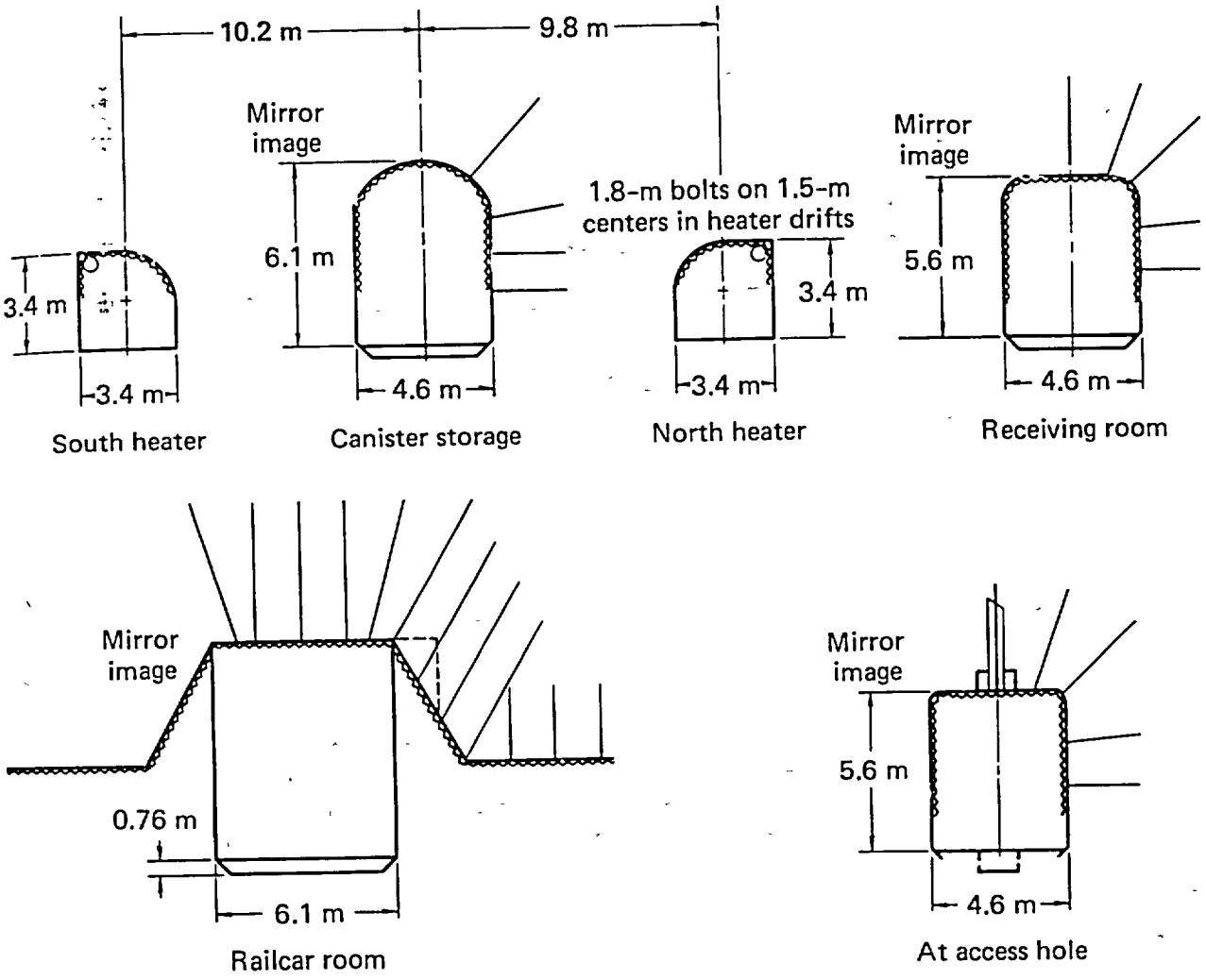

Figure 5-8. Ground support deployed in the SFT—C drifts and rooms (after Patrick and Mayr, 1981).

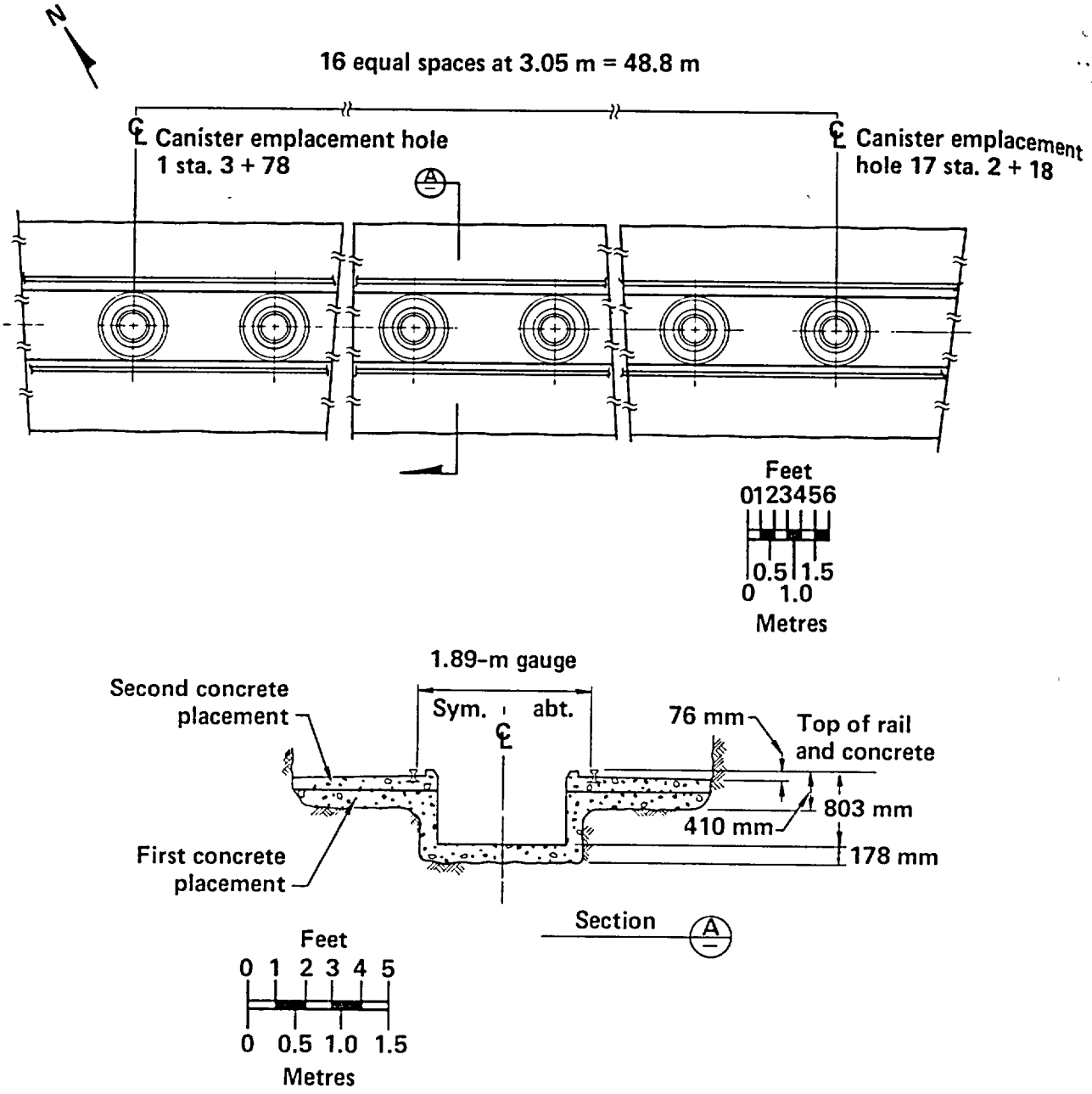

Figure 5-9. Canister storage drift configuration before drilling canister emplacement holes (after Patrick and Mayr, 1981).

The auxiliary heater boreholes consisted of a 1.2-m by 76-mm-diameter upper section and a 3.9-m by 51-mm-diameter lower section, both core-drilled. Ten of these boreholes were located in the floor of each heater drift on 6-m centers. A post-mounted CP-65 drill was used to core these holes.

Numerous boreholes were drilled for installing instrumentation, for geological sampling, and for *in situ* stress measurements. In general, Longyear 38s and 44s, a CP-65, and a Joy 22 were used, depending on the drilling requirements. Descriptions of these boreholes are noted in Chapters 4 and 9.

5.4.5 Data Acquisition System Facilities

Both underground and surface facilities were required to house the data acquisition system (DAS). The former consisted of a cross-cut 4.6 × 9.1 × 3.0 m high enclosed by gypsumboard construction (Fig. 5-5).

The alcove was air-conditioned and was provided with a Halon fire-suppression system and battery-operated uninterruptible power supply (UPS). At the surface, a double-wide trailer 6.1 × 15.2 m housed the uphole portion of the DAS (Fig. 5-1). This specially built trailer included redundant air conditioning systems, smoke alarms, and a Halon fire-suppression system. A UPS was located nearby.

5.4.6 Electrical Power

Power was provided to the site substation by a 34.5-kV highline with a capacity of 1500 kVA. After conversion to 480 V by stepdown transformers, power was distributed to the canister access pad, headframe, ventilation blowers, personnel and materials hoist house, and DAS trailers (Fig. 5-1). Underground power was distributed from a 150-kVA, 2400/480-V underground substation.

5.4.7 Ventilation

During construction, ventilation was provided by a single 400-hp, Buffalo "squirrel-cage"-type blower that exhausted through two 406-mm-diameter ducts. To control potential releases of radionuclides during spent-fuel handling operations, a separate ventilation system was installed. Two squirrel-cage blowers were connected and valved so that they could be operated separately, in parallel, or in series. Provision was made to draw all air through high-efficiency particulate air (HEPA) filters during handling operations. In the subsurface, flows through the three drifts were controlled by means of bulkheads and louvers (Fig. 5-10). Airflow, temperature, dewpoint, and radioactive materials were monitored at selected positions within the airstream (Chapter 9).

5.5 Cost and Schedule Considerations

The total project cost through emplacement of 11 spent-fuel assemblies was $18.4 million, including all construction, equipment fabrication, technical, and scientific activities. These activities were completed between June 1978 and May 1980. Underground excavation and related activities accounted for about $2.5 million of this cost. Through completion of the project in September 1985, total project costs were about $34 million.

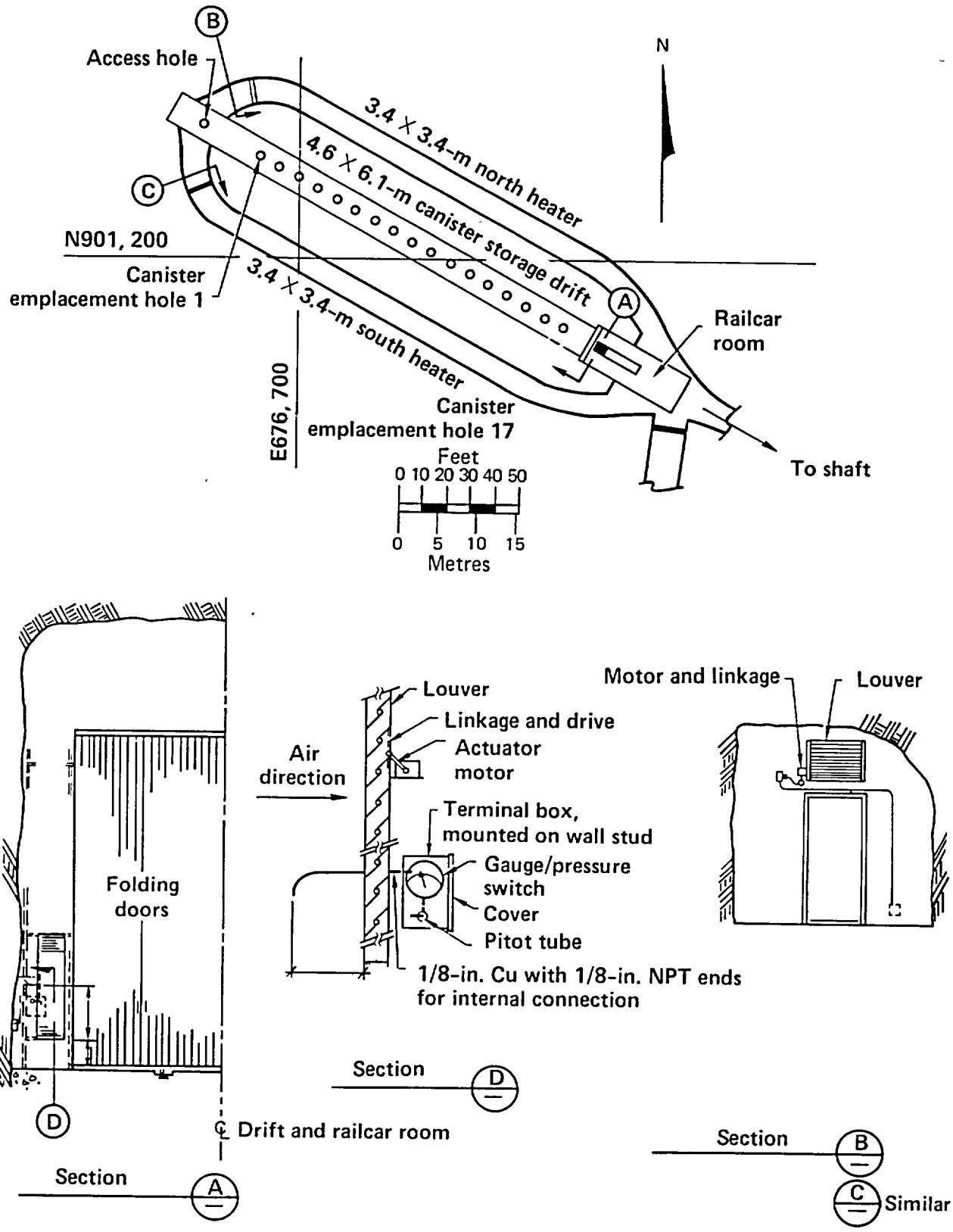

Figure 5-10. Flow regulator system for SFT—C subsurface facilities (after Patrick and Mayr, 1981).

6. Spent-Fuel Characterization*

The 13 spent-fuel assemblies used in the SFT—C were characterized on the basis of reactor history, nondestructive testing, calorimetry, and dosimetry. In addition, the isotope inventory and decay history were calculated using the ORIGEN code (Schmittroth, Neely, and Krogness, 1982). Many of these studies were conducted under separate funding for the Office of Nuclear Waste Isolation (ONWI) by the Hanford Engineering Development Laboratory (HEDL). The results of these studies are summarized here.

6.1 Source and History of Spent Fuel

Thirteen spent-fuel assemblies were selected for use in the SFT—C based on their estimated burnup and age since discharge from reactor core at the anticipated emplacement date at the SFT—C (Chapter 12). This set of assemblies was discharged from Turkey Point Unit 3 following cycles 2, 3, and 4 in the reactor. Operated by Florida Power and Light Company, Turkey Point Unit 3 is a Westinghouse-designed pressurized water reactor (PWR) with a rated capacity of 660 MWe.

Pertinent dimensions and materials of these PWR assemblies are given in Table 6-1. As noted in Table 6-2, the relative power of assembly serial number (S/N) D22 is somewhat lower than that of the other 12 assemblies in the set. This information was the basis for excluding this assembly from the test array until the final exchange (Chapter 11). Even then, it was placed near the end of the emplacement array to minimize the effect of its lower power level on the simulation.

6.2 Nondestructive Testing

To gain a better understanding of the characteristics of spent-fuel assemblies before and after geologic storage, the ONWI funded the HEDL to perform certain nondestructive evaluations of three of the PWR spent-fuel assemblies before their encapsulation for use in the SFT—C. Fifteen rods were selected for nondestructive evaluations and an additional five for destructive evaluations aimed at characterizing the internal conditions of the fuel rods before storage at the SFT—C. These studies were performed at the Battelle Columbus Laboratories under the direction of HEDL (Davis, 1980).

Although the original plan was to select five rods each from S/N D01, D04, and D06, complications related to Nuclear Regulatory Commission (NRC) shipping regulations and rigid test schedules required that testing proceed with 15 rods from D01. Once shipments were on schedule, five of the characterized D01 rods were exchanged with five rods each from S/N D04 and D06. The five (total) rods for destructive testing were removed from D01 and D04 and were replaced with stainless steel rods. As described by Davis (1980), a total of 38 rods were removed from the three assemblies. The reader is referred to this publication for details concerning the positions of the rods selected, the replacement scheme of spent fuel and stainless steel rods, and the techniques for extracting the rods.

6.2.1 Sip Testing

Before shipment to EMAD, eight of the spent-fuel assemblies were wet sip-tested at Turkey Point. They were also gas sip-tested upon arrival at EMAD. The five assemblies shipped through Batelle Columbus Laboratories (BCL) were not tested at Turkey Point, but were wet sip-tested upon arrival and before departure from BCL. They were later gas sip-tested at EMAD.

Wet sip testing was based on analyses for ^{137}Cs, ^{134}Cs, and ^{60}Co using gamma ray spectrometric techniques (Davis, 1980). After filling and flushing the cask cavity with deionized water, samples were drawn immediately and after 2- and 16-h soaking times.

Dry sip testing was performed by drawing a sample of cask cover gas into an evacuated gas-collection cylinder.

Sip testing detected no leaking fuel rods among the 13 assemblies. In general, the concentrations of cesium isotopes were very low. An exception was S/N D01, which showed relatively high concentrations of ^{134}Cs and ^{137}Cs. Davis (1980) reports that this observation may be the result of contamination from the

* Contributed by W C Patrick.

Table 6-1. Characteristics for Turkey Point spent-fuel assemblies used in the SFT—C (after Davis, 1980).

Characteristic	Value
Vendor	Westinghouse Electric Corp.
Type (rod array)	15 × 15
Assembly parameters	
Transverse dimension	8.426 in.
Assembly weight	1420 lb
Assembly length	161.3 in.
Guide tubes	
Number	20
Upper O.D.	0.544 in.
Wall thickness	0.017 in.
Material	Zr-4
Instrument tubes	
Number	1
O.D.	0.544 in.
Wall thickness	0.017 in.
Material	Zr-4
Spacer grids	
Number	7
Material	Inconel 718
Spring material	Inconel 718
Fuel rods[a]	
Number	204
Length	152.0 in.
O.D.	0.422 in.
Wall thickness	0.0243 in.
Material	Zr-4
Fuel length	144.0 in.
Orifice plate material	304 SS
Plenum springs	
Working length	6.80 in.
Material	302 SS
Fuel pellet	
Material	UO_2
Enrichment	2.559 wt % ^{235}U
Weight/assembly	0.448 t/uranium
Planar Smear density	
Dish not smeared in	90.81% theoretical
Dish smeared in	89.72% theoretical

[a] Helium prepressurization level is 465 psig.

Table 6-2. Reactor operation data for SFT—C spent-fuel assemblies (after Davis, 1980).

Beginning of first cycle of irradiation	December 12, 1974
Discharge date	November 19, 1977
Cycles of operation	2, 3, and 4
Total irradiation time in EFPD of core residence	851 EFPD
Specific power	31.203 MW(th)/MTU
Assembly average relative power averaged over all 3 cycles	
Assemblies D09, D16, D18, D34	1.061
Assemblies D01, D15, D35, D47	1.082
Assemblies D04, D06, D40, D46	1.082
Assembly D22	1.008
Accumulated neutron fast fluence per assembly at discharge (nvt > MeV)	5.6×10^{21} n/cm^2

spent-fuel pool at the reactor. Gas testing at EMAD revealed no krypton or xenon concentrations above the detection limits.

6.2.2 Dimensions and Weight

Fuel assembly lengths were measured to an accuracy of ± 0.254 mm (±0.010 in.) using a standard traceable to the National Bureau of Standards (NBS). Variations among the assemblies was less than 1.27 mm (0.050 in.), and length variations corner-to-corner were 0.508 mm (0.02 in.) for S/N D01 and less than

0.127 mm (0.005 in.) for S/N D04 and D06. The average assembly length was reported as 3.903 m (153.65 in.).

Individual rod-length measurements were obtained by resting the rod in a set of V-blocks positioned at 0.61-m (24-in.) intervals on an I-beam. A micrometer was used to make comparative length measurements with reference to a standard. Thermal expansive corrections were employed. Rod lengths varied between 3.878 and 3.872 m (152.663 and 152.426 in.), with an average of 3.875 m (152.561 in.).

Width of the fuel assemblies, measured from flat-to-flat, ranged from 210.1 to 212.1 mm (8.272 to 8.349 in.), with an average of 211.1 ± 0.43 mm (8.312 ± 0.017 in.).

Profilometry studies indicated that minimum rod diameters averaged 10.7 mm (0.420 in.) and ranged from 10.65 to 10.77 mm (0.4194 to 0.4242 in.). The largest variations reported were in the range of 0.127 to 0.254 mm (0.005 to 0.010 in.). Although no major anomalies such as bulges, scars, or blisters were detected, ridges measuring as high as 0.076 mm (0.003 in.) were seen. They appear to occur at the pellet interfaces, as inferred from eddy current and gamma scans (Davis, 1980).

A load cell accurate to ± 1.4 kg (± 3.0 lb) was used to weigh the three assemblies. The average weight was 663 kg (1459 lb) with only 2.3 kg (5 lb) of variation between the high and low values. A load cell accurate to 0.023 kg (0.05 lb) was used to weigh individual rods. Rod weights ranged from 3.10 to 3.09 kg (6.83 to 6.79 lb) with an average of 3.1 kg (6.82 lb).

6.2.3 Flux Measurements

Both neutron and gamma flux measurements were made on the intact D04 assembly before it was disassembled and the rods removed. Individual rods were also gamma scanned.

The neutron field of assembly D04 was characterized using six packages of solid-state track recorders (SSTR) comprising thin mica sheets in contact with fissile isotopes (Davis, 1980). The neutron energy spectrum was determined using $^{235}U(n,f)$, $^{235}U(n,f)$ cadmium covered, $^{232}Th(n,f)$, $^{238}U(n,f)$, and $^{237}Np(n,f)$. Measured neutron fluxes at the assembly midplane are tabulated in Table 6-3. Variations in flux in the axial direction and as a function of distance from the source are displayed in Figs. 6-1 and 6-2, respectively. The average neutron flux and energy at the midplane are 1.06×10^4 n/cm^2/s and 1.4 MeV, respectively. With the exception of the slight upturn in the epithermal neutrons, the axial distribution displays a nearly symmetric pattern about the midplane with a somewhat lower flux near the top of the assembly. Davis (1980) attributed the noted upturn in epithermal neutrons near the top to reflection of higher energy neutrons from the shielded cell walls and the lack of absorption of neutrons in this sampling position, which was 0.3 m (12 in.) from the high-mass fuel assembly. An approximately 1/r attenuation with distance was observed in the higher-energy neutrons.

Thirty-six aluminum-wrapped capsules, each containing five thermoluminescent dosimeters (TLD), were used to determine gamma flux of assembly D04 on September 12, 1979. After 10-min exposure times, the TLDs were counted. Variations in gamma flux along the assembly and as a function of distance from the assembly are shown in Tables 6-4 and 6-5, respectively. Fairly constant gamma flux averaging about 9.11×10^4 R/h was observed along most of the length of the assembly. At the 0.91-m (3-ft) position, the flux is low coinciding with the presence of a support strap. In addition, there is a notable decrease in flux in the upper 0.61 m (2 ft; positions 10, 11, and 12) of the fuel assembly; paralleling a similar decrease in neutron flux.

Table 6-3. Neutron fluxes measured at fuel assembly D04 midplane (after Davis, 1980).

Energy range	Flux (n/cm^2/s)	Estimated uncertainty (%)
Thermal E < 0.5 eV	30	20
Epithermal (0.5 eV - 0.1 MeV)	390	20
Fast (0.1 MeV - 2 MeV)	1.02×10^4	15
High energy (>2 MeV)	4.9×10^3	15
Total flux[a]	1.06×10^4	15

[a] Average energy = 1.4 MeV.

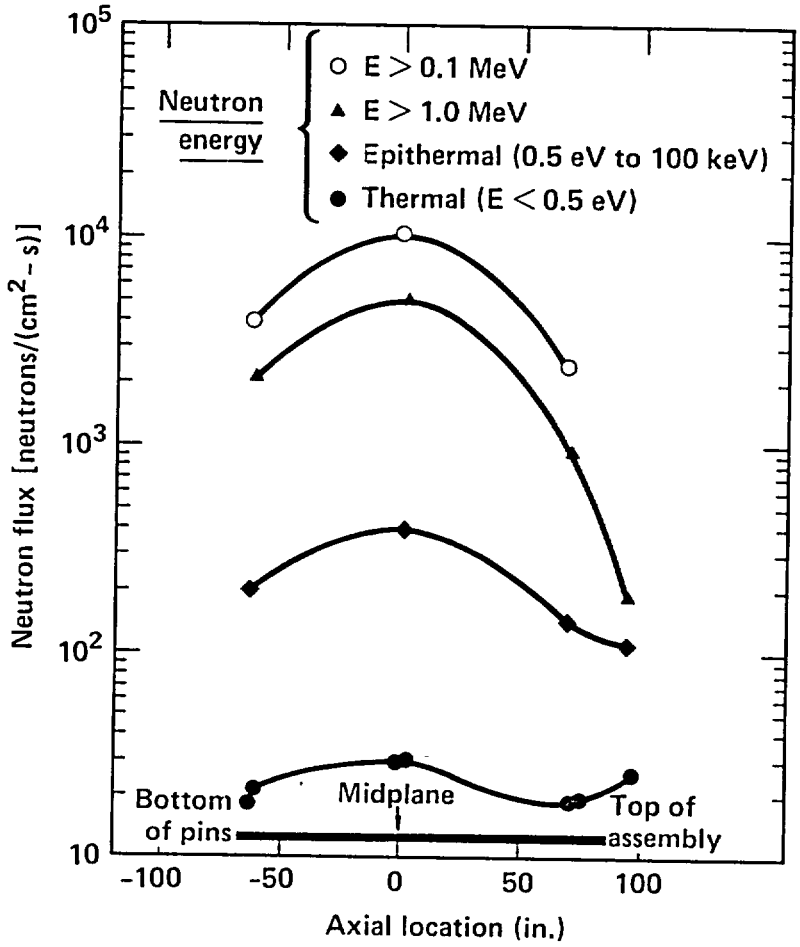

Figure 6-1. Neutron flux as a function of axial location (after Davis, 1980).

Individual rods were gamma-scanned using a motor-driven scanning system consisting of a variable-slit lead collimator [set with a width of 0.635 mm (0.025-in.)] and a germanium-lithium counting crystal spectrometer. Total activity and ^{137}Cs gamma activity were scanned. As reported by Davis (1980), both the total activity and ^{137}Cs activity displayed the typical flat, chopped cosine profiles (Figs. 6-3 and 6-4). Except for about 0.41 m (16 in.) near each end of the rods, the profiles were fairly constant. Gamma depressions of about 10% were seen at the pellet-to-pellet interfaces and at each spacer grid location. The cesium profiles closely tracked those of total gamma, indicating no cesium migration.

Following retrieval of spent fuel from the SFT—C, Van Konynenburg (1984) obtained additional dosimetry measurements. Three Harshaw TLD-700 LiF chips were mounted in each of 24 plastic dosimeter packets to obtain measurements on assembly D34. Six packets that were beta-shielded with 1.6-mm-thick aluminum and six unshielded packets were placed in contact with one of the faces of the fuel assembly for 10 min. each. The positions of the dosimeters were as noted in Fig. 6-5. Two other packets were instrumented with thermocouples. Since the maximum packet temperature was only 30°C, no thermal corrections were required. The remaining packets were shipped and stored with the exposed packets to detect possible unplanned exposures.

Van Konynenburg (1984) reported a contact dose rate of 2.33×10^4 R/h on March 28, 1984. This value includes correction for the small dose received during handling and positioning of the TLDs but does not include correction for gamma attenuation by the beta shield.

6.2.4 Visual Examinations

In-pool examinations of D01, D04, and D06 were conducted at the Turkey Point reactor to provide videotape records of their external appearances. The three assemblies were similar in appearance with all

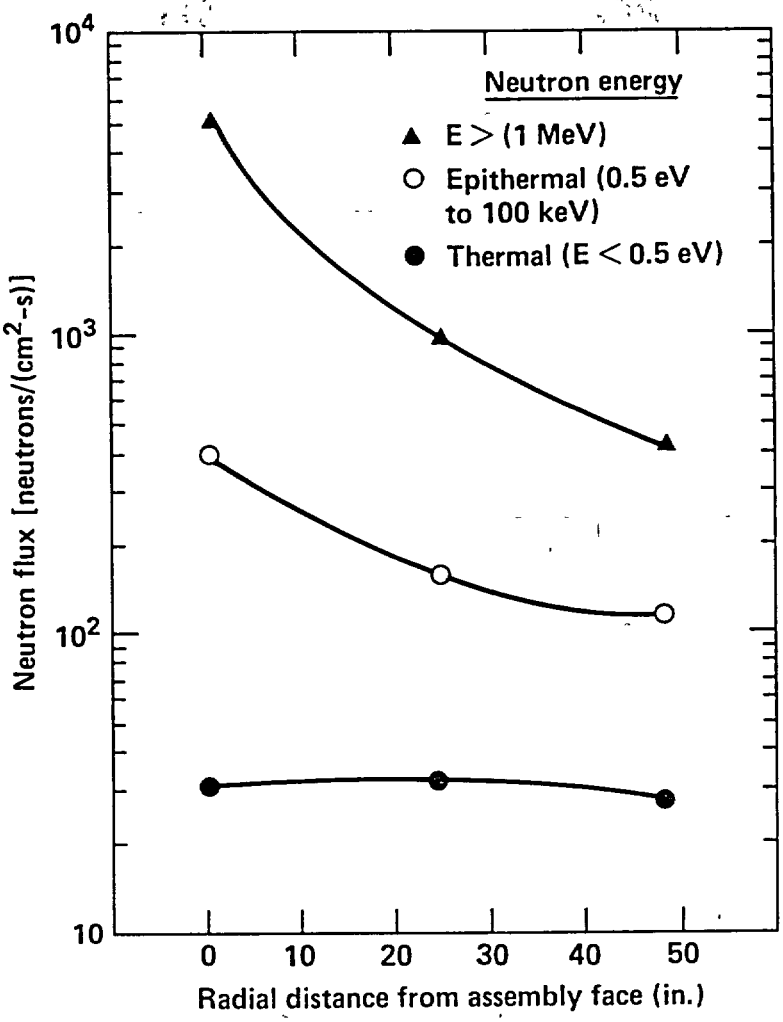

Figure 6-2. Neutron flux as a function of radial distance from the fuel midplane (after Davis, 1980).

Table 6-4. Axial gamma exposure rate from fuel assembly D04 (after Davis, 1980).

Distance from bottom of fuel assembly (ft)	Contact with fuel assembly surface		12 in. from fuel assembly surface	
	Exposure rate (R/h)	1σ uncertainty (%)	Exposure rate (R/h)	1σ uncertainty (%)
0	8.81×10^4	3.4	7.42×10^3	2.4
1	8.91×10^4	3.6	1.21×10^4	0.8
2	9.30×10^4	3.3	1.49×10^4	4.8
3	6.57×10^4	2.6	1.62×10^4	4.1
4	9.25×10^4	1.6	1.62×10^3	4.0
5	9.00×10^4	1.8	1.71×10^4	1.1
6	9.52×10^4	3.5	1.63×10^4	4.1
7	9.37×10^4	1.9	1.58×10^4	2.5
8	9.27×10^4	2.9	1.61×10^4	1.6
9	8.25×10^4	2.3	7.54×10^4	6.2
10	5.48×10^4	4.2	1.42×10^4	4.3
11	1.29×10^4	7.4	1.10×10^4	3.3
12	2.75×10^3	4.4	7.29×10^3	3.8

Table 6.5. Gamma dose rate as a function of distance from assembly D04 midplane (after Davis, 1980).

Distance from assembly midplane (ft)	Exposure rate (R/h)	1σ uncertainty (%)
0	6.30×10^4	3.8
1	1.86×10^4	2.7
2	9.88×10^3	3.3
3	6.81×10^3	4.9
4	4.91×10^3	4.2
5	3.92×10^3	4.1
6	3.34×10^3	2.6
7	2.85×10^3	1.7
8	2.24×10^3	4.2

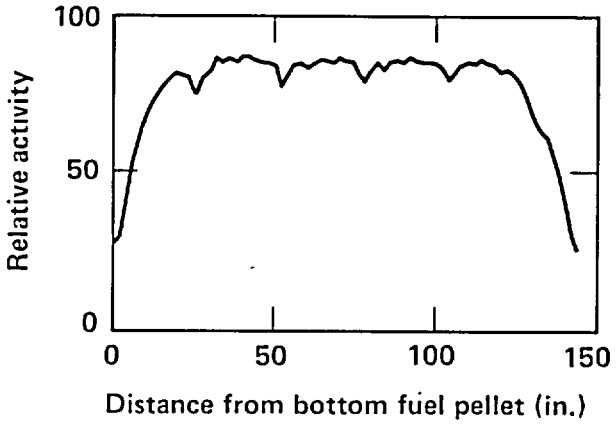

Figure 6-3. Gross gamma scan trace for D01-F7 (after Davis, 1980).

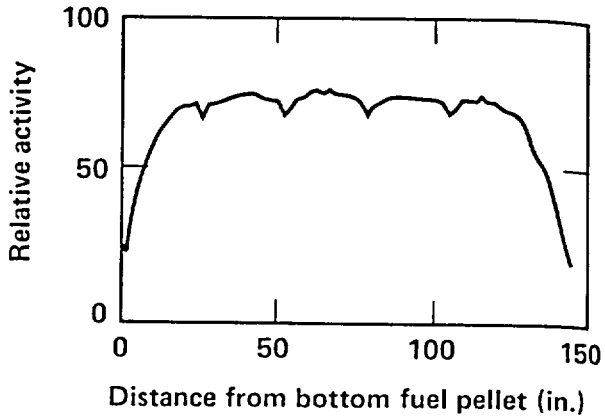

Figure 6-4. Cesium 137 gamma scan for D04-39 (after Davis, 1980).

structural members showing a uniform flat black oxide layer. Minor scratches on grid straps and tiebacks were attributed to handling. About half the rods around the periphery were seated in the bottom tie plate, very few were distorted, and none were in rod-to-rod contact.

Inspection of 20 rods from assemblies D01 and D04 showed them to have generally the same appearance. No gross distortions were reported. The oxidation varied from a flat dark black near the bottom to a uniform light gray near the top. In the range of 1.52 to 2.54 m (60 to 100 in.) from the bottom of the rod was the transition in coloration. In this region, the coloration was spotted with a blotchy combination of black and light gray. Scratches attributable to rod insertion and removal were also noted, in some cases along the entire rod length. Lighter colored circumferential rings were frequently observed, coinciding with the ridges observed during profilometry and occurring at pellet-to-pellet interfaces.

6.3 Thermal Characteristics

The decay heat of the spent-fuel assemblies was calculated and measured (Schmittroth, Neely, and Krogness, 1982) to establish the power-generation curve for use in SFT—C thermal and thermomechanical calculations (Chapter 3). Calculations were performed with ORIGEN2 and calorimetry was performed at EMAD using a boiling-water calorimeter.

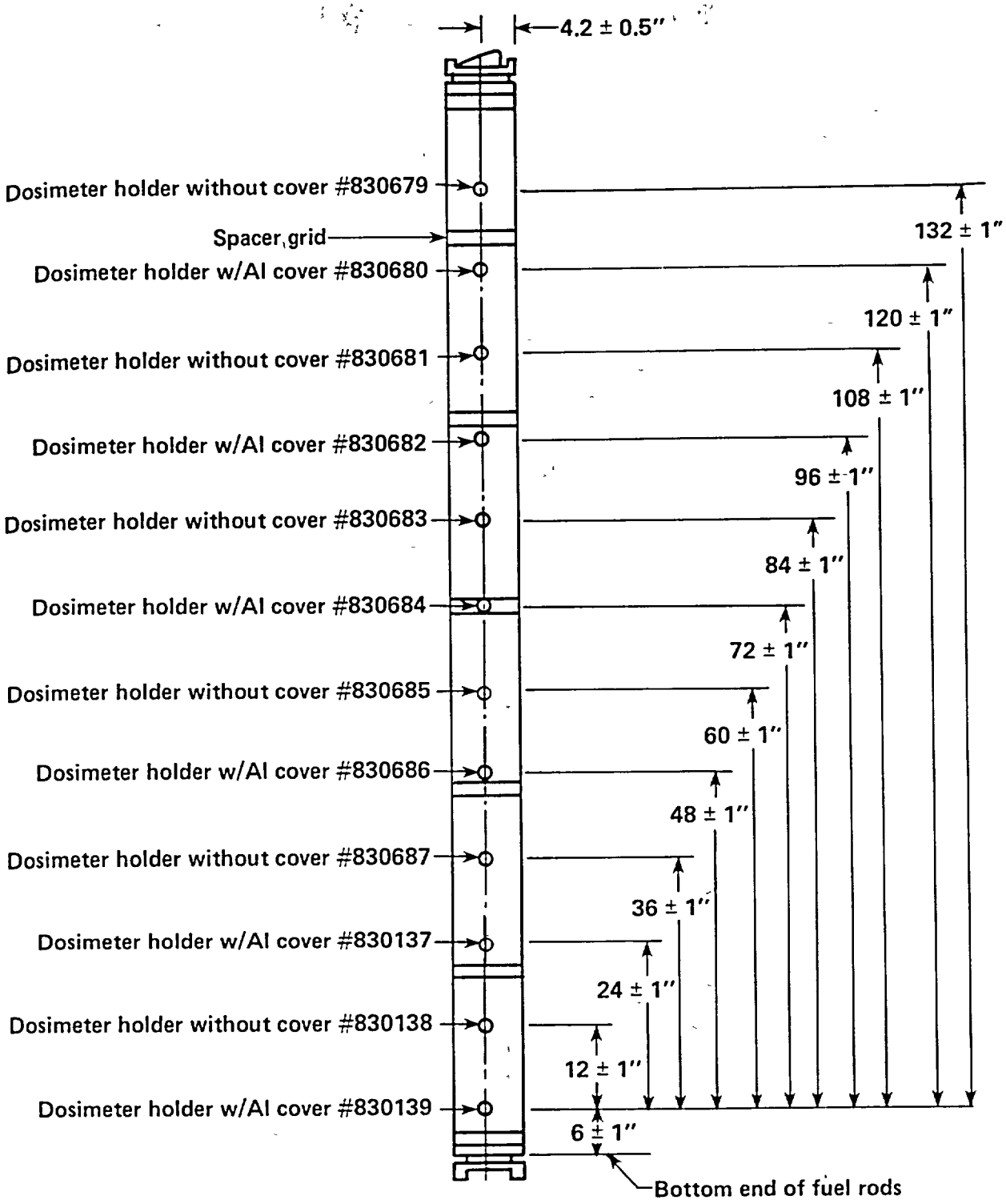

Figure 6-5. Locations of dosimeter holders (after Van Konynenburg, 1984).

Although the concepts of decay heat calculation are well established and commonly employed, there was little validation of the codes in use. This was particularly true for the short decay times of interest in the SFT—C. Factors affecting uncertainty in the calculations include the complexity of the early-time isotope inventory, uncertainties in reactor operating history and spectrum, and uncertainties in the basic nuclear cross-section and decay data.

The ORIGEN2 calculations of Schmittroth, Neely, and Krogness (1982) used the fuel characteristics and reactor history discussed earlier in this chapter. They report a total calculational uncertainty of about 8.6%.

The calorimeter configuration shown in Fig. 6-6 was used to obtain decay heat measurements on assemblies D34, D04, D15, and D22. By evaluating differential steam condensation collection rates, the power contribution of each fuel assembly was determined. Anticipated accuracies were ±5% for powers greater than 1.0 kW, decreasing to ±10% for powers of 0.1 kW.

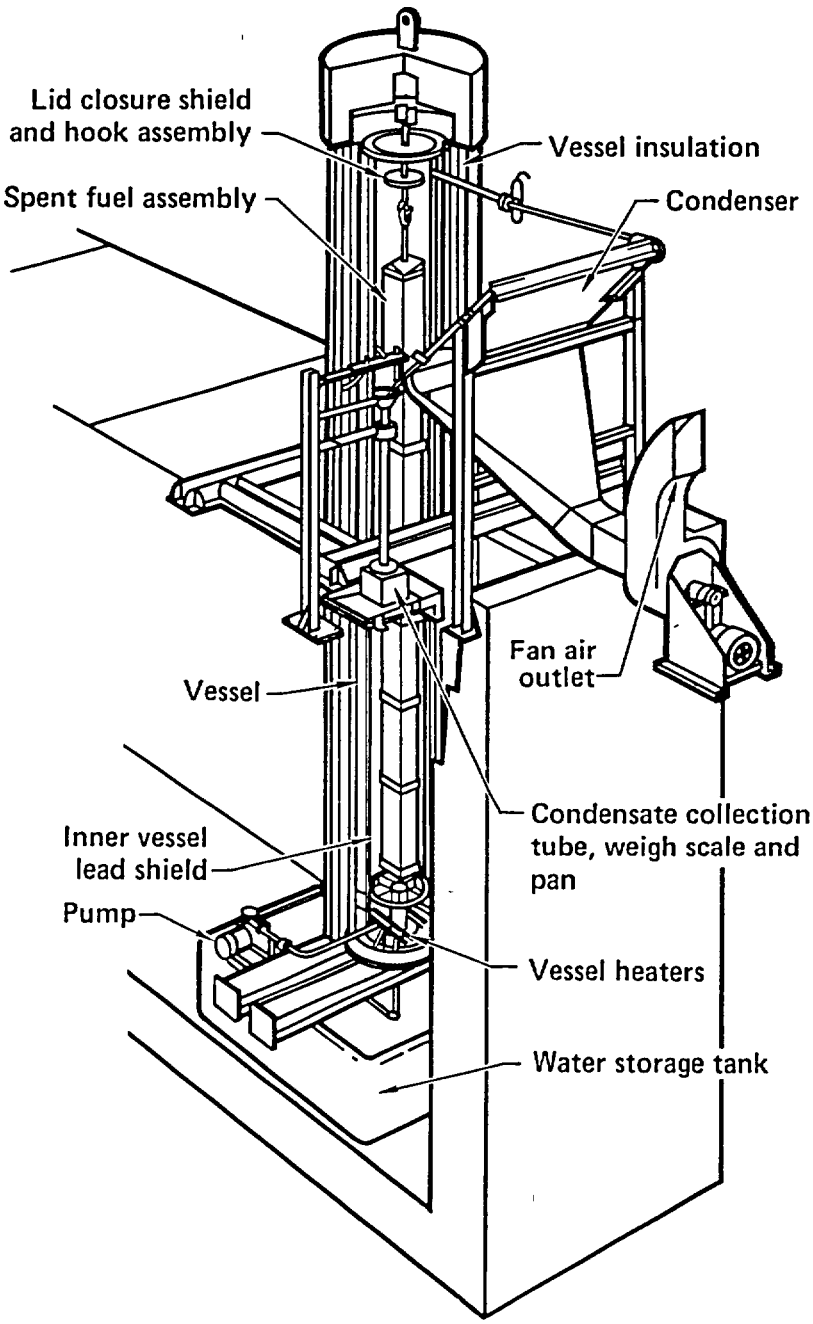

Figure 6-6. Spent-fuel calorimeter (after Schmittroth, Neely, and Krogness, 1982).

Table 6-6 indicates the good level of agreement between the measured and calculated decay heats for these assemblies at early times. With the exception of D04, all agree within 6%. Low confidence is expressed in the D04 measurement because reanalysis of the data indicated that thermal equilibrium was not obtained during calorimetry of this assembly.

Additional calorimetry was conducted throughout the testing period (Table 6-6). Of particular interest is fuel assembly D15, which was calorimetered at EMAD on July 28, 1983, following spent-fuel retrieval. Using essentially the same apparatus as the earlier measurements, a decay heat generation rate of 625 W was measured (Patrick et al., 1984). This is within 3% of the calculated rate of decay heat generation of 609 W.

Table 6-6. Summary results of calorimetry of spent-fuel assemblies used in the SFT—C.

Fuel assembly number	Calculated burnup (MW·d/MTU)	Calorimetry date	Fuel age, (YOC)	Decay heat (W)		Error[c] (%)
				Meas.[a]	Calc.[b,c]	
D04[d]	28,430	05/20/80	2.500	1385[e]	1555	+12.3%
	28,430	08/28/85	7.773	487	N/A	N/A
D15	28,430	07/08/80	2.634	1423	1491	+4.8%
	28,430	01/06/81	3.132	1126	N/A	N/A
	28,430	07/28/83	5.687	625	N/A	N/A
	28,430	08/22/85	7.756	506	N/A	N/A
D22	26,485	07/09/80	2.637	1284	1357	+5.7%
D22	26,485	08/29/85	7.775	451	N/A	N/A
D34	27,863	04/01/80	2.366	1550	1640	+5.8%
D34	27,863	03/29/84	6.357	467[f]	N/A	N/A
D34	27,863	08/21/85	7.754	479	N/A	N/A

[a] Measurement uncertainty is 5%.

[b] Calculational uncertainty is 8.6%.

[c] After Schmittroth, Neely, and Krogness (1982).

[d] Calculated value is reduced by 213/217 to account for the removal of four fuel pins.

[e] Possible calorimetry error.

[f] Invalid calorimetry result.

7. Spent-Fuel Handling System*

A spent-fuel handling system comprising a surface transport vehicle (STV), canister hoisting system (CHS), and underground transfer vehicle (UTV) was designed, fabricated, and deployed to demonstrate the feasibility of handling and storing spent nuclear fuel. In addition to describing this system, we also discuss the spent-fuel canister design and storage configuration and the encapsulation of the spent-fuel assemblies for test storage.

Although the handling system was not intended to be prototypical of what might be used in a future full-scale repository, it incorporated several concepts that should be considered in developing such systems for future repositories, including (Ballou, 1983):

- An integral shielding plug that minimized radiation streaming.
- Transfer cask jacking and shielding gates that reduced excavation height requirements.
- A small-diameter shaft for the sole purpose of transferring spent fuel to and from the underground storage area.
- A wire-line hoisting system with a positive emergency braking system that travelled with the spent-fuel canister.
- A rail-mounted underground transfer vehicle that obviated the need for personnel to be underground during transfer operations.
- Remotely actuated grapples that were insensitive to load orientation.

Note that the entire spent-fuel handling process (after the spent-fuel assemblies were received at EMAD) took place at the DOE-controlled NTS. Thus, the Nuclear Regulatory Commission's and Department of Transportation's regulations governing transport of radioactive materials over public roads did not apply. Consistent with assuring safety and attaining test objectives, cost and development time were strong constraints.

7.1 Preparation and Use of EMAD

One of the attractions of conducting the SFT—C at the NTS was the availability of the EMAD facility. Originally constructed in the 1960s to support the nuclear rocket propulsion program, the facility had recently fallen into disuse. When the DOE began evaluating handling and encapsulation aspects of nuclear waste disposal, the role of EMAD developed to include not only support to the SFT—C but broader aspects of a Spent-Fuel Handling and Demonstration Program (NVO-198). This facility is operated for the DOE by Westinghouse Electric Corporation.

The principal features of EMAD that were important to the SFT—C were its large shielded highbay, adjacent shielded transfer ports and smaller shielded cells, and a variety of remote manipulators for assembling and loading spent-fuel canisters in a shielded environment. Facilities for spent-fuel dosimetry and calorimetry were also developed and used to support the SFT—C. The reader is referred to the EMAD Safety Assessment Document (NVO-198) for a detailed description of the facility and its operations.

7.2 Transport from the Reactor

Thirteen spent-fuel assemblies having the characteristics discussed in Chapter 6 were received at EMAD for use in the SFT—C. These were shipped from the Florida Power and Light Company Turkey Point Unit No. 3 to EMAD in NRC-licensed shipping casks in accordance with Department of Transportation (DOT) regulations (Fig. 7-1).

After arrival at EMAD, the tractor-trailer rig was parked in the highbay and the cask was removed and readied for removal of the spent-fuel assembly. Under remote operating conditions, the shielding head was removed and the spent-fuel assembly was withdrawn from the cask, inspected, and placed in lag storage awaiting encapsulation. Details of these operations are provided by Bensky et al. (1979).

---

* Contributed by W C. Patrick.

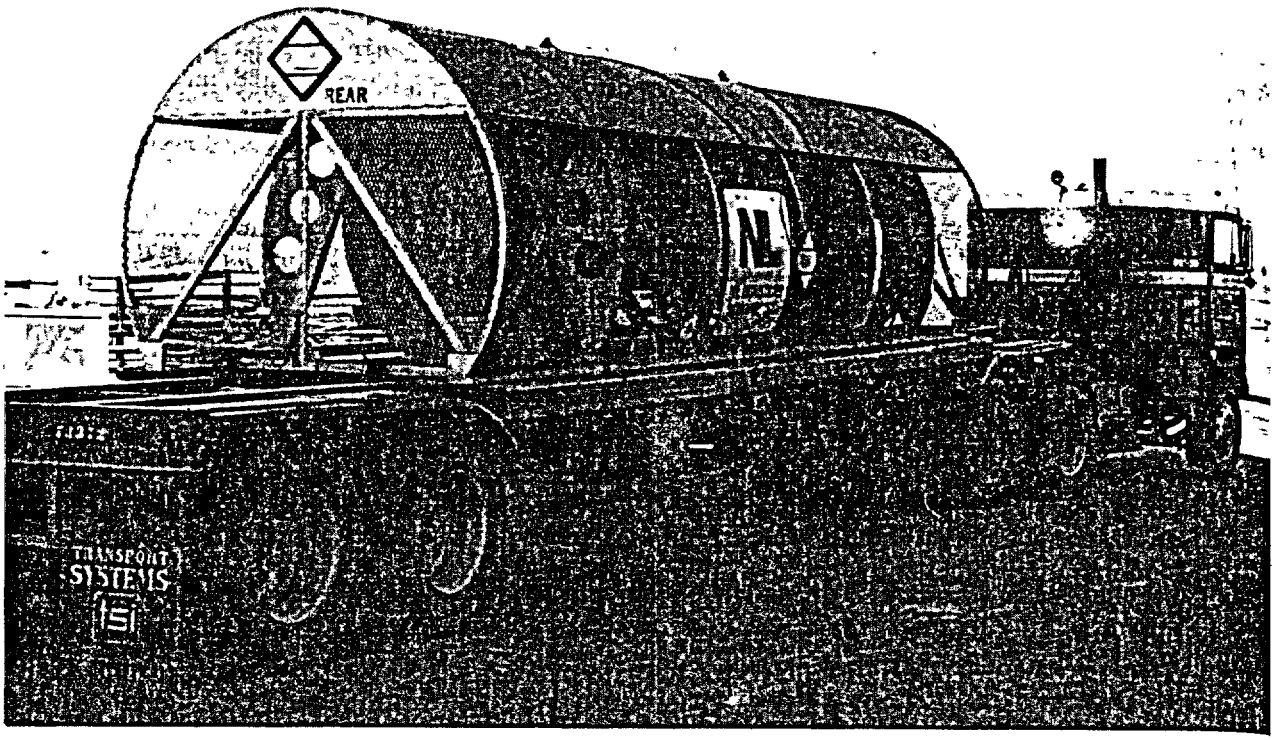

Figure 7-1. NLI 1/2 cask/trailer/tractor as received at EMAD.

7.3 Canister Design and Storage Configuration

The spent-fuel assemblies described in Chapter 6 were encapsulated in gas-tight stainless steel canisters in preparation for transport and storage activities associated with the SFT—C. The total fuel assembly cross section [0.214 × 0.214 m (8.43 × 8.43 in.)] and length [4.097 m (161.3 in.)] were the principal dimensional controls on canister design.

As presented in the SAD (NVO-210), the design basis for the spent-fuel canisters was to provide a corrosion-resistant, leak-tight container with provisions for:

- Containing one fuel assembly (Chapter 6).
- Remote closure and sealing by welding.
- Remote evacuation, gas backfilling, and leak testing.
- Maintaining leak tightness at an internal gas pressure of 200 psig at 200°F and when subjected to 0.7 g of horizontal acceleration.
- Interfacing with EMAD and SFT—C storage wells and shield plugs.

The shield-plug design basis was to provide:

- Radiation attenuation and streaming protection to limit the surface dose rate to 50 mrem/h.
- Mechanical support to maintain the integrity of the canister shield-plug system at horizontal ground accelerations of 0.7 g.
- Means for thermocouple installation.
- An interface with the handling system grapple.

The resulting spent-fuel canister comprised a main body, an upper body, a closure lid, and an ellipsoidal end cap (Fig. 7-2). A standard 356-mm-outside diameter (14-in.), 9.52-mm wall thickness (0.375-in.) Type 304L stainless steel pipe section 3.91 m (154 in.) long formed the main body, and a 9.52-mm wall thickness (0.375-in.) standard ellipsoidal end cap with an internal cruciform fixture of 19.1-mm (0.75-in.) stainless stock formed the bottom closure. On the top of the main body was welded a 356-mm-outside diameter (14-in.) 23.8-mm (0.937-in.) wall 304L pipe section that was machined to include the provisions

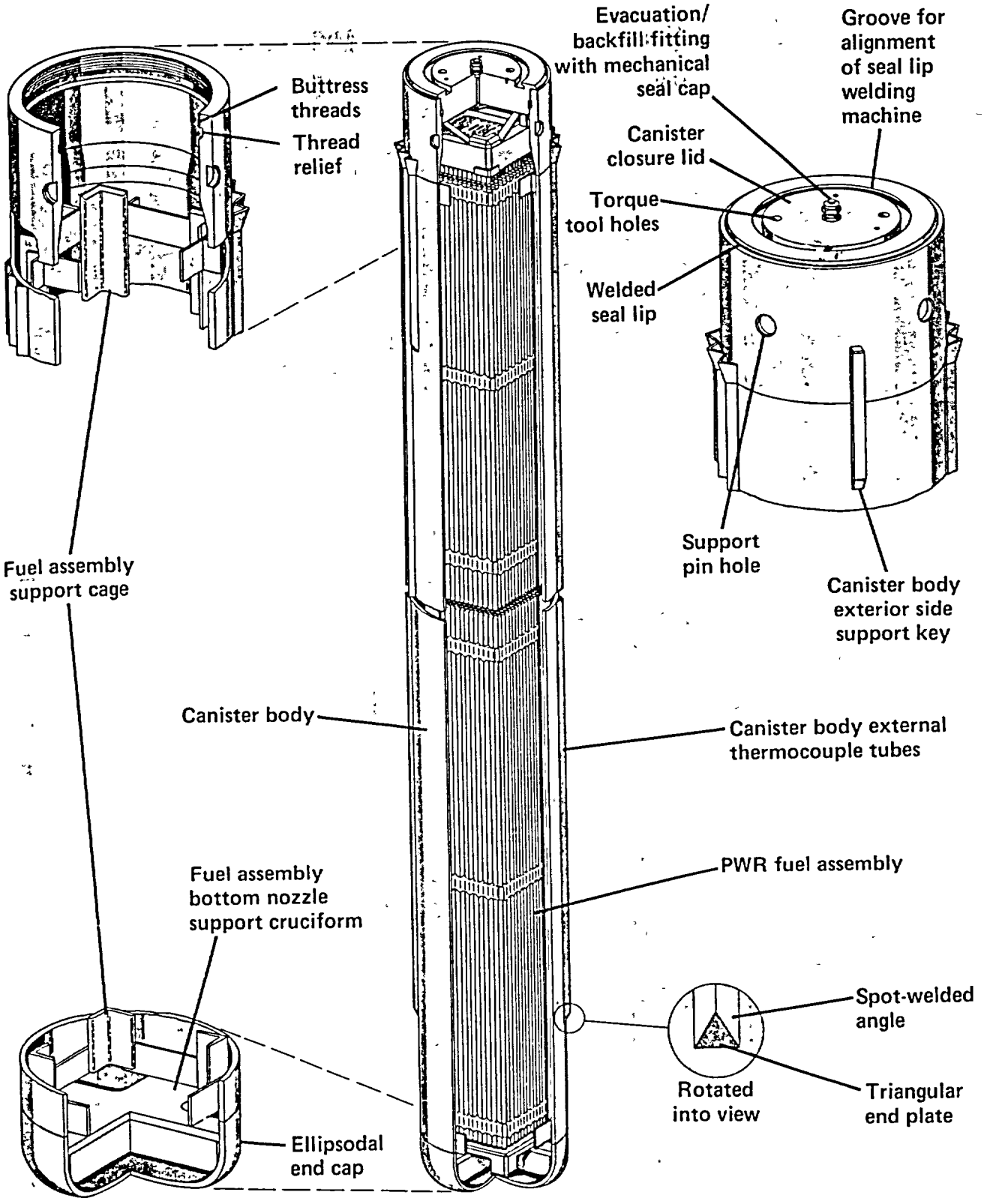

Figure 7-2. Spent-fuel canister assembly (after NVO-210, 1980).

indicated in Fig. 7-2. In addition, an internal support cage was provided to stabilize the spent-fuel assembly during transport and potential ground shaking, limiting its lateral movement to approximately 7.6 mm (0.3 in.). All welds were made using 308L weld wire in accordance with Section IX of the ASME code, and all were dye-penetrant tested.

The canister top closure consisted of a 8.9-cm-thick (3.5-in.) by 318 mm-diameter (12.5-in.) 304L disc with buttress threads machined near the top. A machined lip and capped fitting accommodated seal welding, backfilling, and leak-testing operations, respectively. To enhance conductive heat transfer, the canisters were backfilled with helium. Each canister was leak-tested against a criteria of 1×10^{-5} std cc/s. Other details of this design are discussed in NVO-210 (1980).

On each side of the canister body, three 304L stainless steel angles were welded to provide for thermocouple installation and positioning. These channels were of three lengths to position the thermocouples 0.3 m (1 ft) below the top, at the mid-height, and 0.3 m (1 ft) above the bottom of the spent-fuel rods.

To provide for radiation shielding, a mild steel block was machined for attachment to the spent-fuel canister (Fig. 7-3). Features of this shield plug included a tapered shoulder to minimize streaming radiation, guide tubes for thermocouple sensors, and a grapple lifting knob. The emplacement configuration at the SFT—C is shown in Fig. 7-4.

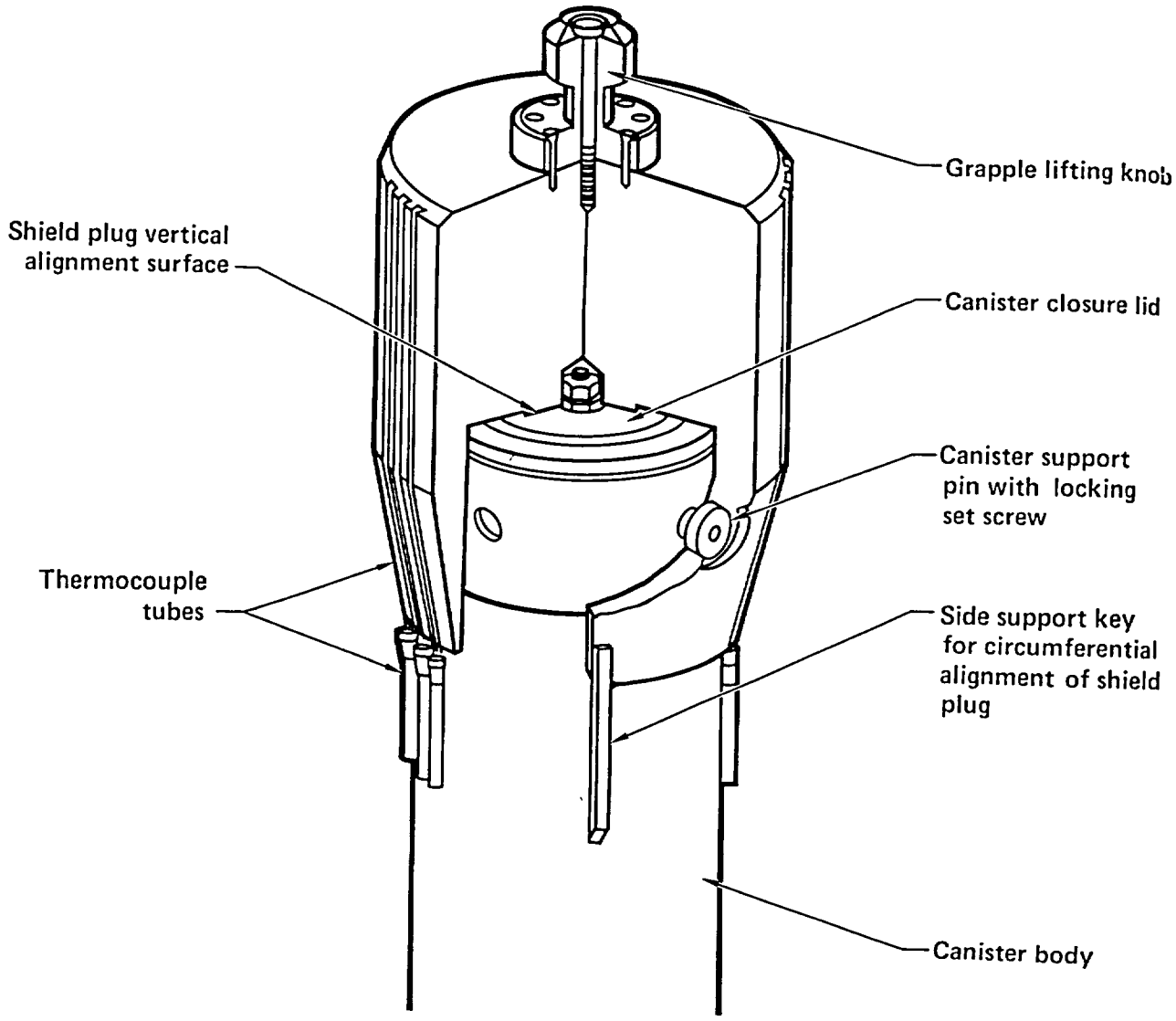

Figure 7-3. Canister/shield-plug mating arrangement (after NVO-210, 1980).

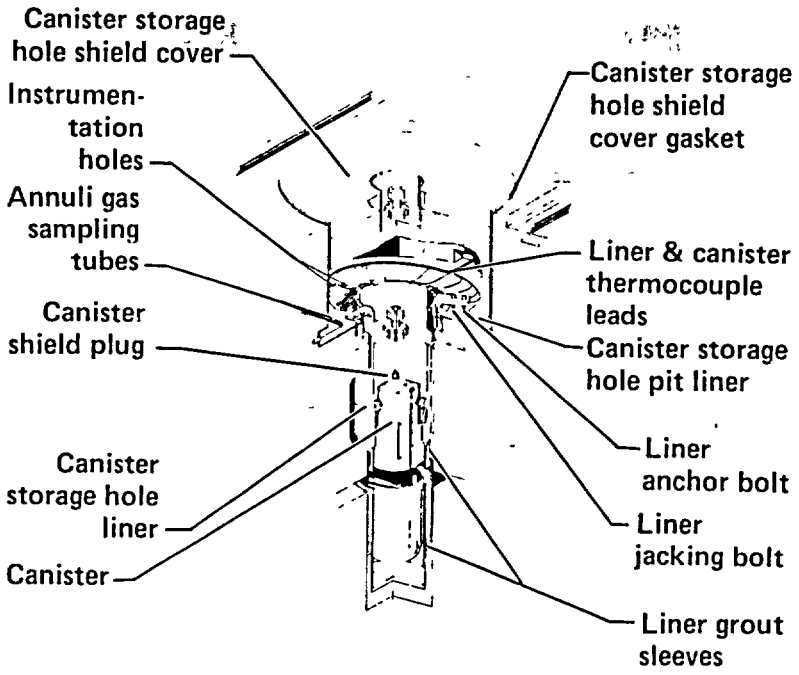

Figure 7-4. Canister storage configuration (after NVO-210, 1980).

We selected 304L stainless steel because of its generally good corrosion resistance. Because potential sensitization could lead to accelerated intergranular corrosion in the presence of chloride ion in the groundwater, we selected a low-carbon type (less than 0.03%). An emplacement borehole liner further limited the likelihood of corrosion by preventing the inflow of water (Chapter 5).

As part of a separate program, a similar canister design was tested on a shaker table to 0.7 g using a dummy fuel assembly (WAES-TME-2906). Negligible wear and impact damage were observed in this study. Additional testing showed successful performance at a pressure of 300 psig at 700°F. These tests confirmed the adequacy of the design.

7.4 Surface Transport Vehicle

The first component of the handling system was the STV, which was designed and fabricated to transport canistered spent-fuel assemblies between the EMAD and SFT—C facilities. The design basis for the STV was to provide:

- Safe and reliable transport of canistered spent fuel between EMAD and the SFT—C.
- Radiation shielding to meet DOE requirements for the transport of radioactive materials under test conditions.
- Heat dissipation to limit fuel cladding temperature to less than 380°C (715°F).
- Interfacing with EMAD and SFT—C site handling systems.
- Remotely controlled movements of a shielding cask and associated shielding gates with appropriate interlocks to minimize radiation exposure.

Based on these considerations, an STV comprising a heavy-duty 16-wheel semitrailer with a remotely operated shielding cask was designed and fabricated. This unit was transported by a standard 10-wheel tractor (Figs. 7-5 and 7-6) and was designed to conform to 49CFR and the State of California Vehicle Code (with the exception of allowable gross weight). Although the basic semitrailer weighed 9000 kg (19,800 lb), the addition of the 1.14-m-outside diameter, 33-cm wall thickness steel cask, closures, and related equipment increased the total weight to 48,000 Kg (105,600 lb).

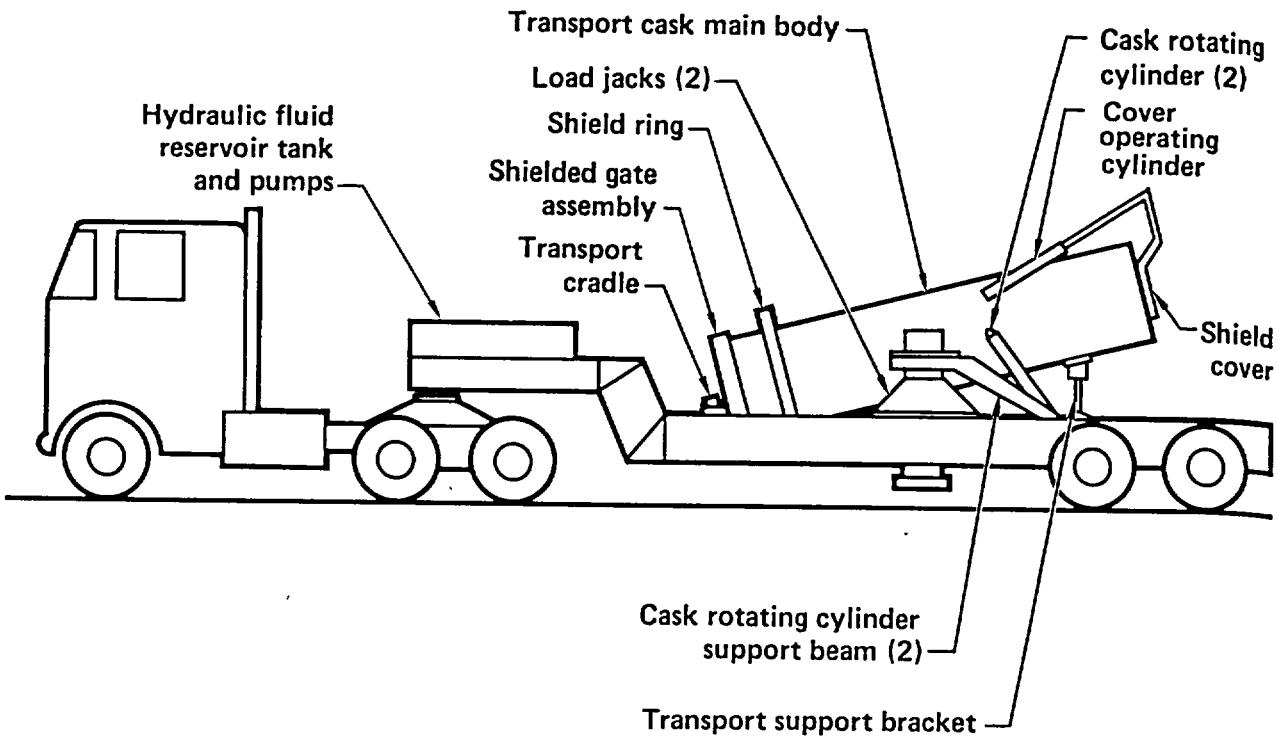

Figure 7-5. Surface Transport Vehicle schematic (after NVO-210, 1980).

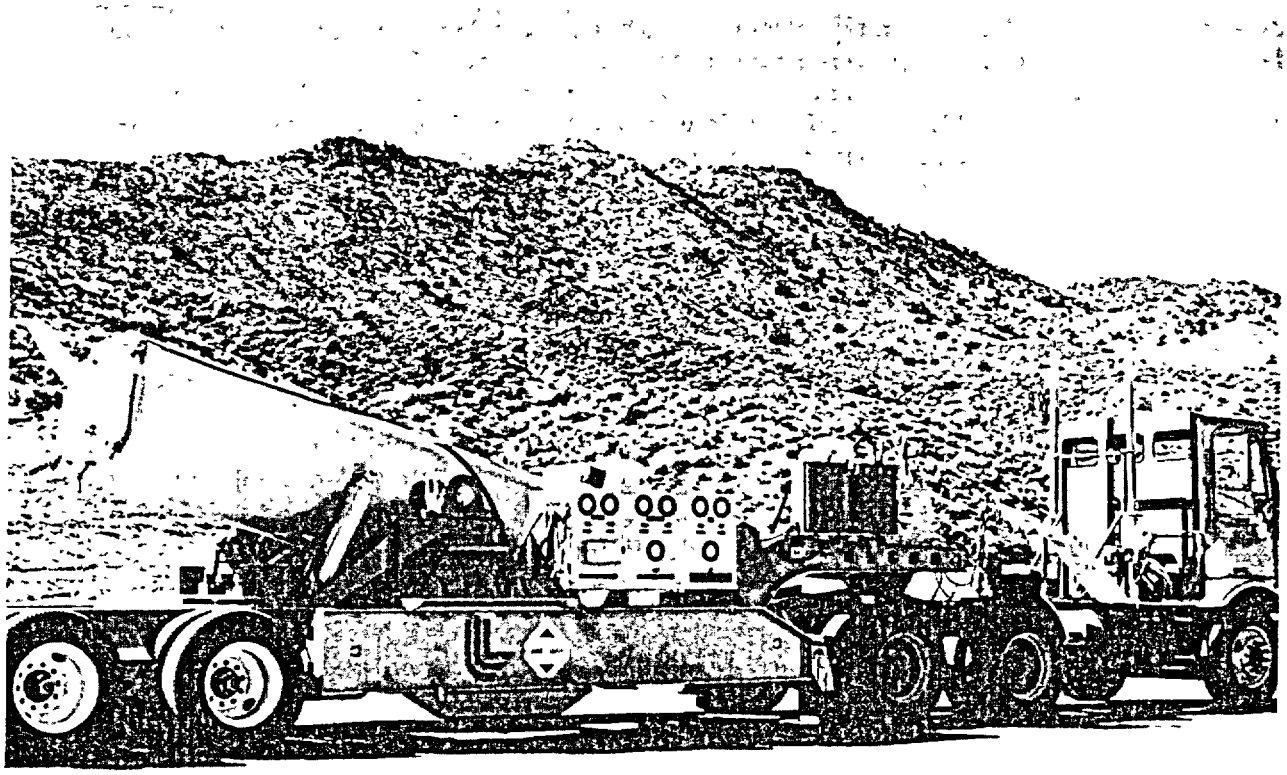

Figure 7-6. Surface Transport Vehicle.

Several inspections and evaluations were conducted to ensure the structural adequacy of the STV trailer. These included review of drawings, independent stress analyses, and magnetic-particle and dye-penetrant testing of critical welds. In addition, a static load test to 159% of the static design load was conducted. No measurable plastic strains were observed (NVO-210, 1980). Finally, dry runs were conducted, using a simulated spent-fuel assembly at dynamic loads up to the 1.5-g design criterion.

The cask consisted of a 1.14-m-outside diameter (45-in.) 4.67-m-long (184-in.) cylinder of low carbon manganese steel with a wall thickness of 330 mm (13 in.). At the top end of the cask, its inside diameter was reduced to about 457 mm (18 in.) to provide lateral support against the canister shield plug. A 241-mm-diameter (9.5-in.) diameter hole was bored in each side of the cask and fitted with trunnions to facilitate cask rotation.

To accommodate loading through the top at EMAD and unloading through the bottom at the SFT—C, both top and bottom closures were provided. Although the upper closure included a lid rotated by a hydraulic cylinder, the bottom closure was a gear-driven sliding gate. The top shield cover was about 184 mm (7.25 in.) thick and weighed about 523 kg (1150 lb). The bottom gate comprised a 432-mm-thick (17-in.), 1545-kg (3400-lb) block supported on slide bars. An elliptical contour on the inside of the gate provided lateral support for the canister during transport and effectively locked the gate closed, precluding accidental opening of the gate. Machined steps in the gate top surface and gate assembly mated with steps in the bottom of the cask to minimize radiation streaming. Pins were incorporated in the design to fix these gates and the entire shielding cask in position for transport.

The cask was oriented vertically during loading and unloading operations. It was rotated through 75° and lowered onto a cradle for stable transport. Transport speeds were limited to about 55 km/h.

The 330-mm (13-in.) steel shielding of the cask kept surface dose rates to about 15 mrem/h gamma and from 70 to 90 mrem/h neutron. Dose rates in the STV tractor cab were about 0.05 mrem/h gamma and 0.5 mrem/h neutron.

The cask rotation and jacking system is shown schematically in Fig. 7-5. See NVO-210 (1980) for a more detailed discussion of the STV, including the hydraulics and interlock systems.

7.5 Canister Hoisting System

The second component of the handling system was the CHS. The principal function of the CHS was to lower or raise the canistered spent-fuel assembly between the STV (which was positioned over the canister access shaft) and the UTV (which was positioned at the base of the canister access shaft 420 m below).

The design basis of the CHS was to provide:

- Safe and reliable lowering and raising of encapsulated spent-fuel assemblies between the STV and UTV.
- Handling and shielding interfaces with the STV and UTV.
- Support of the design loads with adequate safety factors.
- Capability for remote and emergency manual grappling and ungrappling of the canister.
- Means for controlling speed, detecting the canister's position, and sensing the load.
- Redundant means for stopping the hoist with or without electrical power.
- Means for preventing canister free-fall in the event of cable or hoist failure.
- Protection of the hoisting and internal electrical cable.
- Control system to ensure proper sequencing of operation, minimize personnel radiation exposure, and protect equipment.

The principal components of the resulting CHS are the headframe, hoist, hoist cable, emergency brake, grapple, and control system. Each component is discussed briefly here. See NVO-210 (1980) for further information.

7.5.1 Headframe

Located directly over the canister access shaft, the headframe structure comprised four vertical ASTM A-36 steel beams that were anchored to four 1.52-m-square (5-ft) reinforced concrete pads and cross beams that supported the sheave, provided positive stops to the vertical travel of the spent-fuel canister, and provided resistance to the transverse component of cable load (Fig. 7-7). The anchor pads were 0.76 m thick

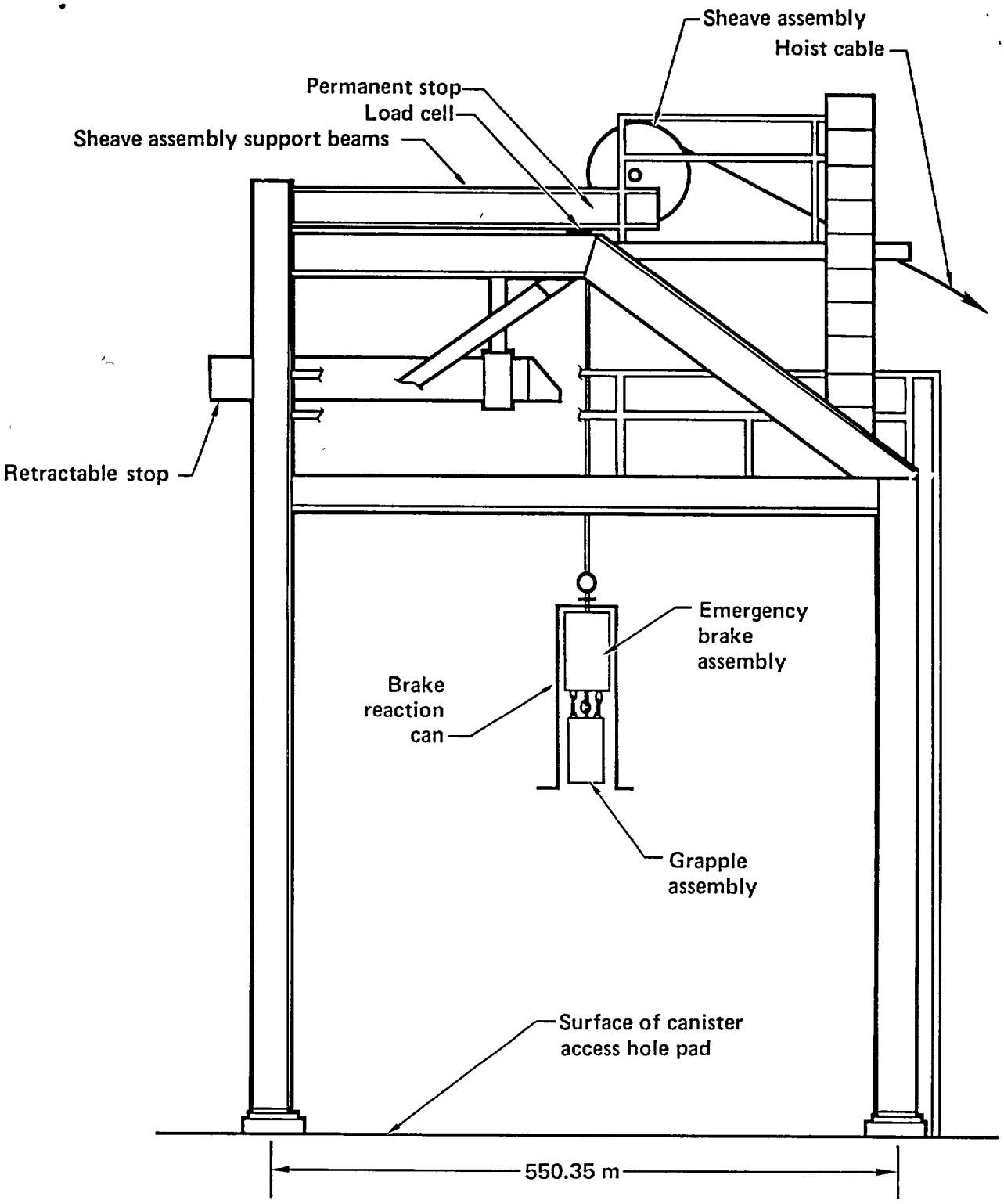

Figure 7-7. Canister access hole head frame (after NVO-210, 1980).

(2.5 ft) opposite the cable and 1.37 m thick (4.5 ft) on the cable side. The headframe was fabricated and erected in accordance with appropriate standards (NVO-210, 1980).

The 797-mm-diameter (31-3/8-in.) cast steel sheave was mounted to two horizontal beams by means of its 88.9-mm-diameter (3.5-in.) steel shaft and two pillow blocks. Load cells and a tachometer were provided to sense cable load and velocity.

A permanent mechanical stop (Fig. 7-7) was provided to prevent the brake and grapple assembly from being raised to where they could damage the sheave. Immediately below this stop were electrical limit switches that were set to stop the hoist when the grapple/brake assembly was within 25 mm (1 in.) of the stop.

To preclude raising a spent-fuel assembly partially out of the shielding cask, a retractable stop was also provided (Fig. 7-7). Once again, limit switches were used to stop the hoist when the grapple/brake was within 25 mm (1 in.) of the retractable stop.

7.5.2 Hoist

The cable drum, drive system, and braking system that made up the hoist were located in a hoist house adjacent to the headframe (Chapter 5) and were bolted to a concrete foundation. The cable drum was a 0.80-m-diameter (31.5-in.) by 1.02-m-wide (40-in.) reinforced steel cylinder with 1.24-m-diameter (49-in.) flanges in each end. A 127-mm-diameter (5-in.) steel shaft riding in two bearing assemblies supported the drum in a steel plate frame.

Because of the close proximity of the headframe and hoist, maximum fleet angles of 1.7° were encountered. To ensure that the five layers of cable could be properly laid on the drum, an air-driven level-winder was provided.

A variable-speed, 20-hp dc motor mounted behind the drum powered it through a worm-gear and chain-drive system. The worm-gear 50-to-1 reducer and drive mechanism were self-braking: the drum could not turn without power even if the brakes were not set.

The hoist braking system comprised spring-set calipertype brakes on each of the drum flanges. In this design, the brakes were set until they were retracted by an air-activated hydraulic pump. Thus, the CHS "failed safe" by applying the brake when power or hydraulic pressure were lost. If cable speeds exceeded certain limits, these brakes automatically set.

7.5.3 Hoist Cable

To provide for signal and sensing communications between the control system and grapple/brake assembly, the 20.7-mm-diameter (0.815-in.) hoist cable was provided with an inner core of 18 No. 20 AWG insulated shielded pairs. These were wrapped around a polypropylene rod. Two contrahelical layers of high-strength galvanized steel wires formed the outer tension member of the cable, which had a tensile strength exceeding 18,180 kg (40,000 lb).

7.5.4 Emergency Brake Assembly

Mounted on the lower end of the hoist cable was an emergency brake assembly capable of preventing the canister from free falling in event of a hoist or cable failure. The 457-mm-diameter (18-in.) by 889-mm-long (35-in.) cylindrical main body of the brake was fabricated from 6061-T6 aluminum alloy. The principal components of the brake are depicted in Fig. 7-8.

During normal operations, the canister payload compressed the activation springs, thus retracting the serrated wedge brake shoes. If loss of load occurred, these wedges were driven out against the canister access shaft casing, stopping the descent of the canister. A brake reaction can (Fig. 7-7) was provided on the headframe to make the brake operable when the canister was in the shielding cask with the bottom gate open.

A motor-driven locking cam was provided to deactivate the brake during those sequences of the handling operation when the canister load was not acting on the brake assembly. In addition, an emergency lifting capability was provided to facilitate recovery of a spent-fuel canister in the event of a cable failure. An upward lifting force on this knob would release the wedge brakes, allowing the canister to be retrieved.

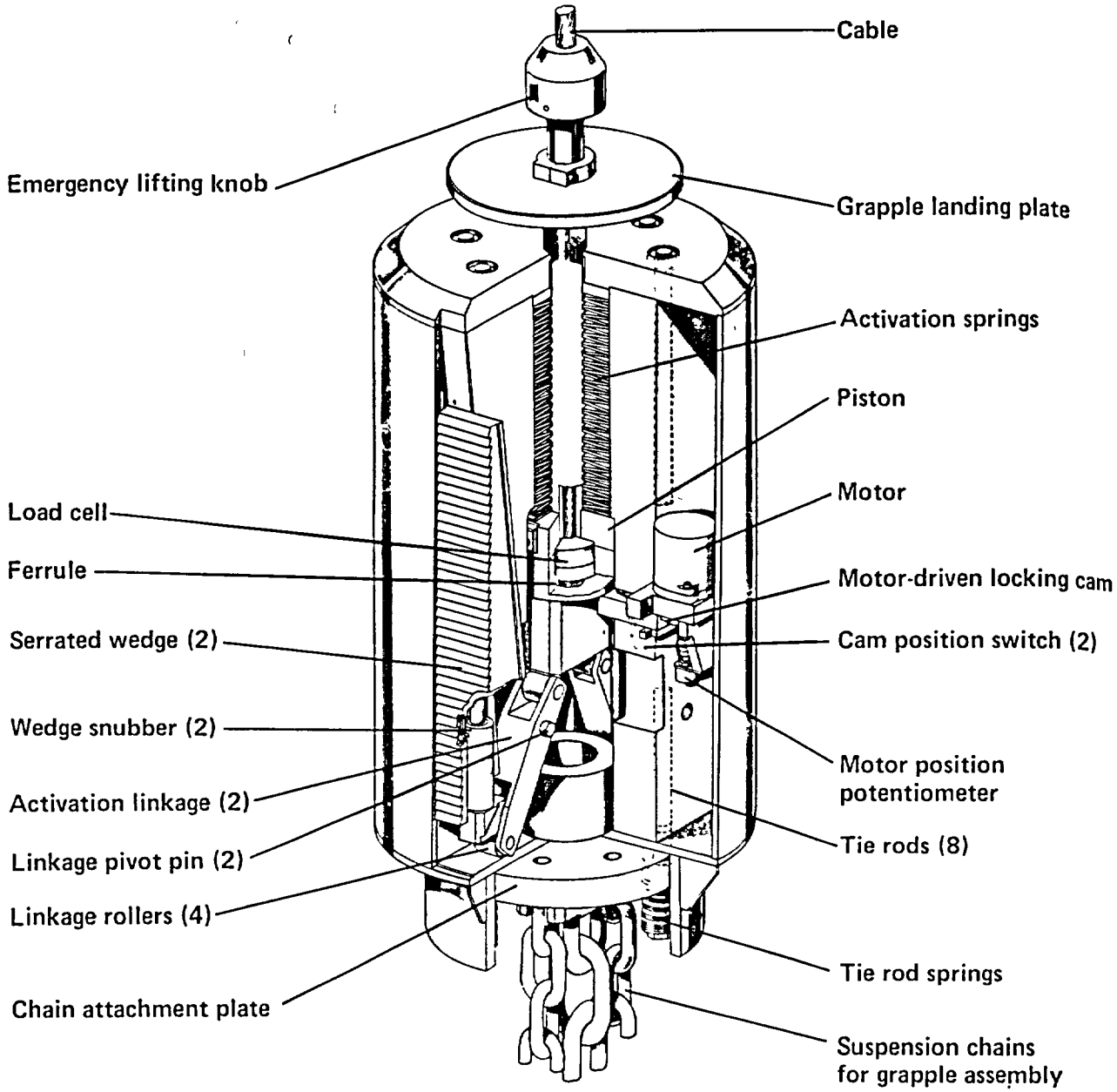

Figure 7-8. Emergency brake assembly (after NVO-210, 1980).

7.5.5 Grapple Assembly

Grapple assemblies were required at each handling interface. A common design was used at EMAD (where it was suspended from the overhead crane), on the CHS (where it was suspended by chain links from the braking system), and on the UTV (where it was suspended from an on-board jib crane).

The 266.7-mm-diameter (10.5-in.) by 558.8-mm-long (22-in.) grapple body housed a motor-driven worm-gear assembly that rotated a spherical locking ball (Fig. 7-9). In addition to electronic control through limit switches, the locking ball was designed to self-lock when carrying a load. This was done by enlarging the internal radius at the load-carrying (closed) position to 73.02 mm (2.875 in.). The 71.76-mm (2.825-in.) radius of the canister lifting knob (Sec. 7.3) rested in this low spot, preventing rotation of the locking ball.

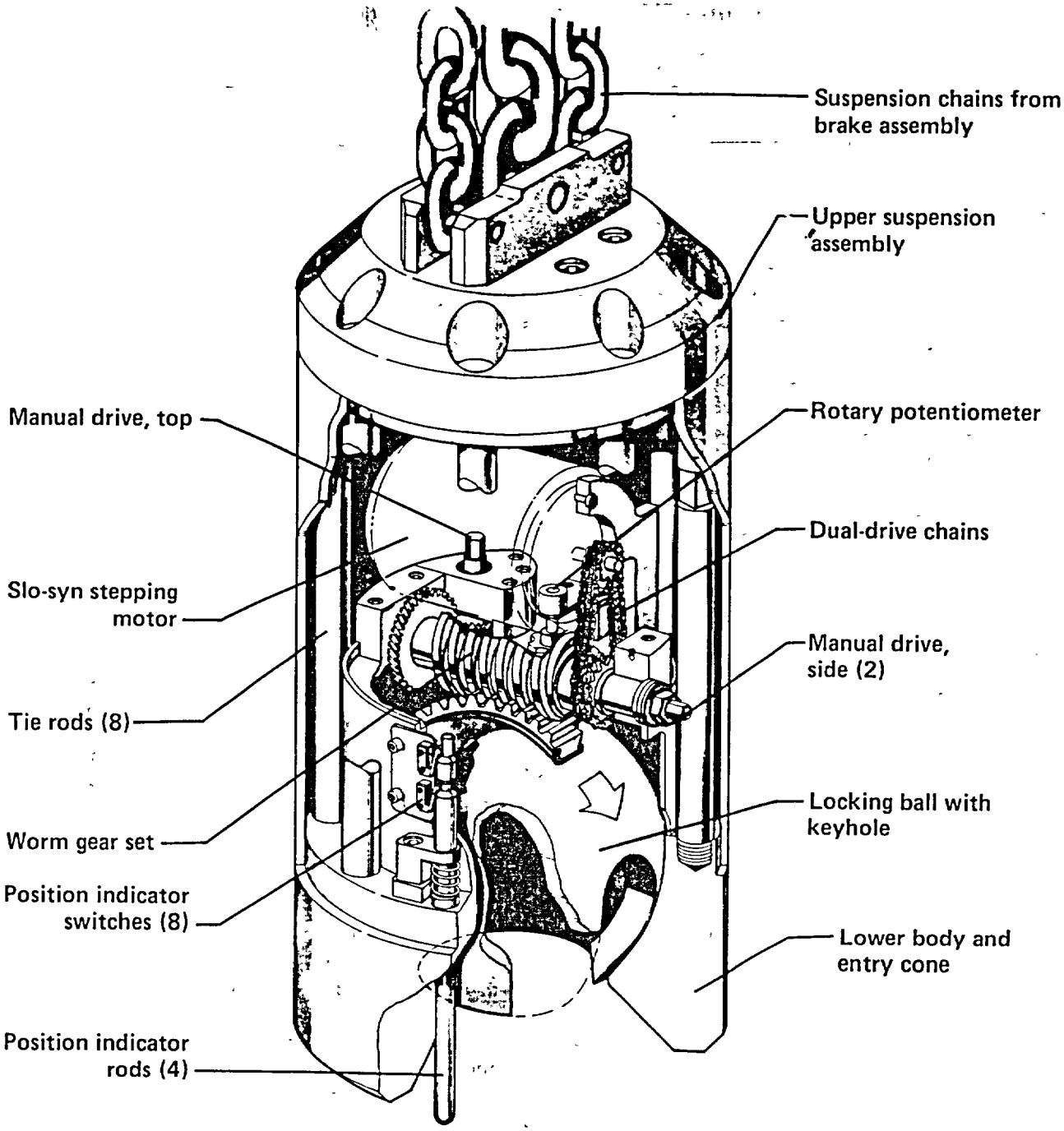

Figure 7-9. Grapple assembly (after NVO-210, 1980).

7.5.6 Control System

A control system located adjacent to the hoist house provided controls for the STV, UTV, and CHS. Pertinent portions of this system relevant to STV operations were duplicated in a control console at EMAD.

The heart of the control system was a solid-state sequential logic controller designed with interlocks and automatic operational controls to prevent unsafe handling configurations. Nearly all positioning operations were automatically controlled by this system. In addition to the logic and electronic interlocks, administrative controls and operating procedures were integral parts of the control system. Cameras were

provided on the headframe and the UTV to provide visual confirmation of critical sequences in the operations.

The principal functions of the STV, CHS, and UTV provided by the control system were:

- STV and UTV cask positioning and gate opening and closing.
- Spent-fuel canister grappling and ungrappling by the CHS and UTV.
- Spent-fuel canister lowering and raising by the CHS and UTV on-board hoist.

7.6 Underground Transfer Vehicle

The third major component of the handling system was the UTV. The principal function of the UTV was to receive a spent-fuel canister at the base of the canister access shaft, to transfer it to and lower it into a canister emplacement hole, and to reverse the process for retrieval operations. The design basis for the UTV was to provide:

- Safe and reliable receipt and transfer of spent-fuel assemblies between the access shaft and emplacement holes.
- Heat dissipation to limit the fuel cladding temperature to less than 380°C (715°F).
- Means for electrical controls and interlocks.
- Support of design loads with adequate factors of safety.
- Means for remote grappling and ungrappling of spent-fuel canisters.
- Means for load monitoring.
- Redundant means of stopping hoist travel with or without electrical power.

The principal components of the UTV are the railcar, transfer cask, hoisting system, and control system. Each component is described briefly here. See NVO-210 (1980) for further information.

7.6.1 Railcar

The railcar chassis was 2.36 m wide (93 in.) and 5.18 m long (204 in.). Its four double-flanged wheels distributed the 59,000-kg (130,000-lb) load on rails located 1.96 m (77 in.) apart (Chapter 5). The two drive wheels were powered by a variable-speed dc motor through a worm-gear box and spur-gear drive.

Power, signal, and television cables were suspended in loops from an overhead support cable that spanned the distance from the railcar room to the receiving room. The three on-board TV cameras monitored all UTV operations, which were controlled from the surface.

7.6.2 Transfer Cask

The transfer cask was constructed from six cylindrical modules that were tied together by 12 external tie rods (Fig. 7-10). Precision-machined stepped interfaces limited the external dose rate to about 105 mrem/h. Because the capacity of the personnel and materials hoist that lowered these sections to the subsurface area were limited, the cask was fabricated in modules. Shields and gate assemblies were located at each end of the 1.14-m-outside diameter (45-in.) 0.483-m-inside diameter (19-in.) main cask body. Both of these gates were made up of opposing V-shaped blocks that were driven on rectangular ways through a pair of travelling nuts on lead screws. Stepping motors and limit switches controlled the movement and position of these gates. The top gate was provided with a 279-mm-diameter (11-in.) port through which the grapple could be attached to the canister with the top gate closed.

Because there was no requirement for rapid movement of the UTV over uneven surfaces, the shielding cask could be maintained in the vertical, upright position. Screw jacks were provided to raise the cask into a shielding collar at the base of the canister access shaft during transfer operations. These jacks also lowered the cask into the pits above each canister emplacement hole to provide a shielded interface during emplacement and retrieval operations.

7.6.3 Hoisting System

A 5-ton-capacity self-supported jib crane with a 3.75-ton double-reaved drum hoist was provided to transfer a spent-fuel canister between the cask and a canister emplacement hole. To remove the storage hole pit plug (Sec. 7.3), the jib was rotated outboard of the cask. Interlocks prevented the grapple from lowering far enough to engage a spent-fuel assembly outboard of the shielding cask. When rotated to the inboard position, the jib crane supported the grappling of a spent-fuel canister.

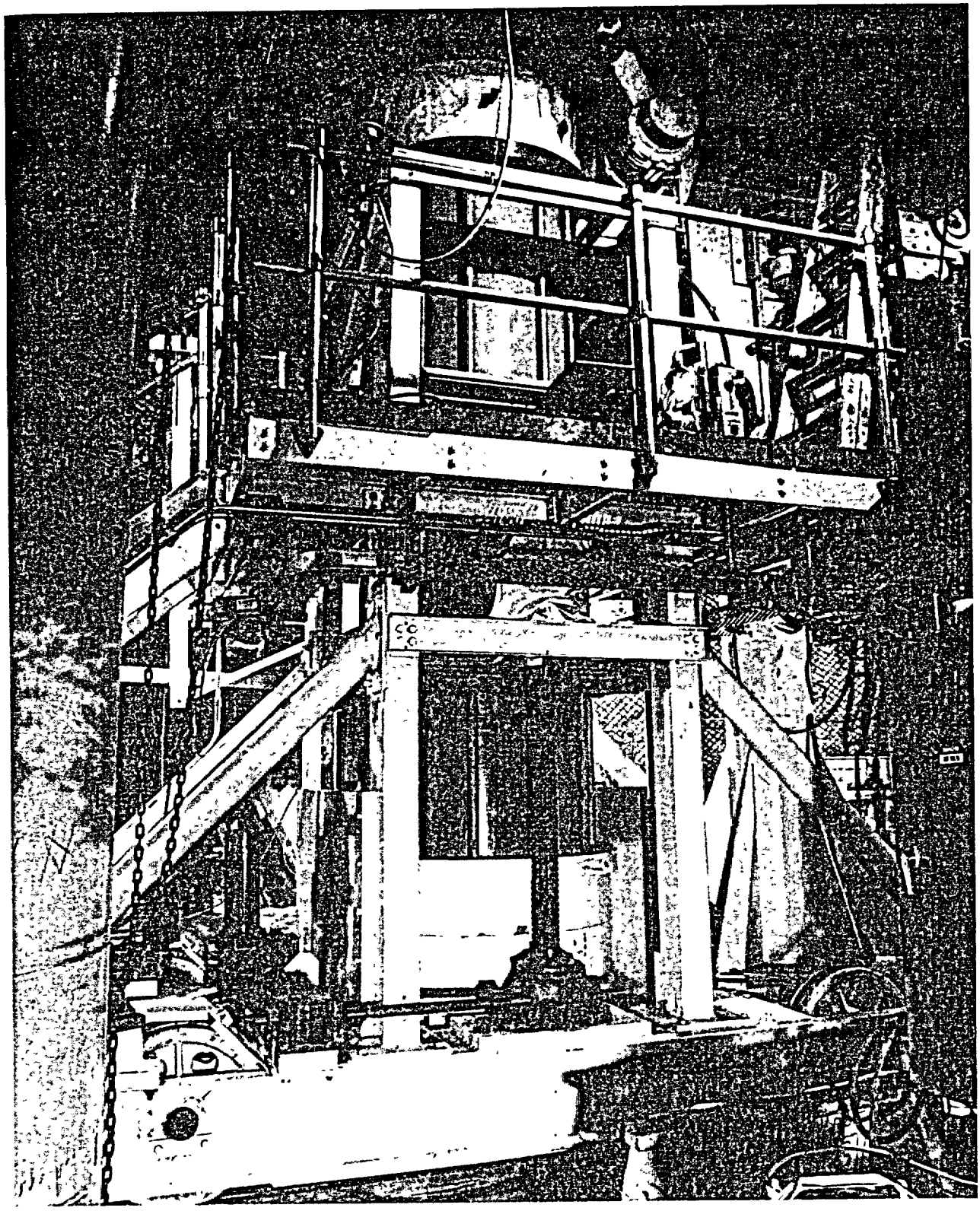

Figure 7-10. Underground Transfer Vehicle undergoing assembly and checkout in the railcar room.

A Weston-type mechanical brake and an electrical brake were provided for controlled lowering and raising of the canisters. In addition, the regenerative dc motor drive controlled lowering of the canister.

Two 12.7-mm-diameter (0.5-in.) stainless steel cables minimized rotation of the canister pit plug. Signals to the grapple were provided through a separate cable rather than through the load-carrying members.

7.6.4 Control Systems

The UTV was controlled at the surface, as discussed in Sec. 7.5. The principal controls were for railcar position and drive actuation, cask jack drive, jib rotation, gate position and drive actuation, jib crane position and actuation, and grapple activation.

8. Safety Assessment*

A Safety Assessment Document (SAD) was prepared and issued in compliance with the environmental, safety, and health (ES&H) program requirements stipulated by the U.S. Department of Energy (NVO-210, 1980). This SAD documented the identification and control of risks associated with the SFT—C. The three main elements of the SAD are the descriptions of:

- The SFT—C site including surface and subsurface structures.
- The equipment and operations used to perform the test.
- An overall assessment of the potential environmental, safety, and health risks, as well as the consequences associated with postulated abnormal conditions, accidents, and natural phenomena.

In addition, the organizational structure and responsibilities of SFT—C project participants were delineated. The reader is referred to the SAD for details on the state of knowledge that existed at the time of its writing. Currently available information on the site and facilities is provided in Chapters 4 and 5 of this report, respectively, and Chapter 7 provides a description of the handling equipment and related facilities. We focus here on a summary of the safety assessment.

8.1 Site Analysis

In analyzing potential ES&H impacts related to the site, we considered both natural phenomena and the influence of activities at nearby facilities.

8.1.1 Effects of Natural Phenomena

As established in a separate SAD for the EMAD facility, spent-fuel assemblies in storage at that location are protected from all credible adverse meteorological conditions (NVO-198, 1978). The direct effects of such events are likewise nonexistent for spent fuel stored 420 m (1400 ft) underground at the SFT—C.

During transport between the EMAD and the SFT—C, the spent fuel was exposed to potentially adverse meteorological events. Several preventive and mitigating factors were identified that minimized the likelihood of occurrence and the potential impacts of an occurrence. First, operational procedures prevented initiation of movement of spent fuel when severe weather was occurring or was forecast. The effects of flash flooding or snowstorms during transport would stop the convoy until conditions improved or were corrected by onsite road-service crews. Second, the SAD for the EMAD showed that tornado-driven missiles could not penetrate the 330-mm-thick (13-in.) transport cask. Furthermore, locking pins and cask closures that required positive mechanical actions to be opened made it highly unlikely that a canistered spent-fuel assembly would come out of the transport cask even if the cask became detached from the STV. Third, the electrical conductance of the thick-walled cask would prevent damage to the canister due to lightning strike. Fourth, although tornado conditions could damage the hoist used to lower the spent-fuel canister underground, the brake (which travels with the canister) would arrest the fall if the hoisting system were disabled. Fifth, loss of electrical power, the most likely meteorological-related event, would have no impact during transfer; the canister would remain in the access shaft until power was restored. Similarly, meteorological events causing loss of site power or damage to surface structures or control systems would not affect the underground transfer or storage operations. Sixth, surface runoff associated with local flash flooding would be prevented from entering the access shaft by means of diversion ditches and a gasketed cover on the access shaft.

The potential effects of earthquakes were also considered. Since the spent-fuel assemblies were contained in gas-tight canisters, the canister would have to be breached to release radioactive contaminants. Shaker-table testing showed that the canisters sustained negligible damage at maximum horizontal ground accelerations of 0.7 g. During the planned 5-year test period, the probability that an event of this magnitude or larger would occur was estimated to be 3.9×10^{-4} (Campbell, 1980). Furthermore, the probability that a stored canister would rupture was estimated to be less than 10^{-3} for the planned 5-year test period. These unlikely seismic effects could also be expected to damage the personnel shaft, canister access shaft, and possibly the underground workings.

*Contributed by W C. Patrick.

If any of these improbable events did occur after all 11 spent-fuel assemblies were emplaced and if all 11 were somehow breached, releasing the fission-product gases, the radiation dose at the site boundary would be no more than 6 mrem; an insignificant amount compared to the Nuclear Regulatory Commission's reference values of 25 rem whole body and 300 rem thyroid (in 10 CFR 100).

8.1.2 Effects of Activities at Nearby Facilities

Because the EMAD and SFT—C are in remote locations on a controlled-access site, the only activities that could have affected the test were well known. The two most likely of these were seismic disturbances and the release of airborne radioactivity from nuclear-weapons testing.

The SAD concluded that the Climax site was unlikely to sustain seismic damage from testing, since then-current testing restrictions precluded the detonation of large events. In addition, any tests in the general area of the test could be and were coordinated and evaluated on a case-by-case basis with the nuclear-weapons test program.

Venting of underground nuclear events is a credible event. All SFT—C activities were coordinated with the NTS Operations Coordination Center, and in no case were personnel permitted to be at the Climax site during nuclear weapons tests.

8.2 Radiological Impact of Normal Operations

Four normal operations were identified as presenting a potential for radiation exposure to site personnel. No operations were found to constitute a radiological hazard to site personnel, the public, or the environment. These activities—emplacement, post-emplacement operations, and retrieval—span the time frame beginning with SFT—C personnel taking custody of a shielded spent-fuel assembly at the EMAD gates for transport to the SFT—C.

Precautions taken to reduce radiation exposures to as low as practicable included:

- Shielding by means of STV and UTV casks and special interfaces between the STV and access shaft collar at the surface, the UTV and the access collar underground, and the UTV and the storage hole.
- Control-system interlocks that prevented personnel from being accidentally exposed to the spent-fuel canister.
- Leak-tight containment of all radioactive materials in canisters.
- Control systems to prevent dropping or breaking (shearing) a canister.
- Operational access control of surface and underground facilities.
- Radiation monitoring and alarming system.
- Personnel dosimetry, special radiation monitoring, and bioassays.
- Marking and controlling access to all radiation areas where dose rates were greater than 5.0 mrem/h.

During transport from the EMAD to the SFT—C (and the reverse process for retrieval operations), the estimated radiation dose at the STV cab was 3 mrem/h. The two personnel in the cab would receive a maximum 13.5 mrem exposure for each 4.5 h of transporting spent fuel.

Preparing the STV at the canister access shaft was estimated to take 16 to 18 min in a maximum 50-mrem/h field, producing maximum exposures of 15 mrem. Preparing the UTV at the shielding pit (where thermocouples were installed) was estimated to produce maximum doses of 8 mrem to the hands and 5 mrem whole body. In addition to the usual film badges and pocket dosimeters worn by all personnel, workers installing thermocouples were monitored to confirm low doses to hands and eyes.

During post-emplacement operations, the spent-fuel assemblies were heavily shielded by a steel shield plug and concrete-filled storage-hole cover. These were calculated to reduce the radiation level to about 0.5 mrem/h on contact.

Retrieval from the SFT—C and transport of the canistered spent-fuel assemblies back to EMAD were calculated to result in similar radiation exposures as were encountered during the analogous emplacement operations. Exposures were anticipated to be somewhat less due to radioactive decay of the fuel during storage at SFT—C.

8.3 Nonradiological Impact of Normal Operations

No normal operation was determined to impose an unacceptable impact on the nonradiological safety of either operating personnel or the general public. Potential hazards were those associated with handling heavy equipment at the surface and in confined underground spaces. Typical mining-related hazards were not present because all construction was completed, including reinforcement of the underground openings. A postulated hazard was radiolytic generation of hydrogen to explosive mixtures, but this was calculated to be impossible for time periods of less than a century.

Precautions taken to minimize the likelihood of nonradiological hazards included:

- Use of personal safety equipment such as hardhats, safety goggles, and safety shoes.
- Use of approved safety and operational procedures and training.
- Availability of fire extinguishers and automatic Halon fire-suppression systems in critical areas.
- Availability of first-aid supplies and a fully equipped mine refuge station.

8.4 Radiological Impact of Abnormal Operations

Abnormal operations that were considered included equipment malfunctions, operator error, or similar problems that were believed to have a potential for serious consequences. Precautions identified to minimize the likelihood of such events included:

- Inspections, testing, and periodic maintenance of all equipment.
- Training and certification of personnel to include dry run operations with nonradioactive canisters.
- Utilization of verified and approved operating procedures.
- Incorporation of conservative designs and fail-safe control systems and interlocks.

For each major fuel-handling operation, potential abnormal conditions were identified. Since radiation exposure of all SFT—C personnel was to be monitored and limited in accordance with applicable DOE requirements, no undue risk to the health and safety of operating personnel or to the public was determined to result from postulated abnormal operations.

In transporting a spent-fuel canister to or from the SFT—C, abnormal conditions such as traffic delays, failure of STV electrical or mechanical systems, collision, or inclement weather could delay the movement. The convoy leader was authorized to correct such situations or to move personnel a safe distance from the vehicle, if necessary. Minor increases in exposure could occur under these conditions.

Any of several abnormal conditions during preparation to lower the canister or receive it from the test level could result in moderate increases in exposures to personnel who took corrective actions. Among the conditions considered were difficulty positioning the loaded STV, trouble disengaging or removing locking pins, and loss of function of hydraulics or electronics systems.

Once the canister was in the access shaft, the likelihood of exposure of personnel decreased to zero. Thus, no radiological impact would occur during corrective actions if the canister remained in the access shaft. A grapple failure after the canister was in the UTV would require personnel to manually operate it, producing some increase in dose.

Certain failures of the UTV drive jacks, grapple, crane, and gates would require personnel to work in a radiation field of up to 100 mrem/h. In some cases, the canister could be returned to the surface while repairs were made. If the estimated time to complete the repair would result in an unacceptable exposure, provisions were made to incorporate additional personnel shielding.

Corrective actions necessary in the event that a thermocouple was broken or improperly installed were postulated to take a short time, and exposure rates would not exceed 25 mrem/h whole body and 75 mrem/h to the hands.

Potential abnormal operations and their consequences were the same for retrieval operations as for emplacement.

Loss of site power would halt all canister handling operations, ventilation, and personnel hoisting. An uninterruptible power supply (UPS) would maintain all data acquisition and radiation monitoring functions. Such a power loss would cause a canister at any point in the transfer process to remain where it was indefinitely. No impact was anticipated to result. Likewise, loss of power when the fuel assemblies were in

storage would produce no hazard. Even with loss of ventilation for extended periods, the spent-fuel cladding temperatures would remain far below the maximum permissible temperature.

8.5 Nonradiological Impact of Abnormal Operations

Except for underground operations, the nonradiological hazards of abnormal operations at the SFT—C were deemed no greater than most other occupational endeavors. Therefore, only potential abnormal occurrences associated with underground operations were considered, including fire and loss of power while personnel were underground.

To limit the potential for underground fires, the quantities of flammable liquids and gases permitted underground were limited, adequate breakers were provided to prevent heating associated with circuit overloads, and the accumulation of wood and related combustibles was controlled. Fire control equipment such as fire extinguishers and Halon fire suppression systems were available at selected locations, and a refuge station was provided.

Short power outages were anticipated to have little or no adverse impacts. Strategically located battery-powered emergency lights allowed safe egress from the storage rooms where temperatures were as high as 40°C. Natural ventilation was shown to be effective in limiting the increase in air temperature that would otherwise accompany loss of forced ventilation. A ladderway in the personnel and materials shaft was available for emergency egress from the underground.

8.6 Radiological Impact of Postulated Accidents

Three postulated accidents had potential radiological impact:

- Fire or explosion.
- Inadvertent removal of a fuel canister from a shielded cask.
- Dropping a canister down the access shaft.

Each of these postulated accidents, associated consequences, and preventive and mitigating factors are discussed briefly below.

8.6.1 Fire or Explosion

As noted in Sec. 8.5, only a limited amount of combustible material was permitted underground at the SFT—C. Therefore, only a fire during transport by the STV was considered credible. The worst-case hypothetical fire was a collision between the STV and another vehicle with the associated ignition of about 400 L (100 gal) of diesel fuel and about 80 L (20 gal) of gasoline.

Preventive and mitigating factors included: slow [48 kph (30 mph)] movement of STV, use of convoy procedures, prohibition of movement under severe weather conditions, back-up emergency braking systems, availability of fire extinguishers, presence of two trained operators in the cab with certain redundant controls, and the low ignition potential of diesel fuel. Furthermore, the thick shielding of the transport cask would limit the effects on the canister. No radiological hazard was determined to result from the postulated fire or explosion.

8.6.2 Inadvertent Removal of a Fuel Canister from a Shielded Cask

In this accident scenario we only considered a single procedural error or equipment failure because the probability of multiple equipment failures or a simultaneous equipment failure and procedural error was considered negligibly low.

Preventive and mitigating factors for surface operations included: use of top- and bottom-gate locking pins, cautious convoy movement of the STV, assured shielding by mechanical interfaces at the upper access-shaft transfer point, mechanical and electrical stops to limit upward travel of the brake assembly/grapple above the canister, electrical (logical) interlocks, and local radiation monitors that would provide immediate warning. For underground operations, preventive and mitigating factors included: remote handling concept (personnel were not underground during transfer operations), shielding by mechanical interfaces at the lower access-shaft transfer point, and electrical (logical) interlocks on the UTV.

Since the preventive and mitigating factors made it highly unlikely that the postulated accident would occur, we concluded that exposure of personnel to excessive radiation was even more improbable.

8.6.3 Dropping a Canister Down Access Hole

Dropping a canister down the access hole causing the canister to break and rupture all the fuel cladding could release fission-product gases to the environment. In this accident analysis we used the calculated fission-product inventory of the gap, and assumed that the entire inventory was released in an instantaneous puff at ground level, and that atmospheric dilution occurred as estimated using Regulatory Guide 1.25. Details of the methodology and results are provided in the SAD (NVO-210, 1980).

Preventive and mitigating factors included: conservative design of handling equipment, positive grappling of canisters, a brake assembly/grapple subsystem that travelled with the canister and would prevent free-fall in the event of hoisting equipment failure, and the remote location of the test facility.

Maximum radiation exposure at the defined site boundary was estimated to be less than 0.5 mrem. No thyroid dose from radioactive iodine was calculated to occur offsite. Likewise, the effect on site personnel would be minimal because surface radiation monitors would alert the personnel and they would evacuate the area around the access shaft. Release of particulates were expected to be largely contained in the underground structure, but a bank of HEPA filters was installed to further limit dispersal at the surface (Chapter 5).

8.7 Nonradiological Impact of Postulated Accidents

In general, we judged that the potential for nonradiological accidents was less for the SFT—C than for other industrial and mining operations. Two hazards associated with the underground structures were identified. First, it was always possible to fall into the access shaft or the personnel and material shaft. The former was provided with two bolted covers and the latter had a heavy steel cover. These covers were in place with security seals attached when unattended. Personnel working near either shaft were required to use safety belts and lines.

Second, the underground structures could partially collapse. Conservative design and construction, including calculation of the thermal effects of canister and heater emplacement in structurally sound rock, made such an event highly improbable. Only a very severe earthquake (a low probability event, as discussed in Sec. 8.1) could lead to a significant collapse of the roof.

8.8 Nuclear Criticality Analysis

The basic nuclear safety criterion used in this analysis was that: "All spent-fuel canister handling operations, storage facilities, and associated equipment shall be designed to preclude achievement of a critical configuration due to the occurrence of any single credible accident including the effects of natural phenomena. Further, the simultaneous occurrence of two likely or related accidents shall not result in criticality. This double accident requirement need not be met in the case of two simultaneous, unlikely, and unrelated accidents, provided that the probability of occurrence of either of the two accidents is judged adequately low."

Assumptions and considerations and the methodology used in the criticality calculations are detailed in the SAD (NVO-210, 1980).

The following preventive and mitigating factors were included:

- The handling system could only move one fuel assembly at a time so two could not be accidently brought into close proximity.
- Only one PWR assembly would fit in a canister.
- Only one canister would fit in the STV, UTV, or storage hole.
- Grapples were designed to prevent dropping a canister.
- An emergency brake and other measures were provided to prevent a canister from dropping down the access shaft.
- Measures were provided to limit the entry of water into the storage locations.
- Canisters were protected by the STV cask from physical damage by tornado winds and missiles.
- Water could not leak into a canister unless it was dropped down the access shaft or after an extremely low probability seismic event.
- Stored canisters were neutronically isolated by at least 2.45 m (8 ft) of intervening granite.

- A steel shield plug and concrete storage hole cover protect the canister from physical damage while in storage.
- The physical integrity of all geometries were maintainable during any credible fire.
- Probability of occurrence of a significant underground fire was very low because of control of flammables.

8.8.1 Flooding of One or More Canister Storage Holes Containing Canisters

The k_{eff} of a fully moderated and reflected unirradiated fuel assembly was reported to be about 0.89. Since the actual source was spent fuel and since the canister interior would likely be dry, the k_{eff} was expected to be even lower. Flooding could not cause criticality.

8.8.2 Physical Damage of Any Type Due to Dropping

Calculations showed that no configuration of dry spent fuel could produce criticality.

8.8.3 Physical Damage of Fuel Assembly in Canister Combined with Flooding

If water did not enter the canister, no fuel configuration could produce criticality. In no case for irradiated fuel with flooding within the canister was k_{eff} calculated to exceed 0.96. Only disintegrated, unirradiated pellets suspended in an optimal uranium-to-hydrogen ratio and fully reflected approached a near-critical configuration.

8.8.4 Physical Damage of Fuel Assembly, Canister Geometry Not Maintained, and Flooding

A severe earthquake or dropping a canister down the access shaft could rupture the canister and severely damage the fuel assembly. No attempt was made to calculate the k_{eff} for this case because the probability of the dropping accident and subsequent flooding was very low, and the consequence of criticality was also very low (because personnel would not be underground).

8.8.5 Fire in the Canister Drift with Flooding Associated with Fire Suppression

A significant fire was highly improbable, and breach of a canister in the STV, UTV, or storage hole as a result of such a fire was not considered credible. As a result, the postulated flooding would produce a noncritical configuration similar to that described in Sec. 8.8.1.

8.9 Conclusion

It is noteworthy, though not surprising, that few of the postulated abnormal occurrences and no accidents took place during the test. No adverse impact resulted to the health and safety of the general public or operating personnel or to the environment.